Dynamic drive concept using speed dependent power electronics reconfiguration : applied to electrical machines for automotive traction

Dynamic drive concept using speed dependent power electronics reconfiguration

Applied to electrical machines for automotive traction

PROEFSCHRIFT

ter verkrijging van de graad van doctor aan de Technische Universiteit Eindhoven, op gezag van de rector magnificus prof.dr.ir. F.P.T. Baaijens, voor een commissie aangewezen door het College voor Promoties, in het openbaar te verdedigen op woensdag 17 juni 2015 om 16:00 uur

door

Thomas Gerrits

geboren te Meerlo-Wanssum

Dit proefschrift is goedgekeurd door de promotoren en de samenstelling van de promotiecommissie is als volgt:

voorzitter:	prof.dr.ir. A.C.P.M. Backx
promotor:	prof.dr. E.A. Lomonova M.Sc.
copromotor:	dr. J.L. Duarte
leden:	prof.dr. P.W. Wheeler (University of Nottingham)
	Univ.-Prof.Dr.-Ing. M. Doppelbauer (Karlsruher Institut für Technologie)
	prof.dr. M.G.J. van den Brand
adviseurs:	dr. J.J.H. Paulides M.Phil. (Advanced Electromagnetics group)
	ir. C.G.E. Wijnands (Prodrive Technologies)

Dynamic drive concept using speed dependent power electronics reconfiguration

Applied to electrical machines for automotive traction

Aan Marlou en mijn ouders

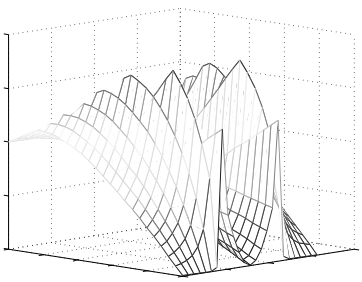

Thomas Gerrits


Netherlands Enterprise Agency

This research is part of the HTAS-EVT-P program (High Tech Automotive Systems - Electric Vehicle Technology - Powertrain). This program is funded by the Netherlands Enterprise Agency, an agency of the Dutch Ministry of Economic Affairs.

T. Gerrits, Dynamic drive concept using speed dependent power electronics reconfiguration: Applied to electrical machines for automotive traction. Eindhoven University of Technology, 2015

Cover design and artwork by TheBruceDickinson productions

A catalog record is available from the Eindhoven University of Technology Library.
ISBN: 978-90-386-3876-8

This thesis was prepared with the pdfLaTeX documentation system.

Summary

Dynamic drive concept using speed dependent power electronics reconfiguration

Applied to electrical machines for automotive traction

The primary objective when designing an electrical vehicle is maximizing its action radius for a fixed battery energy capacity. This objective can be subdivided into, firstly, minimizing the energy required to perform a given vehicle drive-cycle, and secondly, maximizing the efficiency with which the electrochemically stored energy is converted into vehicle motion. The general issue in drive design for vehicle propulsion is the contradiction between the necessary low speed and high torque at the wheels and the arising high machine currents and resulting drive losses. This problem can be solved by means of a high gear-ratio transmission to reduce the torque requirement, but it additionally incorporates mechanical losses reducing the solutions effectiveness.

In this thesis, an unconventional approach is presented that focusses on extending the operating range and boosting the output power of an electrical machine by subdividing it into multiple three-phase winding-sets. By increasing the number of controllable switches in the system, each of the windings can be driven individually or in a combined manner by power electronics reconfiguration. The drive configuration of the proposed system is altered as a function of the angular velocity, such that the limited supply voltage of the inverter can be applied to a matched part of the phase-winding. Effectively, a drive with integrated electrical gearbox equivalent is obtained in this way. Essentially, the weight of the machine is reduced, and the efficiency of the drive is improved by increasing the applied overall voltage. The possibilities offered by choosing this approach are explored, and the possible pitfalls of breakdown due to the expanded complexity are prevented.

Firstly, in Part I the novel dynamic operation concept to maximize the machine angular velocity ratio is proposed. The applied permanent-magnet synchronous-machine model is presented and a method is introduced to transform the infrequent phase currents to stationary balanced-mode and common-mode scalars per-harmonic of the electric rotor angular velocity, to improve controllability. The generalized reconfigurable power electronic topology, required to drive the multi-winding electrical machine, is presented and the advantages and limitations of the proposed system are identified. Based on the general concept, the operating range and output power of a two-windings per-phase drive system are determined and compared to existing solutions, as presented

in literature. The proposed system is implemented and the computed performance is validated by experiments. Additionally, the system reconfiguration steps are explained and a drive configuration transition under full-load-torque is demonstrated.

Secondly, Part II presents two extensions to the open-winding machine drive concept to improve the operating range and reliability of the system. In Chapter 5 a concept is proposed to progressively enhance the inverter voltage range as alternative to field weakening. As a result, the machine can be accelerated above its base angular velocity without the need for a reactive fundamental frequency current. By employing the common-mode current component in the open-winding machine, it is demonstrated that simultaneously the machine can be powered by the fundamental harmonic component of the current while the third-harmonic of the current is used to power the secondary-side inverter through the machine. The analysis is explained and verified by experiments. A relative angular velocity improvement of a factor 1.6 is achieved.

The increased number of switches and windings required for the reconfigurable drive concept enlarges the risk of device and/or winding failures. In Chapter 6 a concept is proposed to cope with different types of faults without the need to stop the vehicle. Principally, the fault-tolerant operation concept is based on the notion that the open-winding machine can be driven in an unbalanced manner with a time-invariant-torque by changing the mutual current phase angles. The modular power electronics structure is used beneficially to re-balance the torque after a failure by applying unbalanced phase currents to the open-winding machine structure. A possible single module breakdown scenario is tested, demonstrating that 80% of the nominal torque can still be produced, thereby validating the concept.

Finally, the conclusions and recommendations of this research are given. The main conclusion is that the presented concepts provide a viable alternative solution to a standard three-phase electrical vehicle drive-line. Each of the presented concepts is validated in practice, and for the benchmark configuration it is demonstrated that an angular velocity ratio improvement of a factor 1.9, and angular velocity range improvement of a factor 3.5 can be achieved when compared to a standard three-phase drive. The increased system flexibility allows for various additional concepts to be explicated. Initiated ideas that can be further elaborated on are presented in the recommendations.

Contents

1

Introduction

"Can't stop the Gods from engineering"

-Red hot chili peppers

1.1 The journey of the automobile

Mankind has always strived for faster and more comfortable methods of transportation. With the invention of the wheel around 3500 BC, and the presence of less fortunate fellow men or animals such as donkeys or, more generally horses, a new standard for transportation was set. Automobiles mark the start of a horseless carriage era in 1770 with the invention of a steam powered, self-propelling vehicle by Nicholas Joseph Cugnot [166]. Later, in 1807, the first vehicle propelled by an hydrogen fuelled internal combustion engine (ICE) was built by Isaac de Rivaz [102]. However, this single cylinder, long-stroke piston engine was considered no vigorous alternative to challenge the steam engine which performance further improved in the meantime. Karl Benz invented and patented the first petrol fuelled automobile in 1886 [11], which he designated as motorwagon. It was considered as the first ICE powered vehicle, or car, that generated its own power, could transport people at a significant speed, and did not look like a horse carriage.

(a)

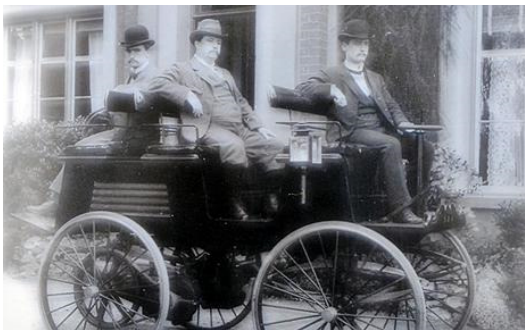

(b)

Figure 1.1: Historical EV implementations; **(a)** electric cart built by Sibrandus Stratingh and Christopher Becker, **(b)** multiple passenger EV invented by Thomas Parker (middle person).

1.1.1 The rise and fall of electrical vehicle propulsion

In 1821, long before Benz invented his motorwagon, Michael Faraday conducted an experiment with which he proved that a wire moving through a magnetic field produces a current [41]. Based on this principle he created the first ever electric machine. Inspired by Faraday, Sibrandus Stratingh and Christopher Becker developed and constructed a self-propelling electric cart which is considered as the forerunner of the electrical vehicle (EV) [132], as shown in Figure 1.1a. The first practical EV with rechargeable batteries was built in 1884 by Thomas Parker [157], as shown in Figure 1.1b.

The EV was favoured by many people over the car in the first decades of the 20$^{\text{th}}$ century for various reasons. Early car designs made a lot of noise, produced stench in the form of exhaust gasses, and leaking oil, and had a bad ease of use, because of for example the starting issues, stationary operation and gear-shifting [169]. The EV, on the other hand, was clean, silent, reliable, and easy to use, which made it especially popular for urban transportation. Therefore, EVs were preferred as taxicabs in different cities worldwide, like Amsterdam, London, and New York. An additional advantage of urban use was the possibility to apply a centralized recharging- or battery-swapping-station [169]. This continuous recharging or swapping of batteries was required as their specific energy was inadequate. Despite the continuous battery development, the specific energy, E_{spe}, only increased from 7.4 Wh/kg in 1881 to 22.2 Wh/kg in 1897 [169]. As a result, the limited driving range remained unsatisfactory and created range anxiety. The high vehicle mass, required to achieve a driving range of 88 km, and resulting battery cost were major disadvantages of the EV. To cope with the aforementioned disadvantages, hybrid vehicles were designed that combined the advantages of high specific energy petrol, being E_{spe} = 12.500 Wh/kg, with electric drive usability. An ICE running at a fixed angular velocity continuously charged a small battery that is in turn powered by one or more electrical machines. The complexity of all these systems combined in one vehicle

made it challenging to produce and maintain, preventing the hybrid EV from becoming a success.

Expansion of the production scale and the standardized production methods introduced by Henry Ford, made the successors of the motorwagon reliable and affordable for the general public, and consolidated the position of the ICE powered automobile. Ford's model T was the first mass-produced car, and with 16.5 million sold vehicles in the period 1908-1927 it is one of the best sold car models to date [1]. The successful development of an ICE starter, water-cooling, clutch, and gear-shift system, improved the ease of use of cars significantly. Continued research and development in perfecting the operation, reliability, and efficiency of ICEs throughout the 20th century, in combination with the availability and energy density of petrol, ensured its position as preferred traction power source. This despite the poor overall energetic conversion efficiency [72].

1.1.2 The re-evolution of electrical vehicle propulsion

In the meantime, the lead-acid battery powered EV developed itself as the preferred transportation method for indoor applications (e.g. fork lifts, loader trucks), repetitive motion (e.g. transit warehouses, airports), off-road (e.g. golf carts), and confined spaces with a minimum air circulation (e.g. mines, construction). In these applications, recharging or battery swapping is easy for the driving area is confined. However, the poor E_{spe} of a modern-day lead-acid battery, i.e. E_{spe} = 50 Wh/kg [72], and the resulting disappointing vehicle driving range remained the main reason for miscarrying a breakthrough of electrical vehicle propulsion (EVP) in the commercial automotive branch. Additionally, the efficiency with which electrochemically stored energy was converted into motion was insufficient due to the usage of DC machines (DCMs), and the dynamic performance was unsatisfactory due to the gross vehicle weight and inevitable gear changes [30]. Nevertheless, there were several inventions that contribute to the renewed interest in, and research funding for, EVP. Each of the following subjects contributed in overcoming the disadvantages that resulted in the diminished technological and economical interest for EVP in the early 1900s [169].

High specific energy batteries

The invention of different mobile devices, but in particular the cell phone, led to a renewed motivation for the development of high energy density batteries. This resulted in the discovery of e.g. nickel metal hydride (NiMH, E_{spe} = 150 Wh/kg) and lithium-ion polymer (LiPo, E_{spe} = 200 Wh/kg) based types [72]. Due to this, the required battery weight for a given amount of stored energy is reduced by a factor 3 to 4 compared to a lead-acid type, thereby significantly reducing the gross vehicle weight, or extending the per-charge driving range. The invention of high specific energy batteries is the key motivator for the renewed potential success of EVP in the 21th century.

A disadvantage of these new battery types is the low nominal cell voltage, i.e. 1.2 V for NiMH and 3.7 V for LiPo. These voltage levels demand for high quantities of series-connected cells to achieve an overall battery pack voltage of a few hundred volts. However, the cell voltages can vary due to internal causes (manufacturing variance, internal impedance, self-discharge rate) and external causes (thermal resistance variation, external impedance). The cell voltages should be balanced to optimize the battery usage, otherwise it can only be used until the weakest cell is considered empty. To efficiently balance the cell voltages passive balancing should be avoided, but conversely accurate modelling [78] and active balancing with power electronics is required [18].

Utility grid interfacing and fast charging

Another major difference between the contemporary situation and that well over a century ago is the vastly improved density of charging locations, and the time required to recharge a vehicle. Where centralized charging of EVs was required a 100 years ago [169], at present, virtually every building is connected to the utility grid. In the Netherlands, this allows for 3.7 kW single-phase up to 29.9 kW three-phase domestic charging or up to 95.6 kW three-phase charging with a common industrial connection.

Fast charging (50% in 10 to 60 minutes) of batteries using power electronics converters is thoroughly investigated in e.g. [164]. A network of 120 kW charging poles, capable of recharging 50% of the model S battery in 20 minutes, is currently being installed by TESLA MOTORS™ in Asia, North-America, and Europe with 279 operational poles to date [158]. With this network of fast chargers, TESLA MOTORS tries to overcome the still existing difference in driving range compared to ICE powered vehicles, and the resulting range anxiety of their customers.

Developments in permanent magnet materials and electrical machines

Electrical vehicle driving range optimization is achieved by maximizing both the battery energy for a given vehicle weight, and the efficiency with which the energy is subsequently converted into vehicular motion. The latter was difficult in the early 1900s for the relatively low DCM efficiency [30, 42]. Additionally, both the AC and DC machine types required a mechanical commutator [46] due to the lack of semiconductor devices, making the machine liable to wear. The development of sintered rare-earth permanent magnet (PM) materials with a high maximum energy product, such as samarium cobalt (SmCo) and neodymium iron boron (NdFeB) have significantly improved the attainable power density of electrical machines [108]. Furthermore, the development of various semiconductor devices greatly improved the controllability and possibilities of electrical power conversion [105]. Power electronics conversion topologies such as the DC to AC inverter topology allow for accurate angular velocity and current control, and provide bidirectional power flow [87].

Modular power electronics

A trend in contemporary power electronics design is the "divide and conquer" method, meaning that by increasing the number of active components, their individual specifications can be derated [43, 98]. The overall system requirements can therefore be met without the need for semiconductor devices capable of conducting the entire load current, and/or applying the whole supply voltage. Two fundamentally different solutions within this framework can be recognized; connecting current sources in parallel, i.e. interleaved [43, 174] and connecting voltage sources in series, i.e. multilevel [92, 98]. The respective current and voltage sources can be composed in various ways. Parallel current sources are applied to increase the overall current rating and interleaved to concurrently increase the effective switching frequency of a converter [43]. By stacking switch modules, the voltage rating per device can be reduced and a higher number of intermediate voltage levels can be applied. As a result of the increased complexity of either system, the characteristics of the whole system can be improved [20], or the required passive filter components can be reduced in value and thus weight, volume, and price [92]. Additionally, these systems can be made tolerant to module failure by either derating the per module usage under nominal load conditions, or derate the post-failure performance.

Each of the new technologies applied for modern-day EVP can be achieved with basic power electronics circuitry:

- Balancing battery cell-voltages is performed with a resistive network [18].
- Fast-charging of an EV is achieved by increasing the utility grid power.
- A three-phase AC machine is normally powered using a standard voltage source inverter (VSI) [105].

Nevertheless, research efforts in different power electronics fields conceived converter topologies that are used to improve the conversion efficiency and system reliability:

- The modular multi-level approach is used to efficiently balance battery cell-voltages by exchanging energy with an active multi-level converter [47].
- Fast-charging with local energy storage reduces the required utility grid power [164], or an alternative energy conversion method improves the efficiency [163].
- The application of interleaved or parallel operated modularity is applied in combination with a multi-three-phase electrical machine structure [93, 108] to provide a scalable-voltage topology and match the limited VSI DC supply voltage, V_{inv}, to the required wide angular velocity electrical machine operating range.

Furthermore, the development of high performance embedded signal processors allows for the application of more complex algorithms to obtain a further improved system controllability and efficiency [39]. Research in electro-mechanics and power electronics with accompanying control systems (CSs) is therefore essential in optimizing the conversion efficiency from utility grid to traction power.

1.2 Longitudinal vehicle acceleration

To get a better insight in the tractive effort required to propel an automobile, a longitudinal acceleration profile based on the torque generated by a machine is derived for a defined case. The dynamics within the presented analysis are restricted to a one dimensional longitudinal movement in combination with a possible incline or decline, based on the available power and torque characteristics. Various textbooks present a thorough description of dynamic effects on ground vehicles; [72, 106, 120] are used for the following description.

Depending on the mutual angle between the road and the surface of the earth, α_r, in a simplified model there are five individual force components (Figure 1.2) and a resultant acceleration force acting on a vehicle when moving forward:

$$\text{Gravitational force:} \quad F_g = m_v g \sin(\alpha_r) \tag{1.1}$$

$$\text{Air-drag force:} \quad F_A = \tfrac{1}{2}\rho_a C_d A_F (u_v + u_A)^2 \tag{1.2}$$

$$\text{Rolling-resistance force:} \quad F_r = \tfrac{1}{2} f_r F_z = \tfrac{1}{2} f_r m_v g \cos(\alpha_r) \tag{1.3}$$

$$\text{Traction force:} \quad F_t = \frac{1}{r_w} T_w = \frac{1}{r_w} \eta_{gb} r_{gb} T_m \tag{1.4}$$

$$\text{Slip force:} \quad F_s = s_N F_t^2 = \left(1 - \frac{u_v}{r_w \omega_w}\right) F_t \tag{1.5}$$

$$\text{Acceleration force:} \quad F_a = m_v a_v = m_v \frac{\mathrm{d}u_v}{\mathrm{d}t} \tag{1.6}$$

$$= F_t - F_g - F_A - 2F_r - F_s = F_t - F_d \tag{1.7}$$

where m_v is the total vehicle mass, g is the gravity acceleration constant, ρ_a is the mass density of air, C_d is the aerodynamic drag coefficient of the vehicle, A_F is the frontal area of the vehicle, u_v is the vehicle velocity in the x-direction, u_A is the air velocity in the x-direction, f_r is the rolling resistance coefficient, r_w is the compressed wheel radius (distance from the centre of the axle to the road surface), T_w is the wheel torque, η_{gb} is the gearbox efficiency, r_{gb} is the gearbox ratio from the electrical machine to the wheels, T_m is the mechanical torque produced by the electrical machine, s_N is the normalized slip, ω_w is the angular velocity of the wheels, and a_v is the acceleration of the vehicle.

Gravity pulls the vehicle backwards with the force F_g if $\alpha_r > 0$ as depicted in Figure 1.2. The air in the atmosphere of the earth, and the air velocity, u_A, with which it is moving in the direction of F_A, counteract the movement of the vehicle with F_A. Equation (1.2) shows that F_A linearly depends on the frontal area of the vehicle, and quadratically on u_v and u_A. The centre of mass of the vehicle is denoted with $\oplus$ in Figure 1.2, and the downforce, F_z, is assumed to be equal on both axes, evenly distributing F_r. The electrical machine applies T_m on the axle, which is transferred with ratio r_{gb} and arm r_w to the road as F_t. The slip force is assumed quadratically dependent on F_t in this analysis. The resultant F_a is defined as the acceleration force, defining it as negative if

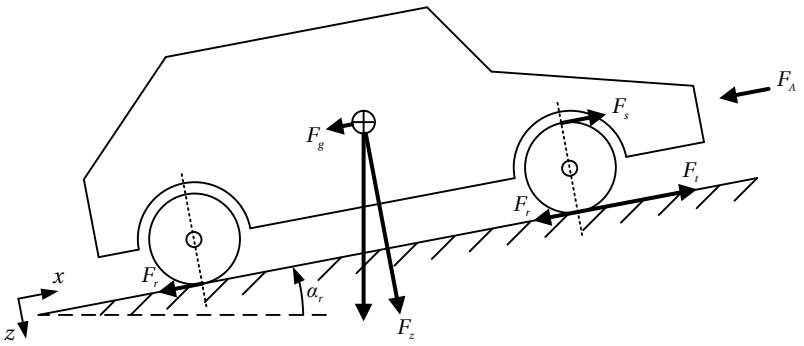

Figure 1.2: Schematic model of a front-axle driven vehicle, showing the different acting force components.

the vehicle is decelerating. Finally, F_d represents the combined drag forces acting on the vehicle.

The dimensionless aerodynamic drag coefficient C_d of a vehicle depends on the body design, surface material, and the direction of the relative air flow. It originates from three sources for the indicated approximated percentages, i.e.: the shape resistance due to the air flow turbulence at the rear of the vehicle (85%), the friction resistance depending on the surface (10%), and the internal resistance due to the flow of air through the vehicle (5%). As a result, C_d can vary from 1.0 for a truck to 0.1233 for the world solar challenge, cruiser class winning, family car of solar team Eindhoven [143]. A typical passenger car has a C_d of 0.2-0.4. The effect of F_z on the tyres is a continuous depression on the road surface as a function of their elasticity and pressure. The depressing and releasing process of rotating tyres is not completely elastic, resulting in heat, and thus loss. This loss is expressed as a ratio between F_r and F_z, or the rolling resistive coefficient f_r, and is typically 0.009-0.015. Furthermore, the wheels of a vehicle slip depending on F_t. The slip is defined as the difference in the velocity of a point on a tractive tyre and u_v, which are equal in e.g. a ball-screw gear transmission. s_N depends on the tyre profile, tyre temperature, road surface, surface condition (wet, dry, temperature), speed, and F_z. Therefore it is usually measured experimentally. In the linear dependency region of s_N versus F_t considered here, s_N is typically 25 μ/N for the tractive axle of the vehicle [106]. By rewriting (1.6), and incorporating (1.7) comprised of (1.1)-(1.5), a_v is expressed as

$$a_v = \frac{1}{m_v}\left(F_t - s_N F_t^2 - \tfrac{1}{2}\rho_a C_d A_F (u_v + u_A)^2\right) - g\left(\sin(\alpha_r) + f_r \cos(\alpha_r)\right). \tag{1.8}$$

Based on F_t, a general solution for the acceleration and speed as a function of time is expressed using (1.8) and (1.6), respectively.

An electric drive is considered as the set of system components transferring the DC (battery) source voltage to mechanical torque, including the control system required

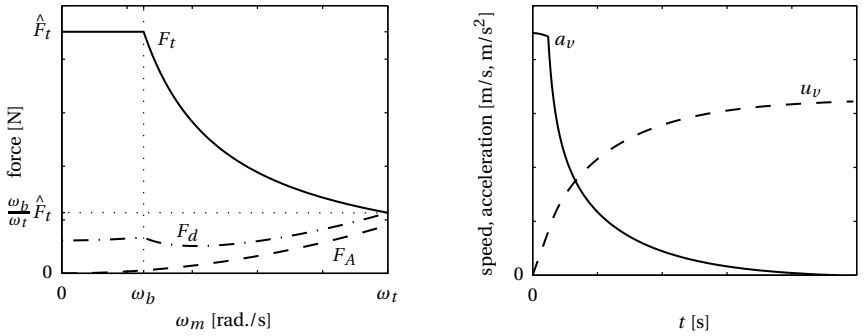

Figure 1.3: Longitudinal vehicle acceleration characteristics; **(a)** traction, F_t, drag, F_d, and air-drag, F_A, forces versus angular machine velocity, ω_m, **(b)** resulting vehicle speed, u_v, and acceleration, a_v, versus time, t.

to do this. The nominal power, $\check{P}$, that an electric drive can produce is presumed to be limited by the voltage that the power electronics can deliver, and the current that the electrical machine can handle. These presumptions determine T_m, and as a result that F_t, (1.4) has a profile versus the mechanical angular velocity, ω_m, as depicted in Figure 1.3a. The peak level of F_t, being $\hat{F}_t$, is limited by the current, while from the base angular velocity, ω_b, it is limited by $\check{P}$. The angular velocity ω_m is limited at the top angular velocity, ω_t. It is assumed that $r_w = 277$ mm (14 inch rim with standard tyre), $r_{gb} = 4.05$, and that $\eta_{gb} = 97\%$. The required vehicle speed range can be obtained using a fixed gear with ratio r_{gb} [109,161], or directly by producing the required range with the electrical machine [143]. This design choice is based on the efficiencies per component and the resultant system efficiency, η_{sys}.

Using F_t and presuming no wind in the Netherlands ($\alpha_r = 0$, $u_A = 0$), a_v is computed using (1.8). From a_v, u_v is derived using (1.6), as shown in Figure 1.3b. The maximum u_v is caused by the finite a_v, which results of the equilibrium between F_t and F_d as illustrated in Figure 1.3a at the maximum angular velocity ω_t. Furthermore, it is indicated that F_d is mainly the result of F_A at high ω_m.

From Figure 1.3, the conclusion is drawn that a high T_m produces a fast acceleration, which is exploited until ω_b. This point, however, also determines the required $\check{P}$ of the electrical machine and as a result for the whole drive. If alternatively the ratio ω_t/ω_b is increased, the same ω_t is obtained with a reduced $\check{P}$. This potentially improves η_{sys} and with it the driving range of the vehicle. Increasing the ratio $\omega_t/\omega_b > 1$ is usually achieved with the field weakening (FW) CS method [28,87], which has limitations and disadvantages. In the following section, different existing electrical, electromechanical, and mechanical drive systems are presented that obtain the required ω_t with a minimized $\check{P}$ in a direct or indirect manner.

1.3 Existing drive systems

The need for a variable transmission ratio in vehicle propulsion is caused by the intention to minimize the overall vehicle mass. To maximize the total transmission ratio of a drive, the required power level of the traction machine for a fixed acceleration is minimized [35]. Generally, the mass of a machine is proportional to the mechanical power it produces. Increasing the angular velocity ratio, $x_s = \omega_t/\omega_b$, and thereby the available average power, reduces the required nominal machine power, $\check{P}$, and thus mass for a given acceleration. However, from [35] it is concluded that this effect of increasing x_s, from 1.5 to 8, reduces the required mechanical machine power, P_m, by a factor 2 for the exemplifying vehicle configuration. However, this effect is greatly reduced if $x_s \geq 4$, i.e. the required power P_m is only reduced from 70 kW to 62.5 kW for $x_s = 4$ to $x_s = 8$, respectively for the presented case. Hence, a trade-off exists between the required drive complexity and power.

In modern-day high-end ICE powered vehicles, this trend translates to high overall gear ratio transmissions, e.g. a manual or automatic eight-stage gearbox [172]. The high number of gears realizes a high angular velocity range, while the automated gear-changing mechanism minimizes the transition time between the different gears, allowing for the fastest possible conversion of the ICE power to the tractive wheels. The best sold car in history (TOYOTA™ Corolla [1]) petrol version is equipped with a five-gear manual transmission with a respective per-gear angular velocity reduction ratio, $r_{gb(1,\,2,\,3,\,4,\,5)}$, and a differential gear with an additional reduction ratio, r_d as indicated in Figure 1.4 [5]. The ICE angular velocity, ω_m, and torque, T_m, are converted to the axle angular velocity, ω_{ax}, and torque, T_{ax}, which are consequently converted to the wheel angular velocity, ω_w, and combined wheels torque, T_w. A schematic representation of these conversions and the torque versus angular velocity relations is depicted in Figure 1.4. In this way, the characteristics of an ICE, with the intended $\check{P}$ but an incorrect T_m versus ω_m relation, are made suitable for traction, and a minimized overall drive-train mass is achieved.

For EVP the situation is slightly different. Naturally, the same physics apply, thus using a high angular velocity ratio x_s reduces the required $\check{P}$, and with that the vehicle mass m_v for predefined longitudinal acceleration performance, but alternative options than a multi-gear transmission exist to improve x_s. The electrical machine has a major advantage when compared to the ICE, i.e. the full T_m is available from $\omega_m = 0$ (Figure 1.5), while ω_t can be chosen up to approximately 1400 radians/second or rad./s with conventional bearings if $\check{P} = 60$ kW [104]. This higher overall angular velocity range for the intended $\check{P}$ allows for a fixed gear-ratio transmission to be applied, avoiding the need for a clutch and subsequent torque interruptions as depicted in Figure 1.5.

The mechanical power P_m produced by a machine is the product of ω_m and T_m, providing two possible strategies to increase P_m. The thermal properties of an electrical machine determine the allowed current density and regarding fixed dimensions thus the

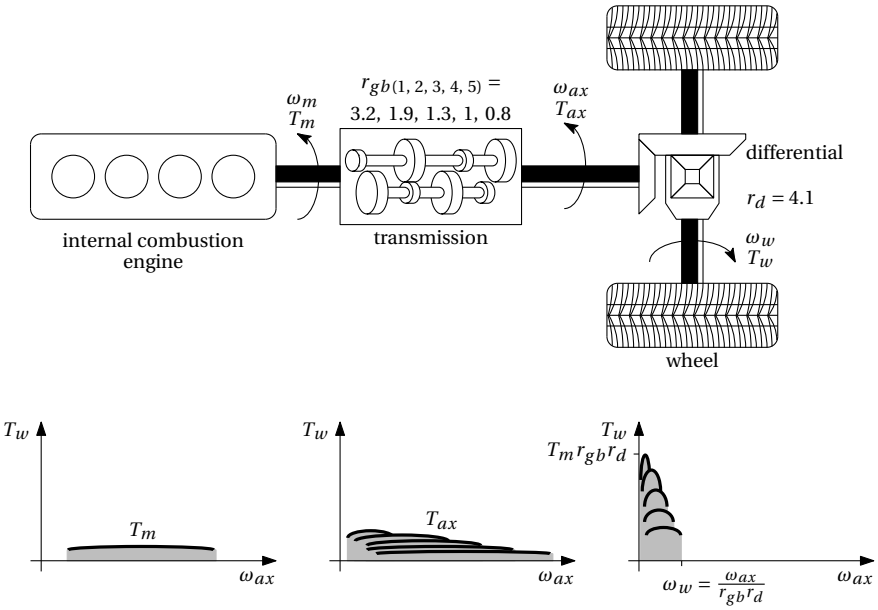

Figure 1.4: Schematic representation of an average mechanical drive-train with ICE, transmission, differential, and wheels. The respective torque versus angular velocity graphs indicate how the ICE torque, T_m, is converted to the required wheel torque, T_w, using the different gear ratios of the transmission, r_{gb}, and the gear ratio of the differential, r_d.

current. Since T_m is proportional to current, an increased torque requires a larger and heavier machine which is undesirable. Therefore, the preferred method of increasing P_m is to increase ω_m. However, the downside is that for a fixed vehicle speed range, increasing ω_m requires a corresponding increase of r_{gb}. Increasing ratio r_{gb} reduces the conversion efficiency as this is inversely proportional to r_{gb}, which is detailed for the commonly applied planetary gear-train transmission type in [25]. *This contradiction between a decreasing electrical machine mass with an increasing nominal angular velocity [106] and consequently decreasing gearbox efficiency with an increasing gearbox ratio, is the breeding ground for vehicle traction research [67].*

A typical mid-sized commercially available EV is the RENAULT^{TM} Zoe [126] with a driveline configuration as shown in Figure 1.5a. An AC radial-flux universal machine was developed for the Zoe, consisting of a three-phase stator winding configuration and a rotor field winding that is powered via slip-rings. This type of electrical machine lacks PMs and the accompanying high power density. However, the reduced torque region is regulated to a fixed P_m by directly regulating the flux linkage produced with the rotor winding. The Zoe has mass m_v of 1500 kg, maximum mechanical power, $\hat{P}_m$, of 63 kW, uniform assumed tyre radius r_w of 0.31 m, maximum torque at the wheels, $\hat{T}_w$, of 2050 Nm, and a wheel angular velocity range of 0-121 rad./s (0-1155 revolutions per-minute (RPM)) which translates to a maximum vehicle speed, $\hat{u}_v$, of 37.5 m/s (135 km/h) [126]. This set of specifications translates via a gearbox with a fixed reduction ratio $r_{gb(R)}$ of 9.32, to a required electrical machine mechanical angular velocity range ω_m of 0-1128 rad./s (10.8 kRPM) combined with a produced mechanical torque range T_m of 0-220 Nm, as shown for the radial-flux electrical machine graph in Figure 1.5b. Other investigated radial-flux based electrical machine solutions to obtain comparable performance with comparable vehicles exist, as for example researched in [33, 109, 123, 154]. The first solution is to match r_{gb} to an existing electrical machine using the transmission ratios available in the vehicle [109]. Secondly, the design of a custom electrical machine for the desired angular velocity range is investigated in [123]. As a third solution, a high-angular-velocity electrical machine combined with a matching transmission ratio is explored in [33]. This concept is further investigated in [154] to minimize the unsprung vehicle mass of an in-wheel EVP concept thereby improving passenger comfort.

Less straightforward solutions are the axial-flux permanent magnet synchronous machine (PMSM), the reconfigurable windings electrical machine, and the so-called twin-speed transmission system. The axial-flux PMSMs generally produces a higher torque than a radial-flux counterpart for an equal $\check{P}$. As such, it allows for a reduced gear-ratio, $r_{gb(A)}$, to achieve the intended characteristics [19, 168, 171, 173], as presented in Figure 1.5b. An automated mechanical two-gears planetary (twin-speed) transmission capable of power-shifting is presented in [140], detailed in [139], and schematically shown in Figure 1.5c. The main intentions with the proposed multi-gear configuration with ratios, $r_{gb(1,\,2)}$, to achieve the required T_w versus ω_w range with a limited ω_m elec-

trical machine, and to try and improve the overall power-train efficiency. The transition between the two gears is chosen such that the most efficient electrical machine operating region is used. The reconfigurable windings electrical machine solution depicted in Figure 1.5d alters the connection method between the VSI and the six windings on the PMSM stator as a function of ω_m [108]. To match the T_m versus ω_m range of the presented PMSM to the intended T_w versus ω_w range, a gearbox with ratio $r_{gb} = 6.7$ is required.

From the electrical drive systems described in this section it is concluded that no unique solution exists to propel a vehicle. However, important features are deduced from the corresponding sub-figures indicated in Figure 1.5 as objectives for innovation, i.e.:

- **(b)** For each of the presented axial- and radial-flux electrical machines, a gearbox is still mandatory to achieve the required torque versus angular velocity range. No solution is suitable for a direct wheel traction drive. However, the required wide constant power angular velocity range shown in Figure 1.5b can destroy the VSI devices in case of a sudden input power loss.
- **(c)** A system with multiple operating ranges has a peak efficiency point per configuration, which can be combined to improve the overall drive efficiency.
- **(d)** By reconfiguring the electrical machine winding configuration (Figure 1.5d) instead of the gear ratio (Figure 1.5c) an inexpensive and straightforward fixed ratio gearbox can be used. However, winding reconfiguration under full-load operation should be possible to optimize the acceleration performance.

Based on these features, solely the power electronics and electrical machine part of a drive system are considered for further investigation. It is assumed that the torque versus angular velocity relation produced by the electrical machine is altered to custom specifications using a fixed ratio gearbox. The intention is thus to maximize the system performance by optimizing the overall angular velocity ratio and efficiency of the system. These intentions are translated to the research goal and objectives of this research, as explained in the following.

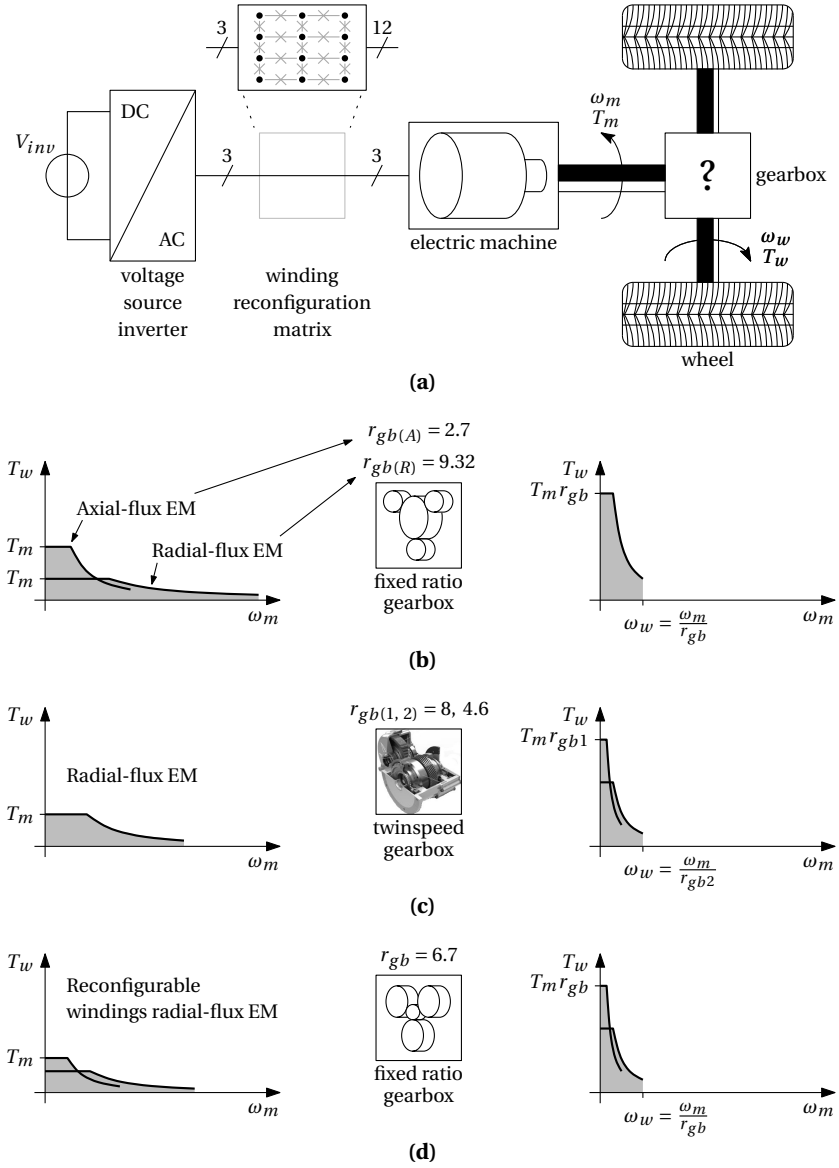

Figure 1.5: Schematic representation of different electrical drive-train solutions; **(a)** general EVP configuration composed of the VSI, electrical machine, gearbox, and wheels, **(b)** conventional configuration with either an axial-flux electrical machine [19,168], with $r_{gb(A)} = 2.7$ based on [171] or a radial-flux electrical machine [33, 109, 123, 154], with $r_{gb(R)} = 9.32$ based on [126], **(c)** radial-flux electrical machine based twin-speed gearbox configuration with multiple T_w versus ω_w graphs [139], **(d)** top indicated intermediate switch matrix solution to alter the configuration of the six stator windings with resulting multiple electrical machine T_m versus ω_m graphs and corresponding T_w versus ω_w graphs [108].

1.4 Research goal and objectives

Natural resources underpin the functioning of the global economy and the level of our quality of life. The pressures on resources are increasing. If current trends continue, by 2050, the global population is expected to have grown by 30% to around 9 billion, and people in developing and emerging economies will legitimately aspire to the welfare and consumption levels of developed countries. Continuing our current patterns of resource use is not an option [36].

Reducing greenhouse gas emissions while maintaining the current level of economical and personal prosperity is a intricate matter. The European commission initiated a flagship initiative with headline targets of 20% greenhouse gas emission reduction, 20% sustainable energy sources, and 20% improvement in energy efficiency, i.e. the 20-20-20 initiative [36]. According to the latest numbers of the European commission [37], about 33% of the total European energy consumption is attributed to the transportation sector, while 24% is consumed by the industrial sector. Therefore, a significant overall reduction of energy usage is achieved if these percentages are lowered.

The goal of the research presented in this thesis is: **devise a drive concept for automotive traction with which the performance of both the power electronics and the electrical machine is advanced, when compared to a standard drive solution.** This goal is compounded since the performance improvement is regarded as the improvement of the achievable machine output power, the drive reliability, and the concept versatility.

By enhancing the obtained output power of a given electrical machine, it is expected that the vehicle weight for a given drive-cycle or vehicle-action-radius is decreased. As a result, the energy required for a given tractive effort is reduced, thereby improving the efficiency with which the vehicle is operated. The reduced energy consumption, in combination with the altered propulsion energy source from fossil fuels to sustainable energy sources, furthermore provides a long-term solution as strived for by the European road transport research advisory council [38].

Augmenting the EV reliability is an important feature for the automotive industry. A flat tyre interrupting the journey is tolerated by the driver, as long as the destination can be reached. The same counts for a reduced vehicle performance for example by deteriorating engine power. The drive system to be developed, should preferably be modular and dividable to improve the reliability, but redundancy should be avoided to optimize component usage, overall weight, and costs. A component is considered redundant if it has no use during normal operation of the drive, but is solely started when one or more normally used components fail.

Improving the drive versatility is widely interpretable. Primarily, the conception of alternative methods to advance the drive performance in terms of output power or

efficiency within the obtained operating range is pursued. Additionally, other functions such as charging the EV by re-using the traction drive components enhances the concept versatility. On the other hand, if the output power of this EVP concept is improved, the idea might be suitable for application in other drive systems (hoisting cranes, drills), generator systems (windmills, tidal-wave generators), and industrial processes (assembly lines, robotics).

To generalize the test-case, a given battery energy capacity, battery voltage, gross vehicle weight, drive-cycle, and user behaviour are assumed for which the driving range of a vehicle should be optimized. The minimum nominal power for a given tractive effort is obtained by maximizing the angular velocity range of the drive as strived for by the solutions presented in the preceding section. The efficiency is optimized by minimizing the required current for a given torque, and by minimizing the number of sequential loss components in the drive-line. Minimizing the required RMS current level for a fixed output power directs towards a scalable output voltage solution that is consistent with the interleaved modular power electronics strategy [43, 174], and the series-to-parallel reconfiguration of an isolated modular switched-mode power supply (SMPS) [29].

Within the research presented in this thesis, the aim is to find a proper solution that meets the proposed goal. The goal is translated into a set of objectives that should be addressed:

1. **Devise a generalized modular drive concept:**
   (a) To make the drive system suitable for general usage, it should be scalable in terms of output power, applied voltage, current, and the number of modules.
   (b) The required power level for a fixed acceleration profile should be minimized. Maximizing the ratio between constant-power speed region and the constant-torque speed region is the most straightforward method to achieve this.
   (c) To minimize the required current level, the available voltage range should be used in an optimal manner. This can be achieved by applying interleaved- or parallel-modules operation.
   (d) Torque interruptions should be avoided. If shifting between configurations or gears is required, this should be possible under full-load conditions.
2. **Devise a method to prevent a total system halt after failure of a subsystem:**
   (a) To avoid (successive) device breakdown, a high field weakening ratio is not allowed. By ensuring that the EMF voltage produced by any of the electrical machine phases is lower than the breakdown voltage of the semiconductor devices, this is prevented.
   (b) Investigate alternative solutions to field weakening to further improve the reliability of the system.
   (c) The system should be composed modular, such that a single or multiple fail-

ures in either the power electronics and/or electrical machine components are not critical to the functioning of the whole drive.

(d) A fault handling strategy should be conceived to continue operation of the drive using all the remaining viable modules. A minimized overall system degradation is ensured in this way.

(e) All system components should be used during healthy operation of the drive, redundancy should not be required to achieve a high reliability.

3. **Verify the devised concepts by experiments:**

   (a) The system should be modelled such that resulting quantities correspond to those in the actual measurements. The system behaviour should be well predictable.

   (b) A proper control method should be proposed and implemented to regulate the system to the intended levels.

   (c) To be able to verify the ideas, a setup should be created, capable of measuring the required quantities.

   (d) Verify the concepts experimentally by simulations and measurements.

1.5 Thesis outline

The preceding research objectives are addressed in the thesis in three main parts. The vehicle speed dependent reconfigurable power electronics topology realizing the dynamic drive operation (DDO) principle covering objective 1 is motivated and detailed in Part I. In Part II, two extensions to the open-winding machine drive concept used for DDO are presented which together cover the subjects mentioned in objective 2. Objective 3 is met per subject in the respective parts. Finally, in Part III conclusions regarding the proposed principles are listed per part, the main contributions are substantiated by comparison with the initial research objectives, and recommendations for further research are given.

1.5.1 Part I: Dynamic drive operation

- Chapter 2 first presents the conventional PMSM model and defines the different angular velocity ranges based on the limitations of both the power electronics and electrical machine. A selection of existing solutions extending the base and top angular velocity of a traction drive system is presented next. Subsequently, an open-winding three-phase machine model is described because this machine winding configuration is required for the concepts analysed in the following chapters. Finally, a general method is proposed to regulate the different current components present in an open-winding drive.

- In Chapter 3, the basic concept of winding reconfiguration, named DDO, is explained and a general power electronics topology capable of driving the electrical machine in the different modes is proposed. Additionally, an angular velocity range comparison with existing drives is executed to demonstrate the improvement and explain the analogy of an electrical gearbox equivalent.
- The transition between different operating modes is demonstrated in Chapter 4, to ensure that this critical step in achieving dynamic drive operation is possible. A motivation, basic explanation, possible implementations, and experimental verification are set forth to specify the procedure.

1.5.2 Part II: Open-winding concept extensions

- An alternative method to FW, named voltage range enhancement (VRE) is proposed and expounded in Chapter 5. The basic principle and main considerations are explained, and a method for minimization of the boosting current required for VRE is detailed and verified by simulation for an idealized electrical machine model. Furthermore, the required topology adaptations to execute both DDO and VRE with one unifying power electronics circuit are explained. Boosting current minimization is explained for the real system, after which experimental verification is used to demonstrate the VRE concept.
- The DDO concept has a higher single device and/or winding failure probability due to the increased number of components and resulting system complexity. In Chapter 6, a general fault-tolerant operation (FTO) concept is presented, allowing for a continued drive operation after failure of one or more components. Using the theory and regulation method presented in Chapter 2, a time-continuous torque is produced, independent of the number of viable drive modules. The required control adaption method to cope with either one of such fault scenarios is explained for the applied system configuration, and the FTO concept is put in practice. A single device failure scenario is expounded after which the output torque is re-stabilized. Experimental verification is performed to demonstrate that the applied modelling is adequate, and that the system behaviour is predicted correctly.

1.5.3 Part III: Closing

The conclusions of the research presented in this thesis are stated in Chapter 7. Moreover, the main scientific contributions are emphasized, a reflection on the objectives of Section 1.4 is given, and recommendations for further research are addressed.

Part I

Dynamic drive operation

2

Drive modelling and angular velocity range

"Discovering physical limitations by modelling and analysis"

Abstract: *In general, drive systems are modelled using a rotating reference frame transformation considering solely the fundamental harmonic of the electric machine frequency. Using this transformation, the basic factors limiting the machine angular velocity and impacting the operating range, are explained. A survey of existing solutions, reducing the effect of these factors, is presented with their advantages and disadvantages. This is followed by the introduction of a per-harmonic rotating reference frame transformation. For this, an extended open-winding model of the permanent magnet synchronous machine is proposed, employing the notion that the harmonics of the electric machine frequency are dominant in a drive. Within the per-harmonic based reference frame transformation, each balanced-mode and common-mode component is extracted from the phase currents using an estimator, as demonstrated. Finally, it is shown that the per-harmonic per-mode components are individually regulated by applying the proposed reference frame transformations and conventional controllers.*

2.1 Introduction

The three-phase balanced AC configuration is the standard system for electric power generation, transportation, and consumption because of the constant output power obtained by combining the per-phase powers [149]. The phase-count of three is the lowest number to achieve a power balance from exciting a single frequency, thereby minimizing the required conductor material for a given power level, clarifying its preference. The three-phase configuration is also the preferred configuration for contemporary EVP drive systems [176], mainly for drawing a constant power from the DC source. A drive system is considered in this work as the combination of one or more VSIs with an electrical machine, as schematically shown in Figure 1.5a. The VSI converts the DC input voltage, V_{inv}, to three AC voltages, v_a, v_b, v_c, with a variable frequency. Each AC voltage powers a phase of the electrical machine, which consequently converts the electrical power to mechanical power at the axle. Numerous books exist on modelling different aspects of the VSI [105, 106], the electrical machine [65, 72, 121], and more specific on the control of drive systems [28, 87].

In this chapter, first a basic model of the PMSM is presented, required for the determination of the angular velocity ranges as explained subsequently. From that, the limitations of a conventional drive become clear. A survey of existing solutions to increase the angular velocity range of a traction drive is given next. Finally, an extended generalized per-harmonic, per-mode machine modelling method is presented which is used throughout this thesis.

2.2 Stationary two-axis model

A stationary two-axis idealized equivalent model can be applied to a rotating balanced three-phase electrical machine, if for that machine the sum of the phase currents is zero. This representation is valid only if the machine is considered as being non-saturated, thereby assuming linear dependencies. The rotor-oriented coordinate system is based on the direct- and quadrature-axis, where the direct, d-axis, is the axis along the radial magnetization of the rotor, and the quadrature, q-axis, lies electrically perpendicular and ahead of the d-axis. The orthogonal reference frame rotates in a counter clockwise direction for positive rotation. This (fundamental angular velocity direct-, quadrature-axis $(d1, q1)$)-axis transformation, as detailed in Figure 2.1, was first described by Park [115, 116], and is therefore called the Park transformation. This method to transform the voltage, current, flux (linkage), inductance, or power is especially useful when combining it with a field orientation based CS [12]. In [130] the advantage in CS bandwidth of the stationary over the synchronous regulator is demonstrated. In the following analysis, the fundamental angular frequency direct, $d1$, and quadrature, $q1$, subscripts are employed to denote the respective quantities. It is furthermore assumed

that no higher order harmonics are present in the transformable quantities.

To transform the stationary three-phase reference frame (a, b, c) to the periodic rotating $(d1, q1)$-axis reference frame, the electrical rotor position, θ_e, is used. The electrical rotor position θ_e is the product of the number of rotor pole pairs, N_{pp}, and the mechanical rotor position, θ_m, with respect to a fixed point on the electrical machine stator $\left(\theta_e = N_{pp}\theta_m\right)$, as illustrated in Appendix B. Throughout this research, position θ_e is aligned with phase a, and used to translate the respective periodic phase quantities, x_a, x_b, x_c to the direct, x_d, and quadrature, x_q, scalar quantities like

$$\begin{bmatrix} x_d \\ x_q \end{bmatrix} = \mathbf{T} \begin{bmatrix} x_a \\ x_b \\ x_c \end{bmatrix} \text{ where } \mathbf{T} = \frac{2}{3} \begin{bmatrix} \cos(\theta_e) & \cos\left(\theta_e - \frac{2\pi}{3}\right) & \cos\left(\theta_e + \frac{2\pi}{3}\right) \\ -\sin(\theta_e) & -\sin\left(\theta_e - \frac{2\pi}{3}\right) & -\sin\left(\theta_e + \frac{2\pi}{3}\right) \end{bmatrix}, \tag{2.1}$$

resulting in a stationary representation, with $\mathbf{T}$ being the stationary three-phase to rotating orthogonal two-axis transformation matrix. The factor $2/3$ in $\mathbf{T}$ is required for an equal amplitude transformation, but because this is valid for the quantities current, voltage, inductance, and flux (linkage), this transformation is power variant. The complete amplitude-invariant transformational relation between the stationary orthogonal, the three-phase, and the rotating orthogonal reference frames is detailed in Appendix B. The inverse transformation from the rotating orthogonal two-axis reference frame quantities to the stationary three-phase quantities is computed with transformation matrix, $\mathbf{T}^{\dagger}$, where

$$\mathbf{T}^{\dagger} = \begin{bmatrix} \cos(\theta_e) & -\sin(\theta_e) \\ \cos(\theta_e - \frac{2\pi}{3}) & -\sin(\theta_e - \frac{2\pi}{3}) \\ \cos(\theta_e + \frac{2\pi}{3}) & -\sin(\theta_e + \frac{2\pi}{3}) \end{bmatrix}. \tag{2.2}$$

2.3 Fundamental permanent magnet synchronous machine model

PMSMs are widely used for EVP [9] because of their high energy density. Throughout this thesis, only non-salient surface permanent magnet synchronous machines (SPMSMs) (Appendices C, D) are applied. The computations and models are therefore also devoted to this electrical machine type. A linear model behaviour of the SPMSM is assumed, therefore saturation, rotor-position related parameter dependency, and temperature dependency are not taken into account.

A wye-connected three-phase electrical machine equivalent circuit including stator resistance, R_{st}, stator inductance, L_{st}, and EMF per respective phase, e_x (with subscript $x \in [a, b, c]$), are expressed in a two-axis equivalent circuit and spacial vector quantities diagram using (2.1), as proposed in [21] and detailed in Figure 2.1. The spacial voltage

vectorial and spacial current vectorial representation of Figure 2.1a is projected on each individual $(d1,q1)$-axis as shown in Figure 2.1b, such that scalars are regulated. The orthogonal $(d1,q1)$-axis reference frame rotates at the angular velocity of the observed harmonic. Usually, solely the fundamental electrical angular velocity, $\omega_e = N_{pp}\omega_m$ is observed, but in Section 2.6.3 this is extended with other harmonics. The frame rotates with respect to the initial position α, which is defined as the position aligned with the spacial flux vector produced by stator phase a as depicted in Figure B.1c. According to the Kirchhoff voltage law (KVL), the fundamental frequency inverter spacial voltage vector,

$$\vec{v}_1 = \vec{v}_{R_1} + \vec{v}_{L_1} + \vec{e}_1, \tag{2.3}$$

where spacial voltage vector, $\vec{v}_{R_1}$ is the $(d1,q1)$-axis transformed fundamental frequency voltage across R_{st}. Equivalently, the same applies for L_{st} with spacial voltage vector $\vec{v}_{L_1}$. Both voltages depend on the fundamental frequency spacial current vector, $\vec{i}_1$. The fundamental EMF spacial voltage vector, $\vec{e}_1$, is by definition aligned with the q-axis, i.e., $|\vec{e}_1| = e_{q1}$. A proportional relation exists between the EMF and ω_m, defined as

$$e_{q1} = K_e\omega_m, \tag{2.4}$$

with K_e being the electrical machine constant if solely the fundamental frequency component is considered. The amplitude-invariant transformations (2.1), (2.2) ensure that no additional constant is required in (2.4).

The spacial vector representation is defined using a set of angles, i.e. the angle between voltages $\vec{v}_1$ and $\vec{e}_1$ is δ (mutual voltage relation), the angle between current $\vec{i}_1$ and voltage $\vec{v}_1$ is φ (current-voltage relation), and the angle between currents $\vec{i}_1$ and i_{q1} is ϕ (mutual current relation). Each angle is defined positive in the direction of rotation i.e. in the direction of the electric angular position, θ_e. As a result, the negative d-axis directed projection of $\vec{v}_1$, being $v_{d1} = \vec{v}_1 \sin(\delta)$, is indeed negative as shown in Figure 2.1b. This definition is used advantageously to translate each spacial quantity to scalar components as depicted in Figure 2.1b. The projections of the machine voltages on each respective $(d1,q1)$-axis are

$$v_{d1} = R_{st}i_{d1} - \omega_e L_{q1}i_{q1} = v_{R_{d1}} - v_{L_{d1}}, \tag{2.5}$$
$$v_{q1} = K_e\omega_m + R_{st}i_{q1} + \omega_e L_{d1}i_{d1} = e_{q1} + v_{R_{q1}} + v_{L_{q1}}, \tag{2.6}$$

where L_{d1} and L_{q1} are the equivalent inductances on each respective axis, composed of magnetizing and leakage components.

The angles in Figure 2.1a are defined such that the respective apparent, active, and reactive electrical machine input power provided by the VSI, being S_{VSI}, P_{VSI}, and Q_{VSI},

respectively, are determined in the conventional manner [165], like

$$P_{VSI} = \tfrac{3}{2}\,|\vec{v}_1||\vec{i}_1|\cos(\varphi), \tag{2.7}$$

$$Q_{VSI} = \tfrac{3}{2}\,|\vec{v}_1||\vec{i}_1|\sin(\varphi), \tag{2.8}$$

$$S_{VSI} = \tfrac{3}{2}\,|\vec{v}_1||\vec{i}_1| = \sqrt{P_{VSI}^2 + Q_{VSI}^2}. \tag{2.9}$$

As a result of the orthogonality of the rotating reference frame, a direct cross-coupling occurs; the voltage across L_{d1}, being $v_{L_{d1}}$, is caused by the $q1$-axis current, i_{q1} (2.5), and vice versa in (2.6), as shown in Figure 2.1c and Figure 2.1d respectively. For a SPMSM, the electromagnetic torque, T_{em}, is expressed in the $(d1, q1)$-axis frame as

$$T_{em} = \tfrac{3}{2} K_t i_{q1}, \tag{2.10}$$

where the torque machine constant, $K_t = K_e$ because of the applied amplitude-invariant transformation. Therefore, no distinction between K_e and K_t is made for the remainder of this research. The resulting electromagnetic power, P_{em}, produced by the SPMSM is derived with

$$P_{em} = \omega_m T_{em}. \tag{2.11}$$

The mechanical response of the rotor based on T_{em} depends furthermore on the load torque, T_l, the inertia of the drive-line, J_m, and the combined mechanical friction coefficient of the bearings of all the drive-line components, B_m. Accordingly, the torque balance equation is written as

$$T_{em} - T_l = J_m \frac{\mathrm{d}\omega_m}{\mathrm{d}t} + B_m \omega_m. \tag{2.12}$$

The Park transformation proves to be very useful for a first-order behavioural approximation of SPMSMs because of the direct relation between i_{q1} and T_{em} (2.10). Therefore, a scalar based CS is applied which is unsensitive to the variable operating frequency of a drive. A major drawback of the two-axis method is that it assumes that the phase currents are balanced, i.e. the sum of the phase currents is zero. This is not necessarily the case in the open-winding configuration in which the electrical machines are used in this research, as clarified in Chapter 3. Furthermore, in Chapter 6 a method to re-stabilize the produced torque after a failure is proposed which requires unbalanced phase currents. Using the method presented in Section 2.6.2, this discrepancy is solved.

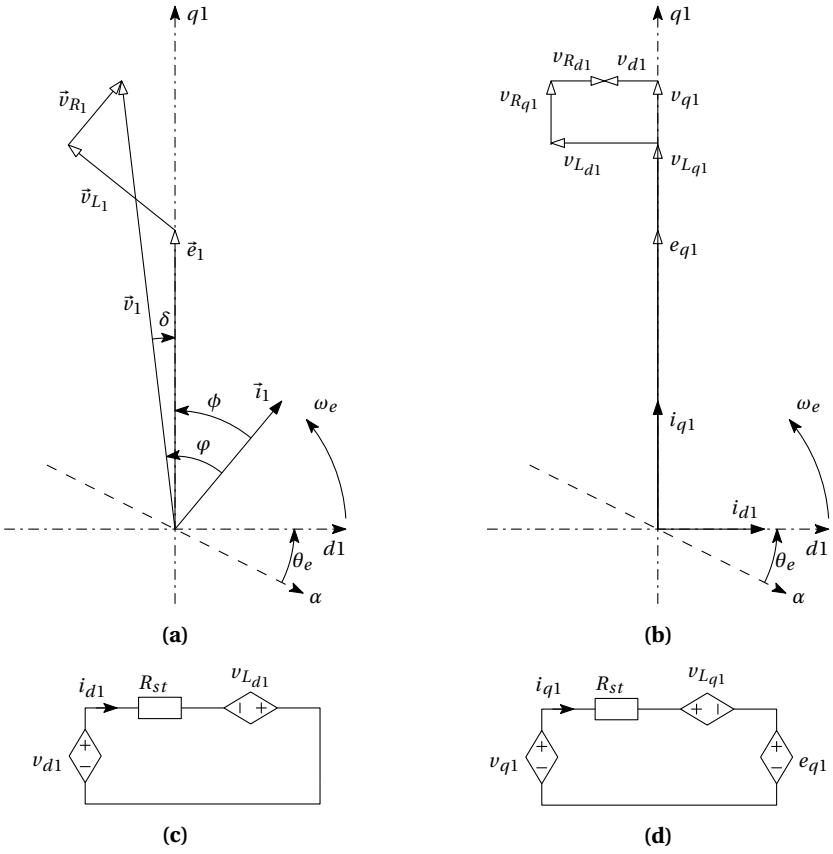

Figure 2.1: The $(d1, q1)$-axis transformed; **(a)** vector diagram rotating at ω_e and with offset angle θ_e with respect to the stationary α-axis, **(b)** scalar diagram rotating at ω_e and with offset angle θ_e with respect to the stationary α-axis, **(c)** $d1$-axis equivalent circuit of **(b)**, **(d)** $q1$-axis equivalent circuit of **(b)**.

2.4 Electrical drive operating regions

Different operating quadrants of an electrical machine are distinguished based on the polarity of the angular velocity and torque. Throughout this thesis, the focus is on the first-quadrant operation of an electrical machine, i.e. motor-mode where $\omega_m, T_{em} \geq 0$. Additionally, within each quadrant different drive modes are identified based on the relation between $\vec{e}_1$ and $\vec{\imath}$. From the existing operating modes [72, 106], only the constant-torque speed region (CTSR)[1] and the constant-power speed region (CPSR)[1] operating modes are considered. The specific angular electrical machine velocities, defining the per-region limit, are explained in the following for the case that only the fundamental harmonic component is present.

Base angular velocity

With an increasing ω_m, the induced EMF, e_{q1}, rises according to (2.4). The base angular velocity, or alternatively named base speed, ω_b, of the system depends on the drive system as a whole. That is; on factors of both the electrical machine and the power electronics converter that supplies $\vec{\imath}$. The nominal RMS per-phase current, $\check{I}_x$, is defined as the current level that the machine can continuously conduct without overheating above a prescribed maximum temperature. If solely the fundamental frequency current is assumed, this results in $\check{\imath}_x = \sqrt{2}\check{I}_x$. Consequently, the maximum steady state fundamental frequency current magnitude $\left|\hat{\vec{\imath}}_1\right| = \check{\imath}_x$. This determines the resulting maximum current contour indicated in Figure 2.2. As shown in Figure 2.1, the magnitude, angle combination of $\vec{\imath}_1$ is rewritten as $(d1, q1)$-axis current components, i_{d1}, i_{q1}, with mutual relation

$$|\vec{\imath}_1| = \sqrt{i_{d1}^2 + i_{q1}^2} \tag{2.13}$$

The primary power electronics based limitation of the drive system is the maximum $\vec{v}_1$ it can apply to the electrical machine. The maximum magnitude contour of $\vec{v}_1$ is also indicated in Figure 2.2. ω_b is defined as the level at which the voltage vectorial sum of $\vec{v}_{R_1}$, $\vec{v}_{L_1}$ and $\vec{e}_1$ in (2.3) is equal to $\left|\hat{\vec{v}}_1\right|$ while supplying $\left|\hat{\vec{\imath}}_1\right|$ to the electrical machine (2.5), (2.6). Analogue to $\check{\imath}_x$, the maximum steady state fundamental frequency voltage magnitude, $\left|\hat{\vec{v}}_1\right| = \check{v}_x$. In the open-winding machine structure case investigated here, space vector modulation (SVM) is disregarded, limiting the pulse width modulation (PWM) amplitude to unity [105].

The idealized electromagnetic power, P_{em}, and torque, T_{em} as a function of ω_m, produced with a drive system under nominal conditions, are depicted in Figure 2.3. The nominal power, $\check{P}$, and torque, $\check{T}$, levels at which the electrical machine temperature

[1] Speed is used here to indicate the angular velocity of the electrical machine axle since this is the commonly applied abbreviation.

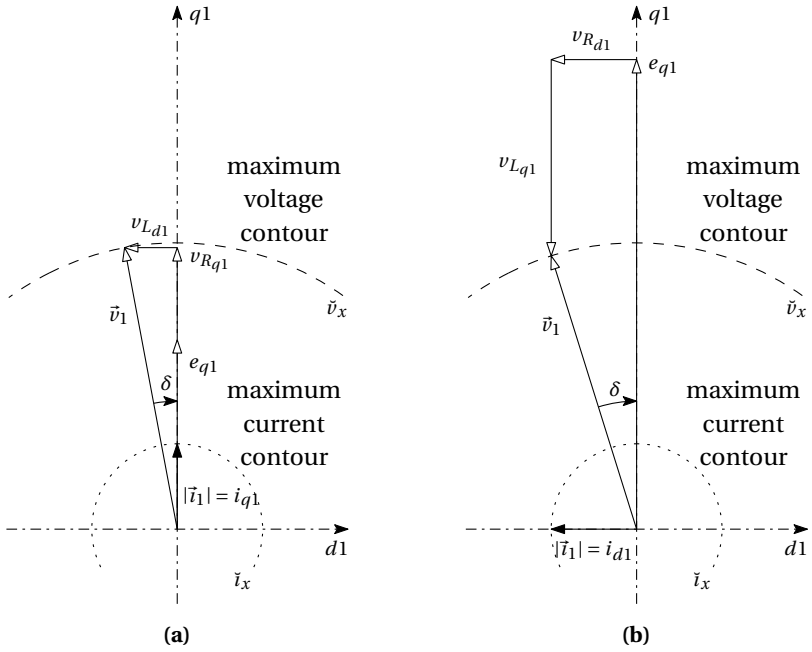

Figure 2.2: The $(d1, q1)$-axis transformed steady state relations for a SPMSM at **(a)** base angular velocity, ω_b, and **(b)** top angular velocity, ω_t, when applying FW.

stabilizes at a safe maximum are indicated. Due to the nominal current requirement to define ω_b, it is a single point (•) instead of a line on both the idealized power and torque versus angular velocity curves in Figure 2.3.

Maximum torque per-ampere

The maximum torque per-Ampère or alternatively named optimum torque per-ampere control mode [87], is a method to maximize the ratio $T_{em}/\vec{\imath}$ in the CTSR for any given machine. The optimal combination of currents i_{d1} and i_{q1} to maximize T_{em} depends on the type of electrical machine and its construction [65, 121]. For the SPMSM this is straightforward as concluded from (2.10), i.e. $|\vec{\imath}_1| = i_{q1}$, as depicted in Figure 2.2a.

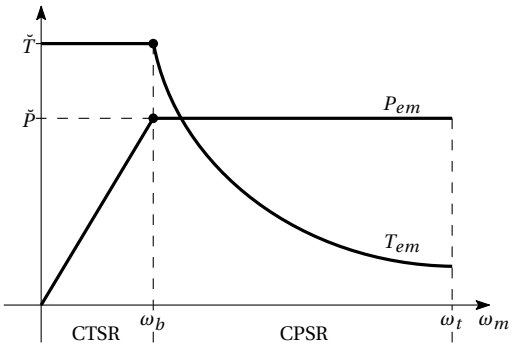

Figure 2.3: Idealized electromagnetic output power and torque of an electrical machine versus the angular velocity, with the indicated constant-torque, (CTSR) and constant-power, (CPSR) regions, left and right of ω_b, respectively.

Field weakening

Without adaption of the current relation as applied in Figure 2.2a, ω_b would be the maximum attainable ω_m in the given configuration. However, by reducing the torque producing current and oppressing a negative i_{d1} (such that $\vec{\imath}_1$ is kept constant according to the maximum current contour, $\check{\imath}_x$, in Figure 2.2b), the effective electrical machine terminal voltage $\vec{v}_1$ is decreased. This allows for a further increase of ω_m until the maximum voltage contour, $\check{v}_x$, is again reached. This principle of altering the current angle to allow for a further increase of ω_m, and with it the EMF, is called field weakening [80, 142]. As a result of the required increase of the reactive current i_{d1} and the overall current limitation, the torque producing current, i_{q1}, is reduced. This process is continued until $|\vec{\imath}_1| = i_{d1}$, as depicted in Figure 2.2b, at which no torque is produced anymore. Numerous references on FW exist, but especially [136] utilizing [137] and the effect of saliency as contemplated in [113, 146], give a thorough description.

Top angular velocity

The top angular velocity, or alternatively named top speed, ω_t, is defined as the maximum ω_m that can be obtained with a drive system when applying FW. The theoretical ω_t of a PMSM is determined by the relation between the magnet flux linkage, Λ_m, current, i_{q1}, and the d-axis inductance, L_{d1}, as detailed in [97, 106]. Depending on that relation, ω_t is finite if $\Lambda_m > L_{d1} i_{q1}$ or theoretically infinite if $\Lambda_m \leq L_{d1} i_{q1}$. Additionally, in [112], an extensive analysis of the underestimated influence of the winding resistance, R_{st} on ω_b and ω_t is expounded.

Angular velocity ratio

The angular velocity ratio, x_s, is defined as the ratio between the top angular velocity and the base angular velocity, considering rotation in equal direction. As such,

$$x_s = \frac{\omega_t}{\omega_b}. \tag{2.14}$$

As conceived from Figure 2.3, an increasing x_s improves the relative CPSR, and with it the time available to accelerate with nominal power, $\check{P}$. In other terms, for a given $\check{P}$ and vehicle parameters, the fastest acceleration is achieved with the highest x_s.

2.5 Existing solutions to increase the base- and top-angular velocity

The overall angular velocity ratio, x_o, of a drive-line is the result of the different angular velocity ratios x_s of all the system components. If, for example, $x_o = 4.2$ is required, this can for example be achieved by combining the angular velocity ratio of an electrical machine ($\omega_b, \omega_t = 100,210$ rad./s, $x_{s(EM)} = 2.1$) with that of a twin-speed gearbox ($x_{s(gb)} = 2$) [139]. Numerous solutions to improve x_s in both the power electronics and the electrical machine field were previously proposed, which are sorted accordingly. The primary research motivation of each of the following solutions is the improvement of x_s, additional advantages are given per solution. The presented selection is non-exhaustive but merely a listing of commonly applied or unconventional ideas in either the power electronics field or applied to a SPMSM. Fully mechanical systems such as [139] or other electrical machine types are not considered since they are beyond the scope of this research. Alternatively, a fixed ratio gear is considered to alter the per-solution achieved range of ω_m and the mechanically produced electrical machine torque, T_m, as long as the electromagnetic drive system provides the required x_o.

2.5.1 Power electronic solutions

The primary goal of the power electronics circuit connected between the DC (battery) supply voltage and the electrical machine is the conversion from a DC voltage to a variable frequency and amplitude AC voltage. Each of the presented methods influences the maximum speed and the overall speed range of an electrically propelled vehicle, and are listed per principle in this subsection.

Due to the discrete voltage breakdown limitation levels of semiconductor switches, v_{br}, the supply voltage of the inverter, V_{inv}, is usually chosen as a fraction of v_{br}. This fraction depends mainly on the chosen safety protection margin. The protection margin

allows for a possible increase of the voltage across the device, v_{dev}, without reaching v_{br}. This can occur due to resonance between parasitic components in the power electronics or regenerative braking of the electrical machine. Essentially, the supply voltage of every VSI should be maximized within the safe operating range of the semiconductor switches. VSI devices are equipped with anti-parallel diodes to ideally limit $v_{dev} \leq V_{inv}$. A relative voltage breakdown rate, K_{br}, is defined to ensure a safety margin between V_{inv} and v_{br} like

$$K_{br} \leq \frac{V_{inv}}{v_{br}}. \tag{2.15}$$

A typically applied value for $K_{br} = 2/3$ in efficiency optimized drives. On account of the discrete v_{br} levels of commercially available semiconductors [75, 77, 150], conduction- and switching-losses of the VSI are greatly influenced by the choice of v_{br}.

Space vector modulation

A PWM technique based on the eight voltage space vectors that are produced by a three-phase VSI is called space vector modulation (SVM), and is first described in [16]. Within this method, the fact is exploited that equal phase-voltages applied to a wye-connected electrical machine cancel each other. The generally chosen approach is to add the third-harmonic to the fundamental frequency in a three-phase electrical machine drive. Only linear PWM is considered in this research to avoid higher harmonic losses, and SVM complies to this requirement. An extensive analysis between conventional PWM and various SVM methods is detailed in [175]. By adding the third-harmonic to a modulation signal with a fixed amplitude ratio and no mutual phase angle, a fundamental frequency modulation signal, $m_{1(SVM)}$, with a peak amplitude of $\hat{m}_{1(SVM)} = 2/\sqrt{3}$ is produced as shown with the "X" in Figure A.1b. The standard sinusoidal PWM fundamental frequency modulation amplitude, $\hat{m}_{1(sin)} = 1$. Therefore, SVM gives a 15% improvement of the peak fundamental voltage vector magnitude, $\left|\hat{\vec{v}}_1\right|$, produced with the VSI, and consequently improves both ω_b and ω_t. SVM is purely a CS technique, allowing application without adding hardware to the system. The main disadvantage of SVM is the wye-connection requirement. For non-wye-connected drives such as the open-winding machine structure applied in this research, the third-harmonic should be actively suppressed as demonstrated in [53], diminishing the effect of SVM. Alternative SVM control techniques are applied to an open-winding electrical machine in [86] to maximize the voltage range of a full-bridge (FB) topology. Despite the effort, the proposed control algorithms still produce a significant common-mode (CM) current with a peak value of 10-100% of the nominal phase-current, depending on the chosen technique.

Inverter DC supply voltage boosting

The first DC supply voltage improvement method is directly boosting the inverter supply voltage, V_{inv}, by inclusion of a half-bridge (HB) bidirectional boost converter between the DC (battery) supply and the VSI legs. As a result, the produced inverter voltage $\left|\hat{\vec{v}}_1\right|$ is enhanced and the peak EMF voltage, $\hat{e}_{q1}$, can be increased. Other topologies are compared to the HB boost converter in [135] for application in a hybrid EV. In [45], angular velocity dependent voltage boosting is analysed, and in [122] a floating capacitor multi-level version diminishing the size and weight of the passive components is presented. The main advantage of adding this boost converter is that V_{inv} may be stabilized independent of the battery voltage, V_{bat}, which can vary due to e.g. the state-of-charge or loading. The most important disadvantage is that solely the angular velocity range is improved, but not the angular velocity ratio, x_s. When designing a drive system, the same effect is achieved, for example, by choosing a different battery voltage, or electrical machine turns/winding count. An EV battery is usually dimensioned based on the required energy capacity for a specified action radius rather than matching V_{bat} proportional to v_{br} [161]. In such a case, an intermediate boost converter can work beneficial for the overall drive efficiency.

A second method to scale $\left|\hat{\vec{v}}_1\right|$ with e_{q1}, is by altering the connection method of multiple battery modules. If the battery consists of, for example, two equal modules, they can either be connected in parallel at low angular velocity, or in series at higher angular velocity, increasing V_{inv} and with that $\left|\hat{\vec{v}}_1\right|$. In [170] this principle is described in detail and tested on an electrical scooter. The authors additionally present a coil reconfiguration principle, with which the windings of the brush-less DC machine is either connected in series or parallel. Finally, also a reconfigurable set of ultra-capacitors is used to store regenerative braking energy. A disadvantage is that the battery current rating should be high enough for series operation, or the torque should be reduced in this mode. Additionally, an energy buffer is required to cope with interruptions of the battery current when altering the configuration. Overall, too many reconfigurable systems are combined in this principle. This requires a vast amount of switches causing high conduction losses which greatly reduce the system efficiency, η_{sys}, and make the system vulnerable to device failure.

Intermediate winding changeover

Variation of the electrical machine winding configuration as a function of the angular velocity is a proven method to increase x_s. The wye-to-delta transformation is applied in numerous applications to provide two fixed angular velocities from a grid connected induction machine, or to start an electrical machine [131]. A different method is dividing each phase into two windings and alter the per-phase connection from a series to a parallel configuration, effectively halving e_{q1} for a given angular velocity. This idea

is patented in [17], and later on applied to a axial-flux PMSM in [19]. A dual-winding machine is proposed in [88], meaning that a tap connection is added to each phase, allowing for the reduction of the number of powered turns and thus EMF per-phase at a predefined angular velocity, ω_x. The major downside of this implementation is that for $\omega_m > \omega_x$ the fill factor of the stator slots is reduced since only a part of the winding is used. This implies higher resistive losses than necessary compared to actual winding reconfiguration.

In [107, 108], a vehicle drive concept is presented to obtain a wide angular velocity operating range using a combination of the wye-to-delta and series-to-parallel configurations. A standard VSI is connected to a six-winding PMSM via a switching matrix composed of thyristors. A combined starter and alternator is proposed in [84] which requires a winding changeover due to the discrepancy between the required torque versus angular velocity characteristics. Next, in [133] a five-phase variant is presented, offering an additional operating mode. However, by observing the per-mode torque, it is concluded that the additional (pentagon) mode only provides a slight torque range improvement at the cost of significantly increased system complexity, when compared to a three-phase machine. Finally, in [93], a survey on series- and parallel-connections of x-phase ($x > 3$) machines is presented, expounding different solutions.

When applying intermediate winding changeover, the FW range per-mode is reduced because the required CPSR per configuration is decreased, lowering i_{d1} and the losses. The detriments of this approach are the required additional hardware, potential losses, transitions between operating modes, and consequently grown system complexity. In [108], a transition from series- to parallel-operation is detailed, requiring that i_x is first reduced to zero, secondly the switching matrix is reconfigured, and finally i_x is restored to the intended level. Furthermore, the switching matrix has constant conduction losses of multiple devices per-phase. Intolerance to single device failure is an extra disadvantage of the mentioned solutions. Due to the addition of a switching matrix, instead of a per-winding empowerment of the electrical machine, the overall reliability is decreased.

Reactive compensation

The d-axis current component used with FW requires, by definition, only reactive power. This property is exploited in reactive compensation by driving the machine in an open-winding manner with one VSI connected at each end. The battery-fed primary-side inverter supplies active power to the electrical machine in the conventional way, while the secondary-side inverter compensates the reactive part by extending $|\vec{v}_1|$. By doing so, no active power is supplied by the secondary-side inverter. Therefore, it is powered from a capacitor fed DC bus, which is charged to the required voltage through the electrical machine by temporarily drawing active power.

Active CM current suppression in a dual-inverter drive system employing two isolated sources is demonstrated in [125, 138, 141, 145]. The advantage of this type of solution is that SVM can be applied to further enhance $|\vec{v}_1|$ without increased losses due to unintended CM currents. The main downside for traction applications is that two sets of batteries are required to power the VSI. To avoid the dual battery requirement, a reactive compensation topology is presented in [82], stating an analysis aiming to reduce the reactive current requirement of the primary-side VSI. A suitable control method for the dual-inverter circuit is proposed in [40, 114], while a clear overview of the possible expansion of the operating range per electrical machine type is shown in [113]. As a result of the solely reactive power requirement on the secondary-side, temporary energy storage in the floating capacitors is satisfactory. Downside of this implementation is that SVM cannot be implemented because this would lead to the flow of unused CM currents, thereby decreasing the efficiency.

In [68], the dual-inverter drive system is used not only to improve the operating range by reactive compensation, but additionally to transfer power from the primary-side main battery to the secondary-side battery using the fundamental frequency machine current. The advantage of this dual VSI solution is that no unintended CM current can flow since no CM return path is present. This allows for SVM drive without increased electrical machine losses, nor a requirement for two battery chargers. The downside of this topology is that, in order to apply the maximum differential voltage, also the secondary-side battery should supply energy to the electrical machine. Therefore, the secondary-side battery should be as large as the primary-side battery when equal voltages are applied, or the solution is not suitable for steady state CPSR operation. The main drawback of reactive compensation is the fact that the power factor (PF) of the added secondary-side inverter is always zero. Likewise, these inverter systems are not tolerant to switching-device- or machine-phase-failures.

2.5.2 Permanent magnet synchronous machine solutions

A large diversion of electrical machine types exists, either designed for a specific task or a broad range of tasks. Not every electrical machine configuration is covered in this section, but some PMSM concepts aiming to improve x_s are explained to demonstrate that solutions exist that cover x_o completely by choosing the appropriate electrical machine and apply FW [109].

High field weakening ratio

The compromise between a high power density and an extended angular velocity range for an in-wheel machine is detailed in [97]. There it is demonstrated that the angular velocity range of a PMSM is highly dependent on the chosen machine construction and winding configuration. An angular velocity ratio $x_s = 5$ of solely the PMSM is achieved in simulations, making it suitable as single solution EVP system. Slightly lower but comparable results are experimentally verified in [103]. The main disadvantage of a high x_s is the resultant reactive power present in the system. As shown in Figure 2.2b, $e_{q1} > \left|\hat{\bar{v}}_1\right|$. Nevertheless, the semiconductor breakdown voltage, v_{br}, is matched to $\left|\hat{\bar{v}}_1\right|$. Therefore, if during FW or regenerative breaking, for example, a VSI switching instance is missed, the drive is turned off to protect the semiconductors. As such, the excess energy generated in the electrical machine air-gap starts to increase the phase voltages. Consequently, the anti-parallel diodes start conducting when the line-to-line EMF voltage, $e_{ll} > V_{inv}$, causing an uncontrollable braking torque, stalling the electrical machine. A wye-connected three-phase electrical machine starts to conduct current when $e_{ll} = \sqrt{3}e_{q1}$.

To inherently protect the drive system, and above all, the passengers, the FW range should be limited such that in case of failures, the peak EMF voltage, $\hat{e}_{q1}$, never exceeds the supply voltage of the applied configuration. In doing so, an uncontrollable braking torque is avoided, which could otherwise lead to dangerous (traffic) situations.

Magnetic field manipulation

A different approach in obtaining a wide angular velocity operating range is the externally intensified or produced magnetic field, as proposed in [81, 156] and [7, 126, 155] respectively. This is achieved by replacing the PMs on the rotor by a field coil [126], increasing the EMF by imposing a positive d-axis current in addition to the PM field [81,156], or by adding DC-field coils to a customary designed stator, avoiding slip-rings [7, 155]. Either way, the proportional relation between the EMF and angular velocity of the electrical machine is varied such, that the intended torque is produced. Furthermore, the required amount of PM material is reduced or diminished within these concepts, reducing the dependency on rare earth raw materials. The main drawback is that the flux linkage is (partially) produced electrically, causing additional losses.

In [110], a different type of field intensification/weakening machine is introduced, i.e. the memory motor. The main advantage of this machine type is that the used AlNiCo PMs are biased by applying a temporary magnetization current, after which the PM magnetic flux density is *memorized*. If a different angular velocity range is required, ω_b is adapted by altering the magnetic flux density with a different temporary magnetization current. However, the main disadvantage of the memory motor is the

reduced efficiency $(\eta < 90\%)$ compared to a conventional PMSM.

The flux switching PM machine [124,177] is an electrical machine type which is a suitable candidate since it combines the advantages of a switched reluctance machine (robust rotor structure, allowing a high peak angular velocity) and of a PMSM (high torque density, wide angular velocity operating range). This combination is achieved by placing the PMs on the stator-side together with the three-phase windings, thereby pre-biasing the magnetic field in the soft-magnetic material [61]. However, due to the nonlinear behaviour caused by saturation and the double-salient structure, modelling and analysis of this electrical machine type becomes difficult [74]. In [70], the VSI restriction is taken into account in the machine design to assure that the required ω_m is reached. A theoretical angular velocity ratio of approximately a factor 2.1 is predicted, however, the influence of R_{st} is neglected. The main disadvantages of this machine type are the limited FW capabilities, increased iron losses due to a doubled flux frequency, and the complicated machine structure. Thorough measurement results of a working flux switching PM prototype machine are presented and discussed in [73].

2.6 Extended permanent magnet synchronous machine model

There are several reasons why the fundamental PMSM modelling method in Section 2.3 is inadequate for this research. Firstly, the per-phase back electromotive force (EMF) of a real electrical machine usually contains higher order harmonics that need to be compensated in the inverter to avoid undesirable currents, torque ripples, and a reduced efficiency. Secondly, the sum of the phase currents in an open-winding machine is not by definition zero, as assumed in Section 2.3. This can cause an unbalance that should be actively suppressed by the CS. Thirdly, failure compensation and an angular velocity range extension concept are explored in this thesis. These methods use phase-current manipulation and the deliberate insertion of higher-harmonic currents, requiring these model extensions [3,44].

2.6.1 Balanced-mode and common-mode quantities

To explain the applied balanced-mode (BM) and common-mode (CM) definitions, first the principle of symmetry applied to signals is defined. Signals are symmetrical when their amplitude and frequency is the same and their mutual displacements in position or in time are equal and not zero. Signals are BM if they are symmetrical and offset free.

CM is usually defined as being (a pair of) signals that are asymmetrical with respect to a reference point [57]. In this research, common-mode is defined as being equal amongst all phases. However, there is a distinction between equal DC signals and equal

AC signals. DC signals which are equal amongst all phases are homopolar. Zero-sequence signals are offset-free AC signals which are of equal amplitude, frequency, and phase angle for all phases. Common-mode signals are the sum of the zero-sequence and homopolar signals. Throughout this thesis, BM and CM quantities are emphasized with superscripts for the sake of clarity. The inductance, L, and flux-linkage, Λ, are no signals, but quantities that are indicated with respect to BM or CM. As such, they are used for signals of that respective mode.

2.6.2 Three-phase model

To allow for the representation of both the BM and CM model components, the open-winding three-phase model based on each physical stator phase and the mutual interactions between their magnetizing inductances are depicted in Figure 2.4. The open-winding configuration allows for both BM and CM signals.

The BM abc-phase currents, $i_a^{\mathrm{bm}}, i_b^{\mathrm{bm}}, i_c^{\mathrm{bm}}$ can generally be written as a sum of odd symmetrical harmonics without offset, being

$$i_a^{\mathrm{bm}} = \sum_{n:\frac{n+1}{2}\in\mathbb{N},\frac{n}{3}\notin\mathbb{N}} I_n^{\mathrm{bm}} \cos\left(n\left(\theta_e + \phi_n^{\mathrm{bm}}\right)\right), \tag{2.16}$$

$$i_b^{\mathrm{bm}} = \sum_{n:\frac{n+1}{2}\in\mathbb{N},\frac{n}{3}\notin\mathbb{N}} I_n^{\mathrm{bm}} \cos\left(n\left(\theta_e - \tfrac{2\pi}{3} + \phi_n^{\mathrm{bm}}\right)\right), \tag{2.17}$$

$$i_c^{\mathrm{bm}} = \sum_{n:\frac{n+1}{2}\in\mathbb{N},\frac{n}{3}\notin\mathbb{N}} I_n^{\mathrm{bm}} \cos\left(n\left(\theta_e + \tfrac{2\pi}{3} + \phi_n^{\mathrm{bm}}\right)\right), \tag{2.18}$$

where n indicates the harmonic number with respect to the fundamental electrical angular frequency, ω_e. I_n^{bm} and ϕ_n^{bm} are the per-harmonic current amplitude and angle, respectively, which are equal for all phases by definition of BM. The amplitude, I_n^{bm}, is equal to $|\vec{\imath}_n|$, in Figure 2.1 and Figure 2.7 because of the applied amplitude-invariant transformation detailed in Section 2.2. Furthermore, $n : \frac{n+1}{2} \in \mathbb{N}, \frac{n}{3} \notin \mathbb{N}$ defines that only the positive, integer, odd harmonics are present, which are no part of the CM harmonics (i.e. $n = 1, 5, 7, \ldots$). Even harmonics are assumed to be zero throughout this analysis, without loss of generality.

The BM per-phase inductance, L^{bm}, is unequal to L_{st} due to the mutual coupling, k, indicated between the phases in Figure 2.4. This coupling is a result of the BM flux produced by one phase and linked to another phase via the stator iron. The BM flux linkage, λ^{bm}, per indicated phase is given by

$$\lambda_a^{\mathrm{bm}} = L_a i_a^{\mathrm{bm}} + k_{ab} L_b i_b^{\mathrm{bm}} + k_{ca} L_c i_c^{\mathrm{bm}} + \lambda_{ma}^{\mathrm{bm}}, \tag{2.19}$$

$$\lambda_b^{\mathrm{bm}} = L_b i_b^{\mathrm{bm}} + k_{bc} L_c i_c^{\mathrm{bm}} + k_{ab} L_a i_a^{\mathrm{bm}} + \lambda_{mb}^{\mathrm{bm}}, \tag{2.20}$$

$$\lambda_c^{\mathrm{bm}} = L_c i_c^{\mathrm{bm}} + k_{ca} L_a i_a^{\mathrm{bm}} + k_{bc} L_b i_b^{\mathrm{bm}} + \lambda_{mc}^{\mathrm{bm}}. \tag{2.21}$$

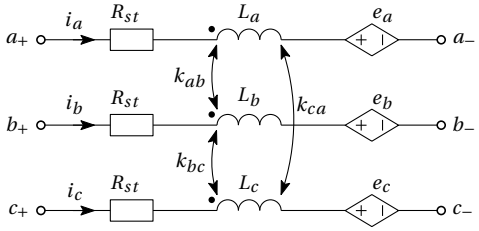

Figure 2.4: Three-phase open-winding electrical machine circuit.

The amplitude of the per-harmonic magnet flux linkage to each phase winding, λ_{mx} (with subscript $x \in [a,b,c]$), depends on the rotor magnet flux linkage, Λ_m. The distribution of the windings on the stator, and the number of turns per-winding, N_{tu}, determine Λ_m. Various other system parameters also influence the shape and amplitude of Λ_m, such as saturation and cross-coupling [151]. Here only winding configuration variations for a fixed electrical machine structure are considered, as applied in e.g. [63]. The resulting per-phase λ_{mx} is described as

$$\lambda_{ma} = \sum_{n:\frac{n+1}{2}\in\mathbb{N}} \Lambda_{mn}\cos\left(n\theta_e\right), \tag{2.22}$$

$$\lambda_{mb} = \sum_{n:\frac{n+1}{2}\in\mathbb{N}} \Lambda_{mn}\cos\left(n\left(\theta_e - \tfrac{2\pi}{3}\right)\right), \tag{2.23}$$

$$\lambda_{mc} = \sum_{n:\frac{n+1}{2}\in\mathbb{N}} \Lambda_{mn}\cos\left(n\left(\theta_e + \tfrac{2\pi}{3}\right)\right), \tag{2.24}$$

where $n:\frac{n+1}{2}\in\mathbb{N}$ indicates that this is a summation of all positive integer odd harmonics, and the angle is a function of the position $\theta_e = \omega_e t$ and the mutual displacement. Whether λ_{mx} is a BM or a CM flux linkage depends solely on the harmonic number, which is therefore also valid for the per-phase EMF e_x.

From (2.19) to (2.24), L^{bm} is derived assuming

$$L_{st} = L_a = L_b = L_c, \tag{2.25}$$

$$k_{st} = k_{ab} = k_{bc} = k_{ca}, \tag{2.26}$$

based on the assumptions that the CS regulates the currents such that only the BM components are present, and the electrical machine is symmetrical. This results in

$$L^{\mathrm{bm}} = \frac{\lambda_a^{\mathrm{bm}} - \lambda_{ma}^{\mathrm{bm}}}{i_a^{\mathrm{bm}}} \tag{2.27a}$$

$$= \frac{L_{st}}{\cos\left(\theta_e\right)}\left(\cos\left(\theta_e\right) + k_{st}\cos\left(\theta_e - \tfrac{2\pi}{3}\right) + k_{st}\cos\left(\theta_e + \tfrac{2\pi}{3}\right)\right) \tag{2.27b}$$

$$= L_{st}\left(1 - k_{st}\right), \tag{2.27c}$$

where mutual inductance, $M_{st} = k_{st}L_{st}$, is the inductance in phase a mutually coupled from phases b, c, in this example. Note that L^{bm} purely depends on k_{st} and the mutual phase displacement, and thus on the stator construction. As a result of the non-salient rotor construction of the electrical machines applied in this research (Appendices C, D), it follows that $L_d = L_q = L^{\text{bm}}$ [65]. The inductance matrix, $\mathbf{L}$ of the SPMSMs is depicted in the respective appendices.

In an open-winding electrical machine it is assumed that, next to BM currents, CM currents can be present. The relation between the phase currents and the CM current, i^{cm}, is defined as

$$i^{\text{cm}} = \tfrac{1}{3}\left(i_a + i_b + i_c\right). \tag{2.28}$$

A distinction is made here between the DC homopolar current component, I^{cm}, and the AC zero-sequence current component per-harmonic number, i_n^{cm}, that combine to i^{cm} as

$$i^{\text{cm}} = I^{\text{cm}} + \sum_{n:\frac{n+1}{2}\in\mathbb{N}} I_n^{\text{cm}} \cos\left(n\left(\theta_e + \phi_n^{\text{cm}}\right)\right). \tag{2.29}$$

The CM current per-phase, $i^{\text{cm}} = i_x^{\text{cm}}$, is equal for all phases by definition of CM. Furthermore, it is emphasized that CM currents of each harmonic can exist (2.29), while BM currents only contain the harmonics which are not integer multiples of three (2.16)-(2.18). Subsequently, the CM stator inductance, L^{cm}, is determined for phase a based on the CM flux linkage, λ^{cm}, as described in [14]. By combining (2.19), (2.25), (2.26), and (2.28),

$$\lambda_a^{\text{cm}} = L_a i^{\text{cm}} + M_{ab} i^{\text{cm}} + M_{ca} i^{\text{cm}} + \lambda_{ma}^{\text{cm}}, \tag{2.30}$$

and, similar to the execution in (2.27), this leads to

$$L^{\text{cm}} = \frac{\lambda_a^{\text{cm}} - \lambda_{ma}^{\text{cm}}}{i_a^{\text{cm}}} \tag{2.31a}$$

$$= L_{st}(1 + 2k_{st}). \tag{2.31b}$$

The BM and CM resistance, $R^{\text{bm}}, R^{\text{cm}}$, are insusceptible to k_{st}, and thus equal to R_{st},

$$R^{\text{bm}} = R^{\text{cm}} = R_{st}. \tag{2.32}$$

Next, the general current per-phase x is written as a sum of the respective CM and BM harmonics based on (2.16)-(2.18), (2.29) as

$$i_x = i^{\text{cm}} + i_x^{\text{bm}}. \tag{2.33}$$

The phasor notation is a convenient method to describe periodic quantities. In this way, the combined three-phase currents are rewritten as

$$\mathbf{i} = \begin{bmatrix} i_a \\ i_b \\ i_c \end{bmatrix} = \begin{bmatrix} I^{\mathrm{cm}} \\ I^{\mathrm{cm}} \\ I^{\mathrm{cm}} \end{bmatrix} + \Re\left(\sum_{n:\,\frac{n+1}{2}\in\mathbb{N}} e^{jn\omega_e t} \begin{bmatrix} \underline{I}_{an} \\ \underline{I}_{bn} \\ \underline{I}_{cn} \end{bmatrix} \right), \tag{2.34}$$

where the phasors are denoted with an underline, i.e., $\underline{I}_{an} = I_{an}e^{j\phi_n}$, etc, and $\Re(\cdot)$ represents the real part of the enclosed complex number. A combined BM and CM components transformation to each harmonic current phasor is constructed analogue to [4, 91, 165] from (2.33) and (2.34) as

$$\begin{bmatrix} \underline{I}_n^{\mathrm{cm}} \\ \underline{I}_n^{\mathrm{bm}} \end{bmatrix} = \frac{1}{3}\begin{bmatrix} 1 & 1 & 1 \\ 1 & a & a^2 \end{bmatrix} \begin{bmatrix} \underline{I}_{an} \\ \underline{I}_{bn} \\ \underline{I}_{cn} \end{bmatrix}, \text{with} \quad a = e^{j\frac{2\pi}{3}}. \tag{2.35}$$

The inverse transformation of (2.35) is given by

$$\begin{bmatrix} \underline{I}_{an} \\ \underline{I}_{bn} \\ \underline{I}_{cn} \end{bmatrix} = \begin{bmatrix} 1 & 1 \\ 1 & a^2 \\ 1 & a \end{bmatrix} \begin{bmatrix} \underline{I}_n^{\mathrm{cm}} \\ \underline{I}_n^{\mathrm{bm}} \end{bmatrix}. \tag{2.36}$$

Subsequently, in the vector notation of (2.34), the instantaneous values of both the BM and CM components are written as

$$\mathbf{i} = \mathbf{i}^{\mathrm{cm}} + \mathbf{i}^{\mathrm{bm}} = \mathbf{I}^{\mathrm{cm}} + \mathbf{i}^{\mathrm{cm}} + \mathbf{i}^{\mathrm{bm}}, \tag{2.37a}$$

$$\text{with} \quad \mathbf{I}^{\mathrm{cm}} = \begin{bmatrix} I^{\mathrm{cm}} \\ I^{\mathrm{cm}} \\ I^{\mathrm{cm}} \end{bmatrix}, \tag{2.37b}$$

$$\mathbf{i}^{\mathrm{cm}} = \Re\left(\sum_{n:\,\frac{n+1}{2}\in\mathbb{N}} \underline{I}_n^{\mathrm{cm}} e^{jn\omega_e t} \begin{bmatrix} 1 \\ 1 \\ 1 \end{bmatrix} \right) \tag{2.37c}$$

$$\mathbf{i}^{\mathrm{bm}} = \Re\left(\sum_{n:\,\frac{n+1}{2}\in\mathbb{N},\,\frac{n}{3}\notin\mathbb{N}} \underline{I}_n^{\mathrm{bm}} e^{jn\omega_e t} \begin{bmatrix} 1 \\ a \\ a^2 \end{bmatrix} \right). \tag{2.37d}$$

The voltages across the phase coils are derived using (2.19) to (2.21), considering both the BM and the CM components per-phase current with

$$\mathbf{v} = \begin{bmatrix} v_a \\ v_b \\ v_c \end{bmatrix} = \begin{bmatrix} v_{a_+} - v_{a_-} \\ v_{b_+} - v_{b_-} \\ v_{c_+} - v_{c_-} \end{bmatrix} = R_{st} \begin{bmatrix} i_a \\ i_b \\ i_c \end{bmatrix} + \frac{\mathrm{d}}{\mathrm{d}t} \begin{bmatrix} \lambda_a \\ \lambda_b \\ \lambda_c \end{bmatrix} = R_{st}\mathbf{i} + \frac{\mathrm{d}}{\mathrm{d}t}\boldsymbol{\lambda}, \tag{2.38}$$

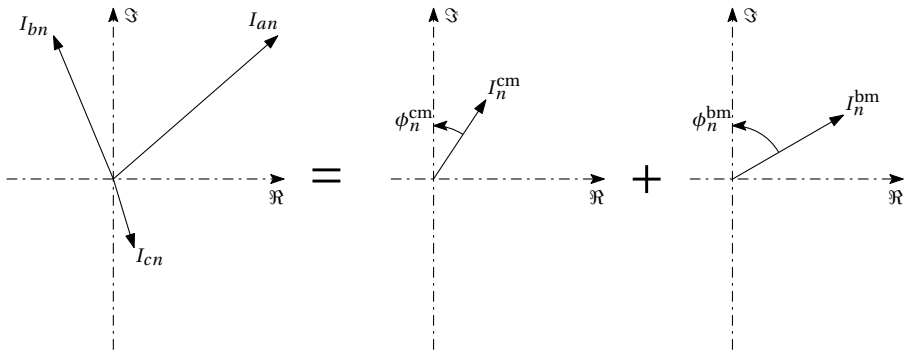

Figure 2.5: Phasor representation of the decomposition of the unbalanced alternating phase currents (left) into the alternating part of the CM current components (middle) and the BM current (right), where $\underline{I}_n = I_n e^{j\phi_n}$

where $\lambda_x = \lambda_x^{\mathrm{bm}} + \lambda^{\mathrm{cm}}$, being the per-phase total flux linkage analogue to the currents in (2.33). The indicated voltages correspond to those at the phase nodes in Figure 2.4.

The phasor relation as derived in (2.36) is shown in the exemplifying graphic in Figure 2.5. The decomposition of the unbalanced phasors on the left-hand-side into the BM and CM phasors on the right-hand-side illustrates that a fixed frequency and fixed amplitude composition can be made of any set of mutually independent phase currents, if equal per-harmonic, per-phase current amplitudes are assumed. This phasor composition is transformed to an alternative two-axis model where the orthogonal frame rotates, and each quantity is regulated as a scalar, as will be explained in the following.

2.6.3 Alternative stationary two-axis model

The potentially unbalanced phase currents of the open-winding three-phase machine in Figure 2.4 is written as a combination of BM and CM currents as detailed in (2.33). By separating the phase currents into BM and CM components, an individual regulation is applied by a stationary two-axis model for the BM (Section 2.3), and a stationary two-axis model with offset for the CM, as detailed in Figure 2.7. The advantage of an additional model for the CM components is explained here.

Due to system imperfections, VSI timing discrepancies and a limited CS bandwidth, unwanted CM currents arise in an open-winding electrical machine, which should be actively suppressed as concluded in [89, 145]. Based on the rotor position and a harmonics unravelling method [23, 24], additional information on the composition of the phase quantities is obtained. The electrical machine produces periodic EMF voltages composed of the angular frequency ω_e and harmonics, as expressed in (2.19)-(2.21). Therefore, the frequency components are derived relative to the angular velocity

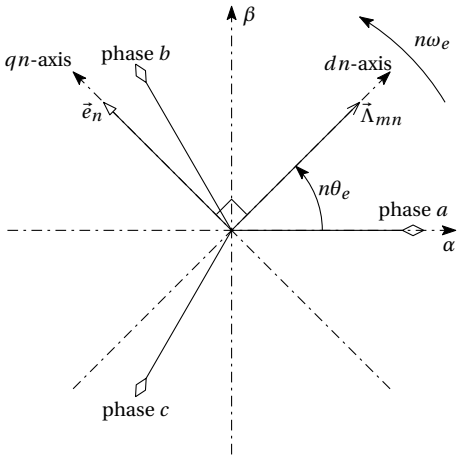

Figure 2.6: Per-harmonic decomposition of the relation between the stationary per-phase quantities and the rotating orthogonal (dn, qn)-axis reference frame based on the rotor magnetic field.

and regulated based on the transformation per-harmonic n as schematically depicted in Figure 2.6. The per-harmonic spacial flux linkage vector, $\vec{\Lambda}_{mn}$, in Figure 2.6, is by definition aligned with the dn-axis, i.e. $\left|\vec{\Lambda}_{mn}\right| = \Lambda_{dn}$. Similarly, the same applies for the per-harmonic EMF vector, $\vec{e}_n$ projected on the qn-axis. This relation is already well known for the transformation of the BM components, but can similarly be used for the individual CM components. An additional decomposition is required to write current i_n^{cm} as (n^{th}-harmonic of $d1, q1$ (dn, qn))-axis components with an offset. As a result, a scalar based CS is applied to regulate each harmonic component individually.

Similar to the transformations in Section 2.3, both the BM and the CM quantities per-harmonic are translated using the corresponding transformation matrices. The BM transformation per-harmonic $x_{an}^{\text{bm}}, x_{bn}^{\text{bm}}, x_{cn}^{\text{bm}}$, to the respective BM direct, x_{dn}^{bm}, and quadrature, x_{qn}^{bm}, quantities are derived using the BM matrix, $\mathbf{T}_n^{\text{bm}}$, and is given by

$$\mathbf{x}_{dqn}^{\text{bm}} = \mathbf{T}_n^{\text{bm}} \mathbf{x}_n^{\text{bm}} \tag{2.39}$$

or

$$\begin{bmatrix} x_{dn}^{\text{bm}} \\ x_{qn}^{\text{bm}} \end{bmatrix} = \frac{2}{3} \begin{bmatrix} \cos(n\theta_e) & \cos\left(n\left(\theta_e - \frac{2\pi}{3}\right)\right) & \cos\left(n\left(\theta_e + \frac{2\pi}{3}\right)\right) \\ -\sin(n\theta_e) & -\sin\left(n\left(\theta_e - \frac{2\pi}{3}\right)\right) & -\sin\left(n\left(\theta_e + \frac{2\pi}{3}\right)\right) \end{bmatrix} \begin{bmatrix} x_{an}^{\text{bm}} \\ x_{bn}^{\text{bm}} \\ x_{cn}^{\text{bm}} \end{bmatrix}, \tag{2.40}$$

with the inverse BM transformation matrix, $\mathbf{T}_n^{\text{bm}\dagger}$, being

$$\mathbf{T}_n^{\text{bm}\dagger} = \begin{bmatrix} \cos(n\theta_e) & -\sin(n\theta_e) \\ \cos\left(n\left(\theta_e - \frac{2\pi}{3}\right)\right) & -\sin\left(n\left(\theta_e - \frac{2\pi}{3}\right)\right) \\ \cos\left(n\left(\theta_e + \frac{2\pi}{3}\right)\right) & -\sin\left(n\left(\theta_e + \frac{2\pi}{3}\right)\right) \end{bmatrix}. \tag{2.41}$$

The transformation from the CM vectors per-harmonic, x_n^{cm}, to the respective CM direct, x_{dn}^{cm}, and quadrature, x_{qn}^{cm}, quantities is performed with the CM matrix, $\mathbf{T}_n^{\mathrm{cm}}$, like

$$\mathbf{x}_{dqn}^{\mathrm{cm}} = \mathbf{T}_n^{\mathrm{cm}} \mathbf{x}_n^{\mathrm{cm}} \tag{2.42}$$

or

$$\begin{bmatrix} x_{dn}^{\mathrm{cm}} \\ x_{qn}^{\mathrm{cm}} \end{bmatrix} = \frac{2}{3} \begin{bmatrix} \cos(n\theta_e) & \cos(n\theta_e) & \cos(n\theta_e) \\ -\sin(n\theta_e) & -\sin(n\theta_e) & -\sin(n\theta_e) \end{bmatrix} \begin{bmatrix} x_n^{\mathrm{cm}} \\ x_n^{\mathrm{cm}} \\ x_n^{\mathrm{cm}} \end{bmatrix}, \tag{2.43}$$

where it is emphasized that $\mathbf{T}_n^{\mathrm{cm}}$ is comparable with $\mathbf{T}_n^{\mathrm{bm}}$ having considered the absence of the symmetrical angular displacement. The computation of $\mathbf{x}_n^{\mathrm{cm}}$ from $\mathbf{x}_{dqn}^{\mathrm{cm}}$ is determined using the transformation function, $\mathbf{W}_n^{\mathrm{cm}}$, like

$$\mathbf{x}_n^{\mathrm{cm}} = \mathbf{W}_n^{\mathrm{cm}} \left(\Pi_n^{\mathrm{cm}}, \phi_n^{\mathrm{cm}} \right) = \begin{bmatrix} -\Pi_n^{\mathrm{cm}} \sin\left(n \left(\theta_e - \phi_n^{\mathrm{cm}} \right) \right) \\ -\Pi_n^{\mathrm{cm}} \sin\left(n \left(\theta_e - \phi_n^{\mathrm{cm}} \right) \right) \\ -\Pi_n^{\mathrm{cm}} \sin\left(n \left(\theta_e - \phi_n^{\mathrm{cm}} \right) \right) \end{bmatrix}, \tag{2.44a}$$

$$\text{with} \quad \Pi_n^{\mathrm{cm}} = \sqrt{\left(x_{dn}^{\mathrm{cm}} \right)^2 + \left(x_{qn}^{\mathrm{cm}} \right)^2}, \tag{2.44b}$$

$$\phi_n^{\mathrm{cm}} = \arctan\left(\frac{x_{dn}^{\mathrm{cm}}}{x_{qn}^{\mathrm{cm}}} \right), \tag{2.44c}$$

where Π_n^{cm} and ϕ_n^{cm} are the respective magnitude and angle of the CM spacial quantity with respect to the qn-axis, as detailed for the current in Figure 2.7a.

The CM and the BM quantities are generated at each (dn, qn)-axis, a spacial quantities diagram per-harmonic is therefore expounded. Figure 2.7a shows the CM mutual current and voltage relations in the alternative stationary two-axis model. There, and in Figure 2.7g, a homopolar difference across voltage vector $\mathbf{v}$ in (2.38) causes an offset value in the $dn^{\mathrm{cm}}_{,} qn^{\mathrm{cm}}$ reference frame from the reference point 0, as indicated by the grey surface. However, this offset does not affect the (dn, qn) vectors due to the rotational line of the frame i.e. the h^{cm}-line, which is aligned with the stationary α-axis as defined in Figure 2.1. Therefore, the $\left(dn^{\mathrm{cm}}_{,} qn^{\mathrm{cm}}\right)$-axis system is a projection of the CM components (Figure 2.7a), comparable to the BM transformation in Figure 2.7b. The respective dn- and qn-equivalent-circuits for both the CM and BM quantities are depicted in Figure 2.7c to Figure 2.7f. The BM spacial quantities diagram in Figure 2.7b is similar to Figure 2.1a, but with addition of the per-harmonic indication. The indicated per-mode, per-harmonic source voltage vectors, $\vec{v}_n$, are constructed on the grounds of orthogonality using scalars, and are produced by the VSI. By unravelling the system in this manner, each quantity is regulated individually and towards a scalar value in steady state.

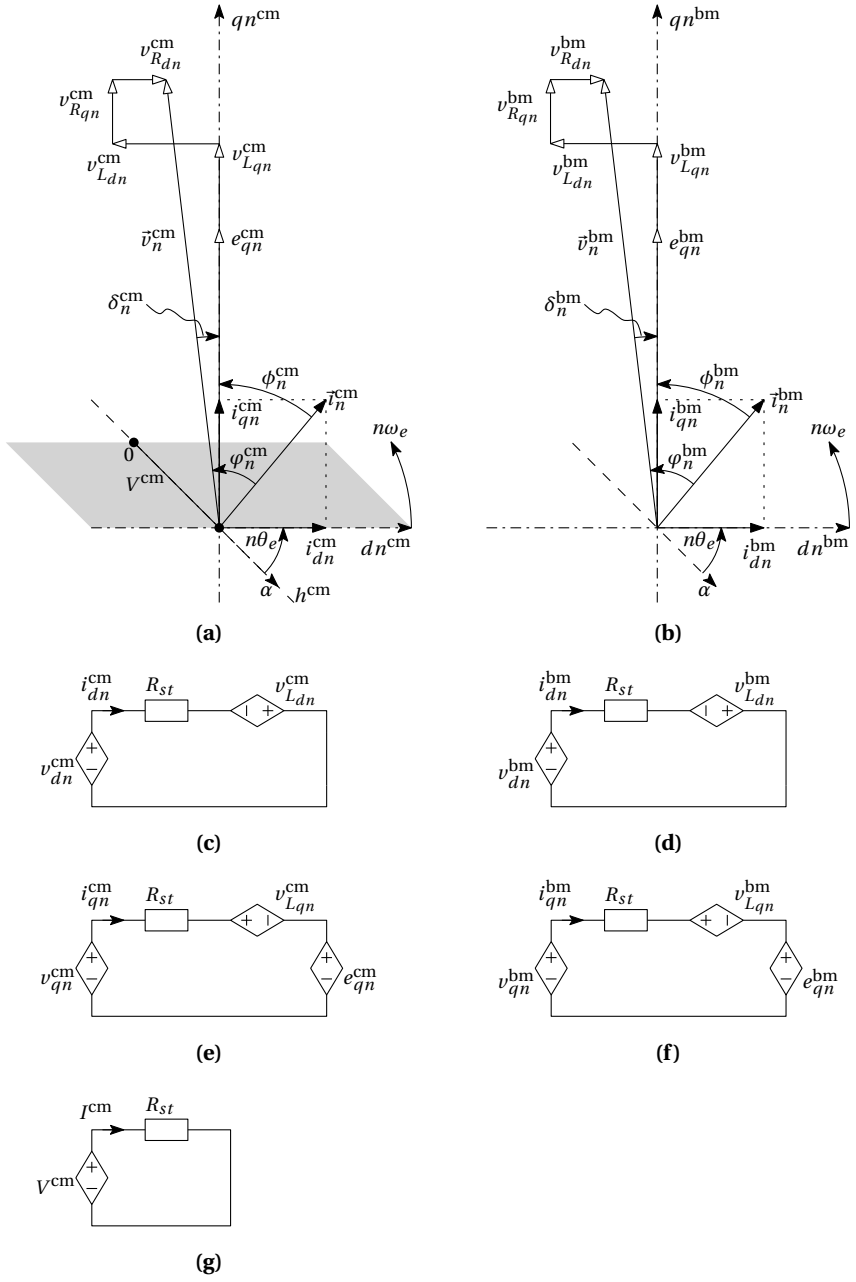

Figure 2.7: The (dn, qn)-axis transformed steady state relations, CM (left-hand-side) and BM (right-hand-side); **(a,b)** spacial quantities diagrams, **(c,d)** dn-axis equivalent circuits, **(e,f)** qn-axis equivalent circuits, **(g)** CM h-line equivalent circuit.

The per-phase EMF, e_x, is defined as the voltage induced in a magnetizing inductance as the result of the variation of the rotor flux linkage versus time [65], like

$$e_x = \frac{\mathrm{d}\lambda_{mx}}{\mathrm{d}t} = \frac{\mathrm{d}\lambda_{mx}}{\mathrm{d}\theta_e}\frac{\mathrm{d}\theta_e}{\mathrm{d}t} = \omega_e \frac{\mathrm{d}\lambda_{mx}}{\mathrm{d}\theta_e}. \tag{2.45}$$

Dependent on the electrical machine construction, the per-phase EMF can contain higher order harmonics. The BM spacial EMF vectors are by definition symmetrical (i.e for $n = 1,5,7,\ldots$). The harmonics for which no BM spacial voltage distribution is possible, are therefore CM components (i.e for $n = 3,9,15,\ldots$). As a result, the CM spacial EMF voltages for the harmonics of which a BM phasor exists, are zero in Figure 2.7e (i.e. for $n = 1,5,7,\ldots$). The total continuous-time EMF voltage of, for example phase a, being e_a, is derived based on Figure 2.6 with (2.22) and (2.45), like

$$e_a = -\omega_e \sum_{n:\frac{n+1}{2}\in\mathbb{N}} n\Lambda_{dn}\sin\left(n\theta_e\right). \tag{2.46}$$

Next, the peak EMF voltage, $\hat{e}$, is computed as a function of the present harmonics using

$$\hat{e} = \omega_e \sum_{n:\frac{n+1}{2}\in\mathbb{N}} -1^{(n-1)/2} n\Lambda_{dn}, \tag{2.47}$$

which is equal for all phases if solely the odd harmonics are considered. The per-harmonic steady state rotating reference frame projection of the EMF, e_{qn}, is derived using (2.46) and the notion that an amplitude-invariant transformation is applied, like

$$e_{qn} = n\omega_e\Lambda_{dn}, \tag{2.48}$$

where $n : \frac{n+1}{2} \in \mathbb{N}$. The EMF harmonics are derived from the Fourier transform (FT) magnitude plot of the measured EMF voltages, or extracted from the electrical machine model by finite-element analysis (FEA). Both methods are applied for the electrical machines used in this research as detailed in Appendices C, D.

The idealized machine constant K_e in (2.4) is based on the assumption that the EMF is solely the result of the fundamental flux linkage, Λ_{d1}. As a result, a direct relation between T_{em} and K_e exists as shown in (2.10). If, however, higher harmonics are present in both flux linkage Λ_m and phase current i_x, higher harmonic torque components arise [63,71]. In this harmonic approach, the torque is solely the result of the electromagnetic interaction between Λ_m and $\mathbf{i}$, no cogging effects [94] are considered and Λ_m is constant since no demagnetization is expected. Consequently, the electrical machine constant per-harmonic, K_{en}, is defined from (2.48) reminding the direct e versus ω_m relation (2.4) with

$$K_{en} = nN_{pp}\Lambda_{dn}. \tag{2.49}$$

The time-dependent instantaneous torque, T_{em}, is derived based on the interaction between flux linkage vector $\boldsymbol{\lambda}$ and current vector $\mathbf{i}$, as defined in (2.38) with

$$T_{em} = \tfrac{1}{2}N_{pp}\left(\boldsymbol{\lambda}^{\mathrm{T}}\cdot\mathbf{i}\right). \tag{2.50}$$

From T_{em}, the average torque is computed by considering the projection of each spacial current vector on the respective qn-axis

$$\langle T_{em} \rangle = \frac{3}{2} \left(\sum_{n:\, \frac{n+1}{2} \in \mathbb{N},\, \frac{n}{3} \notin \mathbb{N}} \left(K_{en} i_{qn}^{\mathrm{bm}} \right) + \sum_{n:\, \frac{n}{3} \in \mathbb{N},\, \frac{n}{2} \notin \mathbb{N}} \left(K_{en} i_{qn}^{\mathrm{cm}} \right) \right), \tag{2.51}$$

where interaction can be distinguished between the BM flux-linkage with the equal harmonic BM current and the CM flux linkage with the equal harmonic CM current. Interaction between a BM and a CM quantity does not produce a net torque by definition, since the per-phase produced torques cancel each other out. Lastly, the interaction between a current and a flux linkage of equal mode (both BM or both CM) but of unequal harmonic produces an instantaneous torque, but is periodic and therefore does not contribute to $\langle T_{em} \rangle$.

From the diagrams and circuits in Figure 2.7, the voltage equations per-mode, per-harmonic are described similarly to (2.3)-(2.6) with

$$\vec{v}_n^{\mathrm{bm}} = \vec{v}_{R_n}^{\mathrm{bm}} + \vec{v}_{L_n}^{\mathrm{bm}} + \vec{e}_n^{\mathrm{bm}}, \tag{2.52}$$

$$\vec{v}_n^{\mathrm{cm}} = \vec{v}_{R_n}^{\mathrm{cm}} + \vec{v}_{L_n}^{\mathrm{cm}} + \vec{e}_n^{\mathrm{cm}}. \tag{2.53}$$

The projections of the (dn, qn)-axis machine voltages are according to their respective equivalent circuits in Figure 2.7 and given by

$$v_{dn}^{\mathrm{bm}} = R_{st} i_{dn}^{\mathrm{bm}} - n\omega_e L^{\mathrm{bm}} i_{qn}^{\mathrm{bm}} = v_{R_{dn}}^{\mathrm{bm}} - v_{L_{dn}}^{\mathrm{bm}}, \tag{2.54}$$

$$v_{qn}^{\mathrm{bm}} = K_{en}\omega_m + R_{st} i_{qn}^{\mathrm{bm}} + n\omega_e L^{\mathrm{bm}} i_{dn}^{\mathrm{bm}} = e_{qn}^{\mathrm{bm}} + v_{R_{qn}}^{\mathrm{bm}} + v_{L_{qn}}^{\mathrm{bm}}, \tag{2.55}$$

$$v_{dn}^{\mathrm{cm}} = R_{st} i_{dn}^{\mathrm{cm}} - n\omega_e L^{\mathrm{cm}} i_{qn}^{\mathrm{cm}} = v_{R_{dn}}^{\mathrm{cm}} - v_{L_{dn}}^{\mathrm{cm}}, \tag{2.56}$$

$$v_{qn}^{\mathrm{cm}} = K_{en}\omega_m + R_{st} i_{qn}^{\mathrm{cm}} + n\omega_e L^{\mathrm{cm}} i_{dn}^{\mathrm{cm}} = e_{qn}^{\mathrm{cm}} + v_{R_{qn}}^{\mathrm{cm}} + v_{L_{qn}}^{\mathrm{cm}}, \tag{2.57}$$

$$V^{\mathrm{cm}} = R_{st} I^{\mathrm{cm}}. \tag{2.58}$$

Summarizing, an extended method for a generalized description of the phase quantities in a rotating reference frame is presented. With this alternative stationary two-axis method, the BM and CM quantities per-harmonic are described separately. Subsequently, a CS per component is developed based on the individual per component circuit (Figure 2.7c-g). Other advantages of this description are that the per-harmonic variant parameters and influences are modelled in a straightforward manner. Exemplifying parameters that are modelled per-harmonic are the feed-forward (FF) e_{qn}, v_R, and v_L compensation [103], winding loss-variation due to the skin- and proximity-effect, and stator-iron loss-variation due to eddy currents and saturation effects [34].

2.6.4 Unified regulation and estimation method

For fixed output frequency converters, such as a grid connected VSI, fixed frequency filtering or a fixed angular velocity reference frame transformation can be applied to extract the different quantities. A commonly applied transformation for such applications is the Clarke transformation [32], as detailed in Appendix B. For a wide operating range drive, the AC frequency varies with the angular velocity of the electrical machine. As a result, it is complicated to extract the different components of for example the phase current in (2.33). However, as utilized for the alternative stationary two-axis model per-harmonic, the electrical rotor position, θ_e, is known from the angular position sensor. This information is used in combination with the transformation matrices to extract the respective d-axis and q-axis component per-harmonic, per-mode, $\mathbf{x}_{dqn}^{(\mathrm{bm,cm})}$, with an estimator. Complementary with the estimator, a per-component regulator is used to construct the per-phase command signal. The homopolar offset regulator and estimator are indicated with a capital letter and subscript 0 because it is the $n = 0$ harmonic. Each of the systems proposed in the following chapters is controlled with this complementary regulator/estimator set, as depicted in Figure 2.8.

Regulator

From the difference between the vector with the intended ($\mathbf{x}^*$) and the estimated ($\tilde{\mathbf{x}}$) values of $\mathbf{x}_{dqn}^{(\mathrm{bm,cm})}$, a complementary regulator per-harmonic, per-mode, $\mathrm{CS}_n^{(\mathrm{bm,cm})}$, tries to mitigate the error, as shown in Figure 2.8a. The applied CS is a conventional controller based on Proportional (P), Integral (I), and Derivative (D) actions, with gains K_p^r, K_i^r, K_d^r, respectively. Other CSs are also possible but are not further investigated in this research. To improve the dynamic behaviour of each CS, a priori known information of the system is added to the output of that controller using the FF input vector per-mode, per-harmonic, $\mathbf{x}_{dqn(FF)}^{\mathrm{bm,cm}}$.

By transforming the sum of both command vectors, $\mathbf{x}_{dqn}^{(\mathrm{bm,cm})}$, using $\mathbf{T}_n^{\mathrm{bm}\dagger}$, $\mathbf{W}_n^{\mathrm{cm}}$, the respective abc-phase command vector per-mode, per-harmonic, $\mathbf{x}_n^{(\mathrm{bm,cm})}$, is determined. The output command vector, $\mathbf{x}$, is the summation of the different components $\mathbf{x}_n^{(\mathrm{bm,cm})}$ as shown in Figure 2.8a. The BM harmonics $(1, n)$ and CM harmonics $(0, n)$ are depicted in Figure 2.8 to indicate the multiple harmonics per-mode principle.

Estimator

In contrast to the regulator, unravelling the vector with measured signals $\mathbf{x}$ into the per-mode per-harmonic components, $\mathbf{x}_n^{(\mathrm{bm,cm})}$ is more complicated. An estimator is used for that. A description for the estimation of BM and tripled harmonics ($n = 0, 3, 6, 9, \ldots$) CM signals is detailed in [23]. However, additional CM signals can also be present in the harmonics for which already a BM component exists ($n = 1, 2, 4, 5, \ldots$). A method to estimate $\mathbf{x}_{dqn}^{(\mathrm{bm,cm})}$ based on the alternative two-axis model is proposed as depicted in Figure 2.8b.

The estimator is based on the notion that $\tilde{\mathbf{x}}_{dqn}^{(\mathrm{bm,cm})}$ can be derived by transforming $\tilde{\mathbf{x}}_n^{(\mathrm{bm,cm})}$ with $\mathbf{T}_n^{\mathrm{bm}}, \mathbf{T}_n^{\mathrm{cm}}$, respectively, and filtering them. The low-pass filter (LPF) ideally averages the input signals to a DC level, effectively retrieving $\tilde{\mathbf{x}}_{dqn}^{(\mathrm{bm,cm})}$. The same LPF transfer function is applied for each component because the respective transformation selects the harmonic. Using $\mathbf{T}_n^{\mathrm{bm}\dagger}, \mathbf{W}_n^{\mathrm{cm}}$, the resulting $\tilde{\mathbf{x}}_n^{(\mathrm{bm,cm})}$ are computed from $\tilde{\mathbf{x}}_{dqn}^{(\mathrm{bm,cm})}$. By adding all the estimated individual components together, $\tilde{\mathbf{x}}$ is composed, and by subtracting this from $\mathbf{x}$, the estimation error, $\boldsymbol{\Delta} = \mathbf{x} - \tilde{\mathbf{x}}$ is determined. The summation of $\boldsymbol{\Delta}$ with each estimated individual component $\tilde{\mathbf{x}}_n^{(\mathrm{bm,cm})}$ is used for the transformation, closing the loop in Figure 2.8b. The bandwidth and noise level of this estimation depends on the applied integration gain, K_i^e. The homopolar component is equal in both domains by definition. However, to avoid propagation of $\boldsymbol{\Delta}$ in $\tilde{\mathbf{X}}^{\mathrm{cm}}$, the same LPF is applied to remove time-variant distortions. Care should be taken that no instability occurs due to the interaction between the regulator CSs and LPF in the estimator.

Estimator simulation example

To demonstrate this method, a multiple current components based estimation system was simulated using MATLAB™/SIMULINK™ [99]. In this example, an open-winding electrical machine rotates at a fixed ω_m, and an *unknown* combination of harmonics and modes are combined to form the phase currents. The intention is to estimate each component of the current vector per-mode, per-harmonic, $\tilde{\mathbf{i}}_{dqn}^{(\mathrm{bm,cm})}$ by minimizing the current error, $\boldsymbol{\Delta}_i$, between the measured and estimated per-phase current, i_a, i_b, i_c and $\tilde{\imath}_a, \tilde{\imath}_b, \tilde{\imath}_c$, respectively $\left(\tilde{\mathbf{i}} = [\tilde{\imath}_a\ \tilde{\imath}_b\ \tilde{\imath}_c]^{\mathrm{T}}\right)$. It is therefore assumed that θ_m, i_a, i_b, i_c are known by measurement. A current estimator is implemented to verify that the method is suitable to control an electrical machine. In total 60 periods of ω_e were simulated to demonstrate the settling behaviour. For this example, ω_e = 350 rad./s, and the simulation time, t, duration is rounded to 1 s. For the time-variant signals in Figure 2.9, i.e. (a) and (c), the last period of the fundamental frequency is depicted.

The *unknown* current amplitude, I, and angle, ϕ, per-harmonic and per-mode that should be unravelled by estimation are listed in Table 2.1. These correspond to the

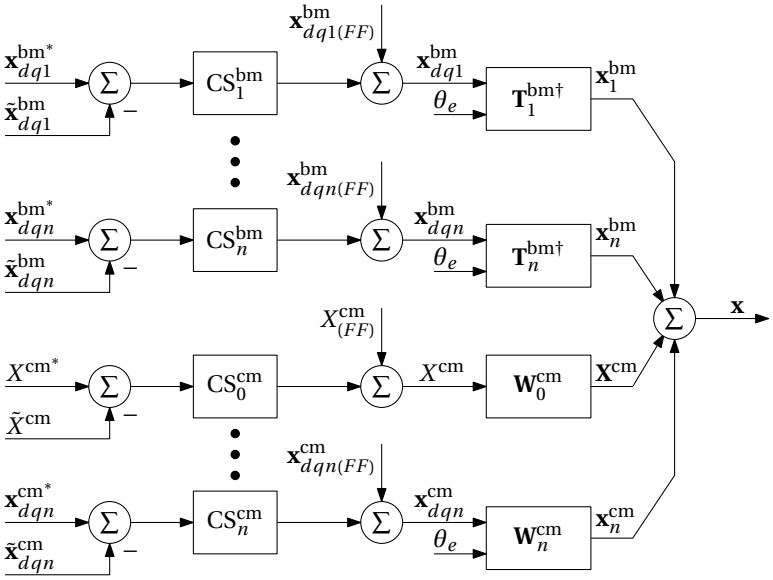

(a)

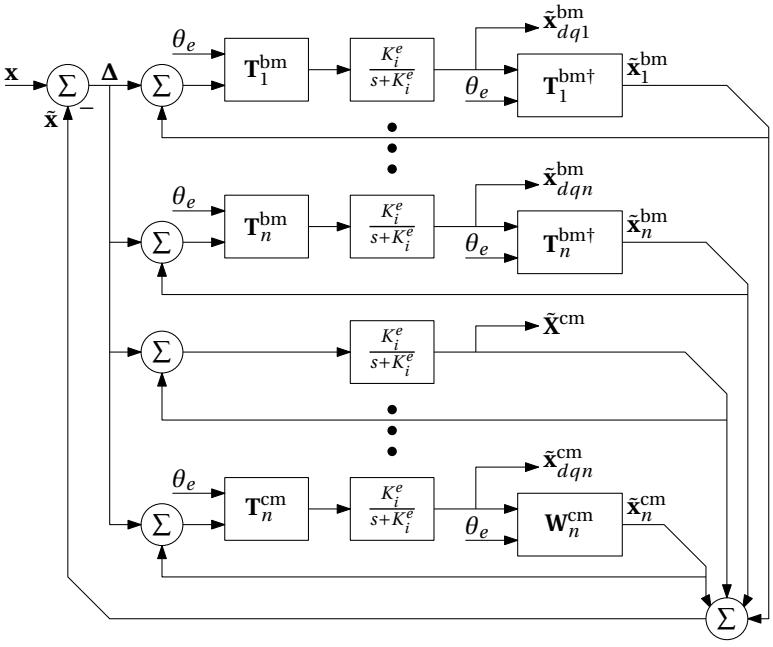

(b)

Figure 2.8: Unified per-harmonic, per-mode regulation/estimation method; **(a)** regulator block diagram, **(b)** estimator block diagram

Table 2.1: Estimator simulation example current components

harmonic, n	0	1	1	3	5	7	Unit
mode	cm	bm	cm	cm	bm	bm	[-]
I_n	$\frac{1}{2}$	1	1	$\frac{1}{3}$	$\frac{1}{5}$	$\frac{1}{7}$	[A]
ϕ_n		$\frac{\pi}{3}$	$\frac{\pi}{3}$	$\frac{\pi}{9}$	$\frac{\pi}{15}$	$\frac{\pi}{21}$	[rad.]
i_{dn}		$\frac{1}{2}$	$\frac{1}{2}$	$\frac{1}{6}$	$\frac{1}{10}$	$\frac{1}{14}$	[A]
i_{qn}		$\frac{\sqrt{3}}{2}$	$\frac{\sqrt{3}}{2}$	$\frac{\sqrt{3}}{6}$	$\frac{\sqrt{3}}{10}$	$\frac{\sqrt{3}}{14}$	[A]

spacial vector definitions in Figure 2.7, and the values are equal to the $(d1, q1)$-axis components in Table 2.1. The combined phases current vector, $\mathbf{i}$, is constructed from the $(d1, q1)$-axis components of Table 2.1 by solely using the FF output of the regulator in Figure 2.8a as plotted in Figure 2.9a,a. The homopolar and (dn, qn)-axis current components per-harmonic in Figure 2.9b are estimated from $\mathbf{i}$ by transformation to each individual component and subsequent filtering, according to the estimator diagram (Figure 2.8b). The applied $K_i^e = 10$ in the presented results. Depending on the required dynamic performance and steady state accuracy, K_i^e can be varied. The settling behaviour is observed in Figure 2.9b. Using the inverse transformation, the time-variant per-harmonic, per-mode currents presented in Figure 2.9c are constructed. By summation of the signals in Figure 2.9c, $\tilde{\mathbf{i}}$ is constructed, as depicted in Figure 2.9a,b, while $\mathbf{\Delta}_i$ is depicted in Figure 2.9a,c.

From $\mathbf{\Delta}_i$ it is concluded that the estimation works well, with a peak error under 1%. It is furthermore concluded that the remaining error is due to $\tilde{\mathbf{i}}_1^{\text{cm}}$ and $\tilde{\mathbf{i}}_3^{\text{cm}}$ since $\mathbf{\Delta}_i$ is periodic in the plotted time (one fundamental period), equal amongst all phases, but not sinusoidal. When comparing the values in Table 2.1 with the corresponding values in Figure 2.9b, it is concluded that the individual components match.

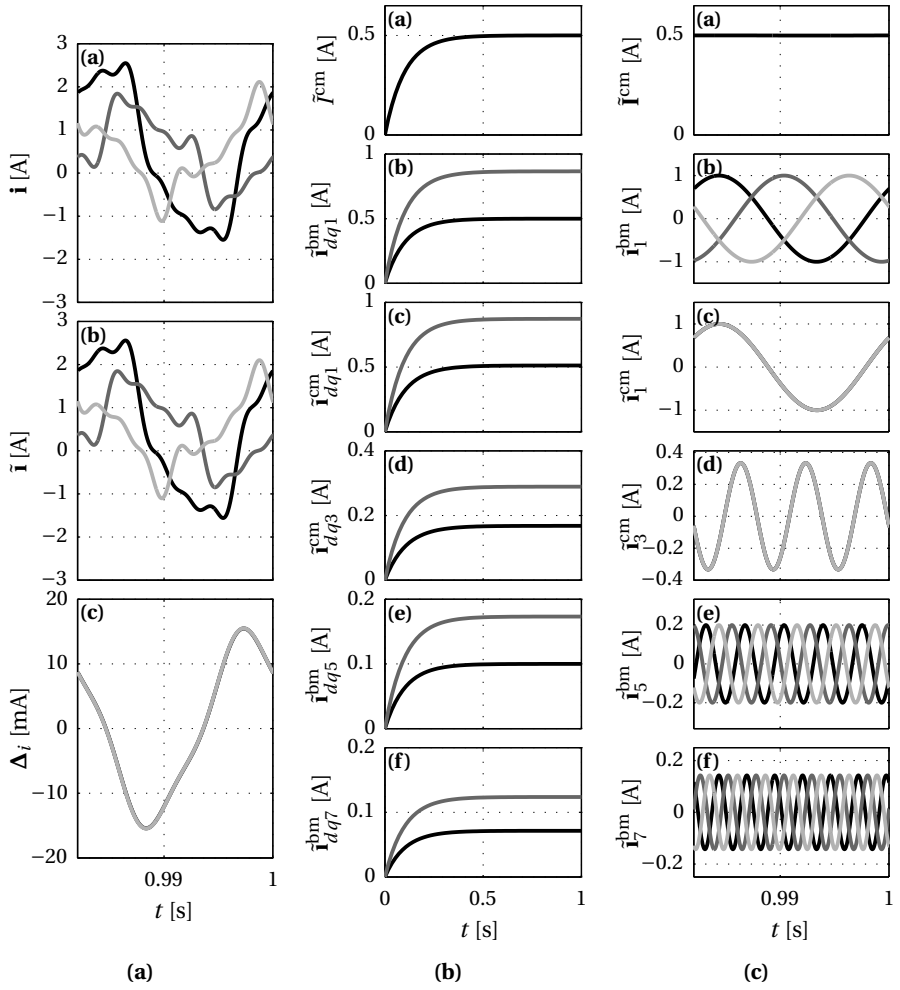

Figure 2.9: Unified per-harmonic per-mode regulation/estimation method simulations, **(a,b)** means figure **(a)**, sub-plot **(b)**, multiple signals are indicated in black (x_a, x_d), grey (x_b, x_q), and light grey (x_c), respectively; **(a,a)** measured currents, $\mathbf{i}$, **(a,b)** estimates of measured currents, $\tilde{\mathbf{i}}$, **(a,c)** error on estimated currents, $\boldsymbol{\Delta}_i$. **(b)** estimated homopolar and $(d1, q1)$-axis current vector per indicated harmonic; **(b,a)** homopolar, $\tilde{I}^{\text{cm}}$, **(b,b)** fundamental BM, $\tilde{\mathbf{i}}^{\text{bm}}_{dq1}$, **(b,c)** fundamental CM, $\tilde{\mathbf{i}}^{\text{cm}}_{dq1}$, **(b,d)** third-harmonic CM, $\tilde{\mathbf{i}}^{\text{cm}}_{dq3}$, **(b,e)** fifth harmonic BM, $\tilde{\mathbf{i}}^{\text{bm}}_{dq5}$, **(b,f)** seventh harmonic BM, $\tilde{\mathbf{i}}^{\text{bm}}_{dq7}$; **(c)** estimated phase current vector per-harmonic; **(c,a)** homopolar, $\tilde{I}^{\text{cm}}$, **(c,b)** fundamental BM, $\tilde{\mathbf{i}}^{\text{bm}}_{1}$, **(c,c)** fundamental CM, $\tilde{\mathbf{i}}^{\text{cm}}_{1}$, **(c,d)** third-harmonic CM, $\tilde{\mathbf{i}}^{\text{cm}}_{3}$, **(c,e)** fifth harmonic BM, $\tilde{\mathbf{i}}^{\text{bm}}_{5}$, **(c,f)** seventh harmonic BM, $\tilde{\mathbf{i}}^{\text{bm}}_{7}$.

2.7 Summary and conclusions

In this chapter, the rotating reference frame model of a symmetrical wye-connected surface permanent magnet synchronous machine is explained. Additionally, the fundamental limitations of the drive components, determining the angular velocity ratio and maximum angular velocity are expounded. Different methods to improve the defined angular velocities and resulting angular velocity range by altering the drive configuration, or the machine properties are listed with their (dis)advantages. The per-harmonic three-phase open-winding machine model that allows for unbalanced currents is presented for usage in the following chapters. By applying the introduced alternative two-axis model in combination with the proposed regulation and estimation, the balanced-mode and common-mode signals per-harmonic can each be regulated independently. This combination allows for full steady state scalar control of each component, independent of the machine angular velocity.

The various existing methods to improve the angular velocity range all have disadvantages such as susceptibility to failure. However, mainly the restraining angular velocity range and system scalability are limitations in obtaining a high performance drive with a minimized nominal power. In the following chapter, an alternative system is presented capable of improving the angular velocity range of a machine and simultaneously improving the fault tolerance capabilities without adding redundancy, nor requiring a high angular velocity ratio.

3

Dynamic drive configurations

"Scaling electrical machine drive electronics towards a converter per turn"

Abstract: *A drive system is presented that combines multiple torque versus angular velocity characteristics. The electrical machine is therefore equipped with multiple sets of three-phase stator windings which are powered by a modular power electronics inverter system. The drive configuration is altered as a function of the angular velocity, such that the limited inverter supply voltage is applied to a matched part of the phase-winding. A machine integrated equivalent of a gearbox is realized by applying the reconfigurable stator winding arrangement. The advantages and limitations of the presented solution are identified and compared to existing solutions as presented in literature. In the experimental verification, the improved angular velocity range that is obtained with the presented system is computed and demonstrated. A relative angular velocity range improvement of a factor 3.49 is achieved for the presented case.*

Parts of this chapter are published in:

- T. Gerrits, C. G. E. Wijnands, J. J. H. Paulides, and J. L. Duarte, "Electrical gearbox equivalent by means of dynamic machine operation," in *Power Electronics and Applications (EPE 2011), Proceedings of the 2011-14th European Conference on*, August - September 2011, pp. 1 –10
- T. Gerrits, C. G. E. Wijnands, J. J. H. Paulides, J. L. Duarte, and E. A. Lomonova, "Machine integrated gearbox for electric vehicles," in *Fisita 2014 - World Automotive Congress*, June 2014, pp. 1–10

3.1 Introduction

The dynamic system presented in this chapter is a reconfigurable power electronics converter topology used to drive a multi-phase electrical machine. The applied power electronics circuit configuration is varied as a function of the machine angular velocity. As such, the drive system is operated dynamically. Essentially, an electrical variant to the mechanical gearbox is created in that manner since each winding configuration has a different base angular velocity. At the base angular velocity, reconfiguration is proposed to allow for a continued operation without the need for a field manipulation method like FW.

Machine winding reconfiguration, or intermediate winding changeover, is not a novel idea as explicated in Chapter 2. Nevertheless, the full potential of the concept is not yet explored in the found literature. In [108] and [133] two examples of sub-optimal usage of the general reconfiguration concept are given. The presented ideas improve the angular velocity ratio x_s by altering the drive configuration, but do not use the full potential of the electrical machine in the high angular velocity mode[1]. In the high angular velocity mode, the drive output power is limited due to the parallel connection of the windings supplied by one HB. The total phase current is limited to the series-connected level by the power electronics, halving the per-winding current in parallel-connected mode. A possible solution would be to double the current rating of the power electronics such that the nominal machine current per-winding is supplied in parallel-connected drive mode. However, this leads to significantly switching losses in the series-connected mode. Since the HBs used in the drive are fixed and an intermediate switching matrix is used, this trade-off remains.

The approach chosen in this work is different. The open-winding electrical machine structure is used to allow for a reconfiguration method without intermediate switching matrix. The switching matrix in [108, 133] dictates that the winding configuration is altered from series to parallel, to allow for a standard three-phase VSI to be used. By incorporating the reconfiguration switches into the power electronics, alteration from series to individual drive modes is achieved here. In contradiction to parallel operation, individual operation allows for a continued nominal current operation in both the power electronics and the electrical machine, without overrating the semiconductors in any of the modes. This results in an improved mechanical output power because the drive angular velocity is increased while maintaining the nominal current.

In this chapter, first the operating principle of dynamic drive operation (DDO) and the proposed modular power electronics topology are explained. Next, different specific modes of DDO are expounded, compared to conventional drive methods, and verified by experiments. In the following chapter, the transition between two modes is detailed.

[1] A two-windings per-phase drive is presented in [108, 133], from which the series and parallel operated modes are considered, thus low and high angular velocity.

3.2 Dynamic drive operation

With the dynamic drive operation principle, the electrical machine characteristics are directly adapted to those required for EVP by means of modular power electronics, [50, 56]. *The isolation between the different per-phase machine winding-sections is used beneficially to decouple the per-module AC output voltages. Consequently, the AC output voltage becomes scalable and can be increased to multiples of the DC supply voltage using the parallel powered inverter modules [49].* To allow for a series-connected winding-configuration, an open-winding machine structure is required for DDO as shown in Figure 2.4. The open-winding electrical machine structure is employed as an alternative to the conventional wye-connected winding machine for the increased system flexibility [128, 144] and possibility to add functionality [68, 147]. The drive mode reconfiguration allows for repeated conformation of the applied inverter voltage to the angular velocity dependent EMF, given in (2.4). In doing so, a continuation of the maximum torque per-Ampère (MTPA) control [87] is allowed, rather than directly requiring FW. DDO is defined as a modular drive concept for a multiple three-phase sets electrical machine with angular velocity dependent reconfiguration of the inverter.

Throughout this work, the word *phase* defines a set of windings which, under normal operation circumstances, conduct the same current. In series-connected mode this is obvious, but in shorter winding strings or individually driven windings, it is assumed that each of the winding currents of that phase are regulated to be equal. Each set of turns on the machine stator that is externally powered by the drive electronics is defined as a *winding*. Finally, the *electrical machine stator* is defined as being a three-phase structure with N^{set} windings per-phase. If the different windings of each phase are electrically in-phase and powered by an equal current, the per-three-phase winding-set, u, produced torque, T^u, is equal. By ensuring this property in the construction of the electrical machine, the overall torque, T_{em} becomes a multiple of T^u according to

$$T_{em} = N^{\mathrm{set}} T^u. \tag{3.1}$$

By increasing $N^{\mathrm{set}} > 1$, different torque versus angular velocity combinations are obtained, resulting in an increased machine power without resorting to a greater machine size.

In Figure 3.1a the per-phase electrical equivalent circuit is depicted for an N^{set} windings per-phase machine. Reconfiguration of the windings is achieved with a bidirectional series connection switch, S_s. The EMF per-winding, e_x^u, winding resistance, R_{st}, and winding inductance, L_{st}, are likewise indicated. The dots next to L_{st} indicate the reference side for mutual coupling with the other phases. Each winding is numbered with either a Roman superscript, $\mathrm{I}, \mathrm{II}, \mathrm{III}, \mathrm{IV}$, the general indication variable u, or with the per-phase last winding, set, thus $\mathrm{I} \leq u \leq \mathrm{set}$. The superscripts $(\mathrm{sr}, \mathrm{in})$ indicate series, individual and represent the respective number of series-connected windings per-string and the parallel operated individually driven winding-strings per-phase in the different

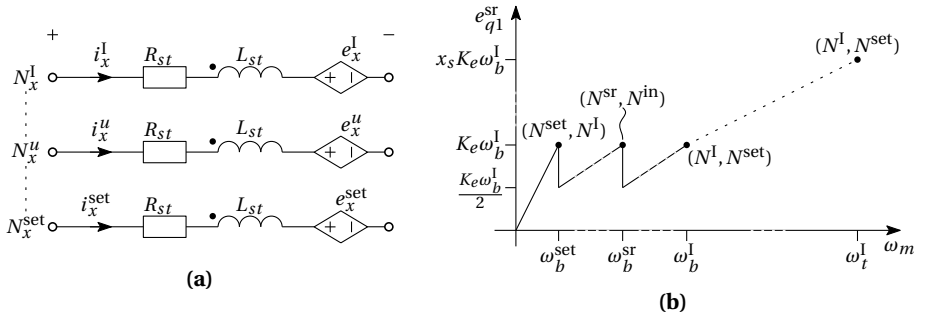

Figure 3.1: (a) Electrical equivalent circuit per-phase (as indicated generic with x) for the N^{set} different open-windings, **(b)** the per-string of N^{sr} series-connected windings EMF, e_{q1}^{sr}, versus ω_m. After each bisection of the set of windings, e_{q1}^{sr} halves, ideally allowing a factor two increase of the angular velocity until the next ω_b. Above the individually operated base angular velocity, ω_b^{I}, the FW operating range is indicated with the dotted line.

configurations depicted in Figure 3.1b. The EMF constant per-set of three-phase windings, K_e^u, is assumed equal for all sets $\left(K_e = K_e^u\right)$, and solely containing the fundamental frequency in the analysis. It is furthermore assumed that each of the windings is driven individually and electrically floating with respect to one another, and the minor mutual influences due to winding couplings are considered to be compensable by the CS.

Accelerating from $\omega_m = 0$ with all the windings per-phase connected in series, results in a fast increase of e_{q1}, due to the number of series-connected windings in that configuration, $e_{q1}^{\mathrm{sr}} = e_{q1}^{\mathrm{set}}$, as depicted in Figure 3.1b. This is due to the high combined set flux linkage, $\Lambda_{d1}^{\mathrm{set}}$, resulting from the total number of windings per-phase in that configuration, like

$$\Lambda_{d1}^{\mathrm{set}} = N^{\mathrm{set}} \Lambda_{d1}^{u}. \tag{3.2}$$

The base angular velocity of the series-connected set, ω_b^{set}, is reached when the maximum $|\vec{v}_1|$ (2.3) is applied while conducting $\hat{i}_1 = i_{q1}$, according to the definition stated in Chapter 2. This point, as indicated with $\left(N^{\mathrm{set}}, N^{\mathrm{I}}\right)$ in Figure 3.1b, is naturally equal for each winding configuration. Phase reconfiguration is required at each ω_b to allow for a further increase of ω_m if the CTSR is to be extended. At ω_b^{set}, each phase is bisected by opening $S_s^{\mathrm{set}/2}$ per-phase (Figure 3.3), halving e_{q1}^{sr} from $K_e \omega_b^{\mathrm{I}}$ to $K_e \omega_b^{\mathrm{I}}/2$ (Figure 3.1b). As a result, ω_m can be further increased until $\omega_b^{\mathrm{sr}} = 2\omega_b^{\mathrm{sr}/2}$ at which S_s^{sr} and $S_s^{3\mathrm{sr}}$ are opened to again allow an increase of ω_m. This process is continued until each S_s is open, and each winding is driven by a separate FB module. This is achieved when $\left(N^{\mathrm{I}}, N^{\mathrm{set}}\right)$ is reached at ω_b^{I}, being the base angular velocity corresponding to solely individually driven windings. Operation applying the nominal per-phase current, i_x, is assumed as required by the base angular velocity definition. From the explanation mentioned

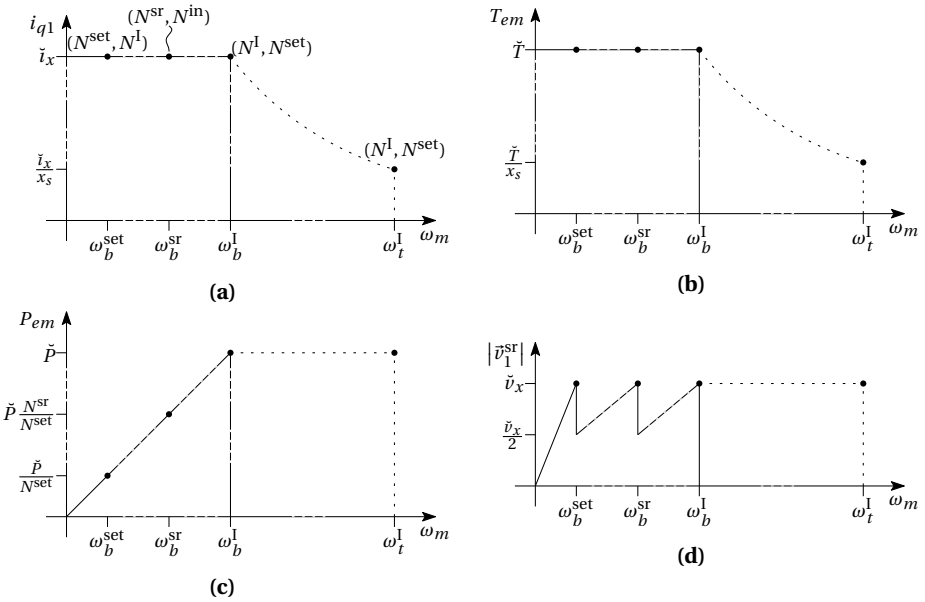

Figure 3.2: Idealized DDO characteristics versus ω_m, where the reduced torque regions are indicated with the dotted lines. The applied winding configuration until each respective ω_b is indicated with $\left(N^{\mathrm{sr}}, N^{\mathrm{in}}\right)$ in **(a)** and a black dot per figure that represents the same configuration; **(a)** i_{q1} corresponding to the nominal phase-current level, **(b)** resulting nominal torque levels, **(c)** resulting nominal power levels, **(d)** required inverter voltage magnitude per series-connected winding string.

above, e_{q1}^{sr} is generally formulated as

$$e_{q1}^{\mathrm{sr}} = K_e N^{\mathrm{sr}} \omega_b^{\mathrm{sr}}. \tag{3.3}$$

The reduced torque, constant power region after ω_b^{I} is indicated with a dotted line because FW or an alternative method like VRE, as detailed in Chapter 5, is required to further increase ω_m. The resulting $\hat{e}_{q1}$ is therefore proportional to x_s and $e_{q1}(N^{\mathrm{sr}}, N^{\mathrm{in}})$ as detailed in Figure 3.1b. Individual operation with N^{in} winding-strings per-phase is considered as parallel operated, individually driven modules, which are regulated to the same current. Series operation with N^{sr} windings, is assumed as series-connected modules. Equal currents are assumed independent of the active mode as a result of that.

From e_{q1} (Figure 3.1b) and i_{q1} (Figure 3.2a), the resulting idealized nominal T_{em} and P_{em} are as detailed in Figure 3.2b and Figure 3.2c, respectively. The ability to reduce e_{q1}^{sr} versus ω_m while applying the nominal current amplitude, $i_{q1} = \check{\imath}_x$, allows for a continuous increase of P_{em} until ω_b^{I}, determining the limit of the CTSR. P_{em} can therefore be boosted by raising N^{set} and expanding the power electronics converter. The restriction on i_{q1} and thus T_{em}, throughout the CPSR is determined by x_s. From the idealized shape

of P_{em} versus ω_m in Figure 3.2c, it is concluded that this is analogue to the performance of a conventional single winding per-phase electrical machine powered by a VSI with

$$\left|\hat{\vec{v}}_1\right| = N^{\text{set}}\check{v}_x \tag{3.4}$$

where $\check{v}_x$ is the nominal inverter phase voltage.

The applied fundamental frequency inverter voltage magnitude per series-connected winding string is indicated with $\left|\vec{v}_1^{\text{sr}}\right|$. Corresponding to the altering behaviour of e_{q1}^{sr}, $\left|\vec{v}_1^{\text{sr}}\right|$ increases throughout the CTSR, and halves from $\check{v}_x$ to $\check{v}_x/2$ at each base angular velocity, as shown in Figure 3.2d. In the CPSR, $\left|\vec{v}_1^{\text{sr}}\right|$ is constantly kept at $\left|\vec{v}_1^{\text{sr}}\right| = \check{v}_x$ to minimize the required i_{d1} as a function of ω_m, as indicated with the dotted line in Figure 3.2d.

The statement that DDO is the electrical machine integrated electrical equivalent of a gearbox is only partly true as concluded from Figure 3.2. A mechanical gearbox solely alters the transmission ratio between the input- and output-axle while the power at both axles is ideally equal. The function of altering the transmission ratio is also true for the DDO principle, but since $\check{T}$ is applied in all operating modes, $\check{P}$ is increased. The overall angular velocity ratio, x_o, obtained with the system is defined as

$$x_o = \frac{\omega_t^{\text{I}}}{\omega_b^{\text{set}}} \tag{3.5}$$

which is larger than the per-configuration angular velocity ratio, x_s, if $N^{\text{set}} > 1$.

From Figures 3.2a, 3.2c, and 3.2d it is concluded that for a fixed i_{q1} and increasing $|\vec{v}_1|$, P_{em} is boosted. With DDO, $|\vec{v}_1|$ is enhanced by increasing N^{set}, and keeping the inverter supply voltage, V_{inv}, fixed. Accordingly, the dynamic operating range is accommodated to fit the desired EVP specifications.

3.3 Modular power electronics

The basic idea of modular power electronics topologies is to increase the flexibility, reliability, or operating range with respect to current or voltage. This principle is applied here to increase all three features in accordance with the objectives set in Chapter 1. Flexibility and operation range are extended to generate a high machine torque or angular velocity range; the reliability is increased to allow for multiple breakdowns without the risk of a full system failure as will be detailed in Chapter 6. The modularity principle [43, 98] is adopted to optimize the usage of an electrical machine by altering the characteristics. By additionally applying a series reconfiguration switch, the electrical machine performance is improved without increasing its current rating, but by scaling the per-winding-set supply voltage with the EMF. In this section, ideal switches

with an anti-parallel diode each are used in the illustrations. These can eventually be implemented in various manners.

A generalized power electronics drive structure is composed using the objectives set in Chapter 1, therefore complying to these design considerations:

1. The layout of the topology should be modular.
2. The per-phase inverter output voltage should be scalable over a wide range, and maximized per operating point.
3. A fixed inverter supply voltage should be assumed, based on the semiconductor breakdown voltage.
4. In case of a single device or winding failure, the system should be capable of continuing operation, and the performance loss should be minimized.
5. The overall efficiency should be maximized.
6. Redundancy should be avoided.
7. A bidirectional current flow is needed to allow for regenerative braking.

3.3.1 Series connectable full bridge modules topology

The series connectable full bridge modules topology as shown in Figure 3.3 was developed based on the aforementioned considerations. Based on design consideration 1, each winding should be driven by a dedicated converter. To maximize the voltage across each winding according to design consideration 2, each converter should be a FB module, and the converters driving each phase requisites a combined operation method. To this end, the series winding connection switches and intermediate operating modes are applied to increase the output voltage without increasing the switching losses caused by continuously powering each winding by an individual FB. To cope with design consideration 4, separate modules should also be able to drive the electrical machine over the full angular velocity range, which is possible by opening some or all of the series switches. By satisfying design considerations 1-4, the converter efficiency is optimized as requested in 5, and there is no redundancy since all modules are used during healthy operation, as required by 6. Solely applying active switches in both the switching legs and the intermediate series switches ensures that bidirectional current flow is possible as requested in 7.

The resulting generalized per-phase version of the N^{set} windings per-phase topology is detailed in Figure 3.3. This per-phase circuit is therefore required three times to compose the complete power electronics converter. The DC source voltage and current are indicated with V_{inv} and i_{inv}, respectively. Each FB converter module is defined as a left HB leg (stroke triangle), and a right HB leg (filled triangle), each consisting of an upper switch (triangle points up), and a lower switch (triangle points down). Each winding N of Figure 3.1a with indicated generic phase, x, and general winding number, u, conducts current i_x^u and is connected to the corresponding FB converter

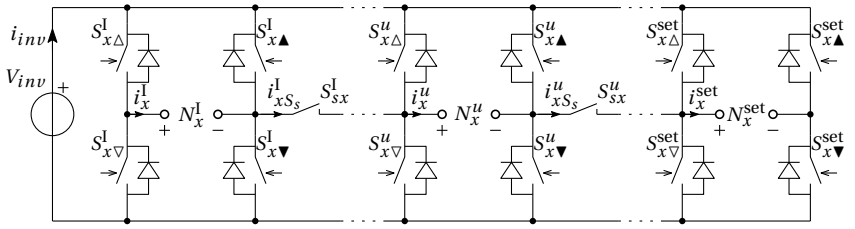

Figure 3.3: Generalized N^{set}-windings reconfigurable per-phase topology to drive an electrical machine with the DDO principle. Each winding of Figure 3.1a with indicated phase, x and winding number, u is connected to the corresponding FB converter module.

module. Each S_s is labelled corresponding to the left-side FB converter, and the current it conducts is indicated with $i^u_{S_s}$ for S^u_s.

The main disadvantage of the presented solution is the vast increase of the total number of semiconductor switches when compared to a conventional VSI. There are, however, multiple reasons why this disadvantage is of minor importance in a contemporary power electronics circuit. The tendency to increase the number of semiconductors used in a power electronics converter is motivated with multiple arguments [83];

- The system flexibility is improved, for example by multilevel [98], by interleaving [43], by parallel driven modules DDO, or by altering between series or parallel connected outputs in a multiple modules DC-DC converter [29].
- Various possibilities exist with a dual-inverter drive structure that are not possible with a conventional VSI, such as battery charging [68], reactive compensation, or VRE (Chapter 5).
- At lower output voltage levels, the switching losses are further reduced by scaling the number of switching elements with the angular velocity by applying a series switch as detailed in Chapter 4.
- The system reliability is improved as will be demonstrated in Chapter 6, because device or winding failure is accommodated for with a minimum system degradation. This is achieved without adding redundancy, and thus normally unused system parts.
- To produce a certain output power, the DDO concept trades an ever increasing current necessity for a scalable output voltage. Considering a fixed electrical machine current density, the design choice flexibility exists to choose between a low number of turns with a high current or a high number of turns with a low current. The intention of DDO is to optimize the system efficiency by minimizing the RMS currents for a required power.

3.3.2 Reconfiguration example

In this example, N^{set} in Figure 3.3 is chosen equal to four to demonstrate all possible operating modes, i.e. the series-connected, an intermediate connected, and the individually powered configuration. The different drive configurations are depicted in the same order in Figure 3.4, and the per-winding connections are indicated analogue to Figure 3.1a.

With $N^{\text{set}} = 4$ windings per-phase, the electrical machine starts accelerating with all three S_s closed as depicted in Figure 3.4a, where the windings, series switches, and switching legs are correspondingly Roman numbered. When ω_b^{IV} is reached, S_s^{II} in the middle of the winding string is opened, bisecting the phase winding after which the intermediate connected operation is applied, as shown in Figure 3.4b. Continued acceleration is possible with two FBs per-phase. Finally, S_s^{I} and S_s^{III} are opened at ω_b^{II}, after which each winding is powered by an individual FB module, as depicted in Figure 3.4c. For the complete acceleration, $(N^{\text{sr}}, N^{\text{in}})$ converges from FB series (FBS) operation, $(N^{\text{IV}}, N^{\text{I}})$, via the intermediate configuration, $(N^{\text{II}}, N^{\text{II}})$, to FB individual (FBI) operation, $(N^{\text{I}}, N^{\text{IV}})$, corresponding to the general case in Figure 3.1b. The respective generalized series-connected winding-string resistance, inductance are

$$R^{\text{sr}} = N^{\text{sr}} R_{st}, \tag{3.6}$$

$$L^{\text{sr}} = N^{\text{sr}} L^{\text{bm}}. \tag{3.7}$$

Series-connected operation, *gear 1*

The circuit configured for series-connected operation $\left(N^{\text{sr}}, N^{\text{in}}\right) = \left(N^{\text{IV}}, N^{\text{I}}\right)$ is detailed in Figure 3.4a, where the per-winding current is equal by configuration. The outer HB switching legs can therefore be used to power the complete string of windings reducing the switching losses, P_{sw}, by a factor four when compared to the FB per-winding configuration. On the other hand, each S_s is conducting, reducing the $(d1, q1)$-axis transformed, maximum fundamental frequency voltage magnitude across all windings combined, $\left|\hat{\vec{v}}_1^{\text{IV}}\right|$. As a result,

$$\left|\vec{v}_1^{\text{IV}}\right| = V_{inv} - 2V_{coS_x} - 3V_{coS_s}, \tag{3.8}$$

where V_{co} indicates the conduction voltage per S_x or S_s, respectively. The switch and diode conduction forward voltages are assumed equal. Furthermore, the combined voltage across the resistance, v_R^{sr} in (3.6), and the inductance, v_L^{sr} in (3.7), is relatively high for $N^{\text{sr}} = 4$. Throughout the CTSR, v_R^{sr} is constant, while v_L^{sr} increases with the electric frequency and thus ω_m. As a result of the configuration dependent V_{coS_s} and v_L^{sr}, the ratio between the subsequent base angular velocities is not exactly two as demonstrated in the experiments. This configuration is used while $0 \leq \omega_m \leq \omega_b^{\text{IV}}$, resulting in $0 \leq P_{em}^{\text{IV}} \leq \check{P}/4$.

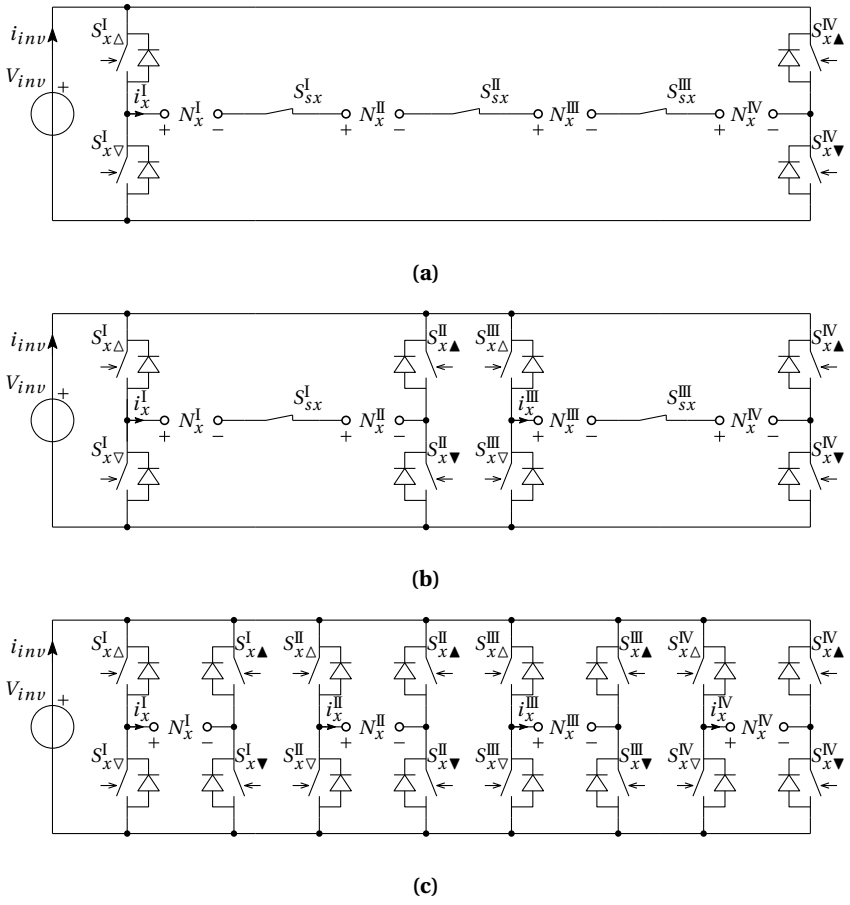

Figure 3.4: DDO configurations with $N^{\mathrm{set}} = 4$-windings per-phase for an increasing ω_m from top to bottom; **(a)** series-connected operation $\left(0 \le \omega_m \le \omega_b^{\mathrm{IV}}\right)$, **(b)** intermediate configuration operation $\left(\omega_b^{\mathrm{IV}} \le \omega_m \le \omega_b^{\mathrm{II}}\right)$, **(c)** individual configuration operation $\left(\omega_b^{\mathrm{II}} \le \omega_m \le \omega_t^{\mathrm{I}}\right)$.

Intermediate configuration operation, *gear 2*

The intermediate operation circuit $\left(N^{\text{sr}}, N^{\text{in}}\right) = \left(N^{\text{II}}, N^{\text{II}}\right)$ is shown in Figure 3.4b, where by configuration $i_x^{\text{I}} = i_x^{\text{II}}$, and $i_x^{\text{III}} = i_x^{\text{IV}}$. It is furthermore presumed that the CS can achieve $i_x^{\text{I}} = i_x^{\text{III}}$, allowing for an equal approach as in the series-connected case. Each series-connected winding-string in this situation is supplied by

$$\left|\hat{\breve{v}}_1^{\text{II}}\right| = V_{inv} - 2V_{coS_x} - V_{coS_s}. \tag{3.9}$$

In this configuration, P_{sw} is half that of FBI, while one S_s per two-winding series-connected FB is conducting. This configuration is used while $\omega_b^{\text{IV}} \leq \omega_m \leq \omega_b^{\text{II}}$, resulting in $\breve{P}/4 \leq P_{em}^{\text{II}} \leq \breve{P}/2$.

Individual configuration operation, *gear 3*

The circuit configured for individual operation $\left(N^{\text{sr}}, N^{\text{in}}\right) = \left(N^{\text{I}}, N^{\text{IV}}\right)$ is illustrated in Figure 3.4c. In this case, the CS is expected to regulate the winding currents such that $i_x^{\text{I}} = i_x^{\text{II}} = i_x^{\text{III}} = i_x^{\text{IV}}$, and because no S_s is used, ideally $\left|\hat{\breve{v}}_1\right|$ is applied per-winding,

$$\left|\hat{\breve{v}}_1^{\text{I}}\right| = V_{inv} - 2V_{coS_x}. \tag{3.10}$$

This configuration is used for the remainder of the CTSR, i.e. $\omega_b^{\text{II}} \leq \omega_m \leq \omega_b^{\text{I}}$, resulting in $\breve{P}/2 \leq P_{em}^{\text{I}} \leq \breve{P}$ and the complete CPSR where $\omega_b^{\text{I}} \leq \omega_m \leq \omega_t^{\text{I}}$, if FW is applied.

3.4 Comparing operating modes with wye-connected

To demonstrate the influence of each VSI and electrical machine parameter on the drive performance, ω_b and ω_t are derived in this section for different drive configurations of the same machine. The series-connected FBS and the individually regulated FBI modes of an $N^{\text{set}} = 2$ windings per-phase electrical machine are compared to the reference configuration i.e. the conventional wye-connection. The general operating range and efficiency computation are detailed for a non-salient SPMSM operated in steady state, and subsequently applied to electrical machine A for which the parameters are detailed in Appendix C. The power electronics related parameters are listed in Appendix F. In the initial analysis, only the fundamental frequency components are considered for clarity. In the experimental results and following chapters, also the higher-order harmonics are taken into account.

In [112], the influence of R_{st} on ω_b and ω_t is detailed, and from it the conclusion is drawn that both ω_b and ω_t are derated if $R_{st} \neq 0$. The influence of R_{st} on ω_b and ω_t is often neglected in literature for simplicity, but is required for an accurate prediction as

will be demonstrated. The derivative terms of i_1 are zero during steady state operation, as assumed in the $(d1, q1)$-transformed circuits of Figure 2.1 and detailed in (2.5), (2.6), respectively.

The maximum steady state voltage that can be applied to a machine phase by the VSI, $\left|\hat{\bar{v}}_1\right| = \check{v}_x$. Since an equal amplitude transformation is applied, this relates to v_{d1} and v_{q1} as

$$v_{d1}^2 + v_{q1}^2 \leq \check{v}_x^2. \tag{3.11}$$

Equivalently, the maximum allowed steady state phase current, $\left|\hat{\bar{i}}_1\right| = \check{\imath}_x$, relates to i_{d1} and i_{q1} like

$$i_{d1}^2 + i_{q1}^2 \leq \check{\imath}_x^2, \tag{3.12}$$

as illustrated in Figure 2.2 for the case that the nominal respective values $(\check{v}_x, \check{\imath}_x)$ are applied. Substitution of (2.5) and (2.6) into (3.11) gives a current constraint relation as a function of ω_e and the electrical machine parameters. The constraint is written as

$$\left(i_{d1} + \frac{\omega_e^2 \Lambda_{d1} L^{\text{bm}}}{\left(\omega_e L^{\text{bm}}\right)^2 + R_{st}^2}\right)^2 + \left(i_{q1} + \frac{\omega_e \Lambda_{d1} R_{st}}{\left(\omega_e L^{\text{bm}}\right)^2 + R_{st}^2}\right)^2 \leq \frac{\check{v}_x^2}{\left(\omega_e L^{\text{bm}}\right)^2 + R_{st}^2}, \tag{3.13}$$

where Λ_{d1} is the fundamental frequency flux linkage of the machine rotor defined on the d-axis, and the BM inductance, L^{bm}, is derived in (2.27).

3.4.1 Voltage source inverter limitations

The available voltage magnitude is lower than the supply voltage $\left(\left|\hat{\bar{v}}_1\right| < V_{inv}\right)$ due to non-ideal behaviour of real semiconductor switches. Firstly, a blanking-time, t_b, at each PWM switching instance is required to avoid cross conduction. Secondly, the conduction voltage across each HB switch, V_{coS_x}, and across each series switch, V_{coS_s}, further reduces $\left|\hat{\bar{v}}_1\right|$, as explained for the exemplifying case in (3.8)-(3.10). Four drive modes are compared in terms of the obtained angular velocity range, for which each mode is schematically depicted in Figure 3.5a. Note that the first three modes apply to series-connected windings, from which the first two are non-reconfigurable and therefore do not need S_s. The first mode is the standard wye-connected three-phase inverter mode, operated with only the PWM fundamental frequency, WYE (3.15). The second mode is the SVM wye-connected three-phase inverter mode, operated with the fundamental and the third-harmonic frequency voltage. The advantage of the wye-connected SVM reference configuration is the fact that the sum of the phase-currents is zero, avoiding CM currents, which would otherwise be produced as a result of the applied third-harmonic voltage. The third-harmonic is applied within SVM such, that the fundamental frequency PWM amplitude is boosted above unity while keeping linear

behaviour, effectively increasing $\left|\hat{\vec{v}}_1\right|$ (3.16). The third mode is the FBS per-phase inverter mode as shown in Figure 3.5a, with only fundamental frequency PWM (3.17). The fourth mode is the FBI per-winding inverter mode, also only with fundamental frequency PWM (3.18).

The third-harmonic applied in SVM is cancelled out by the method of connection in combination with the mutual phase difference. This principle can be applied to an open-winding electrical machine [86], but is at first neglected in FBS and FBI operation for the sake of clarity. The VSI gain,

$$G_{inv} = (1 - G_{CS})\left(1 - \frac{2\,t_b}{T_{sw}}\right), \tag{3.14}$$

with G_{CS} being the control gain which is considered to compensate for errors due to system imperfections [112] and T_{sw} is the time per PWM switching period. The maximum $(d1, q1)$-transformed spacial voltage per series-connected winding-string, $\left|\hat{\vec{v}}_1^{\mathrm{sr}}\right|$, is described per drive mode based on the applied modulation scheme and connection diagram in Figure 3.5a with

$$\left|\hat{\vec{v}}_{1(WYE)}^{\mathrm{sr}}\right| = \left(\frac{V_{inv}}{2} - V_{coS_x}\right) G_{inv}, \tag{3.15}$$

$$\left|\hat{\vec{v}}_{1(SVM)}^{\mathrm{sr}}\right| = \left(\frac{V_{inv}}{\sqrt{3}} - V_{coS_x}\right) G_{inv}, \tag{3.16}$$

$$\left|\hat{\vec{v}}_{1(FBS)}^{\mathrm{sr}}\right| = \left(V_{inv} - 2V_{coS_x} - V_{coS_s}\right) G_{inv}, \tag{3.17}$$

$$\left|\hat{\vec{v}}_{1(FBI)}^{\mathrm{sr}}\right| = 2\left(V_{inv} - 2V_{coS_x}\right) G_{inv}. \tag{3.18}$$

Furthermore, the applied modulation index amplitude is assumed to be maximum, and thus unity, to assure linear behaviour. In the SVM case, the available maximum modulation index within the linear operating range is applied, i.e. $2/\sqrt{3}$, [16, 175].

3.4.2 Machine limitations

The second derating mechanism, enlarging the discrepancy between $|\vec{v}_1|$ and e_{q1}, is the presence of the magnetizing inductances and their intrinsic resistance, as shown in Figure 2.1a. As derived in (2.10) for an $N^{\mathrm{set}} = 1$ winding per-phase SPMSM, T_{em} depends only on the fundamental frequency machine torque constant, K_{e1}, if solely i_{q1} is applied like

$$T_{em} = \tfrac{3}{2} N^{\mathrm{set}} K_{e1}\, i_{q1}, \tag{3.19}$$

meaning that up to and including each ω_b^{sr}, $i_{d1} = 0$ and thus $i_{q1} = \check{\imath}_x$ may be applied based on (3.12). When comparing (3.3) and (3.19) with (2.4) and (2.10), the essential

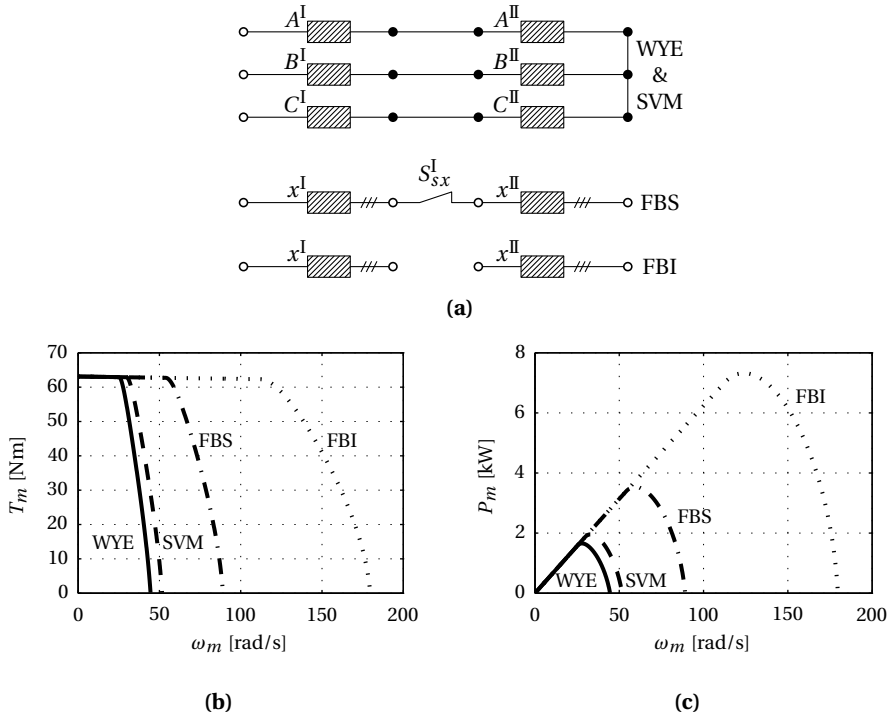

Figure 3.5: Four compared configuration modes; **(a)** schematic representation of different configurations of a fixed electrical machine winding structure, where the circles indicate external connection points which are connected to a HB, while the disks indicate a connection point which is either internal or external, **(b)** resulting mechanical output torque, T_m, versus angular velocity, ω_m, graph per indicated mode, **(c)** resulting mechanical output power, P_m, versus ω_m graph per indicated mode.

advantage of DDO becomes clear; a scalable e_{q1} is combined with a fixed i_{q1} and T_{em}, thereby improving P_{em} as a result of the increased ω_t^{I}.

In the equations (3.20), (3.21), $\left|\hat{\breve{v}}_1^{\mathrm{sr}}\right|$ per-mode in (3.15)-(3.18) is substituted in (3.13) to compute ω_b, ω_t per configuration, being $\omega_b^{\mathrm{sr}}, \omega_t^{\mathrm{sr}}$, respectively. Since the maximum attainable voltage per configuration is applied, the equality sign is used in (3.13), and the passive quantities in (3.6), (3.7) are used. Consequently, ω_b^{sr} is expressed as

$$\omega_b^{\mathrm{sr}} \triangleq \omega_m\left(i_{d1}=0, i_{q1}=\breve{\imath}_x\right) = \frac{-R^{\mathrm{sr}}\breve{\imath}_x\Lambda_{d1}^{\mathrm{sr}} + \sqrt{\left(L^{\mathrm{sr}}\breve{\imath}_x\breve{v}_x^{\mathrm{sr}}\right)^2 - \left(L^{\mathrm{sr}}R^{\mathrm{sr}}\breve{\imath}_x^2\right)^2 + \left(\Lambda_{d1}^{\mathrm{sr}}\breve{v}_x^{\mathrm{sr}}\right)^2}}{N_{pp}\left((L^{\mathrm{sr}}\breve{\imath}_x)^2 + \left(\Lambda_{d1}^{\mathrm{sr}}\right)^2\right)}, \tag{3.20}$$

where only the positive solution of the quadratic formula is considered. Similar to the computation of ω_b^{sr}, also ω_t^{sr} is derived using (3.13). The top angular velocity is reached when the complete $\breve{\imath}_x$ is used to compensate e_{q1}, and no torque is produced anymore. This is the case when $i_{d1} = -\breve{\imath}_x$ based on (3.12) and shown in Figure 2.2b. As such, ω_t^{sr} is expressed as

$$\omega_t^{\mathrm{sr}} \triangleq \omega_m\left(i_{d1}=-\breve{\imath}_x, i_{q1}=0\right) = \frac{1}{N_{pp}}\sqrt{\frac{\left(\breve{v}_x^{\mathrm{sr}}\right)^2 - \left(R^{\mathrm{sr}}\breve{\imath}_x\right)^2}{\left(\Lambda_{d1}^{\mathrm{sr}} + L^{\mathrm{sr}}\breve{\imath}_x\right)^2}}, \tag{3.21}$$

where again only the positive solution of the quadratic formula is considered. Note that theoretically an infinite ω_t^{sr} can be obtained if $\Lambda_{d1}^{\mathrm{sr}} = -L^{\mathrm{sr}}\breve{\imath}_x$ [106].

3.4.3 Operating range per configuration

The power electronics and electrical machine parameters used to derive ω_b and ω_t per-mode are listed in Appendices F and C, respectively. The assumed $V_{co} = 2$ V and is equal for all switches. The applied DC supply voltage, $V_{inv} = 300$ V. The achievable CTSR and CPSR per drive mode are computed applying (3.20) and (3.21), where $\breve{v}_x$ is considered equal to $\left|\hat{\breve{v}}_1^{\mathrm{sr}}\right|$ per configuration as described in (3.15)-(3.18). The mechanical output torque, T_m, as a function of ω_m is depicted in Figure 3.5b. It is based on the overall current limit (3.12), and therefore on the combined constraints indicated in (3.13). In steady state, T_m is derived from (2.12) with

$$T_m = T_{em} - B_m\omega_m. \tag{3.22}$$

The resulting mechanical output power, P_m, versus ω_m is depicted in Figure 3.5c.

3.4.4 Open-winding configurations drive efficiency

A first-order efficiency approximation of the dynamic drive system operating modes was performed. Influencing factors such as temperature, circuit parasitics, and dynamics are therefore not considered. The resulting efficiency contour plots can subsequently be used to determine the optimal drive configuration for each combination of ω_m, T_m. Details and values of the applied parameters and devices are listed for electrical machine A in Appendix C, for S_x in Appendix F, and for S_s in Appendix G, respectively. To determine the drive efficiency, the angular velocity range, $0 \leq \omega_m \leq \omega_t^{\mathrm{I}}$, and the current range, $0 \leq |\vec{\imath}_1| \leq \check{\imath}_x$, are subdivided into $n_\omega = 1000$ and $n_i = 50$ respective levels. For each combination of (n_ω, n_i), the electrical machine output T_m, P_m, and resulting efficiency, η_{sys}, are computed.

Power electronics

The power electronics losses are estimated based on the conduction power loss, P_{co}, and the switching power loss, P_{sw}. The constant assumed device conduction voltage, $V_{co} = 2$ V, allows for the computation of P_{co} with $\vec{\imath}_1$. The duty cycle, D, is averaged over a periodic cycle, therefore $\langle D \rangle = 0.5$. The S_s power loss per device, P_{S_s}, are consequently determined by

$$P_{S_s} = \frac{|\vec{\imath}_1|}{\sqrt{2}} V_{co S_s} \langle D \rangle, \tag{3.23}$$

since fixed configurations are assumed. A fixed VSI switching frequency, $f_{sw} = 8$ kHz is applied and P_{sw} is derived using the total switching energy loss per device, E_{S_x}, proportional to the current it conducts. E_{S_x} is the sum of the required energy per period to turn the active semiconductor on, E_{on}, to turn it off, E_{off}, and the energy needed to recover the anti-parallel diode blocking state reverse-recovery (RR), E_{rr}, respectively [105]. The total per-HB device losses, P_{S_x}, can subsequently be computed with

$$P_{S_x} = \frac{|\vec{\imath}_1|}{\sqrt{2}} \left(V_{co S_x} \langle D \rangle + \frac{f_{sw} E_{S_x}}{I_{spec}} \right), \tag{3.24}$$

where I_{spec} is the current level at which E_{S_x} is specified. The resulting overall power electronics circuit losses, P_{pe}, is the summation of the number of active devices times the loss per device for both S_x and S_s, as used in the specified configuration.

Electrical machine

The electrical machine loss factors taken into account are the resistive losses, P_{re}, the hysteresis losses in the iron, P_{hy}, and the friction losses, P_{fr} as detailed in [121]. The hysteresis losses were computed assuming the material properties of Cogent M600-65A [121] for both the rotor and the stator. The eddy current losses in both the stator and the rotor are neglected for two reasons, i.e. minor influence due to the relatively low ω_e range, and the presence of a copper sleeve around the rotor of electrical machine A, influencing the eddy current losses in the rotor. A thorough FEA should be carried out to predict the electrical machine losses accurately, which is beyond the scope of this research.

Drive efficiency

The resulting overall drive system efficiency, η_{sys}, is computed with

$$\eta_{sys} = \frac{P_m}{P_m + P_{pe} + P_{re} + P_{hy} + P_{fr}}. \tag{3.25}$$

Efficiency contour plots of T_m and P_m per DDO mode are constructed using (3.25) and shown in Figure 3.6. Additionally, the previously computed operating range per-mode is plotted to show the boundaries. In the FBI contour plots, the derived FBS operating range is added for comparison.

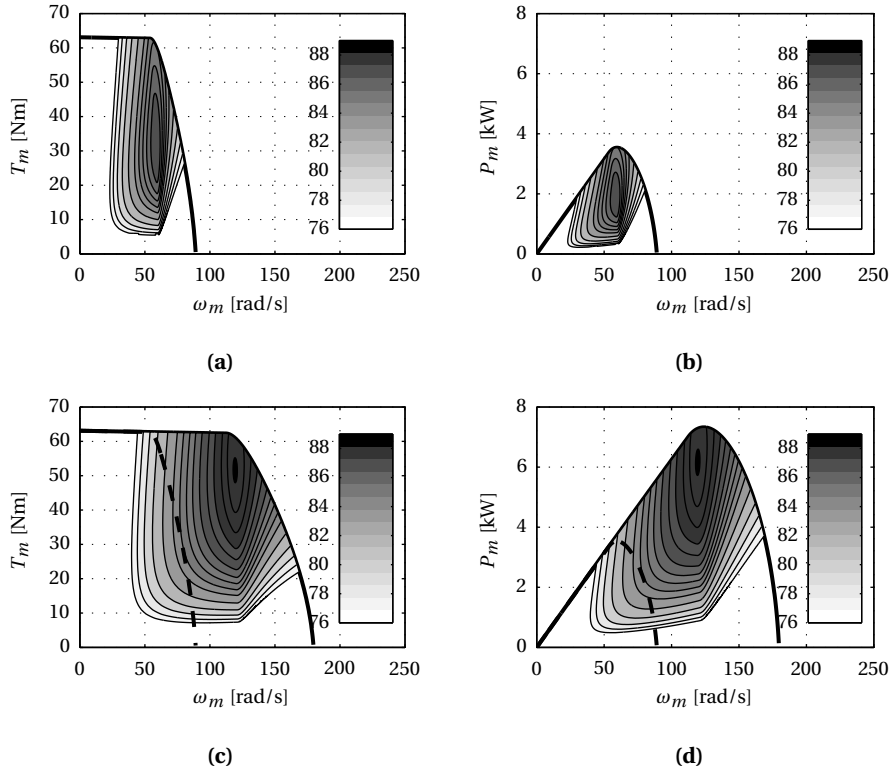

Figure 3.6: Drive efficiency contour plots of the DDO operating modes where the grey-scale bars indicate the computed efficiency percentage; **(a)** FBS T_m versus ω_m, **(b)** FBS P_m versus ω_m, **(c)** FBI T_m versus ω_m, **(d)** FBI P_m versus ω_m. The dashed lines in **(c,d)** represent the respective T_m and P_m range in FBS mode for comparison.

3.5 Experimental verification

Throughout this section, the applied configuration is: machine A (Appendix C), setup B (Appendix F), and $V_{inv} = 300$ V for all VSIs (Figure F.2b). To test the behaviour of the six-winding electrical machine A while powered by the $N^{\text{set}} = 2$ variant of the circuit depicted in Figure 3.3, simulations and measurements were executed. The FB configurations in the CTSR are tested to verify whether the respective base angular velocities are reached under nominal operating conditions, and are therefore computed correctly. Electrical machine A is connected to a load DCM which is powered from the grid by a bidirectional DCM regulator, as depicted for the other experimental setup in Figure F.2b.

3.5.1 System configuration and control

The CS applied to both the simulations and experiments consists of three different control loops. The DCM is angular velocity controlled by a proportional and integral (PI) controller, which determines the reference signal for the current controller as explained in Appendix E, and shown in Figure E.1. A comparable structure is applied to the torque controller with which T_{em} of electrical machine A is regulated. As a result of the direct relation between T_{em} and i_{q1} for an SPMSM (3.19), the torque is controlled by regulating i_{q1}. A PI controller for the whole SPMSM (FBS) or per three-phase winding set (FBI) is applied to regulate the corresponding i_{q1} per drive configuration. The control structure depicted in Figure 2.8a is used, where for the BM control solely $n = 1$ is applied $\left(\text{CS}_1^{\text{bm}}\right)$, while for the CM control solely $n = 3$ is applied $\left(\text{CS}_3^{\text{cm}}\right)$. The CS_1^{bm} is used to ensure MTPA control, while CS_3^{cm} is used to avoid circulating CM currents due to the open-winding structure. The described CS structure is applied per-winding set, therefore equal per-phase winding currents are assumed. Additionally, based on the per-harmonic machine constants listed in Table C.1, the FF inputs of the respective harmonics (Figure 2.8a) are used to compensate for the EMF. Each input $x_{dqn(FF)}$ is determined by $\left(dn, qn\right) = \left(0, \Lambda_{dn}^{\text{sr}}\right)$, where the relation with the per-harmonic electrical machine constant, K_{en}, is detailed in (2.49). The EMF machine constant per-harmonic is BM for $n = 1, 5, 7, 19$ and CM for the other harmonics, i.e. $n = 3, 9, 15$. The disturbance on the error correction of the current PI controller is reduced as a result. The system is configured such that the same CSs are used for both the simulations and the experiments.

The mechanical-set parameters are based on the torque balance equation (2.12) where $T_l = T_{DCM}$, and set-A inertia, J_m^A, and friction, B_m^A, are listed in Appendix E. The resulting T_{em} produced by electrical machine A compensates in steady state for the complete machine-set friction in (3.22).

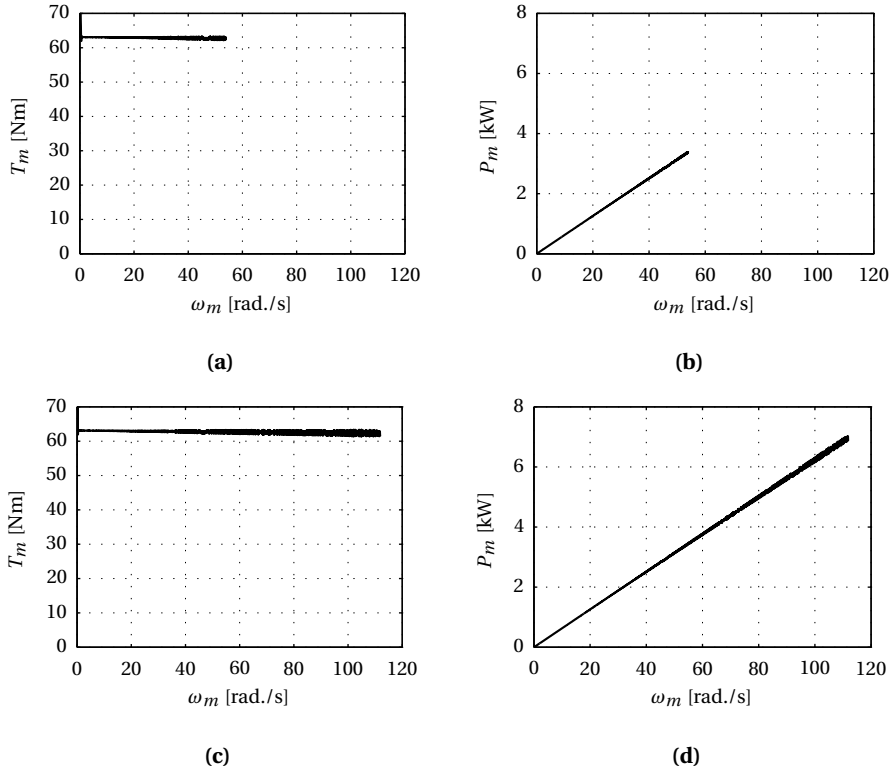

Figure 3.7: Simulated power and torque versus angular velocity characteristics of the DDO operating modes in CTSR; **(a)** FBS T_m versus ω_m, **(b)** FBS P_m versus ω_m, **(c)** FBI T_m versus ω_m, **(d)** FBI P_m versus ω_m.

3.5.2 Simulations

A simulation model of the proposed system is made using MATLAB/SIMULINK. The CS is implemented directly in SIMULINK while the power electronics and electrical machine models are composed using PLECS^{TM} [119]. The model parameters are computed by a discrete-time solver operated at the real-time target (RTT) sample time, T_s, resembling the RTT functionality. The actual cycle-time delay of the RTT is furthermore taken into account to predict the actual behaviour of the electrical machines on the reduced CS bandwidth. The DCM, regulator and angular velocity CS are modelled as a PI controller with an additional gain. Electrical machine A is modelled as indicated in Figure C.1, based on the parameters listed in Appendix C. The simulated T_m and P_m versus ω_m in both drive modes are presented in Figure 3.7.

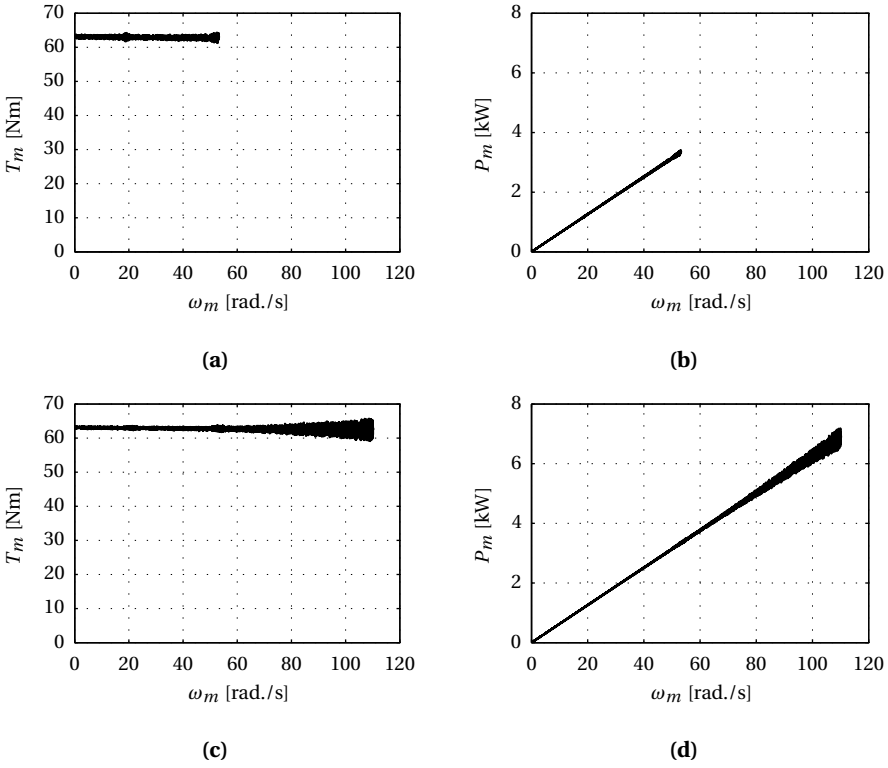

Figure 3.8: Measured power and torque versus angular velocity characteristics of the DDO operating modes in CTSR; **(a)** FBS T_m versus ω_m, **(b)** FBS P_m versus ω_m, **(c)** FBI T_m versus ω_m, **(d)** FBI P_m versus ω_m.

3.5.3 Experiments

For the measurements, both electrical machine A and the DCM driving power electronics converters are controlled from the RTT which is programmed and operated from a SIMULINK model on the engineering computer (EC). The quad three-phase VSI setup from TRIPHASE^{TM} [159] powers electrical machine A based on the modulation signals provided by the RTT, as depicted in Figure F.2a. The DCM armature current, I_a, electrical angular position, θ_e, torque T_{DCM}, and the electrical machine A per-phase per-winding currents, i_x^u, are measured and interfaced to the SIMULINK model by the RTT. The electrical machine A torque is computed based on the $(d1,q1)$-transformation of i_x^u using (3.19). The measured T_m and P_m versus ω_m in both drive modes are presented in Figure 3.8.

3.6 Results

In this section, firstly the results and their interpretation analogue to the indicated sections are given. Next, the computations, simulations, and experiments are compared to verify whether the simplified analysis is a valid method to predict the different angular velocity ranges.

Operating range per configuration

From the per-mode T_m versus ω_m graphs in Figure 3.5b it is concluded that the angular velocity range for a given electrical machine is improved by powering the windings using FB instead of HB converters. Furthermore, x_s is significantly improved by combining different drive modes and reconfigure the windings accordingly. In the SVM case, ω_b = 29.9 rad./s and ω_t = 51.6 rad./s, resulting in x_s = 1.73. When combining the FBS and the FBI drive modes, ω_b^{I} = 53.9 rad./s and ω_t^{II} = 179.9 rad./s, resulting in x_s = 3.34. Looking at ω_b per-mode in Table C.2, it is concluded that for the applied V_{co} small discrepancies of -1.1 rad./s with FBS and of +2.3 rad./s with FBI are achieved with the respective 55, 110 rad./s strived for. Considering (3.20), it is observed that $\left|v_1^{\mathrm{sr}}\right|$ of (3.17) is less than half of (3.18), making an exact ratio of two impossible in practice. The achieved discrepancy is close to the minimum possible value.

As listed in Table C.2, the $x_s = 2$ strived for is achieved in neither configuration. This is mainly due to the construction of electrical machine A, and the relatively high R_{st} due to the vast number of turns per-winding, required to achieve the intended K_e at ω_m = 55 rad./s. The computed CPSR values of the torque in Figure 3.5b and thus also the power in Figure 3.5c differ from the ideal cases depicted in Figure 3.2b and Figure 3.2c. Since $\Lambda_{d1}^{\mathrm{sr}} > L^{\mathrm{sr}}\check{\imath}_x$ is valid for electrical machine A (Figure C.2a), the theoretical maximum ω_t (3.21) of this machine is finite even when ignoring R_{st}. Details on the exact relation between saliency and the actual angular velocity range for various electrical machine types are explicated in [113, 146].

For the fixed winding structure of electrical machine A, it is demonstrated in Figure 3.5c that $\hat{P}_m$ is improved over the conventional wye and SVM configurations because T_{em} is kept constant until the increased ω_b as shown in Figure 3.5b. Consequently, $\hat{P}_m$ is increased from 1.96 kW in the SVM case to 3.54 kW, and 7.32 kW in the FBS and FBI configurations, respectively. This is achieved by enhancing the overall AC voltage applied to the machine windings.

Table 3.1: Mean power per component

Mode	P_m	P_{pe}	P_{re}	P_{hy}	P_{fr}	Unit
FBS	895	149	74	31	19	[W]
FBI	1813	279	74	63	76	[W]

Efficiency per configuration

In Figure 3.5b and Figure 3.5c it is shown that an electrical machine driven according to the DDO principle has multiple angular velocity ranges and that P_m is increased. By combining the FBS and FBI modes based on the highest efficiency per operating point, the highest overall drive efficiency (3.25) is achieved. In the presented $N^{\text{set}} = 2$ case, this is considered in the FBS drive mode operating range, as indicated with the dashed lines in Figure 3.6c and Figure 3.6d. By observing Figure 3.6a and Figure 3.6c, it is concluded that by combining the modes, a higher overall drive system efficiency is achieved compared to only using the FBI mode. The drive-system peak-efficiency point, or sweet spot, $\hat{\eta}_{sys}$, per configuration depicted in Figure 3.6, is $\hat{\eta}_{sys} = 87.0,\ 88.3\%$, for FBS, FBI respectively.

For each of the powers in (3.25), the mean value over the T_m, ω_m domain is computed per configuration, (FBS, FBI) to give an idea of the distribution. The results are listed in Table 3.1. The relatively large P_{pe} is mainly due to $P_{sw S_x}$, because of the number of S_x devices in combination with the applied device-type. Since the insulated-gate bipolar transistors (IGBTs) used in the drive are $v_{br} = 1200$ V types, capable of conducting an RMS phase current, $I_x = 33$ A (Table F.1), they are over-rated for this application in both voltage and current. As such, E_{S_x} per device is higher than necessary. Application of, for example, the more suitable FS10R06VE3 [75], $I_x = 10$ A IGBT type reduces E_{S_x} by a factor 6, and thereby significantly improve η_{sys}.

Simulations

In Figure 3.7, the simulation results are depicted. Figure 3.7a and Figure 3.7b show the FBS driven T_m and P_m respectively, while the respective T_m and P_m in the FBI driven case are shown in Figure 3.7c and Figure 3.7d. The transient peak in T_m, (Figure 3.7a, Figure 3.7c) is caused by a small discrepancy with the initial inductor currents. From Figure 3.7 it is concluded that the computed ω_b in either drive mode is reached, verifying the validity of the computations. The maximum achieved output power, $\hat{P}_m = 3.47,\ 7.19$ kW at ω_b of the simulated FBS and FBI modes respectively.

The increasing noise-level with an increasing ω_m in Figure 3.7 is caused by higher harmonic torque components that occur due to the imperfect FF compensation of the electrical machine A EMF harmonics. The periodic voltage component with the highest

frequency that should be produced by the VSI to match the 19^{th} EMF harmonic in the presented experimental verification is 665 Hz. The small mismatch between the EMF and the produced discrete VSI voltage causes a current that interacts with the EMF, resulting in higher harmonic torque components, according to (2.50).

Experiments

In Figure 3.8, the results of the measurements are shown. Figure 3.8a and Figure 3.8b depict the FBS driven T_m and P_m, respectively. Figure 3.8c and Figure 3.8d detail the respective T_m and P_m in the FBI driven case. Based on Figure 3.8a and Figure 3.8c it is concluded that throughout the indicated angular velocity range, $T_{em} = \check{T}$ and thus that the intended CTSR is achieved. The powers depicted in Figure 3.8b and Figure 3.8d follow from Figure 3.8a and Figure 3.8c, respectively. The maximum achieved output power, $\hat{P}_m = 3.41,\ 7.18$ kW at ω_b of the measured FBS and FBI modes respectively.

The initial definition of ω_b is that while applying $\check{\imath}_x$ and $\omega_m = \omega_b$, the PWM signal amplitude of each phase, $\hat{m}_x$, should be exactly unity to generate $\left|\hat{\vec{v}}_1\right|$ (Figure 2.2a). The actual value of $\hat{m}_x$ is derived from the measurement data for both the FBS and the FBI operation, which are $\hat{m}_{x(FBS)} = 0.986$ and $\hat{m}_{x(FBI)} = 1.065$, respectively. These values are close to the initially intended level and the small discrepancy is mainly due to a slightly higher than nominal $I_x = 6.34$ A, while $\check{I}_x = 6.03$ A. Additionally, variation of V_{inv}, a different V_{co} than presumed, and measurement errors influence the results. The $\hat{m}_x$ applied to the inverter by the CS was limited to unity in both cases.

The discretization effect explained in the simulation results worsened in the experiments. This is due to saturation effects in electrical machine A, reducing the per-harmonic EMF voltage. This effect is not accounted for in the FF compensation, leading to a further increase of the voltage difference, and with that a higher amplitude of the harmonic current components. The increased torque ripple in Figure 3.8 is caused by the interaction of the increased current with the EMF components.

Comparison

By comparing Figure 3.5b, Figure 3.7, and Figure 3.8, it is concluded that the computations, simulations and experiments are in good agreement in the CTSR. The same ω_b and a similar $\hat{P}_m$ is obtained in each case and for both modes. The increasing amount of noise as a function of ω_m in both Figure 3.7 and Figure 3.8 is caused by the finite bandwidth of the CS and the higher-order EMF harmonics. The additional difference between Figure 3.7 and Figure 3.8 is caused by noise on the measured currents, which is not present in the simulations.

3.7 Summary and conclusions

In this chapter, an electrically and electromechanically integrated drive concept is presented for dynamic operation of an electrical machine. It is demonstrated that the angular velocity range and output power for a fixed electrical machine configuration is improved compared to conventional concepts. By combining different drive modes, an electrical machine integrated equivalent of a gearbox is realized. In contrast to a mechanical fixed ratio gearbox which ideally exchanges angular velocity and torque given a fixed power, this solution can improve the output power by increasing the angular velocity while maintaining a fixed electromagnetic torque.

The dynamic drive operation concept of sectioning each phase is enunciated and a reconfigurable power electronics circuit is presented. The electric isolation between the different per-phase winding sections is used beneficially to enhance the AC output voltage. Different utilization options and drive modes of an exemplifying machine are detailed. Additionally, the limitations of both the machine and the power electronics are detailed to explain the discrepancy between the idealized and the actually obtained operating ranges. Based on the limitations, the base and top angular velocities of conventional drive modes and two dynamic drive operation modes are computed, simulated, measured, and compared.

The proposed dynamic drive operation concept is capable of improving the angular velocity range and angular velocity ratio of electrical machine A by applying the indicated drive configurations. These configurations are compared to the conventional wye-connected and space vector modulation cases, and computed to be superior. Additionally, an improved overall system efficiency can be achieved by combining the drive modes. The presented verification of the proposed dynamic drive operation principle using simulations and experiments shows a good agreement with the initial computations. The intended improvement of the constant-torque speed region is demonstrated in both the series-connected and the individually-driven converter configurations. In the case of the presented example, the absolute angular velocity range is improved by a factor 3.49, while the angular velocity ratio is boosted from $x_s = 1.73$ to $x_s = 3.34$ compared to the wye-connected space vector modulation operated configuration. Alternatively, the improved angular velocity ratio can be used to reduce the required $\check{P}$ for a given output performance.

When comparing the presented dynamic drive operation with found literature on winding reconfiguration concepts, the property of extending the constant-torque speed region up to the FB individual is the major advantage of the presented work. From the experimental results, it is concluded that the presented modelling technique is adequate to describe the behaviour of an actual machine in terms of predicting the obtainable torque, angular velocity, and resulting power based on the provided power electronics topology and drive method. Computations, simulations, and measurements show a

good agreement. In addition, the alternative two-axis modelling based regulation and estimation method introduced in Chapter 2 proves to be a suitable control system method.

The main drawback of the proposed solution is the greatly increased number of necessary semiconductor devices, and with that the possibility of a single device failure. In Chapter 6, it is explained how the increased system complexity is used advantageously to improve the system reliability and cope with device and winding failures.

4

Dynamic drive reconfiguration during acceleration

"An electrical equivalent to the Van Doorne variomatic transmission system"

Abstract: *The complete operating range of the presented dynamic drive operation concept can be covered by driving each winding of each machine phase individually. However, this generates significant switching losses due to the high switch count, reducing the drive-line efficiency at low output power levels. Therefore, at a low vehicle speed, this is accommodated by bidirectional series switches, reducing the switching losses, and improving the efficiency. The motivation for the optimal switch configuration is given and a powered transition between the system modes is detailed and demonstrated.*

Parts of this chapter are published in:

- T. Gerrits, C. G. E. Wijnands, J. J. H. Paulides, and J. L. Duarte, "Dynamic machine operation transitions," in *9th Vehicle Power and Propulsion Conference (VPPC)*. IEEE, October 2013, pp. 132 – 137

4.1 Introduction

To avoid the sense of jerk for the passengers, an acceleration should be performed smoothly and with an uninterrupted torque during the gear transitions. Various mechanical and electrical transmission systems exist, capable of a continuous gear-ratio adaption under full-load-torque or power-shifting. Consequently, the vehicle is accelerated without jerk and in the shortest possible time span, as explained in Chapter 1 and shown in Figure 1.5.

A continuously variable transmission (CVT) is very suitable type of gear-box to be used with an electrical machine because of the power-shifting capability, allowing for gear-ratio adaption within the CTSR. The first proposed mechanical CVT system, was based on two sets of conical disks forming pulleys. A push-belt was used to transfer the power from the input pulley to the output pulley. By changing the distance between the disks of one pulley, the belt was shifted varying the conversion ratio of the CVT. This concept was invented and patented by Van Doorne and Ludoph [31]. The push-belt CVT is increasingly applied as automatic transmission in vehicle propulsion because it improves the fuel-efficiency of the ICE [118]. However, when considering the average energy transfer efficiency, $\langle \eta_{gb} \rangle$, of either an hydraulic controlled ($\langle \eta_{gb} \rangle = 84.2\%$) or an electromechanically controlled CVT ($\langle \eta_{gb} \rangle = 90.5\%$) over the full torque range, both system efficiencies are relatively low [162]. This makes them less suitable for a battery powered drive-line. The electromagnetic variable gear-ratio power-shifting alternatives are the electrical CVT [66], and the intermediate winding changeover principles [108]. The electrical CVT is impractical and therefore not considered further.

The intermediate winding changeover principle which is thoroughly described in [108], also suffers from a major disadvantage when looking in-depth at the transitions. The wye-to-delta transition requires that the phase currents are shifted to re-align with the EMF, which is achieved by applying asymmetric intermediate transition configurations. Unfortunately, no measured torque is reported, but by analysing the phase currents it is concluded that torque interruptions are avoided although a jerk-free transition seems unrealistic. Additionally, the reluctance torque of the applied PMSM is used beneficially to shape the torque during the transition, making the principle machine type dependent.

The combined operating modes of DDO offer the possibility to cover a wide-angular-velocity operating range without the need for extensive FW or a variable mechanical transmission, as presented in Chapter 3. However, this requires the transition from e.g. FBS to FBI driven operation. To demonstrate that DDO is a good alternative solution to achieve a wide-angular-velocity operating range, firstly the motivation for the use of series switch, S_s, over a solely FBI operated machine is given and the preferred type of semiconductor is chosen. Next, two possible different drive configuration transitions are detailed and the different steps required to execute a transition are explained. Finally,

an instantaneous power-shift between the two DDO modes is explained, motivated, and experimentally verified. Throughout this chapter, the two windings per-phase machine configuration as introduced in the previous chapter is used.

4.2 Bidirectional series switch

As concluded from the operating range achieved with the FBI drive configuration in Figure 3.5b, the application of a bidirectional series switch is not required. However, the advantage of the per-phase bidirectional series switches, S_{sx} with $x \in [a,b,c]$, as introduced in Figure 3.3, is the reduction of the switching losses in the FB modules, P_{sw}. The required switching frequency of S_s depends mainly on the vehicle speed, u_v, and thus on the driving behaviour and drive-cycle. Therefore, it is in the sub-Hertz to Hertz range, as with mechanical transmission systems. The allowed transition duration, and resulting torque interruption is in the low millisecond range. The fast transition requires the usage of semiconductor devices. However, the switching frequency is low for electrical systems, allowing the device-type selection to be based solely on the conduction losses, P_{co}.

A bidirectional series connection switch composed of semiconductors consists, by definition, of at least two devices. Possible circuits are; a bridge rectifier [85], an anti-series or anti-parallel connection of two IGBTs [153], an anti-series connection of two metal-oxide-semiconductor field-effect transistors (MOSFETs) [27], an anti-parallel connection of two thyristors [108], or a bilateral triode thyristor (TRIAC). Since the conduction losses of the switch are the dominant factor in determining the most efficient solution, the bridge rectifier and the anti-series IGBT circuit are not considered further. In those respective circuits, three or two series-connected components with a fixed minimum conduction voltage are used, increasing P_{co}. The main drawback of the thyristor and TRIAC circuits is the fact that a firing circuit is required, which continuously triggers on zero-crossings to give a pulse to turn on the device. Furthermore, they introduce harmonics as a result of the latching currents at zero-crossings [105, 108]. These harmonics increase the electrical machine losses and cause vibrations as a result of the arising torque ripple. Therefore, these solutions are not further considered.

This leaves two suitable candidates to create a bidirectional switch, which are shown in Figure 4.1. The first option considered is the anti-series connection of two MOSFETs. The anti-series connection can be made in two ways, i.e. with a mutual source, S, or a mutual drain, D, connection. The mutual source anti-series connection of two MOSFETs, allows for a single gate, G, driving signal, making it the preferred solution, as depicted in Figure 4.1a. The per-phase x, switching leg N_x^u is connected to switching leg $N_x^{(u+1)}$ via the drain of each respective MOSFET. The anti-series connection of two devices is required to ensure that in the off-state, S_s blocks the switch current, i_{S_s}, independent of polarity to avoid conduction of the intrinsic diode [105]. As depicted with two pairs

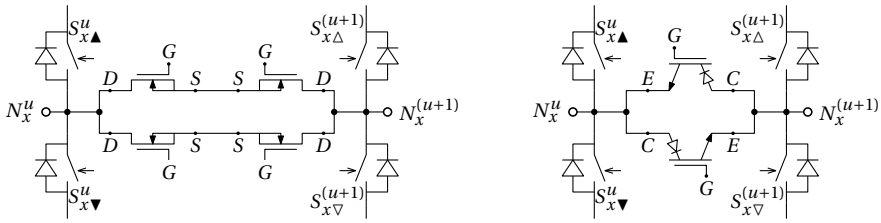

Figure 4.1: Investigated semiconductor composed series switch solutions; **(a)** anti-series connected dual leg MOSFET based, **(b)** anti-parallel connected RB IGBT based.

in Figure 4.1a, multiple parallel MOSFET pairs are used to further reduce to overall S_s on-state resistance. The main advantage of using MOSFETs is their relatively low losses at a low RMS S_s current, I_{S_s}. The second solution is an anti-parallel connection of two reverse blocking (RB) IGBTs [152], as depicted in Figure 4.1b. The diode in the collector path is a monolithic layer integrated in the IGBT device structure to make it reverse blocking. The advantage of this circuit is that only one device is conducting from the collector, C, to the emitter, E, depending on the polarity of the current. The downside, however, is that an IGBT has a minimum forward conduction voltage, V_{co}, [105], resulting in relatively high P_{co} at low I_{S_s} levels. Due to the difference between the resistive MOSFET behaviour and the minimum conduction voltage IGBT behaviour, the favoured solution depends on the application. In the following section, the conduction losses of these two switch types are compared to determine the most efficient solution for the presented case.

4.2.1 Comparison of series switch conduction losses

Whether an IGBT or MOSFET solution is preferable for a certain topology depends on many factors [48], but for a given inverter supply voltage, V_{inv}, the RMS switch current I_{S_s} is decisive. The IGBT collector-emitter conduction voltage, V_{CE}, has a minimum level, while the MOSFET conduction depends on the drain-to-source channel on-state resistance, $R_{DS(on)}$. Both effects are illustrated in [105]. The two windings per-phase version of the dynamic drive topology contains one series switch per-phase as shown in Figure 4.2. A first-order approximation of the conduction losses is made by solely taking into account the series switch semiconductor loss of the three-phase system, represented with V_{CE} and $R_{DS(on)}$. The average conduction loss of S_s as depicted in Figure 4.1 for a three-phase system are computed with respectively

$$P_{co(IGBT)} = 3 I_{S_s} V_{CE}, \tag{4.1}$$

$$P_{co(MOSFET)} = 3 I_{S_s}^2 R_{DS(on)}. \tag{4.2}$$

For the chosen implementation in the previous and this chapter, $V_{inv} = 300$ V. Considering the voltage breakdown rate, $K_{br} = 2/3$ in (2.15), semiconductors with a breakdown voltage $v_{br} \geq 450$ V are required. Therefore, $v_{br} = 600$ V devices are applied. The parameters of the semiconductors used are listed in Appendix G. By equating (4.1) with (4.2), the decisive value of I_{S_s} is found based on the respective semiconductor parameters to determine whether an IGBT or MOSFET based solution is optimal.

The only known range of commercially available RB IGBT types are manufactured by IXYS^{TM} [77], from which the IXRH40N120 is favourable for its minimum V_{CE} and maximum I_{S_s} rating. However, the IXRH40N120 is a device with $v_{br} = 1200$ V, $I_{S_s} = 55$ A, making it suitable but not ideal for this comparison. A broad range of $v_{br} = 600$ V MOSFET devices is produced by numerous manufacturers, of which the STY139N65M5 from STMICROELECTRONICS^{TM} [150] is selected based on [6]. Considering solely conduction losses, the I_{S_s} turning point value, I_{tp}, for which the IGBT and MOSFET S_s losses are equal are determined using (4.1) and (4.2). For the switch configurations as depicted in Figure 4.1, $I_{tp} = 164$ A, neglecting thermal effects. As investigated in [6], this value drops to approximately 100 A if the increased $R_{DS(on)}$ due to the temperature rise is accounted for. Nevertheless, for the nominal assumed electrical machine A RMS stator winding current (6.03 A), the anti-series connected quad MOSFET based solution (Figure 4.1a) minimizes P_{co}.

In the following, a comparison is made between either applying FBS operation in the low angular velocity range, or solely drive the electrical machine using the FBI configuration. The circuit losses of both configurations are computed to determine whether the use of a S_s type is justified.

4.2.2 Switching losses versus conduction losses

When observing the different DDO configurations in Figure 3.4, it is emphasized that a circuit without S_s can produce the required winding voltages over the full range of ω_m, i.e. Figure 3.4c. However, the consequence of only applying individual operation is that $3\left(4N^{\text{set}}\right)$ switches produce switching losses, independent of ω_m. On the other hand, if the circuit in Figure 3.4a is applied for $\omega_m \leq \omega_b^{\text{set}}$, the circuit conduction losses are increased by the $3\left(N^{\text{set}} - 1\right)$ additional conducting devices. As a result, an optimum configuration as function of V_{inv} and the per-phase RMS current, I_x, is derived based on the device parameters of S_s and S_x. Throughout this analysis, a first-order approximation of the losses is derived per presented solution. Practical effects such as temperature influence or parasitic components are not considered. IGBTs are used as HB switching leg devices for their fail-safe capabilities; in case one IGBT in a switching leg breaks down, the other IGBT can still be turned off, avoiding a cross-conduction current, and successive device breakdown.

The simulations are executed using MATLAB/SIMULINK and PLECS. A schematic repre-

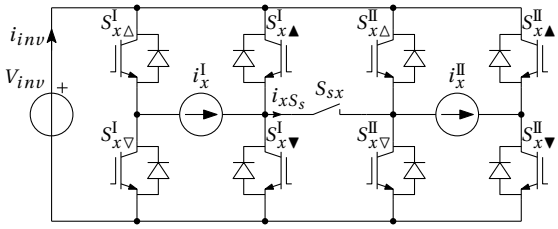

Figure 4.2: Schematic representation of the $N^{\mathrm{set}} = 2$ per-phase circuit with current sources as load, used to perform a loss comparison between the FBS and the FBI modes. In this comparison, each S_x is an IGBT, while S_{sx} is composed of MOSFETs as shown in Figure 4.1a.

Table 4.1: Simulated losses per device and in total for the presented case

Mode	P_{IGBT} [W]	P_{di} [W]	P_{S_s} [W]	P_{total} [W]
FBI	0.51	1.01	-	36.5
FBS	0.51	1.01	0.06	**19.0**

sentation of the simulation model is depicted in Figure 4.2. The IGBT and MOSFET models are constructed in PLECS, taking into account their switching and conduction losses as a function of supply voltage and device current. The semiconductor types and specifications as well as the other test parameters are given in Appendix G. Within this model, the current sources i^{I}_x and i^{II}_x per-phase x emulate a sinusoidal electrical machine current with amplitude $\sqrt{2}I_x$. A pulse signal steers each active HB with a fixed duty cycle, D. S_s is either on or off depending on the configuration, i.e. FBS or FBI. Normally, D varies as a function of the modulation signal, but in this case an averaged loss model is used allowing for a fixed duty-cycle. The resulting losses per S_x IGBT, P_{IGBT}, and diode, P_{di}, and per MOSFET device in S_s, being P_{S_s}, are summarized in Table 4.1. Also, the total three-phase solution losses per configuration, P_{total}, are summed in Table 4.1, to show the different overall VSI losses. When extending this concept to more than two windings per-phase $\left(N^{\mathrm{set}} > 2\right)$, the loss consideration remains the same; two switching HBs versus one conducting series switch, maintaining the same loss ratio.

In Table 4.1 it is shown that P_{di} is higher than P_{IGBT} despite a lower on-state conduction voltage and channel resistance, as listed in Appendix G. This is due to the fact that a relatively low current is applied, and the diodes have a higher on-state conduction voltage at low current levels. The implemented S_s, detailed in Appendix G, can handle an I_{S_s} up to 80 A. In that range it is computed to be more efficient than an RB IGBT based solution [6]. From Table 4.1 it is concluded that the inclusion of a series switch reduces the VSI losses if the drive is operated in the FBS mode. The inclusion of S_s is beneficial for every value of I_{S_s} because of the reduced number of switching devices. In this case, for current levels above approximately 80 A, S_s should be constructed using RB IGBTs to reduce P_{total}. If S_s is to be designed for a different v_{br}, the decisive current level at

which the RB IGBT based switch solution becomes favourable over the MOSFET based is different. Nevertheless, the same approach is applicable to determine the most efficient solution for each system, and chosen set of semiconductors.

4.2.3 Series switch driver considerations

Next to an improved system efficiency, an additional advantage of the MOSFET based solution in Figure 4.1a, is that all the devices per S_s are controlled by a single gate-driver per-phase because of the common source point for all devices. This is not the case for the separated emitter points of the RB IGBT based solution in Figure 4.1b, necessitating two individual driver circuits per-phase. For either device type, the gate-driver should be powered by a galvanically isolated DC-DC converter ensuring voltage potential independence and avoiding duty-cycle dependence as e.g. with a level-shifting gate-driver. When the sequential zero-crossing solution depicted in Figure 4.3d is employed, there are two options; either the S_s state is altered for both directions simultaneously at the zero-crossing of i_{xS_s}, or the non-conducting device is turned off directly, while the conducting device is turned off after the zero-crossing. In the latter case, the per-device unidirectional property of either S_s solution is used advantageously to allow for non-stringent transition timing. However, this requires two gate-driver circuits per S_s.

Different methods exist to reconfigure the drive system used for DDO, from which two possible solutions are explained. The series switch required to perform the reconfiguration is implemented and consists of four MOSFET devices as detailed in Appendix G. In the experimental verification, the implemented series switch is used to demonstrate a reconfiguration from FBS to FBI operation during acceleration.

4.3 Drive configuration transition

A transition from the FBS to the FBI drive configuration is considered in this section, using the per-phase system configuration of Chapter 3, i.e. $N^{\text{set}} = 2$ windings. The winding-sets are indicated with I, II as shown in Figure 4.2. The nominal torque, $\breve{T}$, is applied to electrical machine A during the acceleration time interval, t_a^{I}, as shown in Figure 4.3a. Additionally, the load DCM accelerates the machine-set angular velocity, ω_m, from zero to the FBI drive configuration base angular velocity, ω_b^{I}, as schematically indicated in Figure 4.3b. The investigated transition is executed by opening S_s at the second base angular velocity of electrical machine A, ω_b^{II}, at time, t_a^{II}. The switch condition of the HB legs connected to each series switch are considered to be altered simultaneously with S_s, i.e. when considering Figure 4.3; switches $S^{\text{I}}_{x[\blacktriangle,\blacktriangledown]}$, $S^{\text{II}}_{x[\triangle,\triangledown]}$ are in tri-state (continuously off) when S_{sx} is closed, and start switching in anti-phase with respect to their FB counterparts when S_{sx} is open. The transition from S_s closed to S_s open can be executed in various ways, from which two methods are investigated further; simultaneously for all

phases; *simultaneous reconfiguration* as indicated in Figure 4.3c, or sequentially at the zero-crossing of each respective phase current; *sequential reconfiguration* as indicated in Figure 4.3d.

4.3.1 Simultaneous reconfiguration

The straightforward method to decide which configuration should be applied is by only taking into account ω_m. The per-phase devices for which the switch-state depends on the simultaneous reconfiguration system are detailed in Figure 4.3e. At time, t_a^{II} the phase currents are interrupted simultaneously by opening S_{sx}, of each respective phase. The current through each S_{sx}, being i_{xS_s}, is interrupted as shown in Figure 4.3c and forced to commutate to the free-wheeling diodes of the neighbouring HB switches as depicted in Figure 4.3e. It is emphasized that the current interruption in Figures 4.3c and 4.3d only occurs in S_s, and not in the actual electrical machine windings. Therefore, ideally it does not influence T_{em} as indicated in Figure 4.3a.

4.3.2 Sequential reconfiguration

The sequential reconfiguration strategy uses, next to ω_m, the mutual angular difference between the succeeding phases to sequentially turn off the per-phase S_s at the zero-crossing of the current, as illustrated in Figure 4.3d. This is achieved by measuring i_{xS_s} and switching when $i_{xS_s} = 0$. However, the semi-conducting property of the devices per S_s in Figure 4.1 is used advantageously to stop the conduction in a fluent manner by natural commutation. For a RB IGBT based S_s, this means that each unidirectional switch depicted in Figure 4.3f represents one RB IGBT. For the S_s composed of two anti-series connected MOSFETs this implicates that the MOSFET from which the intrinsic anti-parallel diode is conducting at t_a^{II} is turned off directly, while the other MOSFET is turned off after i_{xS_s} reverses polarity. The exact instance at which the MOSFETs are turned off is not critical within that half period of i_x. However, the RR loss of the intrinsic anti-parallel diodes is minimized by executing the procedure at a minimum $|i_x|$. The resulting per-phase dual unidirectional anti-parallel S_s representation in Figure 4.3f is suitable for sequential per-phase zero-crossing interruption of the per-phase i_{xS_s} for a positive current polarity, $i^+_{xS_s}$, and a negative current polarity, $i^-_{xS_s}$, as shown in Figure 4.3d.

In Figure 4.3d it is furthermore shown that the total duration of a sequential reconfiguration depends on ω_m and the number of pole pairs, N_{pp}, of the applied electrical machine. Assuming that each S_s state is changed at the same phase current level, reconfiguring the total drive system takes t_{seq} seconds, where

$$t_{seq} = \frac{4\pi}{3N_{pp}\omega_m}. \tag{4.3}$$

The time required to perform the sequential reconfiguration is not important for the output performance of the system since the electrical machine currents, and with that the torque, are not influenced.

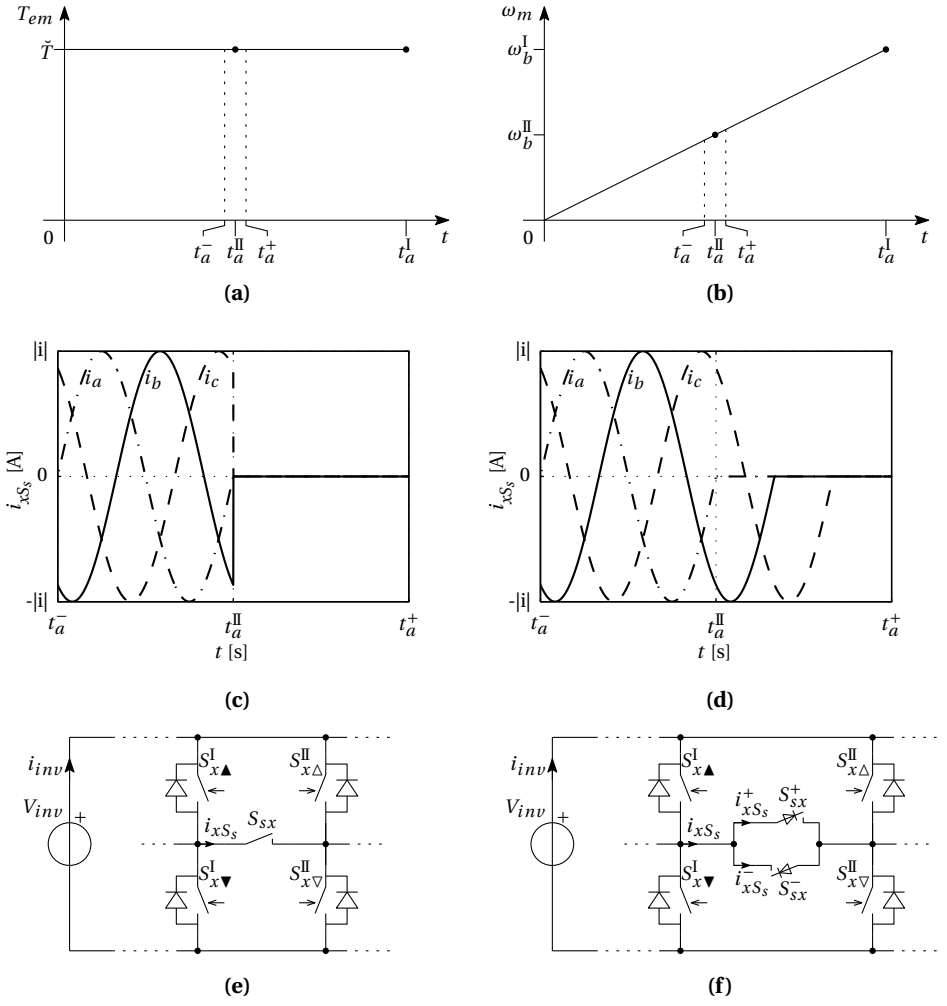

Figure 4.3: Idealized schematic representation of acceleration with reconfiguration at t_a^{II}; **(a)** T_{em} versus t, **(b)** ω_m versus t, **(c)** detail of indicated per-phase current for $t_a^- \le t \le t_a^+$ applying simultaneous opening of S_s, **(d)** detail of indicated per-phase current for $t_a^- \le t \le t_a^+$ applying sequential opening of S_s, **(e)** bidirectional S_s representation suitable for simultaneous interruption of i_{xS_s}, **(f)** dual unidirectional anti-parallel S_s representation suitable for sequential zero-crossing interruption of i_{xS_s} for a positive current polarity, $i_{xS_s}^+$, and a negative current polarity, $i_{xS_s}^-$.

4.4 Experimental verification

To successfully apply the DDO principle, transitions between sequential operating modes should be executed while the angular jerk, ζ, is minimized [54]. Jerk is defined as the rate of change of acceleration over time. In a vehicle equipped with a reconfiguring drive-line, the driving experience is markedly better if the passengers do not experience jerk. Mechanical automatic transmission systems require a complex cooperation between the engine and clutches based on the engine torque and drive-line inertia to smoothen the output torque during a gear transition [58]. In the simulated mechanical twin-clutch transmission system presented in [58], the time required for the gearshift from the first to the second gear, $t_{1\rightarrow 2} = 450$ ms. During this gearshift, the passengers experience a peak mechanical angular jerk, $\hat{\zeta}_m = 6.64$ kNm/s, which is determined with

$$\hat{\zeta}_m = \max\left(\frac{\mathrm{d}T_m}{\mathrm{d}t}\right) \propto \frac{\mathrm{d}\ddot{\theta}}{\mathrm{d}t}, \tag{4.4}$$

where T_m is assumed proportional to the considered angular acceleration, $\ddot{\theta}$. This transition causes a variation of ω_m since ζ_m is high with respect to the drive-line inertia. The potential advantage of the presented electrical solution over a mechanical transmission is that during a transition solely a current redirection is required. The electrical machine current remains the same while the current is redirected from a series switch to the switching legs. Since the electrical machine phase currents are ideally not influenced, the output performance of the drive is neither. As a result of these changes by means of purely electrical quantities, a minimum jerk and transition time is achieved.

The main advantage of a transition under full-load-torque over existing reconfigurable electrical systems [17, 108, 131] is the fact that the transitions ideally is executed instantaneously. No winding reconfiguration is required. The transition time is mainly limited by the switching speed of S_s, being well under a microsecond when using MOSFETs. Unlike the methods presented in [17, 108, 131], the angle between the phase voltage and phase current is equal in the series and in the individual drive modes. Therefore, the angular velocity and angular jerk are determined solely by the accuracy with which the current is controlled during the transition.

The gear transition from FBS to FBI operation executed in this verification is based on a simultaneous series switch reconfiguration. The goal is to achieve this reconfiguration fluently, thus without disturbing T_{em}, thereby avoiding the transition from being noticed by the passengers of a vehicle equipped with a dynamic drive system. Throughout this section, the applied configuration is consistent with Chapter 3: machine A (Appendix C), setup B (Appendix F), and $V_{inv} = 300$ V for all VSIs (Figure F.2b).

4.4.1 Transition configuration and control

To test whether a transition without additional jerk transients can be achieved, a velocity ramp from zero to ω_b^{I}, while the torque $T_{em} = \check{T}$ was simulated during $t_a^{\mathrm{I}} = 8$ s, as schematically depicted in Figure 4.3. At $\omega_m = \omega_b^{\mathrm{II}}$, S_s was opened to decrease the EMF, e_{q1}, by a factor two, and to allow for constant acceleration until ω_b^{I}. The constant acceleration was executed while loading electrical machine A with the nominal torque $\check{T}$. When executing an online transition with a minimized transition time, the S_{sx} are opened simultaneously at t_a^{II}, with

$$t_a^{\mathrm{II}} = \frac{\omega_b^{\mathrm{sr}}}{\omega_b^{\mathrm{in}}} t_a^{\mathrm{I}}. \tag{4.5}$$

The current of at least two of the three phases is therefore unequal to zero as demonstrated in Figure 4.3e. The switches of each phase in connection with S_{sx}, i.e. $S_{x_{[\blacktriangle,\blacktriangledown]}}^{\mathrm{I}}$, $S_{x_{[\triangle,\triangledown]}}^{\mathrm{II}}$ (Figure 3.3), are all equipped with an anti-parallel diode. Thereby it is ensured that the current flowing through S_{sx} is redirected. Next, the switches $S_{x_{[\blacktriangle,\blacktriangledown]}}^{\mathrm{I}}$, $S_{x_{[\triangle,\triangledown]}}^{\mathrm{II}}$ start switching in anti-phase with $S_{x_{[\triangle,\triangledown]}}^{\mathrm{I}}$, $S_{x_{[\blacktriangle,\blacktriangledown]}}^{\mathrm{II}}$ respectively. The time required to execute the whole transition sequence depends mainly on the turn off time of S_{sx}, and the time required to start driving and controlling $S_{x_{[\blacktriangle,\blacktriangledown]}}^{\mathrm{I}}$, $S_{x_{[\triangle,\triangledown]}}^{\mathrm{II}}$ such that the currents of the two coils per-phase are equal.

The switching instance of S_s is chosen as a function of ω_m. However, the acceleration or deceleration leading to an altered angular velocity should be large enough to avoid repeatedly occurring transitions between the two different drive modes. A hysteresis based CS is therefore implemented to ensure that after turning S_{sx} off, ω_m reduces by e.g. 10% before turning S_{sx} on again.

The electrical machine equivalent circuit connected between two HB switching legs is different for each configuration, as indicated in Figure 3.1. In the $N^{\mathrm{set}} = 2$ variant of the dynamic drive system applied here, each electrical machine parameter halves at the per-phase winding bi-partitioning, as indicated in Chapter 3. As a result, the CS parameters are adapted to maintain the same system response for either configuration, which is done using the gain scheduling method [76].

The CS used for the experimental verification is commensurable with the CS of Chapter 3. The error between the actual ω_m and the reference value, ω_m^*, being Δ_ω, is regulated to zero with a PI angular velocity CS, CS_ω, as explained and shown in Appendix E. T_{em}, is regulated based on the direct torque versus q-axis current relation (2.10) with a PI current CS, CS_i. The fundamental frequency current components, i_{d1}, i_{q1}, are computed from the phase currents, i_a, i_b, i_c, using the standard Park transformation matrix (B.5). The per-harmonic EMF components are estimated based on ω_m and added to the per-harmonic, per-mode regulation diagram using FF, as shown in Figure 2.8a. In the FBS drive configuration, the current in winding x^{I}, being i_x^{I}, is equal

to the current in winding x^{II}, being i_x^{II}, as a result of the series connection made with S_{sx}. The single set of transformed BM $i_{d1}^{\text{bm}}, i_{q1}^{\text{bm}}$, and CM i^{cm} currents, is regulated with one PI current CS, i.e. CS_i. However, in the FBI drive configuration, i_x^{I} and i_x^{II} are regulated to the same reference value. The two sets of transformed BM, CM currents are regulated independently with a CS per set, $\text{CS}_i^{\text{I}}, \text{CS}_i^{\text{II}}$, respectively. Each set of phase currents, $i_a^{(\text{I,II})}, i_b^{(\text{I,II})}, i_c^{(\text{I,II})}$ is therefore transformed to the corresponding set of BM, CM currents, $i_{d1}^{\text{bm(I,II)}}, i_{q1}^{\text{bm(I,II)}}, i^{\text{cm(I,II)}}$ and independently regulated to the same reference value. An inverse Park transformation is performed using (B.6) to compute the per-set, per-phase PWM signals, $m_a^{(\text{I,II})}, m_b^{(\text{I,II})}, m_c^{(\text{I,II})}$, from the respective per-set, per-axis voltages, $v_{d1}^{(\text{I,II})}, v_{q1}^{(\text{I,II})}, v^{\text{cm(I,II)}}$.

4.4.2 Experiments

Equivalently to Chapter 3, both electrical machine A and the DCM driving power electronics converters are controlled from a RTT which is programmed and operated from a SIMULINK model on the EC. The quad three-phase VSI setup from TRIPHASE [159] powers electrical machine A based on the modulation signals provided by the RTT, as depicted in Figure F.2a. The series switches are connected to VSIs II and III as indicated in Figure F.2b, and are simultaneously controlled by the RTT based on the measured ω_m.

4.5 Results

The results of the experimental verification are shown in Figures 4.4 and 4.5. The mechanical output performance of the drive as well as the VSI input power are plotted over the complete acceleration duration in Figure 4.4, while the transition is detailed with the different current plots shown in Figure 4.5.

Experiments

The proposed experiment is performed as shown in Figure 4.4a. The intended angular velocity $\omega_m = \omega_b^{\text{I}} = \omega_b^{\text{in}} = 112.3$ rad./s is obtained after an acceleration interval of $t = t_a^{\text{I}} = 8$ s. From T_{dyn} in Figure 4.4b it is concluded that the torque during the acceleration process is constant just under $\check{T}$ due to the frictional losses (2.12) caused by the machine bearings. At the transition instance from FBS to FBI operation, a deviation of T_{dyn} is observed, which is approximately 7 Nm from the intended level, and lasts for $t_{FBS\rightarrow FBI} = 8$ ms. Using (4.4), $\hat{\zeta}_m = 875$ Nm/s, which is significantly lower than for the reference mechanical system in [58]. Due to the relatively low ζ_m during the transition, in combination with the machine-set inertia, J_m^A, no effect is observed in ω_m

(Figure 4.4a). Additionally, $\hat{\zeta}_m$ in the mechanical reference application was simulated, whereas it was measured here.

The angular velocity error, Δ_ω, in Figure 4.4c shows that the transition does not influence the angular velocity of the machine-set. Figure 4.4d depicts the electric input power, P_e, supplied to the VSIs, which has a significant offset level of 760 W, indicating their combined no-load power usage. Additionally, the mechanical output power, P_m, is presented in Figure 4.4d, where only a minor discrepancy is visible at the transition instance. The total electrical input to mechanical output drive system efficiency, η_{sys} = 88.2%, at $\omega_m = \omega_b^{\mathrm{I}}$.

Figure 4.5 shows the significant currents during the acceleration in the CTSR. Figures 4.5a and b show the actual and reference value of i_{q1} for winding set I and II, respectively. As a result of the changing drive configuration and consequently altered impedance, a discrepancy occurs between i_{q1}^* and i_{q1}. The $(d1, q1)$-axis drive voltages are corrected with gain-scheduling, however, due to the integrator-action of the CS, the current correction is too slow. This effect naturally originates from the phase currents, i_a, i_b, i_c, as depicted per winding set I, II in Figure 4.5c, d, respectively.

Practical issues of simultaneous reconfiguration

In this setup, the wires between the VSIs and the series switches in the power electronics cabinet (approximately 1 m long) lead to a high parasitic inductance in series with each S_s. When opening S_s, the simultaneous interruption of i_{xS_s} yields a voltage peak across the S_s devices depending on the parasitic device capacitance and instantaneous value of i_{xS_s}. To minimize this effect and prevent a device breakdown, a snubber circuit [105] consisting of a capacitor and a resistor is included to reduce the peak level of the voltage across each device in S_s.

More reliable solutions to avoid the necessity of a snubber circuit are e.g. sequential drive reconfiguration or a compact drive construction. By reconfiguring the drive in a sequential manner, ideally i_{xS_s} is zero when S_s is opened thereby avoiding a voltage peak. A compact drive construction minimizes the parasitic inductance and therefore also the voltage peak. By using either one of these concepts or by combining them, the voltage stress on the device is reduced.

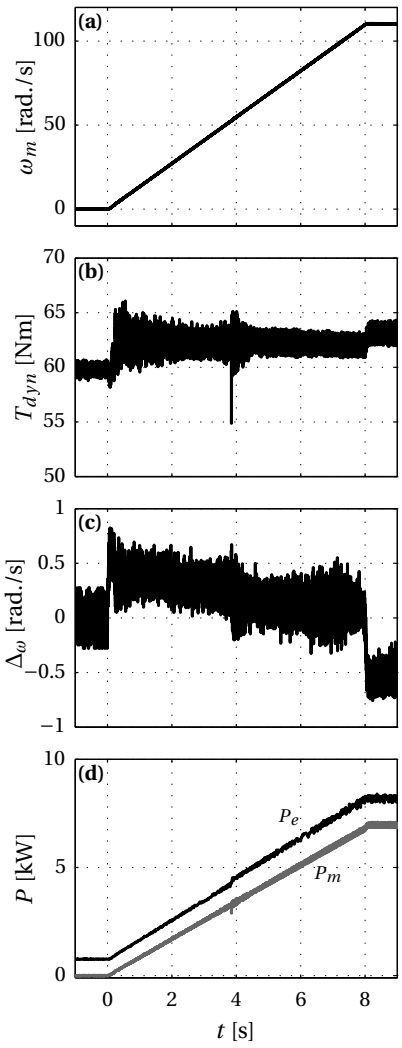

Figure 4.4: Measurement results of a t=0 to $t = t_a^{\mathrm{I}} = 8$ s acceleration under nominal loading with a drive reconfiguration at $t = t_a^{\mathrm{II}} = 3.84$ s; **(a)** angular velocity, ω_m, **(b)** dynamic axle torque, T_{dyn}, **(c)** angular velocity error, Δ_ω, **(d)** electrical VSI input power, P_e, and mechanical output power, P_m.

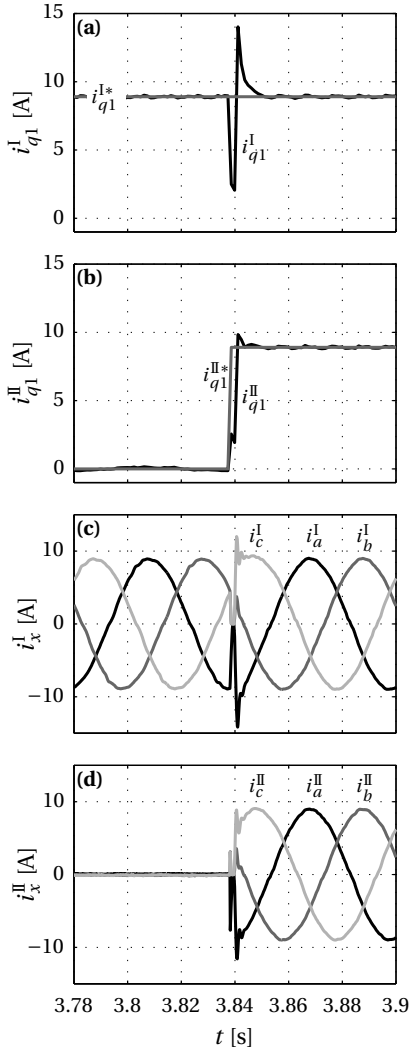

Figure 4.5: Measurement results detail from $t = t_a^-$ to $t = t_a^+$ with the drive reconfiguration at $t_a^{\mathrm{II}} = 3.84$ s; **(a)** set I actual and reference q-axis current, $i_{q1}^{\mathrm{I}}, i_{q1}^{\mathrm{I}*}$, **(b)** set II actual and reference q-axis current, $i_{q1}^{\mathrm{II}}, i_{q1}^{\mathrm{II}*}$, **(c)** set I per-phase currents, $i_a^{\mathrm{I}}, i_b^{\mathrm{I}}, i_c^{\mathrm{I}}$, **(d)** set II per-phase currents, $i_a^{\mathrm{II}}, i_b^{\mathrm{II}}, i_c^{\mathrm{II}}$.

4.6 Summary and conclusions

The use of a multiple gear-ratio transmission is commonly required in traction drives, as expounded in Chapter 1. By realizing the gear transitions under continuous full-load-torque, the longitudinal acceleration time for a given vehicle power is minimized. The full-load-torque transition from the FB series to the FB individual drive mode is detailed and the disadvantages of previously presented winding reconfiguration concepts are explained. The motivation for the application of series switches is given and the most efficient semiconductor based solution is presented. The simultaneous and sequential reconfiguration methods are described, while an actual simultaneous configuration transition is demonstrated experimentally to show the validity of the concept.

In contrast to other reconfigurable windings drive solutions, where the reconfiguration is achieved with an interconnected switch matrix (Figure 1.5a), dynamic drive operation uses an integrated drive solution. The avoidance of a phase current interrupting reconfiguration circuit allows for a full-load-torque transition. The required series switch conduction current and blocking voltage determine whether an IGBT or a MOSFET based switch gives the least losses. For the presented case, the latter solution is chosen based on the semiconductor specifications. In accordance with the objectives set in Section 1.4, the reconfiguration principle improves the drive efficiency. In Chapter 6 it is explained that this is achieved without endangering the reliability.

From the results presented in the experimental verification it is concluded that a low jerk, simultaneous transition from the series-connected to the individual full-bridge per-winding drive mode is achieved. Subsequently, an uninterrupted torque acceleration is demonstrated with the dynamic drive operation principle. The presented experimental results demonstrate a reconfiguration with an 11% relative torque ripple, lasting for only 8 ms. As a result, the intended angular velocity of the machine-set is not influenced by the reconfiguration. Different methods are proposed to further improve the transitional behaviour of the system, for example further improvement of the control system and/or application of sequential series switch opening.

Part II

Open-winding concept extensions

5

Voltage range enhancement

"Harmonics in harmony"

Abstract: *A dual-inverter drive system is proposed, which is capable of enhancing the phase voltages applied to an open-winding electrical machine. A common-mode current at the third-harmonic of the intended output frequency is added to boost the supply voltage of one inverter, thereby extending the operating range of the drive. The need for a reactive fundamental frequency current to weaken the machine field is avoided as a result. A method is introduced for simultaneously optimizing the inverter voltages and minimizing the required boost current, thereby maximizing the overall efficiency. The analysis is explained and verified by experiments. A relative angular velocity improvement of a factor 1.6 is achieved using voltage range enhancement.*

Parts of this chapter are published in:

- T. Gerrits, C. G. E. Wijnands, J. J. H. Paulides, and J. L. Duarte, "Dual voltage source inverter topology extending machine operating range," in *Energy Conversion Congress and Exposition (ECCE), 2012 IEEE*, September 2012, pp. 2840 –2846
- T. Gerrits, C. G. E. Wijnands, J. J. H. Paulides, and J. L. Duarte, "Loss minimization of boost mode dual inverter drive system," in *Power Electronics and Applications (EPE 2013), Proceedings of the 2013-15th European Conference on*, September 2013
- T. Gerrits, J. L. Duarte, C. G. E. Wijnands, E. A. Lomonova, J. J. H. Paulides, and L. Encica, "Twelve-phase open-winding SPMSM development for speed dependent reconfigurable traction drive," in *Proceedings of the Tenth International Conference on Ecological Vehicles and Renewable Energies (EVER)*, 2015

5.1 Introduction

The base angular velocity of a given VSI and SPMSM combination defines the end of the direct relation between the phase current and the torque. Beyond this point, a reactive current component is required to further increase the angular velocity. The standard solution with a single VSI is FW, while different solutions exist for dual VSI drives. When observing previous research on dual-inverter systems to drive an open-winding electrical machine fed by a single energy source, there are two common features in all of the investigated papers [40, 82, 113, 114]. The first aspect is the fact that only the fundamental frequency currents are used, and the second aspect is that no active energy transfer from one VSI to the other is applied, making one VSI solely a reactive power compensation tool as explained in Chapter 2.

In the mentioned literature, CM currents are avoided because they normally only increase the system losses without improving the performance. However, in this chapter a CM current at a specific harmonic of the fundamental electric frequency is employed to extend the angular velocity range of an electrical machine. This alternative method to FW is named voltage range enhancement (VRE). The intention with VRE is to match or improve the torque versus angular velocity profile of an electrical machine when compared to FW.

The basic principle of VRE is explained first, after which this general drive concept is detailed for an idealized three-phase open-winding electrical machine. Next, the concept is extended to allow for operation of an electrical machine with a non-sinusoidal EMF wave-shape. For the non-ideal electrical machine, the viability of the concept is demonstrated in the experimental verification and compared to FW. Additionally, a topology is presented to integrate the principle in the DDO system of Part I.

5.2 Idealized voltage range enhancement principle

The voltage range enhancement principle is defined as a dual-inverter machine drive concept with unequal inverter supply voltages to enlarge the fundamental frequency direct torque control operating range of the system [52]. *To this end, the secondary-side DC voltage is boosted to a higher level than the (battery) source powered primary-side DC voltage. This is achieved by using the electrical machine magnetizing inductances as boost inductors.* The intention is to power the electrical machine with the fundamental frequency BM current, while transferring the power required at the secondary-side VSI using a third-harmonic CM current. The topology required to execute VRE is depicted in Figure 5.1a. This is a single winding per-phase, dual-inverter circuit with balanced supplies, equal to that used for reactive compensation [82, 114]. The balanced supply voltages are required to ensure a power balance between the upper and lower sources,

since an AC CM current is applied. The VRE principle is in this case applied to a conventional open-winding electrical machine, thus with a single winding per-phase, to illustrate the general applicability of this concept. Compared to reactive compensation, the only required physical readjustment of the circuit to perform VRE is the connection of the primary-supply-side midpoint, $p0$, with the secondary-supply-side midpoint, $s0$. In this way, a CM ground current, i_g^{cm}, can flow between the sources on the primary-side, p, and the secondary-side, s. A separation of the BM and CM currents in the drive system is assured; the BM current cannot flow through the ground connection since the sum of the per-phase BM components is zero by definition, while the CM current has no alternative return path. The current from $s0$ to $p0$ is denoted as the ground-level current, i_g^{cm}, and is indicated as CM since it contains solely the DC homopolar and the AC zero-sequence (ZS) current components. In principle, each CM current component can be used to apply VRE. Besides the deliberate insertion of higher-harmonic current components, another difference when comparing VRE to reactive compensation is the completely different method of operating the VSIs. By controlling i_g^{cm} in an adequate manner, the secondary-side supply voltage, V_s, is boosted to a higher steady state level than the primary-side supply voltage, V_p. As such,

$$V_s = V_{s+} + V_{s-}, \tag{5.1}$$

$$V_p = V_{p+} + V_{p-}. \tag{5.2}$$

The magnetizing inductances of the electrical machine are used to carry out the boosting effect. Since this is applied to a CM instead of a BM current, a net flow of energy from one VSI to the other is achieved. The combined VSIs compose a bidirectional full-bridge DC-DC converter per-phase to charge the secondary-side capacitors C_{s+}, C_{s-}. Simultaneously with the charging, C_{s+}, C_{s-} are discharged by delivering active power to the electrical machine at the fundamental frequency. Subsequently, the available fundamental frequency per-phase differential voltage applied to the electrical machine is enhanced to increase the machine angular velocity above the base angular velocity ($\omega_m > \omega_b$) without requiring a reactive fundamental frequency current. The principle of operation and control requirements to achieve VRE are explained in the following. In this section, the conventional single-winding-per-phase circuit version is analysed, as shown in Figure 5.1a.

Whether an electrical machine is capable of carrying out FW depends on the construction [65, 106]. The VRE principle can be applied to every open-winding three-phase electrical machine, thus for machine types unsuitable for FW, VRE is a method to extend the angular velocity range. Essentially, the fundamental d-axis current component, associated with reactive power in FW, is exchanged with a third-harmonic current, enhancing the fundamental frequency inverter voltage independent of the electrical machine type.

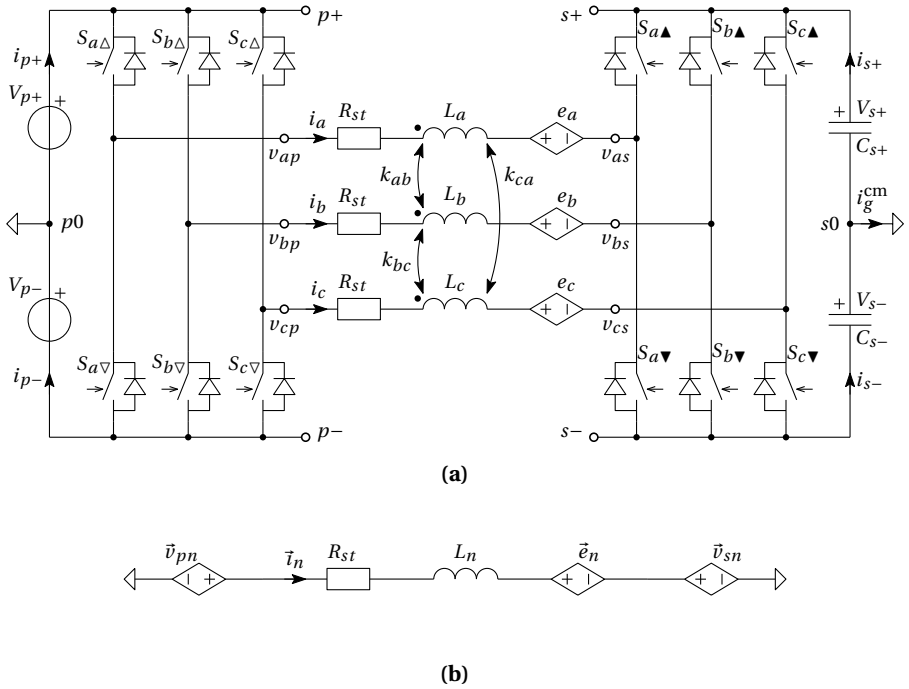

(a)

(b)

Figure 5.1: Single winding per-phase VRE concept; **(a)** dual VSI topology with balanced primary-side, p, and secondary-side, s, supplies and mutual reference connection, **(b)** generalized per-harmonic equivalent circuit on which the transformed (dn, qn)-axis voltage vectorial relations are based.

5.2.1 Voltage vectorial relations

The designated relation between the voltages present in the dual VSI topology displayed in Figure 5.1a are motivated here. Analogue to the method applied in Section 2.6.3, the phase voltages and resulting currents are transformed to a per-harmonic, per-mode vector representation of which the general equivalent circuit is shown in Figure 5.1b. The current components used for VRE throughout this chapter are the fundamental frequency BM spacial current vector, $\vec{i}_1^{\,\mathrm{bm}}$, and the third-harmonic CM spacial current vector, $\vec{i}_3^{\,\mathrm{cm}}$. *The motivation for combining a fundamental frequency current with the third-harmonic originates from the SVM principle; by adding a third-harmonic, the amplitude of the fundamental frequency modulation signal is allowed to be increased above unity, as depicted in Figure A.1b.* The effective fundamental frequency voltage range of the drive is thereby enhanced. By adding the third-harmonic, the aim is to transfer energy to the secondary-side capacitors, C_s, while allowing for an over-unity fundamental modulation amplitude. The method of maximizing the drive voltages is therefore twofold; a higher bus voltage in combination with an over-unity modulation amplitude.

The per-phase, x, per-inverter, y, per-harmonic, n, PWM signal, m_{xyn}, is formulated like

$$m_{xyn} = A_{yn} \sin\left(n\left(\theta_e - \kappa\tfrac{2\pi}{3} + \delta_{yn}\right)\right), \tag{5.3}$$

where A_{yn} is the corresponding amplitude which is the same for all phases, δ_{yn} is the angular displacement, $\kappa = 0,1,2$ for phases a,b,c respectively, and n =1 or 3. Other frequencies or combinations of multiple frequencies could also be applied depending on K_{en} of the electrical machine used. However, this is not further investigated here. The orthogonal rotating reference frame representation of m_{xyn} is determined using the per-harmonic transformation matrix, i.e. $\mathbf{T}_n^{\mathrm{bm}}$ in (2.40) for the fundamental harmonic, $n = 1$, and $\mathbf{T}_n^{\mathrm{cm}}$ in (2.43) for the third-harmonic, $n = 3$. From the resulting d-axis and q-axis values, the spacial voltage vectors, $\vec{v}_{yn}$, depicted in Figure 5.1b are derived, where the angle of $\vec{v}_{yn}$ with the qn-axis is δ_{yn}, as explained in Chapter 2.

The EMF spacial voltage vector per-harmonic, $\vec{e}_n$, in Figure 5.1b is derived based on (2.48). The per-harmonic inductance, L_n, is the result of the stator inductance, L_{st}, and coupling factor, k_{st}, as derived in (2.27) for $L_1 = L^{\mathrm{bm}}$ and in (2.31) for $L_3 = L^{\mathrm{cm}}$. The same type of electrical machine (SPMSM) is used to explain the VRE principle, as applied in Part I. Throughout this section it is assumed that the EMF only contains the fundamental frequency component $\left(\vec{e}_n = \vec{e}_1^{\,\mathrm{bm}}\right)$ for a straightforward concept explanation. In the following section, the influence of a machine with higher-harmonics in the EMF is expounded.

The goal of VRE is to extend the angular velocity range of a given system configuration as far as possible, with a maximized system efficiency η_{sys}. The assumptions made to achieve this are:

#1 Regulate the fundamental frequency BM spacial current vector magnitude to the torque producing $q1$-axis current, i.e.

$$\left|\vec{i}_1^{\,\mathrm{bm}}\right| = i_{q1}^{\mathrm{bm}}, \tag{5.4}$$

thereby assuring fundamental frequency MTPA control [87].

#2 Ensure that the primary- and secondary-side fundamental frequency spacial voltage vectors, $\vec{v}_{p1}^{\,\mathrm{bm}}$ and $\vec{v}_{s1}^{\,\mathrm{bm}}$ respectively, oppose each other in each working point to maximize the differential voltage $\vec{v}_1^{\,\mathrm{bm}}$, where

$$\vec{v}_1^{\,\mathrm{bm}} = \vec{v}_{p1}^{\,\mathrm{bm}} - \vec{v}_{s1}^{\,\mathrm{bm}}. \tag{5.5}$$

With the maximized voltage $\vec{v}_1^{\,\mathrm{bm}}$, the maximum allowed EMF, and thus the maximum angular velocity is obtained.

#3 Minimize the required third-harmonic CM current, $\vec{i}_3^{\,\mathrm{cm}}$, for a demanded electromagnetic power, P_{em}, by ensuring that $\vec{i}_3^{\,\mathrm{cm}}$ is in-phase with the third-harmonic secondary-side VSI spacial voltage vector, $\vec{v}_{s3}^{\,\mathrm{cm}}$. In this way, a reactive CM current at the secondary-side inverter is avoided as illustrated with the unity PF line, $\mathrm{PF}_{s3}^{\mathrm{cm}}$, in Figure 5.2c. The combined power electronics and electrical machine losses are minimized as a result.

#4 Regulate supply voltage V_s to a fixed level in order to achieve a power balance on the secondary-side.

#5 Maximize the combined spacial voltage vectors per-side to minimize the required RMS current for a demanded P_{em}.

The assumptions above stipulate the requirements for the spacial voltage vectorial relations at each side and each harmonic, as depicted for the applied harmonics in Figure 5.2a, and Figure 5.2b, respectively. In Figure 5.2a, the BM fundamental frequency $\left(d1^{\mathrm{bm}}, q1^{\mathrm{bm}}\right)$-axis reference frame is depicted with the accompanying quantities, x_1^{bm}. In Figure 5.2b, the CM third-harmonic, $\left(d3^{\mathrm{cm}}, q3^{\mathrm{cm}}\right)$-axis reference frame is depicted with the accompanying quantities, x_3^{cm}.

To regulate the magnitude of $\vec{i}_1^{\,\mathrm{bm}}$ to i_{q1}^{bm} in Figure 5.2a (assumption #1), the BM resistance spacial voltage vector, $\vec{v}_{R_1}^{\,\mathrm{bm}}$, must be in-phase with $\vec{e}_1^{\,\mathrm{bm}}$, where

$$\vec{v}_{R_1}^{\,\mathrm{bm}} = R_{st}\vec{i}_1^{\,\mathrm{bm}}. \tag{5.6}$$

Consequently, the BM reactance spacial voltage vector, $\vec{v}_{L_1}^{\,\mathrm{bm}}$, is perpendicular to $\vec{e}_1^{\,\mathrm{bm}}$, where

$$\vec{v}_{L_1}^{\,\mathrm{bm}} = j\omega_e L_1 \vec{i}_1^{\,\mathrm{bm}}. \tag{5.7}$$

As detailed in Figure 5.2c, $\vec{i}_3^{\,\mathrm{cm}}$ must be in-phase with $\vec{v}_{s3}^{\,\mathrm{cm}}$ to avoid a reactive CM current (assumption #3). As an example, such a configuration is depicted in Figure 5.2b. The

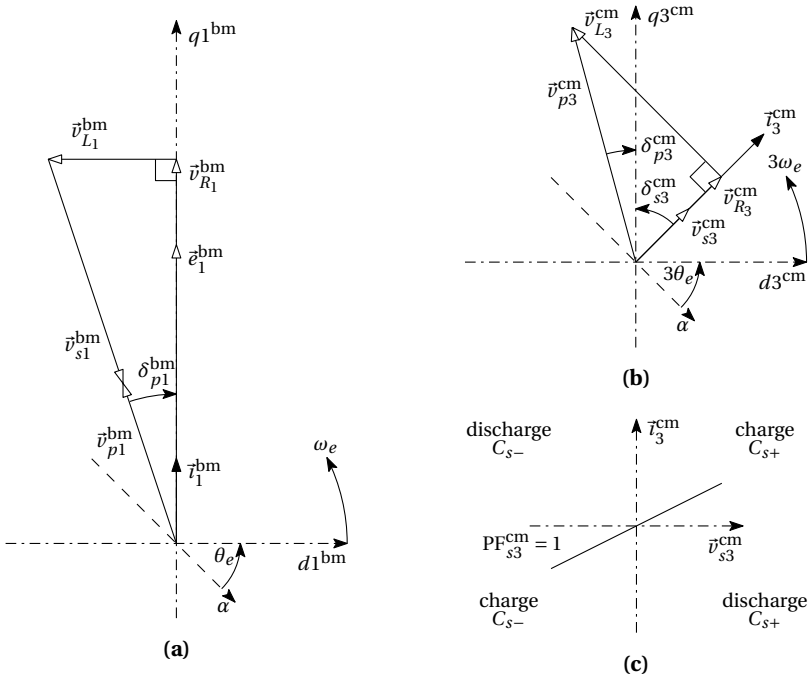

Figure 5.2: Transformed relations in the (dn, qn)-axis; **(a)** exemplifying BM fundamental frequency quantity relations, **(b)** exemplifying CM third-harmonic quantity relations, **(c)** (dis)charge relation between the secondary-side applied third-harmonic spacial voltage vector, $\vec{v}_{s3}^{\mathrm{cm}}$, and the third-harmonic CM spacial current vector $\vec{\imath}_3^{\mathrm{cm}}$. The optimal situation complying with assumption #3 and **(b)** is depicted.

third-harmonic CM resistance spacial voltage vector, $\vec{v}_{R_3}^{\text{cm}}$, is in-phase with $\vec{v}_{s3}^{\text{cm}}$, where

$$\vec{v}_{R_3}^{\text{cm}} = R_{st}\vec{i}_3^{\text{cm}}. \tag{5.8}$$

Consequently, the third-harmonic CM reactance spacial voltage vector, $\vec{v}_{L_3}^{\text{cm}}$, is perpendicular to $\vec{v}_{s3}^{\text{cm}}$, where

$$\vec{v}_{L_3}^{\text{cm}} = j3\omega_e L_3\vec{i}_3^{\text{cm}}. \tag{5.9}$$

The necessary CM third-harmonic mutual displacement angle, δ_3^{cm}, to ensure (5.8) and (5.9) is a function of δ_{p3}^{cm} and δ_{s3}^{cm} as

$$\delta_3^{\text{cm}} = \delta_{s3}^{\text{cm}} - \delta_{p3}^{\text{cm}}. \tag{5.10}$$

The actually applied angle and magnitude relation between the spacial voltage vectors in Figure 5.2a and Figure 5.2b depend on the power exchange levels, as expounded in the following.

5.2.2 Power balance

In order to regulate V_{s+}, V_{s-}, the third-harmonic charging power and the fundamental frequency discharge power are computed here. Additionally, the total input power and the electromagnetic output power are determined. Each power component is derived based on the voltages per-side, per-harmonic, and the per-harmonic current as depicted in Figure 5.2.

The primary-side, secondary-side, and total, fundamental frequency active power delivered by the respective VSI(S) is computed based on the voltage vectorial relations in Figure 5.2a, where

$$P_{p1}^{\text{bm}} = \tfrac{3}{2}\left|\vec{v}_{p1}^{\text{bm}}\right| i_{q1}^{\text{bm}}\cos\left(\delta_{p1}^{\text{bm}}\right), \tag{5.11}$$

$$P_{s1}^{\text{bm}} = \tfrac{3}{2}\left|\vec{v}_{s1}^{\text{bm}}\right| i_{q1}^{\text{bm}}\cos\left(\delta_{s1}^{\text{bm}}\right), \tag{5.12}$$

$$P_1^{\text{bm}} = P_{p1}^{\text{bm}} - P_{s1}^{\text{bm}}. \tag{5.13}$$

The required primary-side fundamental frequency BM voltage vector angle, δ_{p1}^{bm}, to ensure the required active current, (assumption #1) is computed with

$$\delta_{p1}^{\text{bm}} = \arctan\left(\frac{\left|\vec{v}_{L_1}^{\text{bm}}\right|}{e_{q1}^{\text{bm}} + \left|\vec{v}_{R_1}^{\text{bm}}\right|}\right), \tag{5.14}$$

where the EMF is a projection on the $q1^{\text{bm}}$-axis by definition, thus $\left|\vec{e}_1^{\text{bm}}\right| = e_{q1}^{\text{bm}}$. To additionally satisfy assumption #2, the secondary-side fundamental frequency voltage vector angle, δ_{s1}^{bm}, should be in anti-phase with respect to δ_{p1}^{bm} i.e.

$$\delta_{s1}^{\text{bm}} = \delta_{p1}^{\text{bm}} + \pi. \tag{5.15}$$

Based on this opposite angular relation between $\vec{v}_{s1}^{\,\mathrm{bm}}$ and $\vec{i}_{1}^{\,\mathrm{bm}}$, it is concluded that the resulting average secondary-side fundamental frequency power, P_{s1}^{bm}, is negative, and consequently discharges the capacitors C_{s+}, C_{s-}. As a result of the assumption that the EMF only contains the fundamental harmonic, the electromagnetically converted power is found to be

$$P_{em1}^{\mathrm{bm}} = \tfrac{3}{2} e_{q1}^{\mathrm{bm}} i_{q1}^{\mathrm{bm}}. \tag{5.16}$$

The average primary-side active power, P_p, is computed by summation of the per-harmonic power,

$$P_p = P_{p1}^{\mathrm{bm}} + P_{p3}^{\mathrm{cm}}, \tag{5.17}$$

where the third-harmonic active CM power, P_{p3}^{cm}, is derived from the projection of voltage $\vec{v}_{p3}^{\,\mathrm{cm}}$ and current $\vec{i}_{3}^{\,\mathrm{cm}}$ on the q-axis, like

$$P_{p3}^{\mathrm{cm}} = \tfrac{3}{2} \left|\vec{v}_{p3}^{\,\mathrm{cm}}\right| \cos\left(\delta_{p3}^{\mathrm{cm}}\right) \left|\vec{i}_{3}^{\,\mathrm{cm}}\right| \cos\left(\delta_{s3}^{\mathrm{cm}}\right). \tag{5.18}$$

To ensure voltage balance in steady state (assumption #4), the average secondary-side power relation should comply to

$$P_s = 0, \tag{5.19a}$$

$$= P_{s1}^{\mathrm{bm}} + P_{s3}^{\mathrm{cm}}, \tag{5.19b}$$

where P_{s3}^{cm} is the average CM third-harmonic secondary-side active power. P_{s3}^{cm} is derived from the time-variant power, p_{s3}^{cm}, based on the active power requirement (assumption #3), and the notion that the CM current i^{cm} only contains the third-harmonic $\left(i^{\mathrm{cm}} = \vec{i}_{3}^{\,\mathrm{cm}}\right)$. As such,

$$p_{s3}^{\mathrm{cm}} = \tfrac{1}{2} \vec{v}_{s3}^{\,\mathrm{cm}} i_g^{\mathrm{cm}}, \tag{5.20}$$

$$P_{s3}^{\mathrm{cm}} = \langle p_{s3}^{\mathrm{cm}} \rangle = \tfrac{3}{2} \frac{\left|\vec{v}_{p3}^{\,\mathrm{cm}}\right| \left|\vec{v}_{s3}^{\,\mathrm{cm}}\right|}{3\omega_e L_3^{\mathrm{cm}}} \sin\left(\delta_3^{\mathrm{cm}}\right), \tag{5.21}$$

where the ground return current, i_g^{cm}, is the sum of all the CM currents, thus for this analysis $i_g^{\mathrm{cm}} = 3\vec{i}_{3}^{\,\mathrm{cm}}$.

5.2.3 Combined harmonics amplitude optimization

Assumption #5 states that the combination of voltage vectors per-side should be maximized during VRE, to maximize η_{sys}. From the voltage vectorial relations in Figure 5.2 it is concluded that the modulation signals (5.3) per VSI are combined such, that their

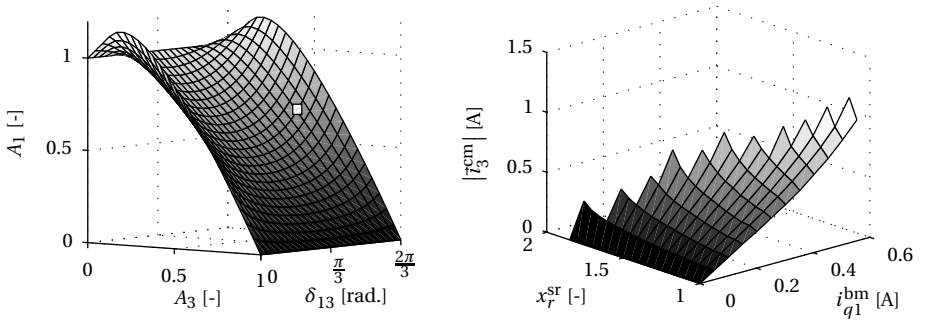

(a) **(b)**

Figure 5.3: **(a)** Numerical solution of the two-frequencies linear PWM amplitude optimization as derived in Appendix A.1, **(b)** idealized VRE CM current, $|\vec{i}_3^{\,cm}|$, minimized as a function of the torque producing current, i_{q1}^{bm}, and the angular velocity ratio, x_r^{sr}, as derived in Appendix A.2.

sum is maximized in the linear PWM range. Therefore, the per-phase modulation signal, $m_x \leq 1$, with

$$m_x = \sum_{n=1,3} A_n \sin\left(n\left(\theta_e - \kappa\tfrac{2\pi}{3} + \delta_n\right)\right) \tag{5.22a}$$

$$= A_1 \sin\left(\theta_e - \kappa\tfrac{2\pi}{3} + \delta_1\right) + A_3 \sin\left(3\left(\theta_e - \kappa\tfrac{2\pi}{3} + \delta_3\right)\right), \tag{5.22b}$$

$$= m_{x1} + m_{x3}. \tag{5.22c}$$

where the angles δ_1, δ_3 correspond to those in Figure 5.2. In Appendix A.1 the procedure to derive the optimal combination of amplitudes is explained. The mutual modulation signal definition, based on (5.3), is depicted in Figure A.1a. The resulting relation between A_1, A_3, δ_1, and δ_3 is derived as shown in Figure 5.3a.

5.2.4 Common-mode current minimization

Using the previously derived voltage, power, and amplitude relations, the minimum required third-harmonic CM current to equilibrate supply voltage V_s while powering the SPMSM is determined [55]. This procedure is executed for different combinations of the torque producing current, i_{q1}^{bm}, and the angular velocity ratio, x_r^{sr}. From the voltage vectorial relations in Figure 5.2 and the result of the mutual amplitude optimization in Figure 5.3a, a computation sequence is determined to conform the system with the obligatory power levels to maintain stability. The optimal combination of voltages to minimize the losses due to the charging current cannot be determined analytically due to the modulation signal relation between different harmonics as shown in Figure 5.3a. Therefore, an optimization procedure is proposed in Appendix A.2, capable of comput-

ing the minimized CM current magnitude, $\left|\vec{i}_3^{\,\mathrm{cm}}\right|$. The resulting minimized $\left|\vec{i}_3^{\,\mathrm{cm}}\right|$ is shown in Figure 5.3b and the experimental verification results are presented in Section 5.6.

5.3 Practical approach to voltage range enhancement

The assumption that the per-phase EMF of a practical electrical machine is purely sinusoidal, is generally a first-order approximation, since other harmonic EMF components can be present. This is also the case for the two SPMSMs that are used in this research (Appendices C and D). The theory presented in the preceding section is extended to attain a solution that is demonstrated in practise.

5.3.1 Voltage vectorial relations

Independent of the higher-harmonic-content in the EMF, the assumptions explained in the previous section remain valid. Therefore, the described fundamental frequency voltage vectorial relation visualized in Figure 5.2a remains the same. Electrical machine B, as detailed in Appendix D, is used to explain the VRE principle for a non-sinusoidal electrical machine. Besides the fundamental frequency EMF component, $\vec{e}_1^{\,\mathrm{bm}}$, this electrical machine also produces a prominent third-harmonic EMF component, $\vec{e}_3^{\,\mathrm{cm}}$. This makes the third-harmonic voltage vectorial relation shown in Figure 5.2b invalid. The intended relation between the third-harmonic CM voltages taking into account $\vec{e}_3^{\,\mathrm{cm}}$ is depicted for the general case in Figure 5.4a. Both angles $\delta_{p3}^{\mathrm{cm}}, \delta_{s3}^{\mathrm{cm}}$ are chosen freely to minimize $\left|\vec{i}_3^{\,\mathrm{cm}}\right|$, while $\vec{i}_3^{\,\mathrm{cm}}$ is kept parallel to $\vec{v}_{s3}^{\,\mathrm{cm}}$ to comply with assumption #3. However, an average third-harmonic electrical machine torque component, $\langle T_{em3}^{\mathrm{cm}} \rangle$, arises from the interaction between $\vec{i}_3^{\,\mathrm{cm}}$ and $\vec{e}_3^{\,\mathrm{cm}}$, according to (2.51). By limiting $\delta_{s3}^{\mathrm{cm}}$ to $\left(-\pi/2 < \delta_{s3}^{\mathrm{cm}} < \pi/2\right)$, the resulting $\langle T_{em3}^{\mathrm{cm}} \rangle$ is used advantageously to increase the total electrical machine torque, T_{em}. Eventually, $\langle T_{em3}^{\mathrm{cm}} \rangle$ is avoided by ensuring that $\vec{i}_3^{\,\mathrm{cm}}$ is perpendicular to $\vec{e}_3^{\,\mathrm{cm}}$, which is achieved if $\delta_{s3}^{\mathrm{cm}} = \pm\pi/2$ in the optimization, as illustrated for $\delta_{s3}^{\mathrm{cm}} = -\pi/2$ in Figure 5.4b.

The equations defining the voltage vectorial relations (5.3) - (5.10) remain valid, but the optimization constraints change as explained in the non-ideal EMF CM current minimization in Appendix A.3.

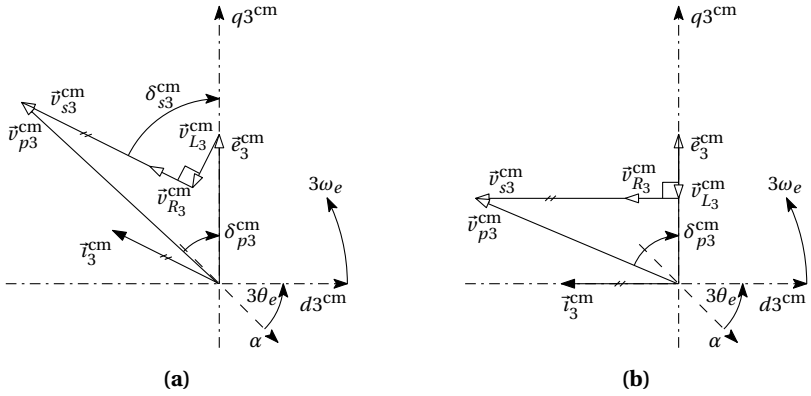

Figure 5.4: Exemplifying $(d3, q3)$-axis transformed CM third-harmonic quantity relations in the presence of a third-harmonic EMF component; **(a)** general solution complying with assumption #3, **(b)** specific solution of **(a)** where $\vec{i}_3^{\mathrm{cm}}$ is perpendicular to $\vec{e}_3^{\mathrm{cm}}$, avoiding the generation of a third-harmonic torque.

5.3.2 Time-variant power and torque

Transferring power to the secondary-side VSI using $\vec{i}_3^{\mathrm{cm}}$, in combination with the presence of an EMF component at that harmonic, being $\vec{e}_3^{\mathrm{cm}}$, results in a third-harmonic CM time-variant electromagnetic machine power, p_{em3}^{cm}, and torque, T_{em3}^{cm}. As such,

$$p_{em3}^{\mathrm{cm}} = \tfrac{3}{2} e_{q3}^{\mathrm{cm}} \vec{i}_3^{\mathrm{cm}}, \tag{5.23}$$

$$T_{em3}^{\mathrm{cm}} = \tfrac{3}{2} K_{e3} \vec{i}_3^{\mathrm{cm}}. \tag{5.24}$$

Using the time-variant p_{em3}^{cm} and T_{em3}^{cm}, and taking into account that the average current is given by the projection on the $q3$-axis, the respective average values are computed. The average power is computed from (5.16) and (5.23) as

$$P_{em} = P_{em1}^{\mathrm{bm}} + \langle p_{em3}^{\mathrm{cm}} \rangle, \tag{5.25a}$$

$$= \tfrac{3}{2} \left(e_{q1}^{\mathrm{bm}} i_{q1}^{\mathrm{bm}} + e_{q3}^{\mathrm{cm}} i_{q3}^{\mathrm{cm}} \right), \tag{5.25b}$$

while the average torque is subsequently derived from (2.10) and (5.24) as

$$T_{em} = T_{em1}^{\mathrm{bm}} + \langle T_{em3}^{\mathrm{cm}} \rangle, \tag{5.26a}$$

$$= \tfrac{3}{2} \left(K_{e1} i_{q1}^{\mathrm{bm}} + K_{e3} i_{q3}^{\mathrm{cm}} \right). \tag{5.26b}$$

By applying (5.26a), the total average torque produced using VRE is derived. as shown in the following section.

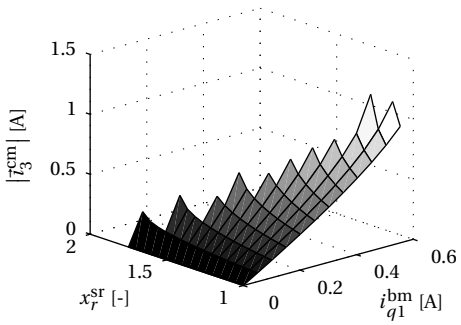

Figure 5.5: Non-ideal VRE CM current, $|\underline{i}_3^{cm}|$, minimized as a function of the torque producing current, i_{q1}^{bm}, and the angular velocity ratio, x_r^{sr}, as derived in Appendix A.3.

5.3.3 Common-mode current minimization

The described CM current minimization procedure is repeated with the adapted electrical machine power, P_{em} (5.25a), as detailed in Appendix A.3. Based on the renewed constraints and with boundary conditions according to the cases illustrated in Figure 5.4, the minimum required third-harmonic CM current to apply VRE to electrical machine B is computed, as shown in Figure 5.5. The experimental results of the extended optimization are presented in Section 5.6.

5.4 Concept integration and extension

The VRE concept provides an angular velocity range extension method, mainly as an alternative to FW. In the following, a topology is proposed to integrate the VRE requirements in the reconfigurable DDO topology, presented in Part I. Additionally, a possible circuit extension is presented to allow for the boosting of the secondary-side supply voltage.

5.4.1 Unified topology

One of the intentions of the research expounded in this thesis is to provide a solution to advance the driving range of an electrical machine beyond the state-of-the-art as indicated in objective 1b in Chapter 1. Although at first sight the topology used for VRE (Figure 5.1a) looks different from the generalized topology used for DDO (Figure 3.3), a combined version of the circuit in Figure 5.1a is applied. This allows for usage of one drive system applying DDO in the CTSR and applying VRE in the CPSR.

The proposed topology, capable of combining the requirements of both principles, is depicted in Figure 5.6. The primary-side sources, which are depicted in a balanced manner in Figure 5.1a are replaced by a single (battery) source with voltage V_p. A balanced capacitive divider is formed with capacitors C_{p+}, C_{p-} to create the primary-side zero-voltage node, $p0$, equivalent to the secondary-side and corresponding to Figure 5.1a. Each FB module of each phase, FB_x^u, is composed of one switching leg connected to the primary-side, p, and one switching leg connected to the secondary-side, s. By connecting the series switches, S_s, alternatingly from s to p, each FB is identical, as shown in Figure 5.6. This allows for an equal control strategy per sequential series-connected winding-string. The secondary-side capacitors, C_{s+}, C_{s-}, are charged through the diodes, D_+, D_-, in the respective positive and negative DC-link path. By using diodes, ideally $V_s = V_p$ during DDO, while $V_s \geq V_p$ during VRE. Downside is that during regenerative breaking, the capacitors are charged, and since the energy in C_{s+}, C_{s-} cannot return to the primary-side source, V_s increases. However, this effect only takes place if ω_m is higher than the individually driven base angular velocity, ω_b^{in}. If $\omega_m > \omega_b^{\mathrm{in}}$ is to be expected, diodes D_+, D_- are to be replaced with switches to actively ensure that $V_s = V_p$, and allow for regenerative charging of V_p.

The equations used in this chapter are valid for the case of a single winding per-phase $\left(N^{\mathrm{set}} = 1\right)$ as depicted in Figure 5.1a. If a $N^{\mathrm{set}} > 1$ topology variant is used, the determined power is the per-winding-set power. For the sequential multiple-sets version shown in Figure 5.6, each set is controlled individually. This ideally requires equal spacial voltage vectors per-set, as displayed in Figure 5.2 and Figure 5.4.

5.4.2 Voltage limitations

The breakdown voltage of the devices applied in a VSI determines the maximum supply voltage according to the breakdown rate, K_{br} (2.15). If an inverter is equipped with $\upsilon_{br} = 600\,\mathrm{V}$ devices and $K_{br} = 2/3$ is assumed, V_p is limited to $V_p \leq 400\,\mathrm{V}$, obstructing $V_s > V_p$. Therefore, devices with $\upsilon_{br} = 1200\,\mathrm{V}$ are required on the secondary-side to permit a boosting of $400 \leq V_s \leq 800\,\mathrm{V}$. This also effects the efficiency of the drive in DDO. Research on dual-inverter drives for reactive compensation shows that either the intended $V_s = V_p$ [113], or that $V_s > V_p$ [82]. No information on applied device types, nor the intention to maximize the supply voltage versus the breakdown voltage, are reported.

The necessary υ_{br} of S_s to avoid breakdown while executing VRE depends on the chosen circuit configuration. If the sequential leg-configuration is applied, as depicted in Figure 5.6, ideally

$$\hat{\upsilon}_{S_s} = \tfrac{1}{2}\left(V_p + V_s\right). \tag{5.27}$$

Considering for example $V_p = 400\,\mathrm{V}$, $V_s = 800\,\mathrm{V}$, and $K_{br} = 2/3$ according to (2.15), $\upsilon_{br\,S_s} \geq 900\,\mathrm{V}$, practically determining that $\upsilon_{br\,S_s} = 1200\,\mathrm{V}$.

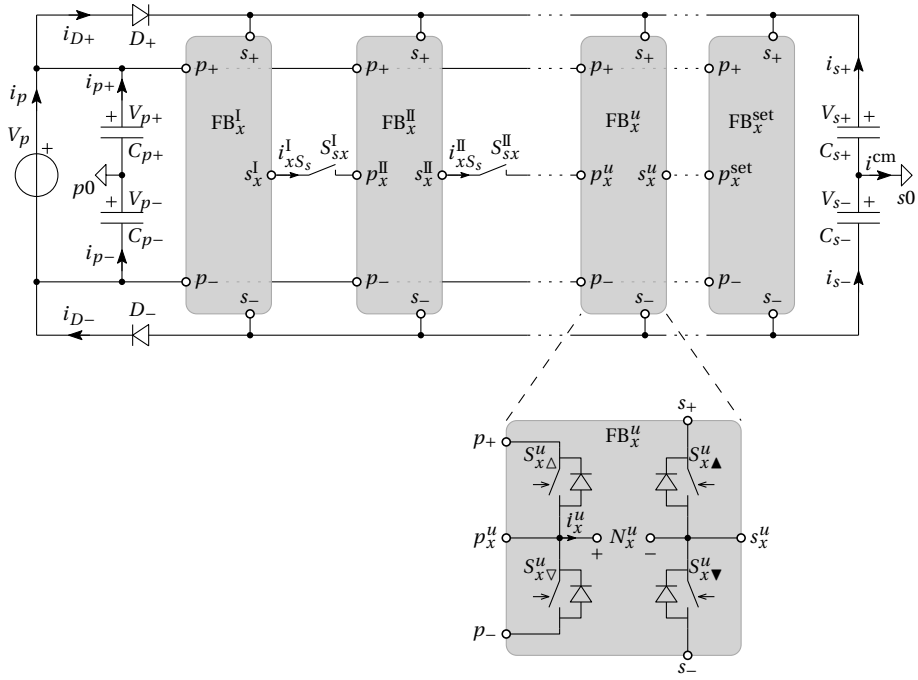

Figure 5.6: Generalized N^{set}-windings per-phase circuit to drive a combined DDO and VRE principles operated electrical machine. The switching legs are connected alternately to the primary- and secondary-side (sequential). Each winding of Figure 3.1a with indicated phase- and winding-number is connected to the corresponding FB converter module.

Multilevel alternative topology

A possible solution to boost V_s without the requirement to use $v_{br} = 1200$ V devices, is the utilization of a multilevel inverter structure on the secondary-side. A three-level flying-capacitor multilevel topology is proposed in Appendix A.4 that allows for the usage of equal devices at both the primary- and secondary-side, thereby combining the advantages of $v_{br} = 600$ V devices with the possibility to apply $V_s = 800$ V.

5.5 Experimental verification

The VRE principle, as explained in the aforementioned, was verified experimentally. Throughout this section, the applied configuration is: machine B (Appendix D), setup B (Appendix F), while $V_p = 350$ V, and $V_s = 700$ V (Figure 5.1a).

The modulation signals to drive the VSIs are computed off-line. The optimization procedure lasts more than an hour, making it impracticable to do on-line computations based on the measured momentary current and position. This is mainly due to the numerical solving process, demanded by the combined harmonics optimization, detailed in Figure 5.3a. Therefore, lookup graphs are derived to apply the requested modulation signal per VSI as a function of the torque producing current, i_{q1}^{bm}, and the relative angular velocity ratio, x_r^{sr}, variable set, i.e. $\left\{i_{q1}^{\text{bm}}; x_r^{\text{sr}}\right\}$. Measurement locations in the viable solution domain for which no solution is computed are approximated by interpolation of the surrounding results. Throughout this section, the VRE principle is tested at one fixed point in the viable solution range, i.e. $\left\{i_{q1}^{\text{bm}}; x_r^{\text{sr}}\right\} = \{353\text{ mA}; 1.2\}$, representing $\{T_{em}; \omega_m\} = \{2\text{ Nm}; 91\text{ rad./s}\}$.

5.5.1 System configuration and control

Electrical machine B was used in the FBS connected configuration throughout the experiments. Four bidirectional DC supplies were used to resemble the different voltage sources as depicted in Figure 5.1a, i.e. V_{p+}, V_{p-}, V_{s+} and V_{s-}, respectively. The models used for both the simulations and the experiments were implemented using MATLAB/SIMULINK.

A balanced dual DCM configuration per-side is used to allow for a bidirectional supply current flow (Figure F.2b), thereby avoiding the risk of an over-voltage for the VSIs. The secondary-side voltage, V_s, is artificially regulated to the intended 700 V to demonstrate VRE in steady state without the risk of a transient instability. The different inverter supply voltages, V_{inv}^{u}, are indicated in Appendix F, where $V_p = V_{inv}^{\text{I}}$, and $V_s = V_{inv}^{\text{IV}}$. In the series-connected configuration as applied throughout the verification, the series switches are closed and the VSIs II and III are consequently not used.

From the presented optimization procedure, a FF based CS is constructed, as shown in Figure 5.7. The FF lookup graphs are constructed from the per-harmonic, per-axis voltages computed with the optimization procedure and shown per VSI in Figure A.5 and Figure A.6, respectively. Each lookup graph is composed as a function of the optimization parameters, i_{q1}^{bm}, and x_r^{sr}, as indicated in Figure 5.7. Based on the intended mechanical torque, T_m, and angular velocity, ω_m, within the viable solution domain, the corresponding i_{q1}^{bm} and x_r^{sr} are selected. T_m is derived from the electromagnetic machine torque, T_{em}, and ω_m using (3.22). The load DCM angular velocity, ω_{DCM}, and with that ω_m, is regulated with the machine regulator (MR) as explained in Appendix E. The per-side (p,s), per-axis $(d1,q1)$, per-harmonic-mode, (bm 1) and (cm 3), voltages are computed by interpolation of the lookup graphs at the intended combination of $\left\{i_{q1}^{\mathrm{bm}}; x_r^{\mathrm{sr}}\right\}$. Subsequently, transformation matrices per indicated harmonic-mode combination, $\mathbf{T}_1^{\mathrm{bm}\dagger}$ and $\mathbf{W}_3^{\mathrm{cm}}$, are used to determine each set of respective phase voltages, which are combined in the vectors $\mathbf{v}_{(p,s)1}^{\mathrm{bm}}$,$\mathbf{v}_{(p,s)3}^{\mathrm{cm}}$, as

$$\mathbf{v}_{(p,s)1}^{\mathrm{bm}} = \mathbf{T}_1^{\mathrm{bm}\dagger} \begin{bmatrix} v_{(p,s)d1}^{\mathrm{bm}} \\ v_{(p,s)q1}^{\mathrm{bm}} \end{bmatrix}, \tag{5.28}$$

$$\mathbf{v}_{(p,s)3}^{\mathrm{cm}} = \mathbf{W}_3^{\mathrm{cm}} \begin{bmatrix} v_{(p,s)d3}^{\mathrm{cm}} \\ v_{(p,s)q3}^{\mathrm{cm}} \end{bmatrix}, \tag{5.29}$$

as derived in (2.41) and (2.44a), respectively. The resulting per-side FF phase voltage vector, $\mathbf{v}_{(p,s)FF}$, is used to drive each respective VSI. The regulation method, as proposed in Section 2.6.4, is not applied on account of the lookup graph based drive. However, the per-harmonic, per-mode estimation is used to determine the different current components.

The average value of the mentioned time-variant power and torque components is derived using a LPF with a cut-off frequency of 10 rad./s. Dependent on whether a continuous- or discrete-time model is required, a corresponding filter is implemented.

5.5.2 Simulations

Simulations to verify the VRE principle were subdivided into two sections; using ideal voltage sources to represent the VSIs, and with ideal HB switching legs. With the ideal voltage sources, the basic principle is demonstrated, while the discrete-time representation required for the experiments is tested with the HB switching leg model.

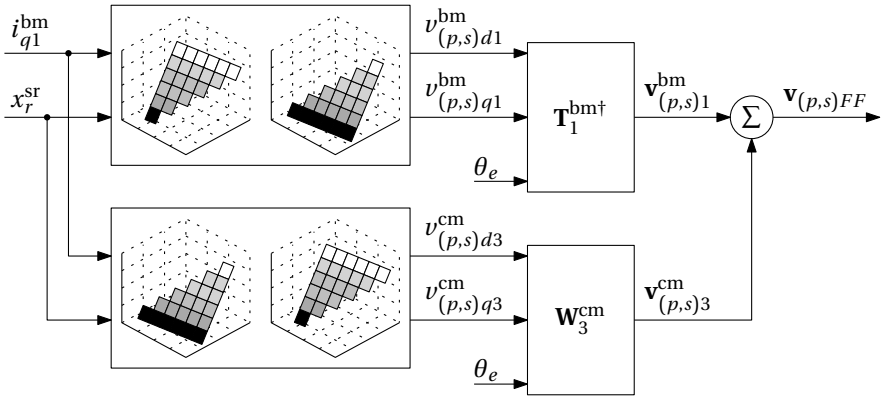

Figure 5.7: Block diagram of the FF CS per-side (p,s) to apply the VRE principle, composed of the voltage lookup graphs as shown for the primary-side inverter in Figure A.5 and for the secondary-side inverter in Figure A.6.

Ideal sources

The simulations demonstrating the principle operation of VRE were performed with ideal voltage sources, driving the machine phases according to the intended voltage vectorial relations, as shown in Figure 5.7. A continuous-time model implementation is used as no discrete states are required in either the controller, nor the VSI. This is because analog to digital converter (ADC) and zero-order-hold (ZOH) delays and resulting phase-angle errors are no essential issues in this case, since the basic operating principle is demonstrated. Each VSI is represented by three behavioural voltage sources, which are directly driven with the respective voltage vectors, $\mathbf{v}_{(p,s)FF}$. The modulation signal vectors, $\mathbf{m}_p$ and $\mathbf{m}_s$ are derived from the corresponding $\mathbf{v}_{(p,s)FF}$ according to their respective supply voltage, as

$$\mathbf{m}_p = \frac{2}{V_p}\mathbf{v}_{pFF}, \tag{5.30}$$

$$\mathbf{m}_s = \frac{2}{V_s}\mathbf{v}_{sFF}. \tag{5.31}$$

The results of simulation with ideal sources are shown in Figure 5.13 and Figure 5.14.

Ideal switches

In Figure 5.8, a more detailed simulation model of the setup presented in Appendix F is shown, in accordance with the discrete-state operation of the VSI switches and the digital RTT CS implementation of the experiments. Different discrete delay factors, k, in the setup are accounted for in the simulations to avoid additional phase errors in the measurement acquisition during the experiments.

The delays in the drive system are caused by the RTT computation, $[k_{RTT}]$, and the ZOH functionality in the PWM, $[k_{PWM}]$[1]. In the block diagram of the discrete-time system implementation, depicted in Figure 5.8, the voltages are computed from the lookup graphs, as shown in Figure 5.7. The modulation signal vectors, $\mathbf{m}_{(p,s)}$, are derived using equations (5.30) and (5.31), respectively. The measured electrical angular position, θ_e, is delayed with respect to the actual position at the time the RTT uses it to transform the $(d1, q1)$-axis lookup values to the continuous-time voltages. Therefore, the actual position, θ_e, is estimated based on the discrete-time value of both the electrical rotor position, $[\theta_e]$, and the mechanical angular velocity, $[\omega_m]$. The rotor angular advancement, $\left[\Delta_{\theta_e}\right]$, that occurs during the cycle time of the system, T_c, is computed as

$$\left[\Delta_{\theta_e}\right] = N_{pp}\omega_m\left([k_{RTT}] + [k_{PWM}]\right)T_s, \tag{5.32a}$$

$$= \omega_e T_c. \tag{5.32b}$$

By advancing θ_e by the angular velocity dependent difference Δ_{θ_e}, the estimated value of the actual rotor position, $\tilde{\theta}_e$, is found.

Neglecting $\left[\Delta_{\theta_e}\right]$ results in an electrical position error of 164 mrad. at $\omega_m = 75$ rad./s, which is a 2.6% relative error for this system. Especially, the secondary-side power balance (5.19a) is not achieved as a result, due to the high sensitivity of the third-harmonic transformation on the rotor position.

The PWM signals are generated by comparing the ZOH discrete-time modulation signals, $\left[m_{(p,s)}\right]$, to a symmetrical triangular carrier signal. Subsequently, the VSIs are driven by their respective steering signal, $\left[\mathbf{s}_{(p,s)}\right]$, as shown in Figure 5.8. The measured signals are fed back to the RTT by ADCs. The delay caused by the ADC is negligible in comparison to T_s, and is therefore not taken into account. The results of the ideal HB switching-legs simulation are shown in Figure 5.15 and Figure 5.16.

[1] The square brackets indicate that the delay is relative to the discrete sample time of the system, T_s.

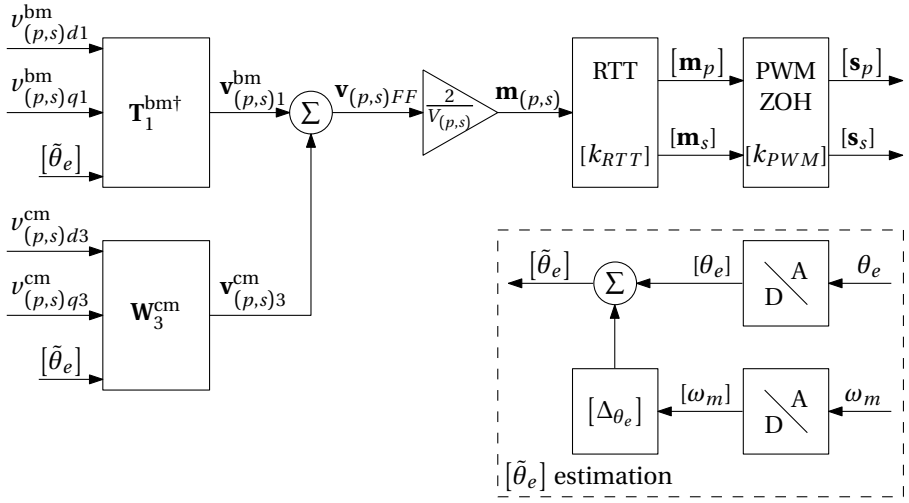

Figure 5.8: Discrete-time delay block diagram visualization of the VRE FF CS per-side (p,s); the (dn,qn)-axis voltages from the lookup graphs in Figure 5.7 are transformed to continuous-time voltages based on the estimated electrical rotor position, $[\tilde{\theta}_e]$. The estimation is derived from the measured electrical position, $[\theta_e]$, and angular velocity, $[\omega_m]$, with which subsequently the angular advancement, $[\Delta_{\theta_e}]$ is predicted to compensate for the system delays, $[k_{RTT}]$, $[k_{PWM}]$, and apply the correct voltages at each position.

5.5.3 Experiments

Practicing VRE with the actual experimental setup (Appendix F) was done based on a fixed-step-size discrete-time SIMULINK model. The compiled model was downloaded to the RTT which derives the steering signals, $[\mathbf{s}_{(p,s)}]$, in the same manner as the described simulation models (Figures 5.7 and 5.8). An important difference with the ideal switches based simulations is the reduced magnitude of inverter voltages $\mathbf{v}_{(p,s)FF}$ due to the switching-leg blanking time, t_b. To allow for application of the same lookup graphs, the supply voltages, V_p and V_s, were increased such, that the magnitude reduction in the measurements is compensated. Therefore, the supply voltages applied during the measurements, $V^{meas}_{(p,s)}$, are computed based on t_b and T_{sw} according to

$$V^{meas}_{(p,s)} = V_{(p,s)} \left(1 - \frac{2t_b}{T_{sw}}\right)^{-1}. \tag{5.33}$$

The results of the experiments are shown in Figure 5.17 and Figure 5.18.

5.5.4 Field weakening

To put the electrical machine B torque versus angular velocity range obtained with the VRE principle into perspective, a comparison is made with the classical FW control technique [80, 142][2]. The FW experiments were also conducted with electrical machine B (Appendix D) in the FBS drive configuration with $V_{inv} = 350$ V, and are performed using the setup detailed in Appendix F [49].

Classical FW control with a robust reference current computation [112] is applied in the CPSR, as depicted in Figure 5.9. As such, ideally only fundamental frequency phase currents are produced. To achieve this, the per-harmonic EMF components are matched by an equal inverter voltage, v_{qn}, which is achieved by the FF control as proposed in Figure 2.8a and indicated per-harmonic in Figure 5.9a. In Figure 5.9a, the computation of the phase voltages vector, $\mathbf{v}$, is shown. Firstly, the intended per-axis fundamental frequency current components, $i^{\mathrm{bm}*}_{(d1,q1)}$, for FW are computed from T^*_{em}, ω_m, and the average peak fundamental inverter voltage, $\langle \hat{v}_1 \rangle$, which is initially equal to V_{inv}. Secondly, the per-axis fundamental current components, $i^{\mathrm{bm}}_{(d1,q1)}$ are derived with the associated transformation matrix, $\mathbf{T}^{\mathrm{bm}}_1$, using θ_e from the BM phase currents vector, $\mathbf{i}^{\mathrm{bm}}_1$. The per-component current error signal, $\Delta^{\mathrm{bm}}_{(d1,q1)}$, is subsequently used as input per respective CS, being $\mathrm{CS}^{\mathrm{bm}}_{(d1,q1)}$. In parallel, the per-harmonic decoupling FF compensation [103, 127] is used to derive the per-axis fundamental frequency voltages, $v^{\mathrm{bm}}_{(d1,q1)FF}$, the electrical machine B EMF voltages, $e^{\mathrm{bm}}_{q1}, e^{\mathrm{cm}}_{q3}$, and the continuous-time third-harmonic FF impedance voltage, v^{cm}_{Z3FF}. As such,

$$v^{\mathrm{bm}}_{d1FF} = N^{\mathrm{sr}} \left(R_{st} i^{\mathrm{bm}}_{d1} - N_{pp} \omega_m L^{\mathrm{bm}} i^{\mathrm{bm}}_{q1} \right), \tag{5.34}$$

$$v^{\mathrm{bm}}_{q1FF} = N^{\mathrm{sr}} \left(R_{st} i^{\mathrm{bm}}_{q1} + N_{pp} \omega_m L^{\mathrm{bm}} i^{\mathrm{bm}}_{d1} \right), \tag{5.35}$$

$$e^{\mathrm{bm}}_{q1} = N^{\mathrm{sr}} K_{e1} \omega_m, \tag{5.36}$$

$$e^{\mathrm{cm}}_{q3} = N^{\mathrm{sr}} K_{e3} \omega_m, \tag{5.37}$$

$$v^{\mathrm{cm}}_{Z3FF} = N^{\mathrm{sr}} \sqrt{(R_{st} i^{\mathrm{cm}})^2 + \left(N_{pp} \omega_m L^{\mathrm{cm}} i^{\mathrm{cm}} \right)^2}, \tag{5.38}$$

where i^{cm} is the per-phase CM current of $\mathbf{i}^{\mathrm{cm}}$. The additional FF voltages (5.34)-(5.38) reduce the error Δ that needs to be compensated by the CS. The EMF components $e^{\mathrm{bm}}_{q1}, e^{\mathrm{cm}}_{q3}$ are added to their respective transformation matrix, after which $\mathbf{v}$ is composed of the fundamental frequency BM voltage vector, $\mathbf{v}^{\mathrm{bm}}_1$, and the third-harmonic CM voltage vector, $\mathbf{v}^{\mathrm{cm}}_3$, using $[\tilde{\theta}_e]$. The difference between θ_e and $\tilde{\theta}_e$, as explained in Figure 5.8 is required due to the system delays indicated in Figure 5.9c. The constant electrical position offset, θ_{3FF}, is added to $[\tilde{\theta}_e]$ to further reduce the undesired i^{cm}.

[2] SVM control is not considered since the generated CM voltages applied to the open-winding electrical machine structure deliberately produces CM currents [86], therefore classical FW is applied.

To fully employ the available DC supply voltage, the VSI ideally applies an AC voltage with a peak value that is exactly equal to the supply voltage throughout the CPSR. However, the discrepancy between the modelled and actual drive system, results in a difference between the predicted (Figure 5.9a) and applied per-phase inverter voltage. Consequently, the achievable angular velocity range is affected. Different methods to compensate this difference and exploit the complete voltage range for a solely fundamental frequency operated drive system are explained in [103, 112]. However, multiple harmonic EMF components cause these methods to be inaccurate in the case presented here. The sum of the different flux linkages lead to a peak EMF, $\hat{e}$, as determined with (2.47). Note that $\hat{e}$ is not necessarily located at the peak value of the fundamental component as assumed in [103, 112]. Therefore, a different method is applied to drive the electrical machine with a unity peak-modulation-value, analogue to the approach stated for VRE in Appendix A.1.

A per-electric-rotation PWM peak-detection is combined with a voltage error, Δ_v, correction to regulate the time-variant peak modulation vector, $\hat{\mathbf{m}}$, to unity as shown in Figure 5.9b. The peak voltage per-electric-rotation is derived with the cyclic peak-detector (CPD) for both $\mathbf{v}$ and v^{cm}_{Z3FF}, being $\hat{\mathbf{v}}$ and $\hat{v}^{\mathrm{cm}}_{Z3FF}$, respectively. The total peak CM voltage, $\hat{v}^{\mathrm{cm}}_{3}$, and the unused VSI supply voltage range, Δ_v, are derived after which a voltage correction CS, being CS_v, is applied to diminish Δ_v. CS_v is a controller with an integrating action to reach $\hat{\mathbf{v}} = V_{inv}$, and thus $\hat{\mathbf{m}} = 1$. The peak disturbance voltage, $\hat{v}$, is subtracted from V_{inv} to find the allowed peak fundamental voltage, $\hat{v}_1$. Subsequently, the average value of $\hat{v}_1$ over a defined number of cycles, $\langle \hat{v}_1 \rangle$, gives the available fundamental frequency voltage range for the FW CS introduced in Figure 5.9a. The per-phase steering signals, $[s_x]$, are derived from $\mathbf{v}$ and V_{inv}, taking into account the respective RTT and PWM delays, k_{RTT}, k_{PWM}, as indicated in Figure 5.9c. The experimental results of the FW measurements are presented in Figures 5.20 to 5.23.

Finally, in Figure 5.24 the CPSR torque versus angular velocity range is depicted for the VRE and the FW method based measurement results for comparison. There, the results obtained with FW are scaled down such, that the applied per-phase RMS current level is equal to that used for VRE.

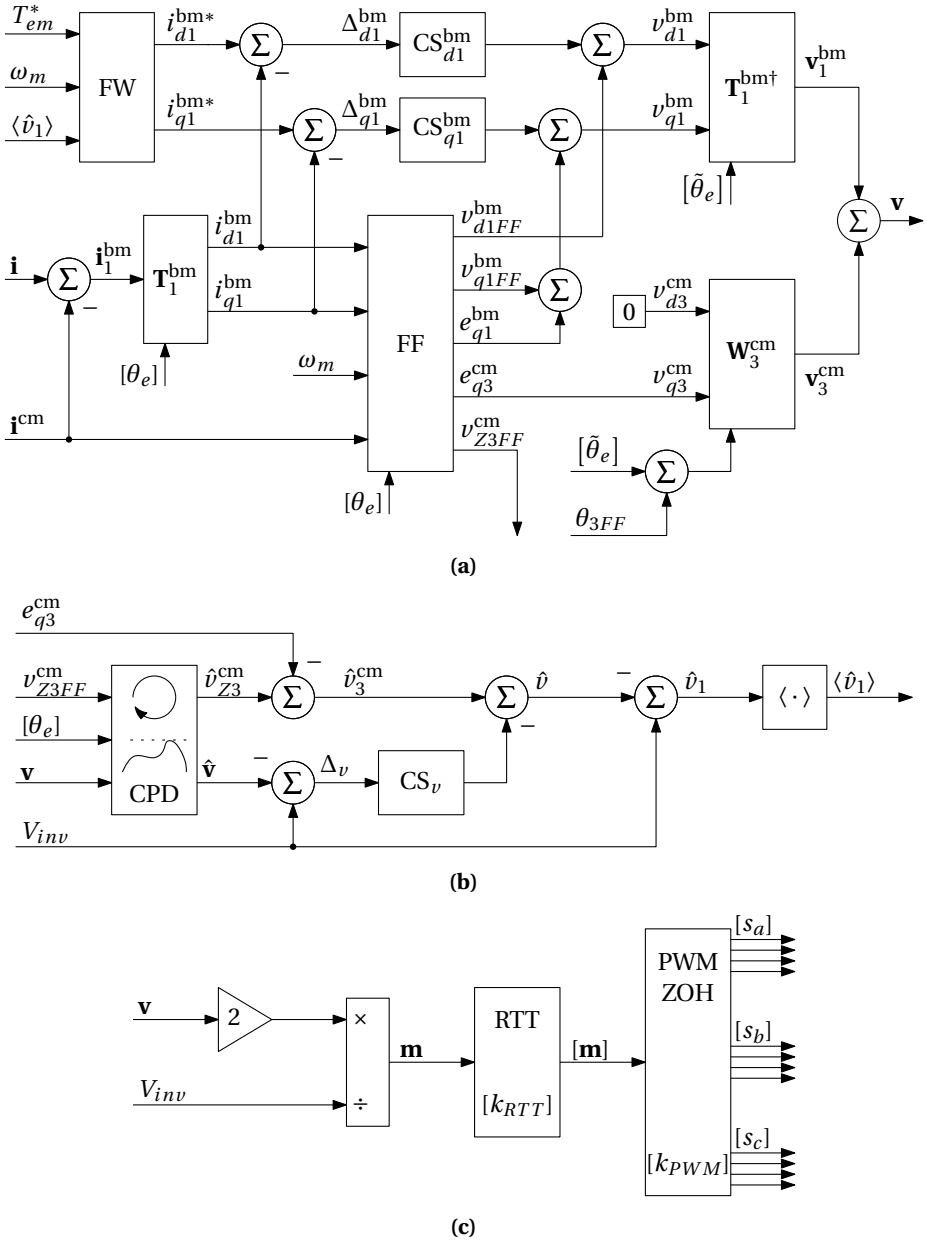

Figure 5.9: Block diagrams of the FW CS composed of feed-forward and feed-back components; **(a)**, phase voltages vector, **v**, computation based on measurements and model information, composed using the fundamental- and third-harmonic-transformation matrices, **(b)**, computation of the peak fundamental inverter voltage, $\hat{v}_1$, over a number of cycles, $\langle \hat{v}_1 \rangle$ based on the remaining voltage-range, **(c)** FB discrete-time per-phase steering signals, $[s_x]$, computation.

5.6 Results

The results of the optimizations, simulations, and experiments are presented and explained in this section. Additionally, the results of the different approaches are compared to verify the validity of the applied models, and quantify the discrepancies. Both the simulations and the experiments are executed on the basis of the same operating point in the viable optimization solutions domain, i.e. $\left\{i_{q1}^{\mathrm{bm}}; x_r^{\mathrm{sr}}\right\} = \{353\ \mathrm{mA}; 1.2\}$.

5.6.1 Optimization

The complete domain of viable solutions for the idealized electrical machine and the practical electrical machine B optimization methods conform the constraints-set is presented in Appendix A. Due to the quantization of the optimization domain, the solutions found are presented as discrete points.

Idealized voltage range enhancement principle

The results of the idealized voltage range enhancement principle, neglecting the third-harmonic EMF $\left(e_{q3}^{\mathrm{cm}} = 0,\ \text{thus}\ K_{e3} = 0\right)$, are shown in Figure 5.10. The maximum achievable fundamental frequency torque producing current, i_{q1}^{bm}, and the correspondingly required third-harmonic spacial current vector magnitude, $\left|\vec{i}_3^{\mathrm{cm}}\right|$, to ensure secondary-side power balance, are plotted versus the angular velocity, ω_m, in Figure 5.10a. These results are obtained from the optimization shown in Figure 5.3b, taking into account the base angular velocity corresponding to this machine configuration. Furthermore, it is shown that for a fixed i_{q1}^{bm} in combination with an increasing ω_m, it follows that $\left|\vec{i}_3^{\mathrm{cm}}\right|$ increases to maintain the secondary-side power balance. This is due to the higher power, P_{s1}^{bm}, that is transferred to the secondary-side capacitors, C_{s+}, C_{s-}. Consequently, T_{em} (Figure 5.10b) produced by the machine is proportional to i_{q1}^{bm} since only the fundamental frequency EMF is assumed in this idealized electrical machine. The base angular velocity of this idealized series-connected windings electrical machine is lower (68.7 rad./s) than the electrical machine B base angular velocity, ω_b^{sr} (76.7 rad./s in Table D.4). This is due to the increased peak EMF, $\hat{e}$, since only the fundamental frequency machine constant, K_{e1}, is considered, according to (2.47) and (2.49). The top angular velocity, ω_t, that is achieved by employing the VRE principle to the system configuration presented here is 129.2 rad./s, leading to an angular velocity ratio, x_r^{sr} =1.85.

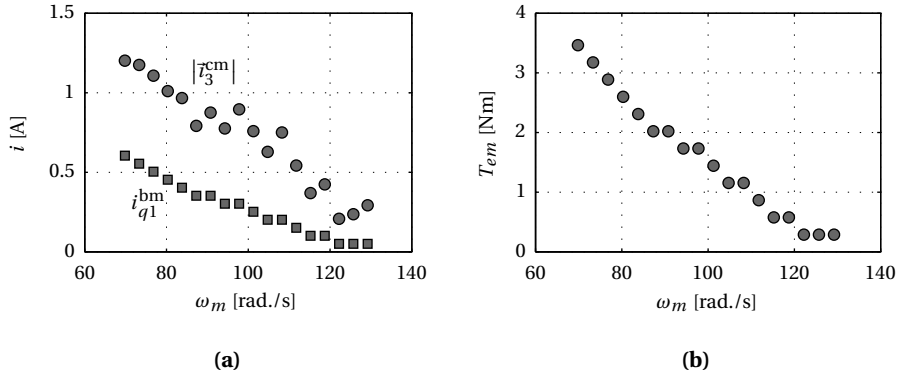

Figure 5.10: Idealized VRE CM current minimization results; **(a)** maximum achievable i_{q1}^{bm} and therefore required $|\vec{i}_3^{\,\mathrm{cm}}|$ versus ω_m, **(b)** resulting electromagnetic torque, T_{em} versus ω_m.

Practical approach to voltage range enhancement

The identified electrical machine B parameters are applied for the practical optimization from which the results are depicted in Figure 5.11. In this case, the third-harmonic of the EMF is present $\left(e_{q3}^{\mathrm{cm}} \neq 0 \text{ thus } K_{e3} \neq 0\right)$. The required $|\vec{i}_3^{\,\mathrm{cm}}|$ to ensure secondary-side power balance while driving electrical machine B with i_{q1}^{bm}, is plotted as a function of angular velocity ω_m in Figure 5.11a. These results are obtained from the optimization shown in Figure 5.5. Similar effects as in the idealized case are shown. However, the start value of ω_m is obviously equal to the base angular velocity ω_b^{sr}, since the complete model of electrical machine B is accounted for. The computed electromagnetic machine torque, T_{em}, is shown in Figure 5.11b. The ω_t, that is achieved by employing the VRE principle to the system configuration presented here is 128.9 rad./s, leading to an angular velocity ratio, x_r^{sr} =1.7.

Comparing idealized with practical

By comparing the results of the idealized and practical optimization, two important differences exist as depicted in Figure 5.12. Firstly, T_{em} at each angular velocity is lower for the practical case as shown in Figure 5.12a. This is caused by the negative average third-harmonic torque component, $\langle T_{em3}^{\mathrm{cm}} \rangle$, produced by the interaction between the third-harmonic EMF component, e_{q3}^{cm}, and the q-axis component of the CM current, i_{q3}^{cm}, as formulated in (5.26b). As concluded from the optimization procedure in Appendix A, no solution with a positive or zero $\langle T_{em3}^{\mathrm{cm}} \rangle$ exists. Secondly, the increased base angular velocity for $K_{e3} \neq 0$ in combination with an equal top angular velocity leads to an angular velocity ratio reduction from x_r^{sr} =1.85 to 1.7 for the presented case. As a result

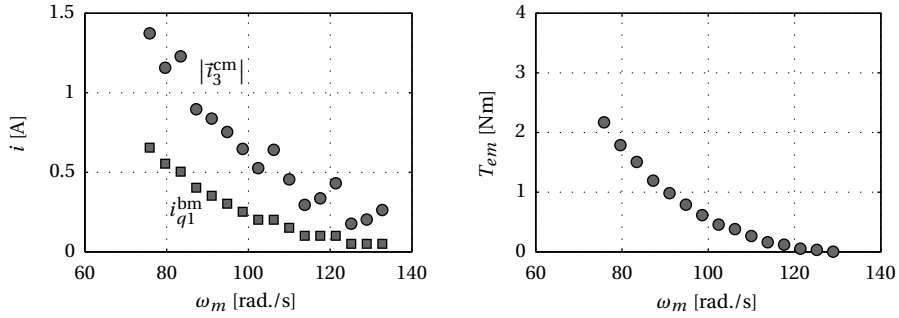

(a) **(b)**

Figure 5.11: Non-ideal VRE CM current minimization results; **(a)** maximum achievable i_{q1}^{bm} and therefore required $|\bar{i}_3^{cm}|$ versus ω_m, **(b)** resulting electromagnetic torque, T_{em} versus ω_m.

of the decreased T_{em} for the practical case, the electromagnetic output power, P_{em} is proportionally lower, as shown in Figure 5.12b.

5.6.2 Experimental verification

For each of the three experimental verification cases in this section, the results are presented in the same manner. In the experimental verification of the VRE principle, the machine-set is rotating at a fixed angular velocity, dictated by the DCM. The inverter voltages corresponding to $\left\{i_{q1}^{bm}; x_r^{sr}\right\} = \{353\text{ mA}; 1.2\}$ are applied. Assumption #2, defining the voltage vectorial relations, is achieved by ensuring an anti-phase relation between the fundamental frequency inverter voltage vectors, thereby maximizing the applied per-phase voltage. The other assumptions are discussed in the results.

The continuous-time results for the ideal sources simulations, the ideal switches simulations, and the experiments are shown in Figure 5.13, Figure 5.15, and Figure 5.17, respectively. The periodic continuous-time signals are plotted over approximately two fundamental frequency periods for details, while the average active power and rotating reference frame signals are plotted during one second to show settling behaviour. The modulation signal of phase a for both the primary-side, m_{pa}, and the secondary-side, m_{sa}, are shown in Figure 5.13a, Figure 5.15a, and Figure 5.17a, respectively. In Figure 5.13b, Figure 5.15b, and Figure 5.17b, the phase a fundamental frequency current, i_{a1}^{bm}, third-harmonic current, i_{a3}^{cm}, and total current, i_a are depicted for each of the respective experimental verification cases. The per-harmonic current components are estimated based on the phase currents using the unified estimation method explained in Section 2.6.4. The fundamental frequency rotating reference frame $(d1, q1)$-axis currents, i_{d1}^{bm}, i_{q1}^{bm} and their respective reference values, $i_{d1}^{bm*}, i_{q1}^{bm*}$, are plotted for the three cases

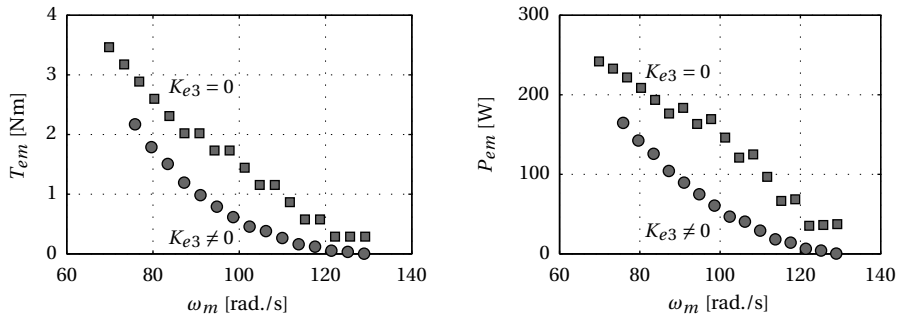

(a) **(b)**

Figure 5.12: Comparison of the presented VRE CM current minimization methods either neglecting the third-harmonic electrical machine constant, $K_{e3} = 0$, or considering it, $K_{e3} \neq 0$; **(a)** electromagnetic torque, T_{em} versus ω_m, **(b)** electromagnetic output power P_{em} versus ω_m.

in Figure 5.13c, Figure 5.15c, and Figure 5.17c. Equivalently, the third-harmonic rotating reference frame $(d3, q3)$-axis currents, $i_{d3}^{\text{cm}}, i_{q3}^{\text{cm}}$ and their respective reference values, $i_{d3}^{\text{cm}*}, i_{q3}^{\text{cm}*}$, are plotted for the three cases in Figure 5.13d, Figure 5.15d, and Figure 5.17d. The relevant periodically varying powers, i.e. the secondary-side CM power, p_{s3}^{cm}, and the electromagnetic power, p_{em}, are given per case in Figure 5.13e, Figure 5.15e, and Figure 5.17e, respectively. From p_{em}, the average value, P_{em}, is obtained and plotted together with the average primary-side inverter power, P_p, and average secondary-side inverter power, P_s, in Figure 5.13f, Figure 5.15f, and Figure 5.17f.

In order to verify whether the experimental results correspond to the intended vectorial relations shown in Figure 5.2a and Figure 5.4a, XY-plots[3] are presented for the ideal sources simulations, the ideal switches simulations, and the measurements in Figure 5.14, Figure 5.16, and Figure 5.18, respectively. To conform that i_{a1}^{bm} is in-phase with the fundamental frequency EMF of phase a, being e_{a1}^{bm}, current i_{a1}^{bm} is plotted versus e_{a1}^{bm} for each respective case in Figure 5.14a, Figure 5.16a, and Figure 5.18a. Equivalently, in Figure 5.14b, Figure 5.16b, and Figure 5.18b, i_{a3}^{cm} is plotted versus the third-harmonic secondary-side CM voltage of phase a, being v_{sa3}^{cm}, to verify per-case whether the intended vectorial relation is met.

[3] XY-plots are used here to show the mutual amplitude- and phase-relation between two periodically time-variant quantities, and are based on the last two periods of the displayed signals, equitable to the displayed periodic continuous-time signals.

Simulations with ideal sources

The continuous-time simulation results with ideal voltage sources representing both VSIs are presented in Figure 5.13. In both m_{pa} and m_{sa} in Figure 5.13a, the third-harmonic frequency component is recognized. Additionally, the intended unity peak value for both m_{pa} and m_{sa} is achieved according to assumption #5. Phase current i_a in Figure 5.13b results from the drive inverter voltages generated from m_{pa} and m_{sa}. The difference in amplitude between i_{a1}^{bm} and i_{a3}^{cm} is approximately a factor 2.4, corresponding to the current ratio, r_{i31}, in Figure A.4b. In Figure 5.13c, the actual per-axis fundamental currents i_{d1}^{bm} and i_{q1}^{bm} approximate to their respective reference levels, $i_{d1}^{\text{bm}*}$ and $i_{q1}^{\text{bm}*}$. The small discrepancy of i_{d1}^{bm} with $i_{d1}^{\text{bm}*}$ is caused by the combined error due to the lookup deviations in the combined harmonics optimization graph (Figure 5.3a), the error-tolerance in the optimization procedure, and the simulation tolerance. The absolute value of the steady state error is 20 mA, and assumption #1 is met when disregarding this discrepancy. An equal absolute error exists between $i_{d3}^{\text{cm}*}$ and i_{d3}^{cm} and between $i_{q3}^{\text{cm}*}$ and i_{q3}^{cm} for the same reason. Additionally, a periodic error signal with an amplitude of 2 mA is present on both i_{d3}^{cm} and i_{q3}^{cm} due to a mismatch between the actual and the estimated per-phase CM current. The periodicity of p_{s3}^{cm} transferred through electrical machine B from the primary- to the secondary-side, is shown in Figure 5.13e. The minimum value of p_{s3}^{cm} is zero, indicating that the CM secondary-side PF, $\text{PF}_{s3}^{\text{cm}}$, is unity according to assumption #3. The offset of p_{em} is caused by the BM fundamental frequency interaction (5.16) while the periodic component is caused by the CM third-harmonic interaction described in (5.23). With the average powers in Figure 5.13f it is demonstrated that in steady state, the drive system executes the VRE principle as intended. Secondary-side supply voltage balance is reached according to P_s as intended with assumption #4.

The vectorial simulation results with ideal voltage sources representing the VSI are presented in Figure 5.14. The steady state error of i_{d1}^{bm} causes the phase difference between i_{a1}^{bm} and e_{a1}^{bm}, which is less than 1%. The diagonal trend in Figure 5.14a indicates that i_{a1}^{bm} and e_{a1}^{bm} are in-phase as intended by assumption #1. Equivalently, the mutual phase difference between i_{a3}^{cm} and v_{sa3}^{cm} is small, as depicted in Figure 5.14b, determining that these signals are in-phase, according to assumption #3.

The average value of power p_{s3}^{cm}, being P_{s3}^{cm} (5.21), is very close to P_p. As such, the power supplied by the primary-side VSI is first transferred to the secondary-side VSI with i_3^{cm}, after which it is supplied to the electrical machine by both VSIs using i_1^{bm}. This effect is caused by the higher DC supply voltage at the secondary-side. For the presented case, the electrical machine B efficiency is 95.7%, taking solely the resistive machine losses into account.

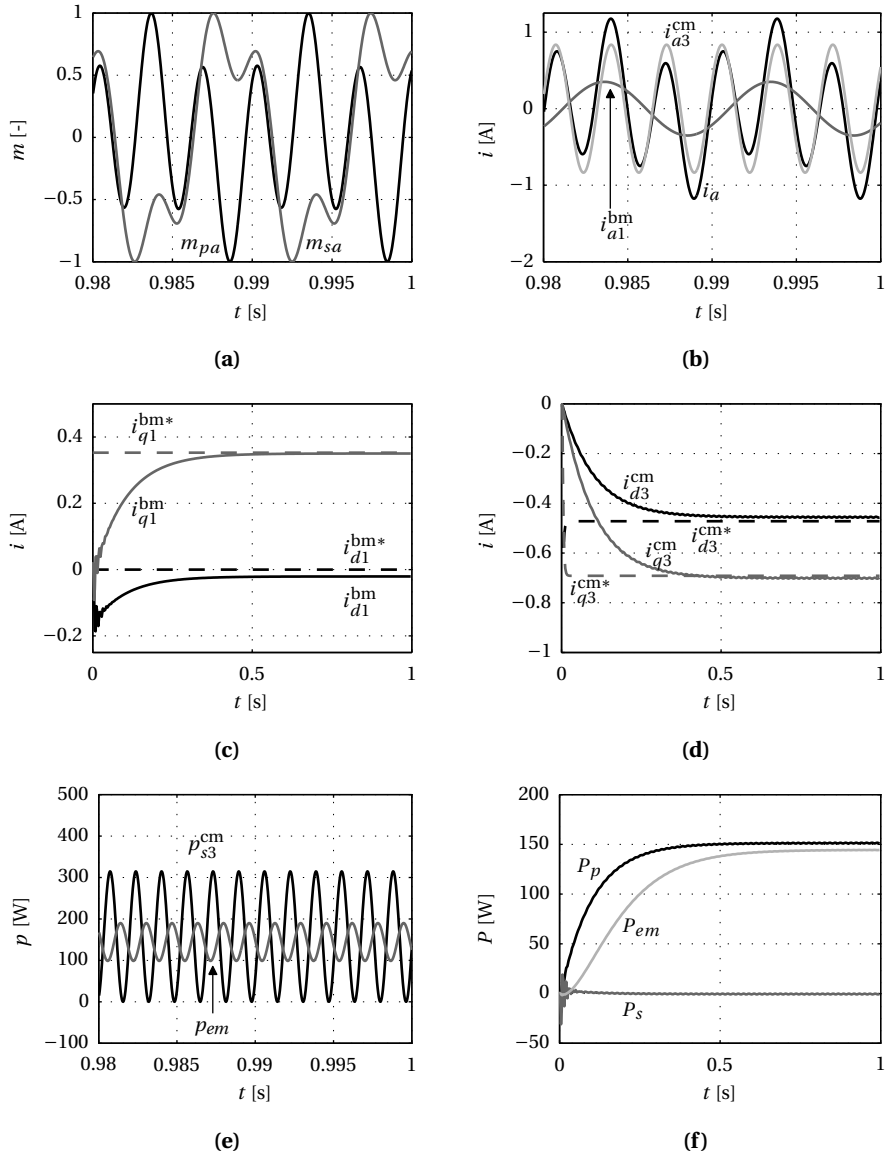

Figure 5.13: Open-loop FF VRE principle simulation results for $\left\{i_{q1}^{\mathrm{bm}}; x_r^{\mathrm{sr}}\right\} = \{353\,\mathrm{mA}; 1.2\}$ with ideal sources representing the VSIs; **(a)** phase a modulation signal per-side, m_{pa}, m_{sa}, **(b)** phase a fundamental, third-harmonic, and total current, $i_{a1}^{\mathrm{bm}}, i_{a3}^{\mathrm{cm}}$, and i_a, **(c)** reference and actual BM $(d1,q1)$-axis currents, $i_{d1}^{\mathrm{bm}*}, i_{q1}^{\mathrm{bm}*}$ and $i_{d1}^{\mathrm{bm}}, i_{q1}^{\mathrm{bm}}$, **(d)** reference and actual $(d3,q3)$-axis CM currents, $i_{d3}^{\mathrm{cm}*}, i_{q3}^{\mathrm{cm}*}$ and $i_{d3}^{\mathrm{cm}}, i_{q3}^{\mathrm{cm}}$, **(e)** time-variant third-harmonic CM and electrical machine power, $p_3^{\mathrm{cm}}, p_{em}$, **(f)** averaged primary-side, secondary-side, and electrical machine power, P_p, P_s, and P_{em}.

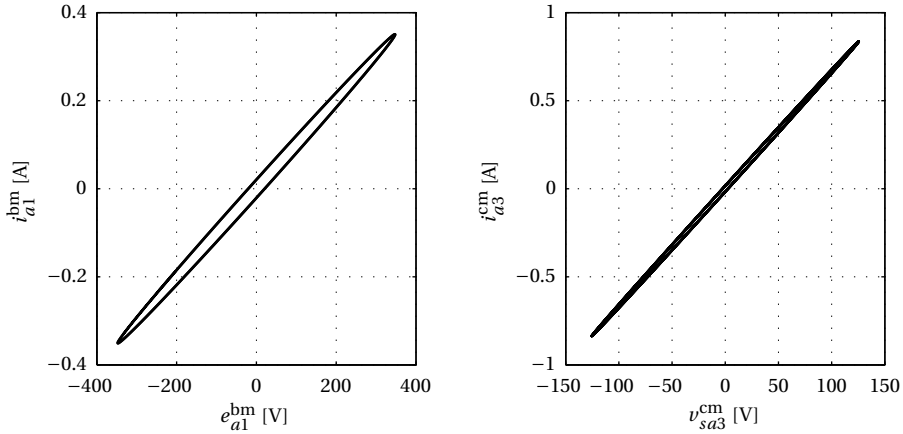

Figure 5.14: XY-plots of the open-loop FF VRE principle simulation results for $\left\{i_{q1}^{\mathrm{bm}}; x_r^{\mathrm{sr}}\right\}$ = {353 mA; 1.2}, with ideal sources representing the VSIs; **(a)** phase a fundamental frequency current, i_{a1}^{bm}, versus EMF, e_{a1}^{bm}, **(b)** phase a third-harmonic current, i_{a3}^{cm}, versus secondary-side inverter voltage, v_{sa3}^{cm}.

Simulations with ideal switches

The continuous-time simulation results with ideal switching legs representing both VSIs are presented in Figure 5.15. Additionally, the discrete-time RTT CS implementation with delay factors is taken into account. Solely the variations compared to the ideal sources simulation are mentioned for clarity. The third-harmonic current reference values, $i_{d3}^{\mathrm{cm}*}, i_{q3}^{\mathrm{cm}*}$ (Figure 5.15d), show an initial transient behaviour because during that time the machine-set ω_m is regulated such that x_r^{sr} is equal to the reference value. This effect is created by the combination of a fixed $i_{d1}^{\mathrm{bm}*}$ (Figure 5.15c), with a changing ω_m, leading to a P_{em} adaption, and with that the power that is transferred to the secondary-side supply, P_{s3}^{cm}, by $i_{d3}^{\mathrm{cm}}, i_{q3}^{\mathrm{cm}}$. The periodic fluctuation of i_{d3}^{cm} and i_{q3}^{cm} in the ideal sources simulations (Figure 5.13d) is not present in this case (Figure 5.15d), as a result of a different estimator LPF implementation, as depicted in Figure 2.8b. Correspondingly, P_{em} settles faster in Figure 5.15f compared to Figure 5.13f, which is also the result of the estimator LPF implementation.

The vectorial simulation results with ideal switching legs representing the VSIs are presented in Figure 5.16. No significant variations compared to Figure 5.14 exist in either Figure 5.16a or Figure 5.16b. By comparing Figure 5.16 with Figure 5.14 it is concluded that the implemented position estimation and discrete-time delay integration in the simulation model works as intended (Figure 5.8).

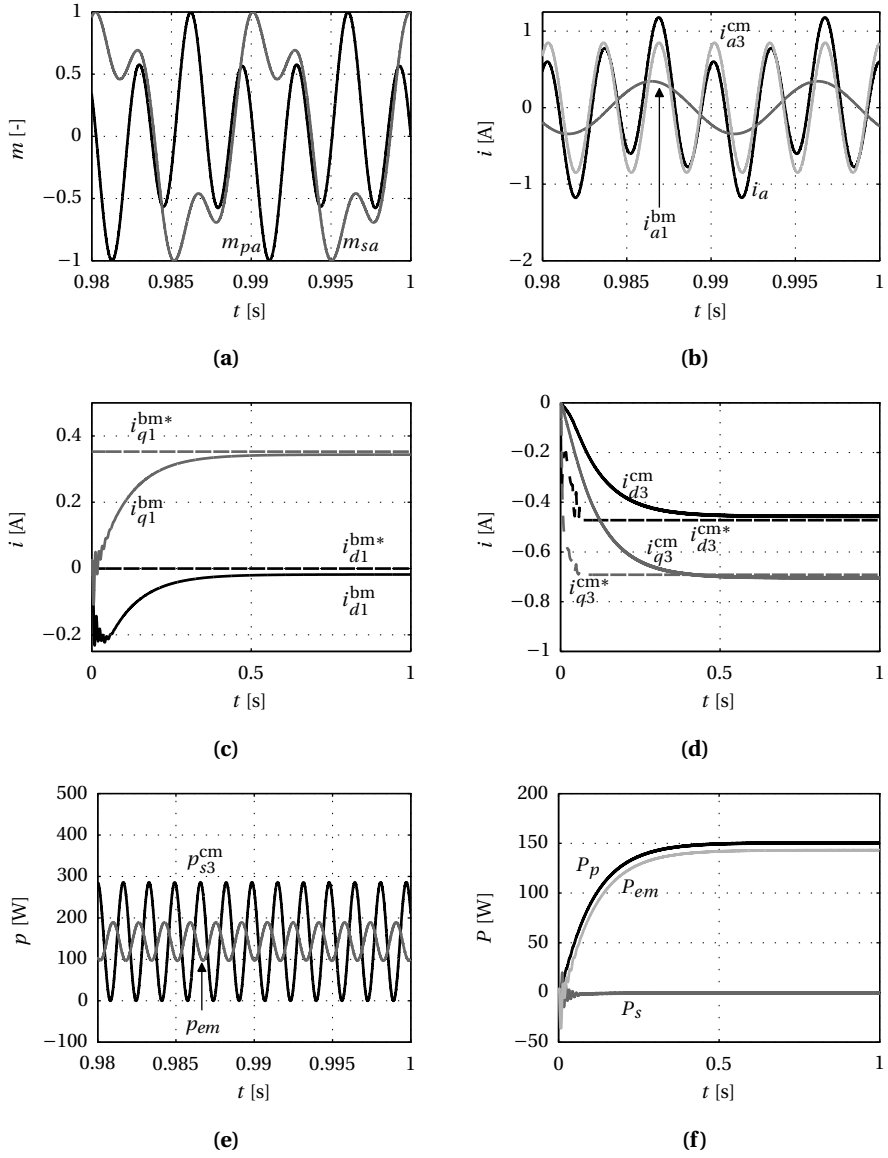

Figure 5.15: Open-loop FF VRE principle simulation results for $\left\{i^{\mathrm{bm}}_{q1}; x^{\mathrm{sr}}_r\right\} = \{353\ \mathrm{mA}; 1.2\}$, where the VSIs are modelled with ideal switches; **(a)** phase a modulation signal per-side, m_{pa}, m_{sa}, **(b)** phase a fundamental, third-harmonic, and total current, $i^{\mathrm{bm}}{}_{a1}, i^{\mathrm{cm}}{}_{a3}$, and i_a, **(c)** reference and actual $(d1,q1)$-axis currents, i^*_{d1}, i^*_{q1} and i_{d1}, i_{q1}, **(d)** reference and actual $(d3,q3)$-axis currents, i^*_{d3}, i^*_{q3} and i_{d3}, i_{q3}, **(e)** time-variant third-harmonic CM and electrical machine power, $p^{\mathrm{cm}}_3, p_{em}$, **(f)** averaged primary-side, secondary-side, and electrical machine power, P_p, P_s, and P_{em}.

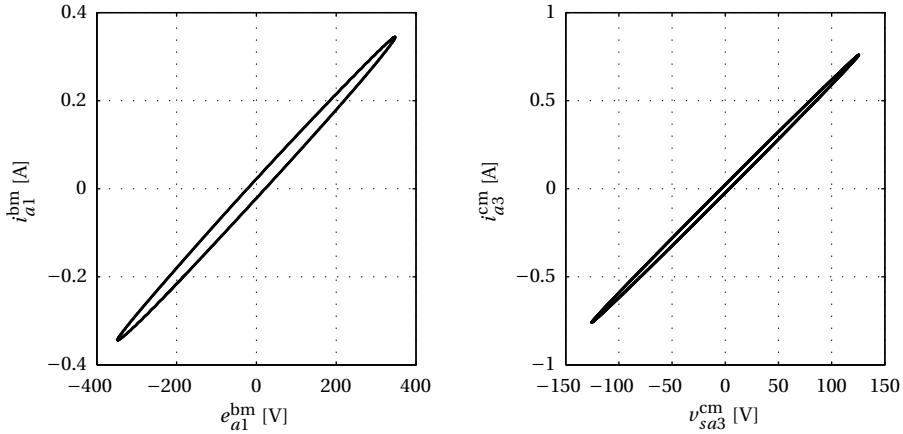

Figure 5.16: XY-plots of the open-loop FF VRE principle simulation results for $\left\{i_{q1}^{\mathrm{bm}}; x_r^{\mathrm{sr}}\right\}$ = {353 mA; 1.2}, where the VSIs are modelled with ideal switches; **(a)** phase a fundamental frequency current, i_{a1}^{bm}, versus EMF, e_{a1}^{bm}, **(b)** phase a third-harmonic current, i_{a3}^{cm}, versus secondary-side inverter voltage, v_{sa3}^{cm}.

Experiments voltage range enhancement

The continuous-time measurement results are presented in Figure 5.17. Again the discrepancies with the previous results are highlighted. The phase current plot in Figure 5.17b shows that i_a contains minor higher-order harmonics that are not estimated in the per-harmonic current components i_{a1}^{bm} and i_{a3}^{cm}. However, i_a furthermore contains an offset level of -300 mA, that is not considered in estimating i_{a1}^{bm} and i_{a3}^{cm}. This offset originates from an unbalance between the primary- and secondary-side supply voltages. The resulting DC voltage difference across the CM resistance, R^{cm}, generates a homopolar CM current, I^{cm}, introduced in Section 2.6.2. In Figure 5.17d it is shown that the third-harmonic current levels are not met. While the other reference current levels in both Figure 5.17c and Figure 5.17d are reached, differences in either the machine impedance or coupling at this current level, or a small encoder angle misalignment introduce a discrepancy between $i_{q3}^{\mathrm{cm}*}$ and i_{q3}^{cm}. Since a lookup graph based drive system is used, no error feedback is applied. Therefore, modulation signal adaptations to solely adjust i_{q3}^{cm} are not possible. The higher-harmonic components in i_a are also visible in p_{em}. The offset level of p_{em} is slightly lower compared to Figure 5.15e by reason of the larger i_{q3}^{cm}, which furthermore causes the increased p_{s3}^{cm}. The increased P_p in Figure 5.17f, when compared to the simulation results, is caused by the negative P_s. The sum P_p and P_s is slightly larger than P_p in the simulations, considering that P_s is zero in that case. The measured efficiency of electrical machine B is 89.5%, and the difference

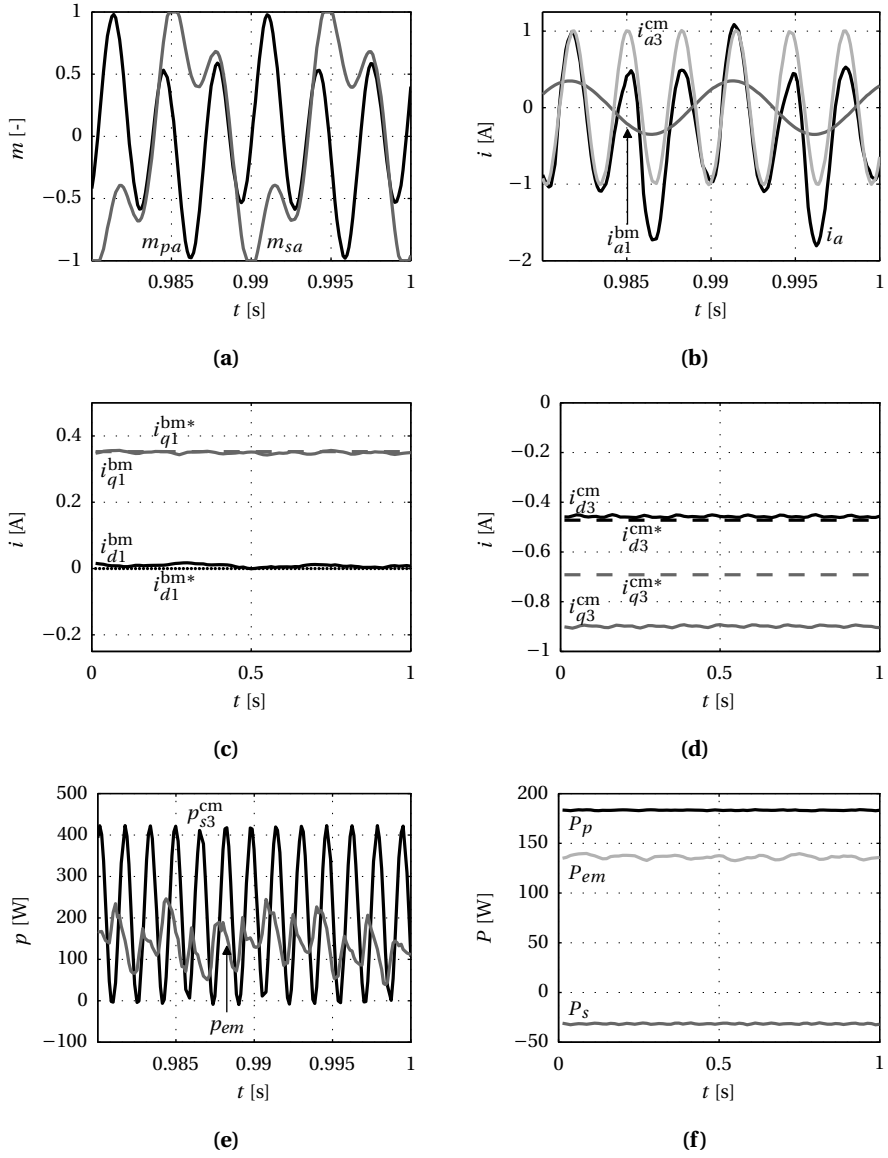

Figure 5.17: Open-loop FF VRE principle measurement results for $\left\{i^{\mathrm{bm}}_{q1}; x^{\mathrm{sr}}_r\right\} = \{353\ \mathrm{mA}; 1.2\}$ captured during 1 s from the trigger instance; **(a)** phase a modulation signal per-side, m_{pa}, m_{sa}, **(b)** phase a fundamental, third-harmonic, and total current, $i^{\mathrm{bm}}{}_{a1}, i^{\mathrm{cm}}{}_{a3}$, and i_a, **(c)** reference and actual $(d1, q1)$-axis currents, i^*_{d1}, i^*_{q1} and i_{d1}, i_{q1}, **(d)** reference and actual $(d3, q3)$-axis currents, i^*_{d3}, i^*_{q3} and i_{d3}, i_{q3}, **(e)** time-variant third-harmonic CM and electrical machine power, $p^{\mathrm{cm}}_3, p_{em}$, **(f)** averaged primary-side, secondary-side, and electrical machine power, P_p, P_s, and P_{em}.

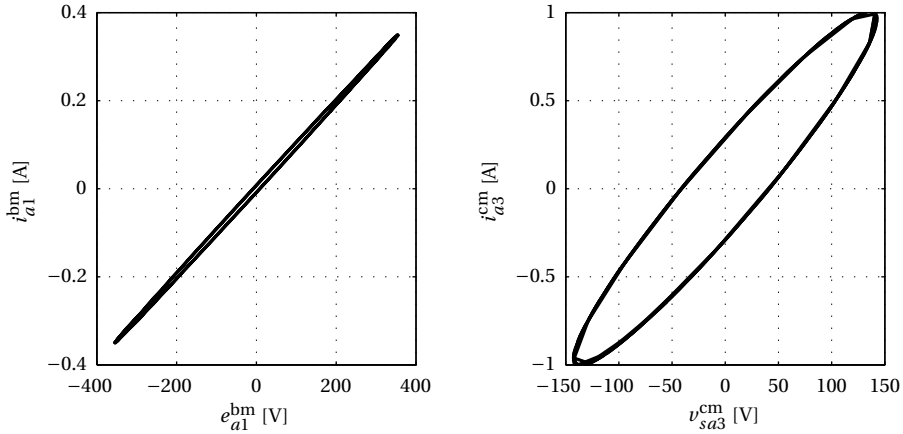

Figure 5.18: XY-plots of the open-loop FF VRE principle measurement results for $\left\{i_{q1}^{\mathrm{bm}}; x_r^{\mathrm{sr}}\right\}$ = {353 mA; 1.2} captured during 1 s from the trigger instance; **(a)** phase a fundamental frequency current, i_{a1}^{bm}, versus EMF, e_{a1}^{bm}, **(b)** phase a third-harmonic current, i_{a3}^{cm}, versus secondary-side inverter voltage, v_{sa3}^{cm}.

with the simulated efficiency is deduced from the increased i_{q3}^{cm}, the homopolar current, I^{cm}, and the iron losses neglected in the simulations.

The vectorial relation experimental results are presented in Figure 5.18. The phase a fundamental frequency EMF, e_{a1}^{bm} and current, i_{a1}^{bm}, are in-phase as shown in Figure 5.18a. However, since i_{q3}^{cm} is too large, as shown in Figure 5.17d, the amplitude and angle of i_{a3}^{cm}, are not as intended. This leads to a misalignment with the secondary-side phase a third-harmonic CM voltage, as displayed in Figure 5.18b. This discrepancy causes the secondary-side power in-balance, $P_s \neq 0$, as displayed in Figure 5.17f.

The obtained torques from the ideal switches simulations and measurements are plotted in Figure 5.19. The periodicity of the third-harmonic electromagnetic torque component, T_{em3}, at twice the electric angular velocity, i.e. $6\omega_e$, is clearly visible in Figure 5.19a. Since the fundamental frequency torque component, T_{em1}, is constant, the total electromagnetic torque, T_{em}, is also periodical. To assure a constant ω_m, the DCM torque, T_{DCM}, varies equivalently but with an amplitude that is half that of T_{em3}. This is due to the gearbox ratio, r_{gb} (Appendix F).

The main difference between the measured and the simulated electrical machine B torque in Figure 5.19b and Figure 5.19a, respectively, are the effects of the higher-order current components on T_{em}. Furthermore, the measured T_{DCM} is different from the simulated value, which is caused by;

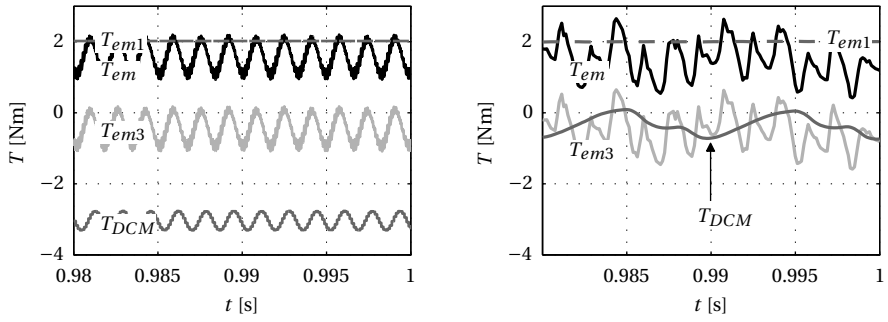

Figure 5.19: Continuous-time torque comparison of the open-loop FF VRE principle simulation and measurement results for $\left\{i_{q1}^{\text{bm}}; x_r^{\text{sr}}\right\} = \{353\text{ mA}; 1.2\}$; **(a)** ideal switching legs simulation torques, T_{em}, T_{em1}, T_{em3} and T_{DCM}, **(b)** measured torques T_{em}, T_{em1}, T_{em3} and T_{DCM}.

- A limited angular velocity controller bandwidth, preventing the DCM from adequately anticipating on the T_{em} fluctuations.
- The previously measured machine-set friction coefficient, B_m^B, applied in the simulations appears to be incorrect when looking at the average value of the measured T_{DCM}.
- A 100 Hz frequency component is visible in T_{DCM}, which is most probably caused by a malfunctioning phase leg of the active rectifier in the machine regulator.

The limited amplitude fluctuation of the measured T_{em} shown in Figure 5.19b, in combination with the machine-set inertia, J_m^B, narrows the angular velocity variation to 0.3 rad./s.

Experiments field weakening

The measured torque and power levels when applying the FW CS proposed in Figure 5.9 are shown in Figure 5.20. In Figure 5.20a, T_{em} is approximately constant until $\omega_m =$ 75.6 rad./s, confirming the predicted CTSR until $\omega_b^{\text{sr}} = 76.7$ rad./s. Subsequently, the CPSR is executed for $75.6 \leq \omega_m \leq 269.6$ rad./s, which is close to the intended $\omega_t^{\text{sr}} = 277$ rad./s. When considering the normalized relation between i_{d1} and i_{q1} plotted for $0 \leq \omega_m \leq$ 269.9 rad./s in Figure 5.21, the CPSR should be extended until $\left(i_{d1}^{\text{bm}}, i_{q1}^{\text{bm}}\right) = (-\breve{\imath}_x, 0)$ to determine the exact value of ω_t^{sr} as defined in Figure 2.2b. The actually produced torque, T_{dyn}, measured with the torque sensor (TS) shows the influence of the friction and iron losses to the electrical machine performance. The powers versus angular velocity corresponding to the torques T_{em}, T_{dyn} are depicted in Figure 5.20b with P_{em}, P_{dyn}, respectively. The intended *constant-power* angular velocity region is not achieved, since

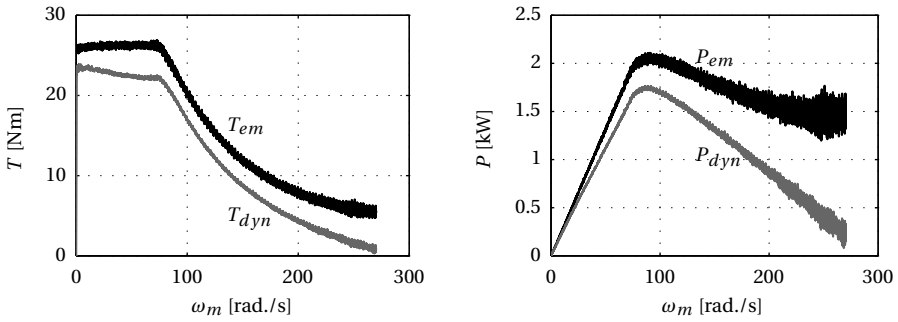

Figure 5.20: Measurement results of FW control based performance as a function of the angular velocity, ω_m; **(a)** electromagnetically produced torque, T_{em}, and TS measured torque, T_{dyn}, **(b)** electromagnetically produced power, P_{em}, and TS measured power, P_{dyn}.

the power decreases with an increasing ω_m, as shown in Figure 2.3.

The optimized voltage range usage striving for $\hat{m}_{xy} = 1$ (Figure 5.9) works as intended as shown with m_{ap}, and m_{as} for $\omega_m \approx \omega_b^{\text{sr}}$ in Figure 5.22a, and for $\omega_m \approx \omega_t^{\text{sr}}$ in Figure 5.23a. The maximum deviation of the FW CS based measurement results without the cyclic peak-detector correction (Figure 5.9b) is 20% or 70 V, emphasizing its added value. The influence of e_{q3}^{cm} is clearly visible when comparing m_{ap} and m_{as} in Figure 5.22a and Figure 5.23a, showing that e_{q3}^{cm} becomes dominant over $v_{(d1,q1)FF}^{\text{bm}}$ at higher ω_m values. Additionally, the measurement resolution limited by the discrete sample time, T_s, is noticeable when comparing Figure 5.22 and Figure 5.23. In Figure 5.22b and Figure 5.23b, the per-phase currents, i_x are shown. The intended sinusoidal wave-shape is approximately achieved, with the CM current, i^{cm}, in Figure 5.22c and Figure 5.23c as only disturbance. The CM current minimization by applying FF works effectively with a relative RMS disturbance, I^{cm}/I_x, of 2.4% and 5.2% at $\omega_m = 75.6$ rad./s (Figure 5.22) and $\omega_m = 269.6$ rad./s (Figure 5.23), respectively. The achieved angular velocity ratio of the series-connected drive configuration operated with FW, x_r^{srFW} =3.57.

Comparing voltage range enhancement with field weakening

To verify the behaviour of electrical machine B operated with the VRE principle, the predicted non-ideal T_{em} versus ω_m range shown in Figure 5.11b is verified by measurements. The measured VRE T_{em} is depicted with indication T_{em}^{VRE} in Figure 5.24. The angular velocity range achieved during the measurements, x_r^{srVRE} =1.6, which is obtained with a RMS phase current, I_x, of 822 mA, being 25% of the nominal current level. Additionally, the scaled down FW torque, T_{em}^{FW}, is shown for the same per-phase RMS

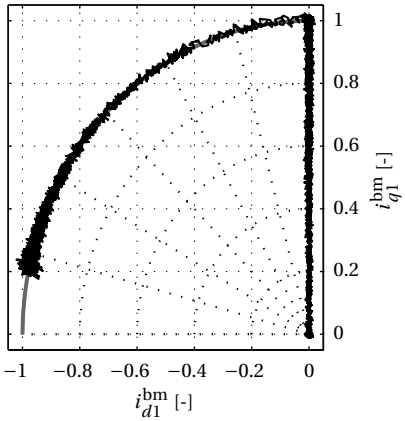

Figure 5.21: XY-plot of the closed-loop current control FW measurement results for $0 \leq \omega_m \leq 269.6$ rad./s; normalized fundamental frequency BM q-axis current, i_{q1}^{bm}, versus d-axis current, i_{d1}^{bm} (black) on top of the reference current (grey).

current level. In this way a fair comparison is made between the different methods. By comparing T_{em}^{VRE} and T_{em}^{FW} in Figure 5.24, it is concluded that both the obtainable torque and angular velocity range are larger when applying FW. The ratio between T_{em}^{FW} and T_{em}^{VRE} is a factor 2.1, while the depicted CPSR angular velocity range is a factor 4.2 higher for FW.

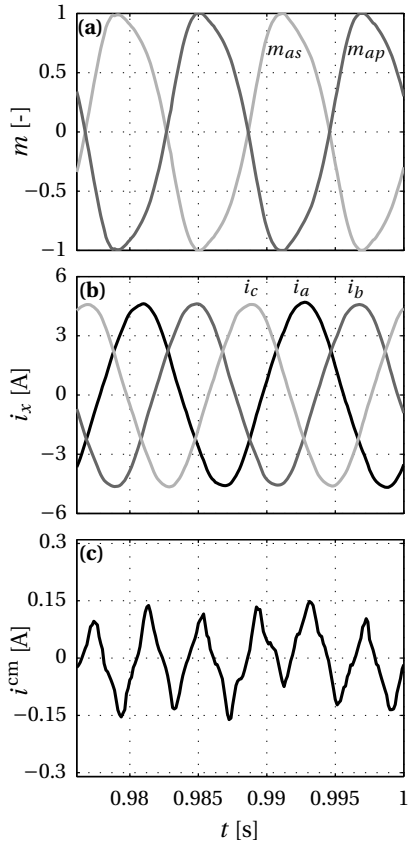

Figure 5.22: Measurement results detail at approximately the series-connected base angular velocity, ω_m=75.6 rad./s; **(a)** per-side VSI phase a modulation signal, $m_{a(p,s)}$, **(b)** per-phase currents, i_x, **(c)** CM current, i^{cm}.

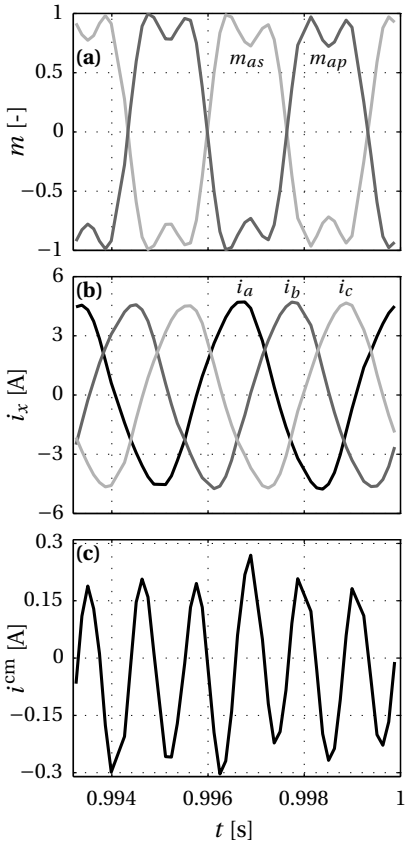

Figure 5.23: Measurement results detail at approximately the series-connected top angular velocity, ω_m=269.6 rad./s; **(a)** per-side VSI phase a modulation signal, $m_{a(p,s)}$, **(b)** per-phase currents, i_x, **(c)** CM current, i^{cm}.

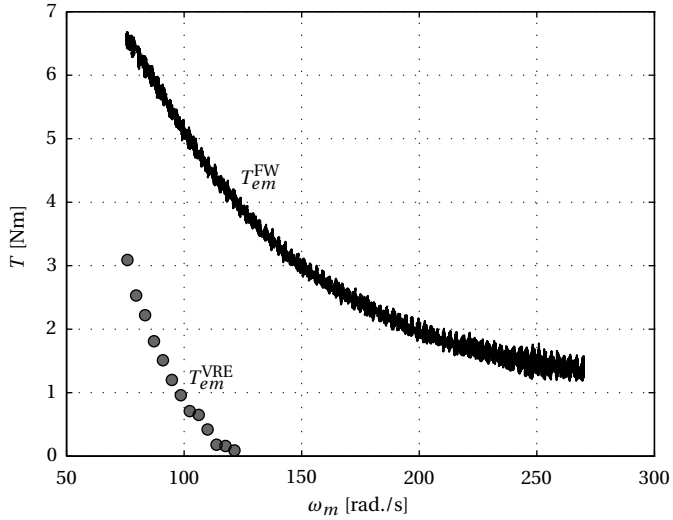

Figure 5.24: Equal RMS current based comparison of the achievable electromagnetic torque, T_{em} per indicated angular velocity range enhancement strategy; VRE torque, T_{em}^{VRE}, and FW torque, T_{em}^{FW}.

5.7 Summary and conclusions

In this chapter, a new concept named voltage range enhancement is presented to improve the operating range of a dual-inverter machine drive system. This is achieved by boosting the supply voltage of one of the inverters, and consequently enhancing the output voltage of the drive. A deliberate insertion of a third-harmonic common-mode current is used to alter the supply voltage of one of the inverters, thereby using the open-ended machine windings. The balanced-mode fundamental frequency current produces the machine torque.

The principle of operation of the voltage range enhancement concept is detailed for an idealized electrical machine, after which the theory is extended for a more practical machine type, such as electrical machine B. Furthermore, a topology is proposed to apply both the dynamic drive operation and voltage range enhancement principles to a multiple windings per-phase open-winding machine. The introduced concept is verified in simulations as well as experiments. Especially for electrical machines that are unsuitable for field weakening operation by cause of construction, voltage range enhancement provides a type independent alternative to extend the angular velocity range.

Relying on the aforementioned results, it is concluded that the voltage range enhance-

ment principle works as intended. Based on the minimized current strategy, an efficient method to combine harmonics is devised, capable of achieving a theoretical machine efficiency of 95.7% at the tested point, when solely considering the resistive losses. The idea of separating the different functions of the dual-inverter drive system works in principle. The secondary-side inverter is powered by the third-harmonic common-mode current while the machine is powered the conventional manner by the fundamental frequency balanced-mode current. From the optimization and experimental verification it is concluded that an angular velocity ratio improvement of a factor 1.6 is obtained in the practical case.

The voltage range enhancement concept is not as effective as field weakening in improving the angular velocity range of machine B. Both in the achieved torque range as well as the achieved angular velocity range, field weakening is superior to voltage range enhancement for the system configuration applied here. The assumptions used to maximize the efficiency with which voltage range enhancement is executed limit the achieved operating range. Furthermore, the compared performance at equal loading shows that field weakening remains the preferred solution.

The nominal machine current level is not reached when applying voltage range enhancement due to the stringent assumptions. The assumptions by which the concept operation is optimized can be relaxed to extend the current usage and improve the torque and angular velocity range accordingly. The interaction between the third-harmonic EMF and the third-harmonic boosting current introduces unfavourable third-harmonic torque components that produce vibrations and increase the drive losses by reducing the effective output torque.

Considering the solely feed-forward based control, the per-harmonic current component reference levels could not be reached because no independent per-component regulation is possible. The intended secondary-side power balance was therefore not obtained in the measurements, when compared to the simulations.

Voltage range enhancement provides an alternative method to extend the angular velocity range of a drive system above the base angular velocity, as strived for in the objectives and demonstrated in the experimental verification. Consequently, the EMF voltage is not elevated to a level higher than the combined semiconductor breakdown voltages. This potentially avoids a system failure or shutdown in case of irregularities, as strived for in the research objectives.

6

Fault-tolerant operation

"Re-balance by unbalancing"

Abstract: *A fault-tolerant operation method is presented to increase the reliability of the dynamic drive concept compared to a conventional drive system. The increased number of semiconductor devices and connection leads, required for dynamic drive operation, increase the risk of a failure. The modular power electronics structure is used beneficially to re-balance the torque after a failure by applying unbalanced phase currents to the open-winding machine structure. As a result of this method, continued operation with a minimum performance reduction is guaranteed while the reliability is improved since no single component is essential for the drive operation. For the applied two-windings per-phase machine configuration, a possible single module fault scenario is shown, during which continued operation with 80% of the nominal torque is demonstrated. The accompanying theoretical analysis of the fault scenario is presented, while simulations and experiments are executed to show the validity of the method.*

Parts of this chapter are published in:

- T. Gerrits, C. G. E. Wijnands, J. J. H. Paulides, and J. L. Duarte, "Fault-tolerant operation of a fully electric gearbox equivalent," in *IECON 2011 - 37th Annual Conference on IEEE Industrial Electronics Society*, November 2011, pp. 3686 –3691
- T. Gerrits, C. G. E. Wijnands, J. J. H. Paulides, and J. L. Duarte, "Fault-tolerant operation of a fully electric gearbox equivalent," in *Industry Applications, IEEE Transactions on*, vol. 48, no. 6, November - December 2012, pp. 1855 – 1865

6.1 Introduction

Vehicle reliability and "limp home" functionality are important considerations for the automotive industry. For example, by allowing drivers to autonomously replace a flat tyre or a malfunctioning light-bulb, a safe continuation of the journey is guaranteed.

In literature, different definitions of redundancy exist. Throughout this work, a dictionary definition [111] is applied which is stated here to avoid misconception: *redundancy; the inclusion of extra components which are not strictly necessary to functioning, in case of failure in other components.* The cost and success rate of adding redundancy to a certain system is different when comparing the hardware and software of a drive system, for the risk of occurrence is also very different [15]. Applying modularity is essentially a non-redundant solution to improve the reliability of both hardware [92] and software [26] based systems. Within electro-mechanics and power electronics for drives, this topic is covered in fault-tolerant operation (FTO) of VSI topologies in combination with a multi-winding electrical machine. A clear distinction should be made between drives with redundancy, modularity, or redundancy and modularity.

Solely redundant topologies are equipped with additional components to allow for continued post-failure operation [13, 14, 96, 148]. However, in [13, 14, 96] the post-failure output torque of the electrical machine is equal to that during healthy operation. This is achieved by increasing the per-phase current in the viable windings. Assuming that the electrical machine is normally operated at the nominal torque, this results in undesired local overheating of the still functioning windings after the fault. The solely modular topologies employ each module during healthy operation, enforcing a performance derating and different control method after a failure [51, 53, 59, 62]. In order to guarantee continued post-failure behaviour without output performance degradation, redundancy and modularity are combined by using more modules than required for healthy operation [98]. The preferred FTO strategy is mainly dependent on the application for which the system is designed. Vehicle weight and overall costs are important parameters for the automotive industry, while a (temporary) performance degradation is considered less decisive. Drive system redundancy is undesired for the increased weight, component count and thus costs. A strictly modular fault-tolerant traction drive is therefore preferred, as mentioned in Chapter 1. Additionally, modular solutions can cope with the occurrence of multiple failures by applying a control method that optimizes the system performance based on the modules still functioning [62].

In [167] various FTO strategies are compared, based on the number of redundant components. The three-phase open-winding FB per-phase topology[1] is the only mentioned fault-tolerant solution without redundancy. However, due to the single winding per-phase structure, only a single fault is allowed to occur, while the post-failure performance is only 58% of the nominal torque, $\check{T}$. By increasing the number of windings

[1] Named cascaded inverter topology in [167].

per-phase, the relative performance reduction is lowered, as suggested in [79]. Alternatively, the same effect is achieved by increasing the number of machine phases ($x > 3$) powered by a HB switching-leg per-phase [93, 117]. With the five-phase drive system proposed in [117], the machine can still be operated after losing two phases without adding redundancy, as required in conventional three-phase drives. However, the main disadvantage of an x-phase ($x > 3$) drive is that it is not modular and unsuitable for the dynamic drive operation principle introduced in Chapter 3. In [64, 100] a modular FTO machine-winding concept based on separate power electronics systems is proposed. The idea is that by avoiding mutual dependency between each combination of two windings, they are electrically, magnetically, thermally, and physically independent of one another. This is achieved mainly by applying concentrated windings in an alternate-teeth wound stator configuration, where each of the six windings is powered by a FB inverter. In this way, the machine windings are uncoupled and the system is considered as multiple independent simplex systems rather than one multiplex system [65], improving fault-handling capabilities.

The modular drive structure, introduced for DDO in Chapter 3, is used advantageously to continue operation after a fault occurrence. In this chapter, it is demonstrated that the produced post-failure torque of a two-windings per-phase electrical machine (described in Appendix C) is significantly improved compared to a single-winding per-phase electrical machine. The possible failure situations that are considered, and the consequences to the performance of the drive-system are described. A method to cope with a single module breakdown is proposed, and validated experimentally.

6.2 Failure possibilities and consequences

An effective FTO circuit utilizes all components and has no redundant parts during healthy operation. In case of failure of one or more system components, only the faulty parts should be inactivated. Ideally, all functioning components should keep working, ensuring a minimized performance derating after isolating the fault, as investigated in [62]. The drive system should be designed for fast detection and response to various open-circuit and short-circuit fault conditions to ensure correct operation of the remaining modules. A fault can be detected for example by comparing the measured per-winding currents of a phase amongst each other or to a reference value. However, fault detection is not considered in this research.

The considered per-module faults are the four most plausible situations, i.e. single device open-circuit, single device short-circuit, leg short-circuit, and single winding open-circuit, as explained in [167]. For the modular dynamic drive shown in Figure 3.3, this implicates that there are 7 unique failure possibilities that should be accounted for, as illustrated in Figure 6.1. Firstly, there are the failure possibilities to the HB switching leg devices S_x, which are the device open-circuit in Figure 6.1a, the device short-circuit

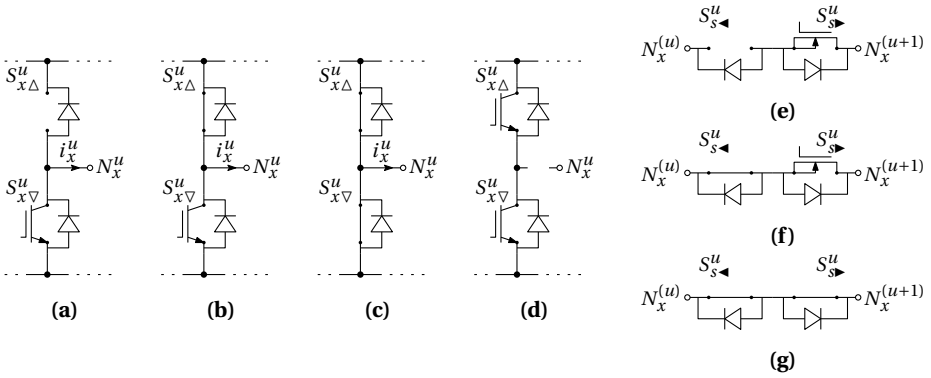

Figure 6.1: Schematic representation of the different investigated fault situations; **(a)** switching-leg, S^u_x, device, $\triangle$, open-circuit, **(b)** $S^u_{x\triangle}$ short-circuit, **(c)** S^u_x cross-conduction short-circuit, **(d)** winding, N^u_x, open-circuit (internal or external), **(e)** series switch, S^u_s, device, $\blacktriangleleft$, open-circuit, **(f)** $S^u_{s\blacktriangleleft}$ short-circuit, **(g)** S^u_s short-circuit.

in Figure 6.1b, and the leg short-circuit in Figure 6.1c. Secondly, a winding, or winding connection lead, can break due to mechanical and/or thermal stresses, leading to a winding open-circuit as depicted in Figure 6.1d. Thirdly, the same failure possibilities considered for S_x can also occur to the series switch, S_s, devices. This are the device open-circuit in Figure 6.1e, the device short-circuit in Figure 6.1f, and the switch short-circuit in Figure 6.1g.

6.2.1 Switching leg faults

The IGBT is the preferred semiconductor type in modern drives for their robustness and short-circuit turn off capabilities [160], and if required, a defined conductive post-failure status [60]. In a MOSFET based drive, it is more complex to realize fail-safe operation [134]. The IGBT properties are used beneficially to preserve the possibility to turn off a complete FB module if a single device in that module fails. Since the IGBT based switching leg is considered, the anti-parallel diode is a separate device. Breakdown of the diode is not considered in this analysis, which therefore remains viable after failure of a switch.

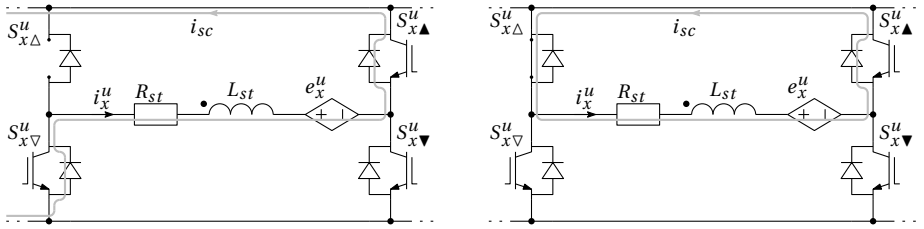

Figure 6.2: Schematic representation of two different fault situations leading to an unipolar diode conduction short-circuit current, i_{sc}, both caused by a failure of switching-leg device $S^u_{x\triangle}$, where the peak value and shape of i_{sc} is determined by the EMF voltage, e^u_x, and the winding impedance; **(a)** DC supply short-circuit fault caused by the open-circuit failure of $S^u_{x\triangle}$ thereby making the application of a flux-linkage manipulation method impossible, **(b)** winding short-circuit fault caused by the short-circuit failure of $S^u_{x\triangle}$.

Open-circuit device fault

The open-circuit fault of device $S^u_{x\triangle}$ shown in Figure 6.1a is isolated by turning the other three devices of that module in tri-state (permanently off). The winding current, i^u_x, becomes uncontrollable as a consequence of the faulty device, as denoted with the short-circuit current, i_{sc}, in Figure 6.2a. This means that VRE, FW, or other flux-linkage manipulation methods are not possible, prematurely limiting ω_m. Considering that the viable windings of faulty phase x are powered individually, i_{sc} in the faulty module remains zero until the EMF voltage, e^u_x, becomes larger than the inverter supply voltage, V_{inv}, and the conduction voltage of the anti-parallel diodes, V_{CE}, combined. From this, the short-circuit angular velocity, ω_{sc}, at which the diodes start to conduct i_{sc} is computed with

$$\omega_{sc} = \frac{V_{inv} + 2V_{CE}}{K_e} \tag{6.1}$$

Short-circuit device fault

A short-circuit fault of device $S^u_{x\triangle}$ shown in Figure 6.1b requires a different approach as suggested in [100]. Since only the electrical machine winding impedance is connected across e^u_x, an unipolar i_{sc} is generated and conducted by the diode of switch $S^u_{x\blacktriangle}$, as depicted in Figure 6.2b. The exact shape and amplitude of i_{sc} naturally depend on R_{st}, L_{st}, e^u_x, and therefore on ω_m. The relatively high value of L_{st}, applied for DDO, minimizes i_{sc} for a given ω_m as demonstrated in [100]. Within the CS of the drive, no further measures can be taken to reduce i_{sc} since the active devices do not conduct current. A

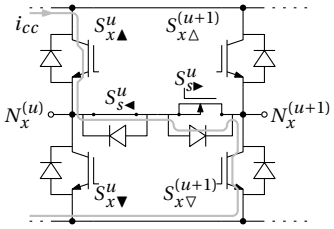

Figure 6.3: Schematic representation of a cross-conduction current, i_{cc}, caused by the short-circuit failure of series switch, S^u_s, device, ◄.

mechanical disconnection of either N^u_x or the return path of i_{sc} is subsequently required to diminish i_{sc}.

Short-circuit switching leg fault

It is assumed that the viable S_x device forming a HB switching leg with a faulty S_x device is turned off while conducting the cross-conduction short-circuit current, i_{cc}. Therefore, the fault illustrated in Figure 6.1c is accommodated for by turning the viable device of that leg in tri-state. The possibility that both devices in a leg simultaneously break down is not considered since this is prevented with the anti-parallel diode in case of an over-voltage and by the turn off capability in case of i_{sc}. Therefore, it is assumed that a switching-leg cross-conduction short-circuit must be treated as a device short-circuit.

6.2.2 Winding open-circuit fault

An internal or external open-circuit fault of an electrical machine winding (Figure 6.1d) naturally gives the advantage of fault propagation avoidance. Therefore, the post-failure solution is to turn the switches of the module containing the faulty winding to tri-state and subsequently drive the remaining viable windings of that phase in FBI drive mode, or an intermediate drive mode.

6.2.3 Series switch faults

In Chapter 4, the preferred device type to implement S_s is determined to be a MOSFET. However, the approach to accommodate a single device or complete S_s failure is not fundamentally dependent of the applied semiconductor device-type.

Open-circuit device fault

In the presented S_s design, multiple devices are connected in parallel (Figure 4.1a) to reduce the on-state resistance. Therefore, after an open-circuit failure of one device (Figure 6.1e), the other (parallel) device can safeguard the continued operation of S_s, provided that no thermal runaway occurs. In the case of a resulting thermal instability, the faulty S_s is turned to tri-state, while the windings of the concerning phase x are powered in the FBI drive mode, or an intermediate drive mode[2]. The latter solution is the only possibility if no parallel devices are used or if the RB IGBT based S_s solution is applied, as depicted in Figure 4.1b.

Short-circuit device fault

When observing the intended S_s^u behaviour, a device short-circuit failure (Figure 6.1f) directly leads to a cross-conduction current, i_{cc}, if the adjoint S_x devices start switching. This effect, as shown in Figure 6.3, occurs after a drive configuration change, enabling the depicted S_x devices, i.e. $S^u_{x(\blacktriangle,\blacktriangledown)}, S^{(u+1)}_{x(\triangle,\triangledown)}$. Considering that the S_x devices are turned off while conducting i_{cc}, this fault is isolated by changing the state of $S^u_{x(\blacktriangle,\blacktriangledown)}, S^{(u+1)}_{x(\triangle,\triangledown)}$ to tri-state, turn S_s device $S_{s\blacktriangleright}$ on, and continue operation in the FBS drive mode, or an intermediate drive mode[2]. Since the FBI drive mode cannot be used anymore, ω_m is limited.

Short-circuit switch fault

As depicted in Figure 6.3, turning on device $S_{s\blacktriangleright}$ does not influence the indicated cross-conduction fault. The S_s short-circuit failure (Figure 6.1g) is therefore treated equal to the aforementioned S_s device short-circuit. Subsequently, the drive operation is continued in the FBS drive mode, or an intermediate drive mode[2].

6.2.4 Conclusions on modular drive fault-handling

For each of the considered failures, a fault-handling method is proposed. In contradiction to previously presented work, no redundancy in terms of for example, fuses, switching legs, or TRIACs is required to make the drive fault-tolerant. Within each described fault, either a machine winding impedance is limiting the short-circuit current or the faulty situation is ended by disabling a FB switch module. The relatively high winding impedance as applied for DDO works beneficially to minimize the short-circuit

[2]Depending on the position of the faulty S_s in the drive system and the total number of three-phase winding sets of the considered system.

current. In the following, a method is presented to continue operation after a failure solely requiring adaptations to the drive CS.

6.3 Fault-handling strategy

In contradiction to the six-phase modularity proposed in [64, 100], the three-phase, two-windings per-phase based drive system operated with the DDO method proposed in Chapter 3 is applied here. The advantages of the DDO principle over the modular six-phase system are enunciated in Part I. The assumed post-failure situation is that module $a\mathrm{I}$, powering winding A^{I} in Figure C.2b, is unusable as indicated in Figure 6.4a. This situation is caused by for example a device or winding open-circuit fault, as indicated in Figure 6.1a, d. Due to this, the winding current in the faulty module, i_a^{I}, is assumed to be zero. The viable winding A^{II} is therefore powered in the FBI drive mode, while the windings of phases b, c are powered in the FBS drive mode. No higher-harmonic current components are considered in the presented analysis, as indicated in Figure 6.4. The equations related to the fundamental frequency quantities of the electrical machine are therefore applicable.

The mechanical displacement between the per-phase windings is fixed, thus the mutual angle between the phase currents i_a, i_b, i_c should be adapted to re-balance T_{em}, and avoid torque ripples due to the unbalanced drive system. The current through the viable windings should be adapted such, that the post-failure torque, T_{em}^{f}, is optimized without increasing any of the per-winding currents above their nominal value to avoid local overheating. The general solution to cope with any of the aforementioned failures is to unbalance the phase currents to compensate for the unbalanced magnetomotive force (MMF) space vector distribution of the viable windings. An alternative solution is to solely continue operation with the viable three-phase winding set, halving T_{em}. The approach chosen here is to optimize T_{em} by employing each viable winding.

6.3.1 Phasor adaption

Prior to the fault, the nominal per-winding fundamental frequency current phasors, as indicated per-set I, II, and per-phase a, b, c in Figure 6.4b, produce a balanced healthy torque, T_{em}^{h}, by interaction with the corresponding flux-linkage induced in the respective per-set I, II, per-phase A, B, C windings, as described in (2.50). The spacial equivalent of the BM current phasors in Figure 6.4b is the healthy situation fundamental frequency MMF current space vector, $\vec{\imath}_1^{\mathrm{h}}$, as indicated in Figure 6.4a. If the fault in module A^{I}, indicated in Figure 6.4a, is not compensated, the post-failure fundamental frequency MMF current space vector, $\vec{\imath}_1^{\mathrm{f}}$, contains a time-variant part, leading to a time-variant T_{em}^{f}. To avoid local electrical machine overheating in steady state, an increase of the phasor

amplitude above the nominal value is not considered. Alternatively, the phase angle, ϕ_1', of the viable phases b,c current phasors is adjusted to re-balance T_{em}^{f}.

To produce a constant $\left|\vec{\imath}_1^{\mathrm{f}}\right|$, a set of BM per-phase current phasors with reduced amplitude is constructed, as indicated with $\underline{I}_{x1}'$ in Figure 6.4c. However, since this amplitude is over the nominal value in phase a and under the nominal value in phases b,c, an additional CM current phasor, $\underline{I}_1^{\mathrm{cm}}$, is added. In this way, the per-winding amplitude requirement is satisfied for this scenario, thereby compensating the inadequacy of phase a with phases b,c. In Figure 6.4c, the link between the per-mode and the per-winding current phasors is visualized. The inner dashed circle of $\vec{\imath}_1^{\mathrm{f}}$ in Figure 6.4a is represented by the inner dashed circle in Figure 6.4c, which is composed of the BM phasors $\underline{I}_{x1}'$. To match the outer dashed circle of $\vec{\imath}_1^{\mathrm{h}}$ in Figure 6.4a with the combined winding currents of phases b,c, being $\underline{I}_{b1}^{(\mathrm{I}+\mathrm{II})\prime}$, $\underline{I}_{c1}^{(\mathrm{I}+\mathrm{II})\prime}$, CM current phasor $\underline{I}_1^{\mathrm{cm}}$ is added such that the per-winding amplitude corresponds to the intended nominal value. Solely an angular shift of phases b,c is required, as indicated with ϕ_1' in Figure 6.4d. As a result, the machine is re-balanced, and satisfactory operation of the electrical machine is achieved. The CM current phasors $\underline{I}_1^{\mathrm{cm}}$ produce no time-variant torque because each phasor by definition interacts only with the BM fundamental frequency magnet flux-linkage, Λ_m.

6.3.2 Analysis

The shifted current angle ϕ_1', necessary to achieve smooth torque operation, can be determined in various ways, for example by computing the instantaneous torque and vanishing the time-variant component. In the following, however, the angle is computed using goniometric formulae based on the representation in Figure 6.4. The phasors projected on the $\Re$-axis, aligned with the magnetic axis of phase a (α-axis in Figure 6.4a), represent the instantaneous current values.

By applying the following normalization for healthy operation (Figure 6.4b):

$$\|\underline{I}_{a1}^{\mathrm{I}}\| = \|\underline{I}_{a1}^{\mathrm{II}}\| = \|\underline{I}_{b1}^{\mathrm{I}}\| = \|\underline{I}_{b1}^{\mathrm{II}}\| = \|\underline{I}_{c1}^{\mathrm{I}}\| = \|\underline{I}_{c1}^{\mathrm{II}}\| = 1, \tag{6.2}$$

$$\|\underline{I}_{a1}\| = \|\underline{I}_{b1}\| = \|\underline{I}_{c1}\| = 2, \tag{6.3}$$

and for the considered FTO scenario (Figures 6.4c, 6.4d):

$$\underline{I}_{a1}^{\mathrm{I}\prime} = 0, \tag{6.4}$$

$$\underline{I}_{a1}^{\mathrm{II}\prime} = \underline{I}_{a1}^{\mathrm{II}}, \tag{6.5}$$

$$\|\underline{I}_{b1}^{\mathrm{I}\prime}\| = \|\underline{I}_{b1}^{\mathrm{II}\prime}\| = \|\underline{I}_{c1}^{\mathrm{I}\prime}\| = \|\underline{I}_{c1}^{\mathrm{II}\prime}\| = 1, \tag{6.6}$$

$$\|\underline{I}_{a1}'\| = \|\underline{I}_{b1}'\| = \|\underline{I}_{c1}'\| = \Gamma, \tag{6.7}$$

with Γ being the normalized per-phase current phasor amplitude in faulty operation. Subsequently, the angle of phases b,c with the $\Im$-axis, being ϕ_1', and Γ is derived by

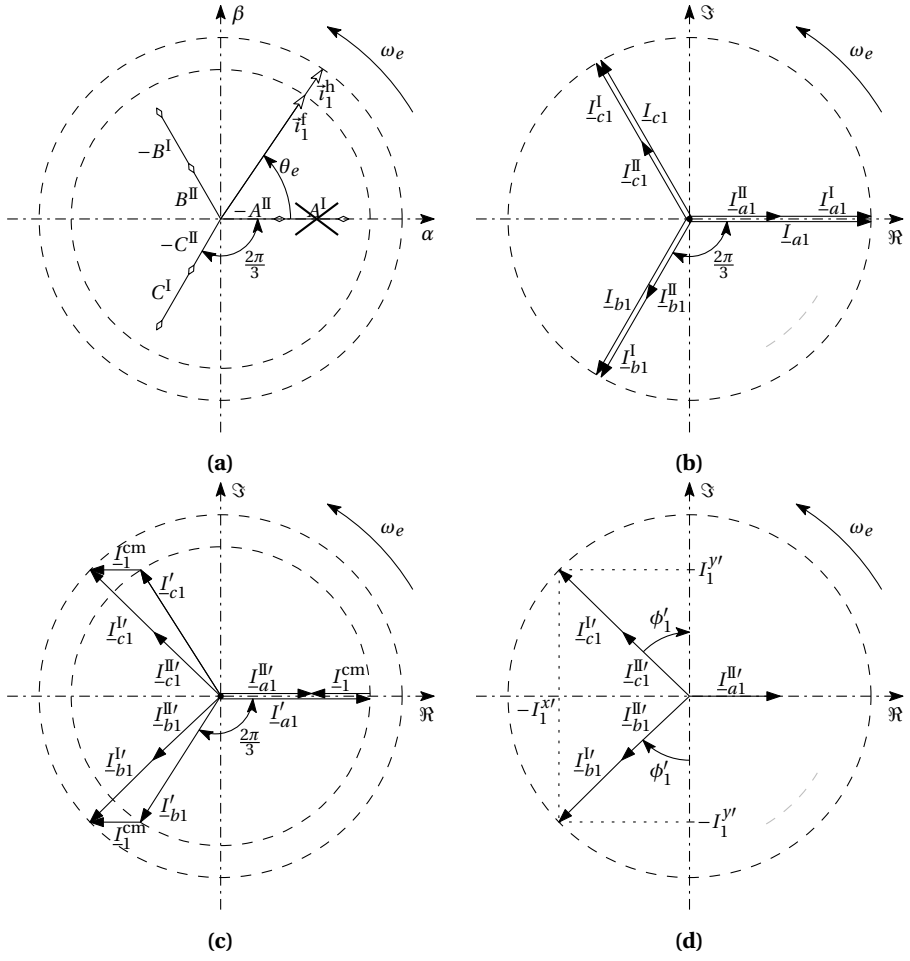

Figure 6.4: **(a)** MMF space vector representation of the machine stator windings with indicated module A^{I} failure and the resulting balanced fundamental frequency current space vector in healthy, $\vec{\imath}_1^{\,\mathrm{h}}$, and faulty, $\vec{\imath}_1^{\,\mathrm{f}}$, condition, **(b)** per-set per-winding and combined per-phase fundamental frequency BM current phasors, $\underline{I}_{x1}$, related to MMF space vector $\vec{\imath}_1^{\,\mathrm{h}}$ in **(a)**, **(c)** intended per-phase fundamental frequency BM current phasors, $\underline{I}'_{x1}$, related to MMF space vector $\vec{\imath}_1^{\,\mathrm{f}}$ in **(a)**, and required fundamental frequency CM current phasors, $\underline{I}_1^{\mathrm{cm}}$, to match the available per-winding current phasors with altered phase angles, **(d)** the per-winding fundamental frequency current phasors of viable modules with indicated adapted phase-shift to phases b, c, i.e. the phase-shift ϕ'_1, and per-phase per-axis projections on $(\Re, \Im)$ as (x, jy).

solving

$$\|\underline{I}_1^{\mathrm{cm}}\| = 1-\Gamma, \tag{6.8}$$

$$\|I_1^{x\prime}\| = 2\sin\left(\phi_1'\right), \tag{6.9}$$

$$\|I_1^{y\prime}\| = 2\cos\left(\phi_1'\right) = \Gamma\sin\left(\tfrac{\pi}{3}\right), \tag{6.10}$$

$$\|I_1^{x'}\| = \|\underline{I}_1^{\mathrm{cm}}\| + \Gamma\cos\left(\tfrac{\pi}{3}\right), \tag{6.11}$$

where $I_1^{(x,y)\prime}$ are the projections of both $\underline{I}_{b1}^{(\mathrm{I}+\mathrm{II})\prime}$ and $\underline{I}_{c1}^{(\mathrm{I}+\mathrm{II})\prime}$ on the $(\Re,\Im)$-axis, respectively, as indicated in Figure 6.4d. Consequently, for the presented FTO scenario; $\phi_1' = 0.795$ rad., and $\Gamma = 1.618$. With respect to T_{em}^{h}, the relative post-failure torque T_{em}^{f}, during the illustrated single module FTO scenario presented here, is

$$\frac{T_{em}^{\mathrm{f}}}{T_{em}^{\mathrm{h}}} = \frac{\Gamma}{2} = 0.809. \tag{6.12}$$

From (6.12) it is concluded that during a single module failure, the ideally achievable output torque is 80.9% of the healthy operation torque, if the nominal currents (6.5), (6.6), and the proposed compensation are applied. Taking into account the decreased current usage of 83.3% of the nominal value (5 out of 6 windings), the expected relative fault situation torque versus a balanced system with the equivalent current is 80.9/83.3 = 97.1%.

The intended CM current phasor

$$\underline{I}_1^{\mathrm{cm}} = (1-\Gamma)\underline{I}_{a1}^{\mathrm{II}\prime}, \tag{6.13}$$

is derived from the measured instantaneous $\underline{I}_{a1}^{\mathrm{II}\prime}$ in accordance with Figure 6.4c. $\underline{I}_1^{\mathrm{cm}}$ compensates for the imbalance of the phase currents. In doing so, a rotating MMF with constant magnitude is produced with unbalanced currents.

6.3.3 Multiple failures

The reliability of a drive is enhanced significantly if multiple faults can be accommodated by reconfiguration of the viable modules [62]. By not only increasing the number of modules in a system, but additionally adapt the configuration after a failure, optimal use is made of the viable modules. The obtainable output power as a function of the number of viable modules is derived in [62]. By applying the CM current as demonstrated in the analysis, the per-fault-scenario resultant T_{em}^{f} is optimized by extending the FTO control strategy using a renewed ϕ adaption. By assuming that faults occur independently and are isolated after occurrence, reconfiguration is repeated and continued operation with a time-invariant T_{em} is achieved until the second last viable module breaks down[3].

[3] Assuming that the last two viable modules are not of equal phase.

6.4 Experimental verification

To verify whether the presented analysis is a correct method to compensate for a single module fault, simulations and experiments were executed. The setup used for the verification is presented in Appendix E, while the parameters of the applied electrical machine A are listed in Appendix C. Within the simulations and experiments, the fault was assumed to be a priori known, no detection is considered therefore. As indicated with the phasors in Figure 6.4d, the respective per-winding currents are equal; $\underline{I}^{\mathrm{I}\prime}_{b1} = \underline{I}^{\mathrm{II}\prime}_{b1}$ and $\underline{I}^{\mathrm{I}\prime}_{c1} = \underline{I}^{\mathrm{II}\prime}_{c1}$. This is assured in the experiments by a series-connected configuration, i.e. FBS operation. To guarantee that the comparison is fair, and the losses in each viable winding of electrical machine A are equal, an equal RMS current was applied in all the simulations and experiments according to Figure 6.4. In the faulty situation, the phase a current is solely that in winding A^{II} as indicated with (6.4) and (6.5).

6.4.1 System configuration and control

The angular velocity of the machine-set, ω_m, was regulated to the intended series-connected base angular velocity, ω_b^{sr}=55 rad./s by the DCM, which is controlled with the MR as indicated in Figure E.1. The electrical machine A torque was regulated by controlling the winding currents in the $(d1,q1)$-axis rotating reference frame. Due to the FBS drive configuration, only a single CS is used for both the healthy and the single module breakdown faulty operation, as depicted in Figure 6.5. The inverter supply voltage, V_{inv}, used for the presented experiments was 300 V. During the test, the nominal electrical machine A torque, $\check{T}$, was applied during healthy operation, $T^{\mathrm{h}}_{em} = \check{T}$, while the reduced post-failure torque $T^{\mathrm{f}}_{em} = \check{T}\Gamma/2$, as derived in (6.12).

To regulate the machine behaviour, the phase currents vector, $\mathbf{i}$ is filtered with a LPF at frequency, f_{LPF} = 5 kHz, and transformed to the rotating orthogonal reference frame based on the angular position, θ_e, using the fundamental frequency transformation matrix $\mathbf{T}_{\equiv\vee}$, as proposed in (B.5). Subsequently, the fundamental frequency BM $(d1,q1)$-axis current components, i_{d1}, i_{q1}, and the CM current component, i^{cm}, are subtracted from their reference value (Figure 6.5). The fundamental frequency $d1$-axis current reference, i^*_{d1}, is zero as the CTSR is used in these experiments. The fundamental frequency $q1$-axis current reference, i^*_{q1}, depends on the torque reference according to (3.19) for either the healthy, $T^{\mathrm{h}*}_{em}$, or the faulty, $T^{\mathrm{f}*}_{em}$, situation. The CM current reference, $i^{\mathrm{cm}*}$, is zero in the healthy situation and depends on $i_a = \underline{I}^{\mathrm{II}\prime}_{a1}$ according to (6.13) in the faulty situation, as indicated with the switch in Figure 6.5. The per-component current error, $\Delta_{d1}, \Delta_{q1}, \Delta^{\mathrm{cm}}$ respectively, is used as input for each respective CS. After the inverse transformation with matrix $\mathbf{T}_{\vee\equiv}$ (B.6), the four PWM signals per-phase, $s_x, x \in [a,b,c]$, are computed by discrete-time comparison of the per-phase modulation signals, m_x, with the triangular reference signal at switching frequency, $f_{sw} = (T_s)^{-1}$.

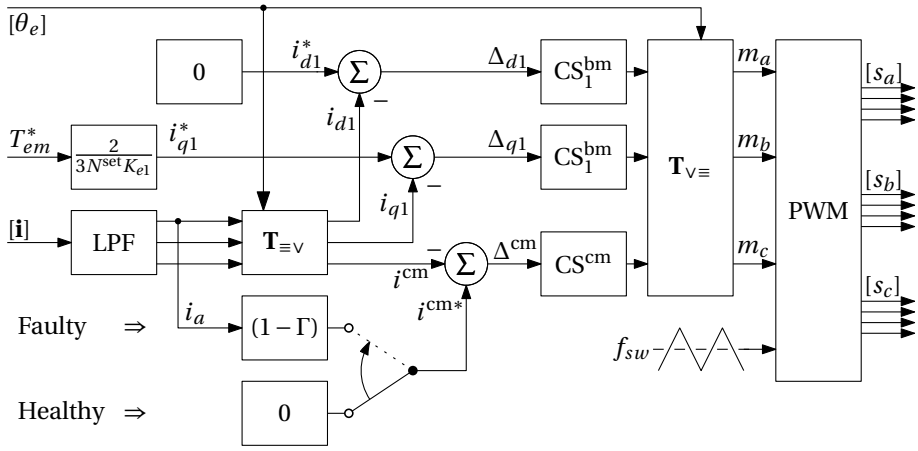

Figure 6.5: Block diagram of the CS used to regulate the FTO drive system BM and CM currents.

6.4.2 Simulations

The principle explained in the analysis and illustrated in Figure 6.4 was verified with simulations in MATLAB/SIMULINK. Using θ_e and ω_m, the per-viable-winding current, i_x, as indicated for the healthy situation in Figure 6.4b and for the faulty situation in Figure 6.4d is constructed. The BM and CM components are separated from i_x using the CM definition in (2.28), as shown with $i_x^{(\mathrm{bm,cm})}$ in Figures 6.6 and 6.7 for the respective situations. Additionally, the $(d1,q1)$-axis BM current components, $i^{\mathrm{bm}}_{d1}, i^{\mathrm{bm}}_{q1}$, are derived from i_x by applying the fundamental frequency ($n=1$) BM transformation matrix, $\mathbf{T}^{\mathrm{bm}}_n$ in (2.39), as proposed in Section 2.6.3.

For both the healthy and faulty situation, e_x and T_{em} are firstly derived for an ideal electrical machine with solely a fundamental frequency EMF. Secondly, they are derived for the harmonic components model of electrical machine A as listed in Table C.1. The fundamental frequency e_{x1} and T_{em1} are shown in (a,b), while the electrical machine A harmonic components based e_x and T_{em} are shown in (c,d) of Figures 6.8 and 6.9 for the respective situations.

6.4.3 Experiments

The setup used to test the proposed FTO scenario is depicted in Figure E.2. V_{inv} used for the presented experiments was increased to 317 V, which is slightly higher than the 300 V whereupon the angular velocities are based (Table C.2). This was required to maintain linear PWM operation.

A SIMULINK model is constructed for application with the DSPACE^{TM} interfaced setup, which is controlled from the control-desk user interface. The PWM signals s_x are transferred to the VSIs by an optical interface board, while the measured currents and voltages are filtered with a 5 kHz bandwidth LPF. As a result of the complexity of the compiled model running on the DSPACE system, the required cycle time, T_c, to derive the PWM signals is $T_c = 4T_s$. Since s_x can only be varied once per cycle, this significantly reduces the CS bandwidth. The required PI controller bandwidth of the BM $(d1, q1)$-axis components is low, since in the quasi-steady-state situation of a constant ω_m and T_{em}, their reference value is fixed. However, i^{cm} depends directly on i_a (6.13) as illustrated in Figure 6.5, making the achievable bandwidth of CS$^{\mathrm{cm}}$ crucial in obtaining the destined behaviour.

The measured and subsequently derived signals are shown side-by-side to compare the different situations, with the healthy situation in Figures 6.10 and 6.12, and the faulty situation in Figures 6.11 and 6.13, respectively. An equal BM $q1$-axis reference current in both the healthy (Figure 6.12b) and the faulty situation (Figure 6.13c) is applied during the experiments instead of the reduced BM phasor amplitude as used in the simulations (Figure 6.7d). This difference is accounted for with the reduced overall machine constant, K_e.

6.5 Results

Analysis simulations

In the healthy situation, i_x is balanced. Therefore, i^{cm} and i_{d1}^{bm} are zero, and $i_{q1}^{\mathrm{bm}} = \left|\underline{I}_{x1}^{u}\right|$, as illustrated in Figure 6.6 and phasor representation Figure 6.4b. Consequently, the healthy situation MMF space vector $\overline{i}_1^{\mathrm{h}}$ is position- and time-invariant. The simulations in Figures 6.6 and 6.8 show that for the healthy idealized situation, the per-phase currents i_x (Figure 6.6a) are balanced. The interaction of e_{x1} (Figure 6.8a) with i_x produces a time-invariant torque T_{em1} (Figure 6.8b) according to (2.50). In Figure 6.8c, the healthy case electrical machine A EMF is depicted, as based on the identified harmonic components listed in Table C.1. The interaction of the higher-order EMF harmonics ($n > 1$) with i_x produces a periodic time-variant torque component on top of T_{em1}, together forming T_{em}, as shown in Figure 6.8d.

The simulation results of the introduced single module breakdown scenario are shown in Figures 6.7 and 6.9. In Figure 6.7a, it is shown that i_x are of equal amplitude but their mutual phase angles are not equal. The balanced part of i_x, being i_x^{bm} (Figure 6.7b), shows that the amplitude, $\left|i_x^{\mathrm{bm}}\right| = \Gamma/2\left|\underline{I}'_{x1}\right|$, as intended. Additionally to i_x^{bm}, i_x contains a fundamental frequency CM component (Figure 6.7c) of which the amplitude, $\left|i_x^{\mathrm{cm}}\right| = \Gamma/2\left|\underline{I}_1^{\mathrm{cm}}\right|$, as intended by the phasor representation. The BM phase currents i_x^{bm} are in-phase with e_x, leading to the fundamental frequency $(d1, q1)$-components $i_{d1}^{\mathrm{bm}}, i_{q1}^{\mathrm{bm}}$, as depicted in Figure 6.7d. The EMF experienced by the viable modules of the VSI in faulty operation is shown for solely the fundamental frequency, and all harmonics of electrical machine A in Figure 6.9a,c, respectively. The torque resulting from the interaction of e_x with i_x is illustrated in Figure 6.9b,d for solely the fundamental frequency, and all machine A harmonics, respectively. From the constant T_{em1} it is concluded that a position- and time-invariant faulty situation MMF space vector $\overline{i}_1^{\mathrm{f}}$ is produced with i_x^{bm}. In Figure 6.9d, the influence of the higher-order frequency components additional to T_{em1} is shown for electrical machine A, which is again periodic, as with the healthy situation.

Experiments

The results of the experimental verification are shown in Figures 6.10 to 6.13. The increased inverter supply voltage is required due to the higher than expected winding coupling and resistance, and the reduced voltage produced by the inverter as listed in Table C.2. The increased electrical machine A coupling results in a higher than expected BM inductance, L^{bm}. The EMF voltages shown in Figures 6.10b and 6.11b are measured at $\omega_m = 55$ rad./s in a no-load test. The other measurement figures are based on the indicated loaded tests.

In the healthy situation, the measurement results show a good overall agreement with the simulations, e_x (Figure 6.10b) and ω_m (Figure 6.10c) are as intended. Furthermore, the peak modulation amplitude, $\hat{m}_x$, is close to unity (Figure 6.10a) as intended at the series-connected base angular velocity ω_b^{sr}. The phase currents in Figure 6.12a have the expected nominal magnitude, and a slight phase-angle offset, leading to the transformed BM components $i_{d1}^{\mathrm{bm}}, i_{q1}^{\mathrm{bm}}$ in Figure 6.12b. The discrepancy of $i_{d1}^{\mathrm{bm}}, i_{q1}^{\mathrm{bm}}$ with their respective references, $i_{d1}^{\mathrm{bm}*}, i_{q1}^{\mathrm{bm}*}$, is caused by the small angular position misalignment. The CM current i^{cm} in Figure 6.12c is not completely suppressed by the CS as intended by reference $i^{\mathrm{cm}*}$. This is the result of the time-varying in-product (2.50) of the non-sinusoidal e_x with the sinusoidally destined BM current components. The derived errors between the aimed and actual current values are depicted in Figure 6.12d. Despite achieving the intended nominal current amplitude in Figure 6.12a, the average value of the electrical machine A torque $\langle T_{em}^{\mathrm{h}}\rangle = 56.5$ Nm in Figure 6.10d, which is only 89.8% of $\check{T}$. This difference originates from the reduced i_{q1}^{bm} compared to the measurement results in Chapter 3, leading to a proportionally reduced T_{em}.

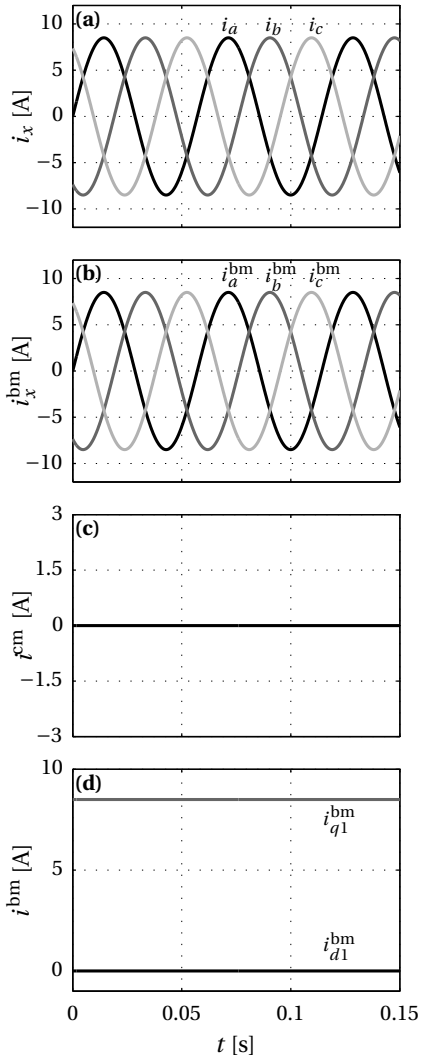

Figure 6.6: Simulation results detail of the healthy situation currents; **(a)** per-phase currents, i_x, **(b)** BM currents, i_x^{bm}, **(c)** CM currents, i^{cm}, **(d)** fundamental frequency BM transformed $(d1,q1)$-axis components, $i_{d1}^{\mathrm{bm}}, i_{q1}^{\mathrm{bm}}$.

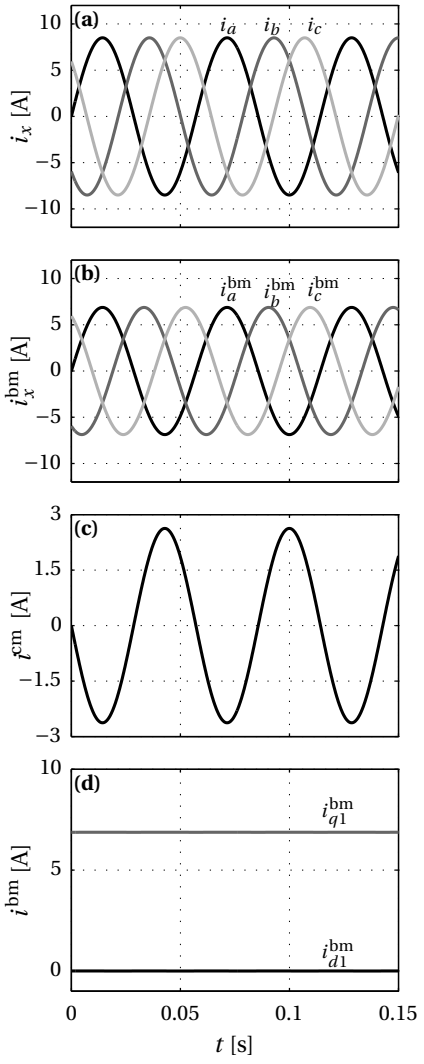

Figure 6.7: Simulation results detail of the faulty situation currents; **(a)** per-phase currents, i_x, **(b)** BM currents, i_x^{bm}, **(c)** CM currents, i^{cm}, **(d)** fundamental frequency BM transformed $(d1,q1)$-axis components, $i_{d1}^{\mathrm{bm}}, i_{q1}^{\mathrm{bm}}$.

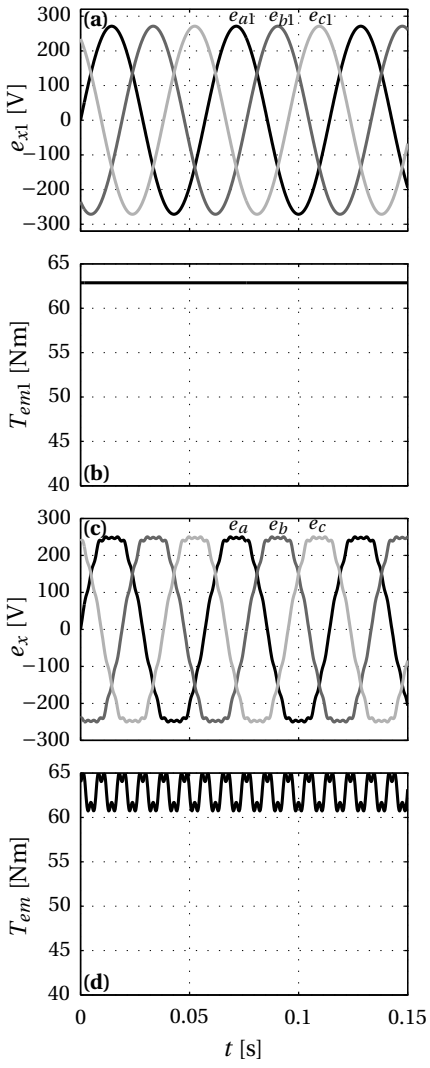

Figure 6.8: Simulation results detail of healthy situation EMF and torque; **(a)** per-phase idealized fundamental frequency EMF, e_{x1}, **(b)** fundamental frequency electromagnetic torque, T_{em1}, **(c)** per-phase EMF, e_x, of electrical machine A, **(d)** electrical machine A electromagnetic torque, T_{em}.

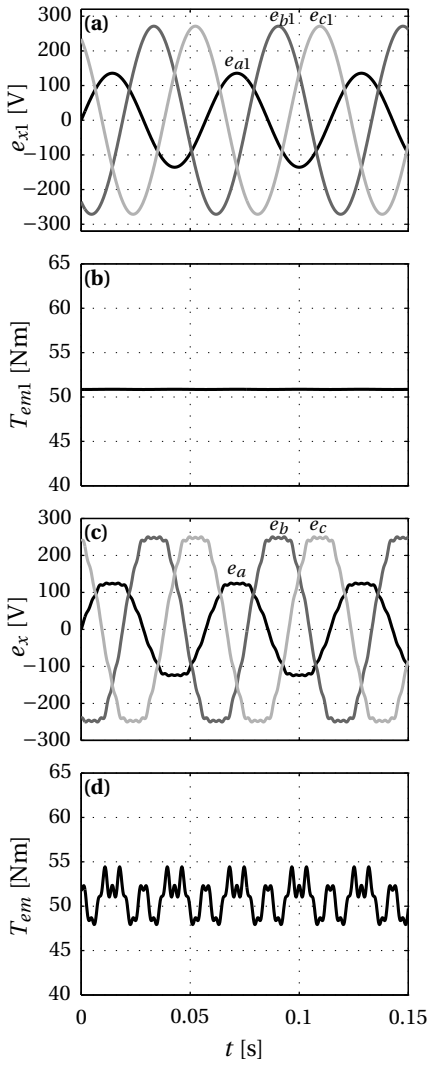

Figure 6.9: Simulation results detail of faulty situation EMF and torque; **(a)** per-phase idealized fundamental frequency EMF, e_{x1}, **(b)** fundamental frequency electromagnetic torque, T_{em1}, **(c)** per-phase EMF, e_x, of electrical machine A, **(d)** electrical machine A electromagnetic torque, T_{em}.

Table 6.1: Measured powers and derived efficiency of electrical machine A

Situation	P_{em} [W]	P_R [W]	P_e [W]	η [%]
Healthy	3245	302	3547	91.5
Faulty	2585	252	2837	91.1

The measurement results of the post-failure situation experiments in Figures 6.11 and 6.13 show a good overall agreement with the simulations and are in agreement with the healthy case. The modulation signal of phase a in Figure 6.11a is proportionally smaller than in Figure 6.10a due to the reduced e_a in Figure 6.11b. The slight ω_m variation of 0.15 rad./s (or 2.7‰) in Figure 6.11c is caused by the minor torque variation in Figure 6.11d. However, this variation is negligible since the torque variation is comparable to that in the simulated (Figure 6.9d) and measured healthy situation (Figure 6.10d). The average T_{em} measured in Figure 6.11d, $\langle T_{em}^{\mathrm{f}} \rangle$ = 44.9 Nm, which is 79.5% of $\langle T_{em}^{\mathrm{h}} \rangle$ in Figure 6.10d. This percentage is slightly lower than the computed 80.9% in (6.12), which is caused by the mean error between $i_{q1}^{\mathrm{bm}*}$ and i_{q1}^{bm}, as illustrated in Figure 6.13b,d. As depicted in Figure 6.13a, the mutual phase-angle difference, as proposed in Figure 6.7a, is not completely achieved. Due to the negative $\langle i^{\mathrm{cm}} \rangle$, the phase currents i_x in Figure 6.13a are shifted downwards. In Figures 6.7a,c it is shown that every other local minimum of $i^{\mathrm{cm}*}$ is only around -1.6 A, instead of the intended -3 A in accordance with (6.13), which is due to the unbalanced i_a. The CS bandwidth required to regulate i^{cm} towards $i^{\mathrm{cm}*}$ in Figure 6.13c is sufficient. The per-component error, Δ, in Figure 6.13d is increased compared to Figure 6.12d. This is mainly due to the shifted offset rather than the intended shifted phase angle.

The efficiency of electrical machine A in the healthy, and the proposed single module faulty operation scenario, is derived from the measurement results, and depicted in Table 6.1. The efficiency, η, is based on the electrical machine A electromagnetic output power, P_{em}, and the resistive losses, P_R, from which the electric input power, P_e is derived. The mechanical friction losses and the hysteresis losses are the same in both configurations since ω_m is fixed, and are therefore not taken into account. From these results, the ratio between the healthy and faulty efficiencies is derived. This ratio is 99.6%, which is higher than the computed 97.1%.

From the experimental verification it is concluded that the proposed method of current phase-angle adaption is suitable to regulate the system. By comparison of Figure 6.8 with Figure 6.9, and subsequently of Figure 6.10 with Figure 6.11, it is concluded that both the control strategy as well as the implementation works as intended. From Figure 6.7b-d, it is concluded that the method of deriving $i^{\mathrm{cm}*}$ based on i_a is not ideal since i_a is both a time- and angular-velocity-variant signal. This limits the control bandwidth of the CM current required to re-balance the drive. By adapting the CS such that the $(d1, q1)$-axis components of both the BM and the CM currents are regulated independently, the destined per-component values are derived independent of ω_m.

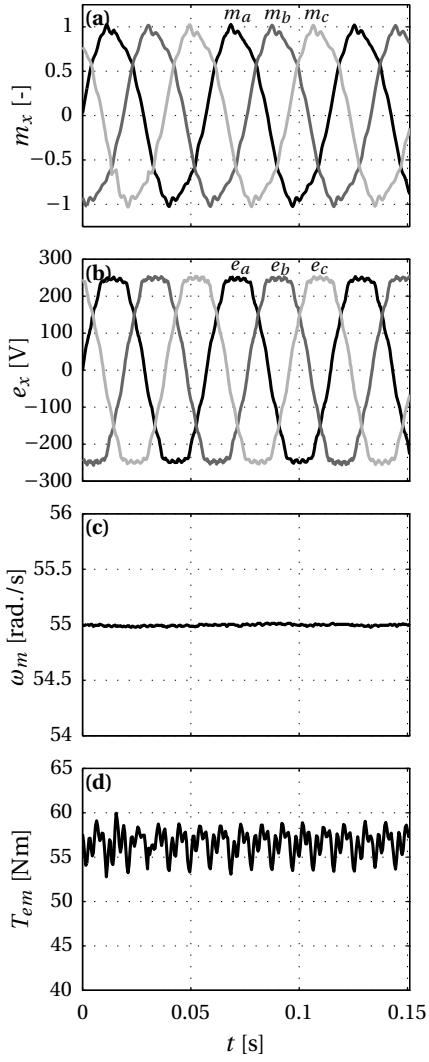

Figure 6.10: Measurement results detail of healthy situation VSI steering and electrical machine A signals; **(a)** per-phase modulation, m_x, **(b)** per-phase EMF, e_x, **(c)** mechanical angular velocity, ω_m, **(d)** electromagnetic torque, T_{em}.

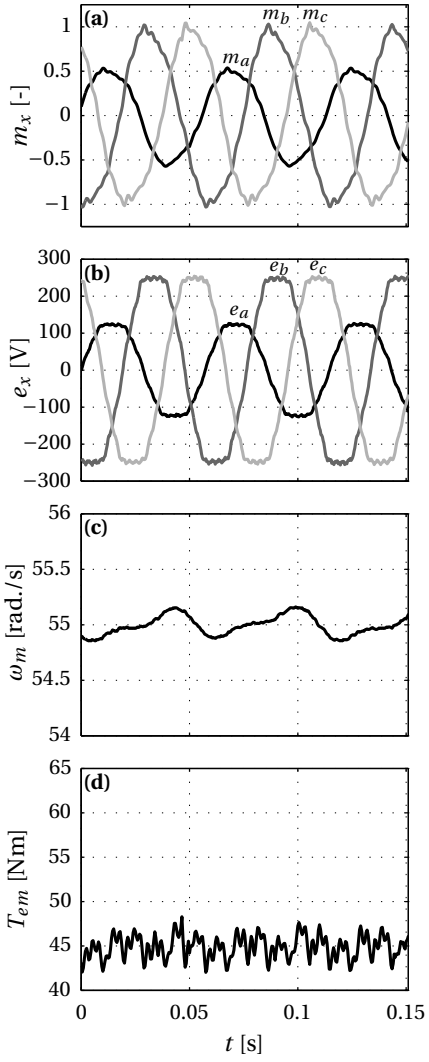

Figure 6.11: Measurement results detail of faulty situation VSI steering and electrical machine A signals; **(a)** per-phase modulation, m_x, **(b)** per-phase EMF, e_x, **(c)** mechanical angular velocity, ω_m, **(d)** electromagnetic torque, T_{em}.

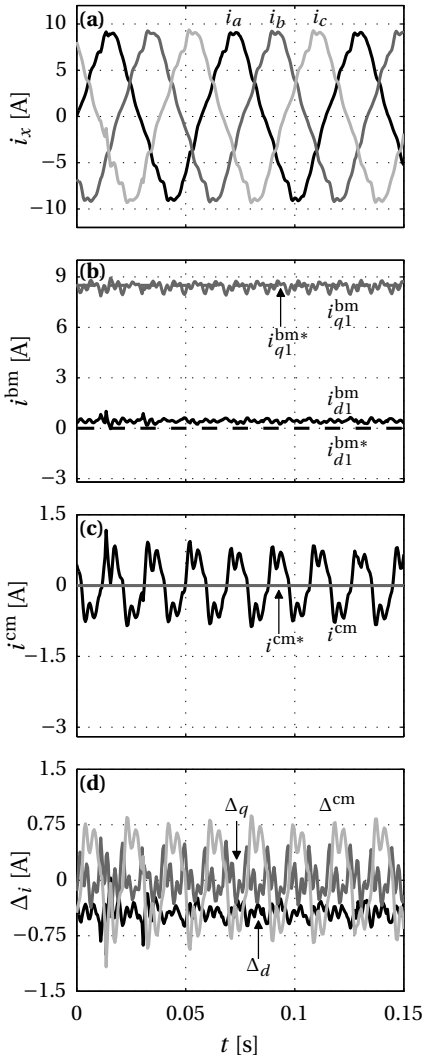

Figure 6.12: Measurement results detail of healthy situation currents; **(a)** per-phase currents, i_x, **(b)** fundamental frequency transformed $(d1,q1)$-axis references and actual currents, $i_{d1}^{\mathrm{bm}*}, i_{q1}^{\mathrm{bm}*}, i_{d1}^{\mathrm{bm}}, i_{q1}^{\mathrm{bm}}$, **(c)** reference and actual CM currents, $i^{\mathrm{cm}}, i^{\mathrm{cm}*}$, **(d)** per-component current error, Δ.

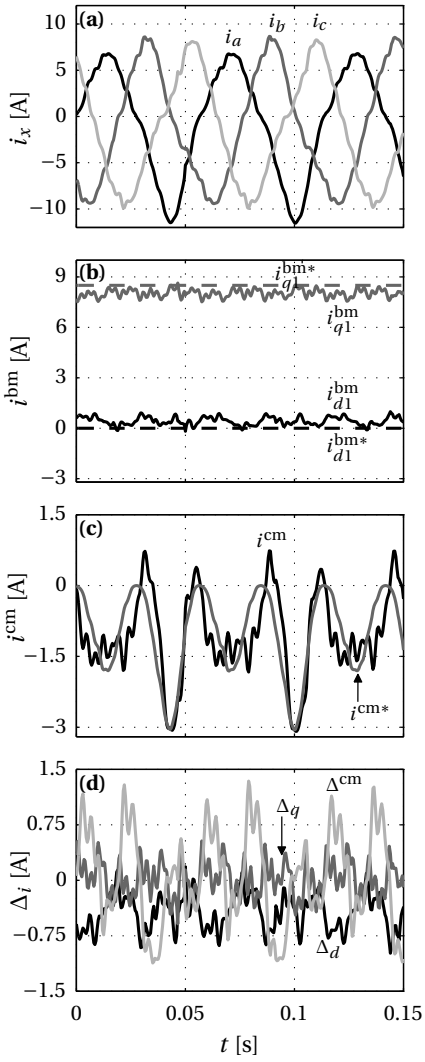

Figure 6.13: Measurement results detail of faulty situation currents; **(a)** per-phase currents, i_x, **(b)** fundamental frequency transformed $(d1,q1)$-axis references and actual currents, $i_{d1}^{\mathrm{bm}*}, i_{q1}^{\mathrm{bm}*}, i_{d1}^{\mathrm{bm}}, i_{q1}^{\mathrm{bm}}$, **(c)** reference and actual CM currents, $i^{\mathrm{cm}}, i^{\mathrm{cm}*}$, **(d)** per-component current error, Δ.

6.6 Summary and conclusions

Modularity defines the system composition applied for the dynamic drive concept as introduced in Part I. Since a vast increase in the number of semiconductor devices is mandatory to implement this concept, the failure possibility of any single device in the system is high, when compared to a standard three-phase drive. The modular drive construction is used beneficially to increase rather than decrease the overall system reliability by means of continued operation with all the viable modules. This is achieved by isolating the faulty module, after which the per-module current angle of each viable winding is adapted to re-balance the magnetomotive force, and with that, the torque produced by the electrical machine. The different plausible failure possibilities of the dynamic drive operation topology are enunciated, a generalized fault handling strategy is proposed, and the viability of this strategy was experimentally verified.

The proposed fault tolerance scenario shows that, in case of a single full-bridge module shutdown, the machine can still be operated with an equal torque ripple, if the angle between the current phasors is adapted. For the addressed single full-bridge module fault scenario, the machine is still capable of delivering 80% of the nominal load torque, $\check{T}$, when the nominal winding currents are applied. This is achieved with a reactive current component of 2.9% of the per-phase current, reducing the measured system efficiency by only 0.4%. This is a significant improvement over the single winding per-phase solution with one faulty winding (58% of $\check{T}$), and the applied dual winding per-phase solution with a complete winding-set shutdown (50% of $\check{T}$) to maintain a constant torque. In contradiction to previously presented fault handling strategies, a continued operation without the need for overloading any of the electrical machine windings is achieved. However, this method comes at the price of increased reactive power flow in the system, reducing the efficiency. But, as computed and shown, the efficiency decrease for the presented single full-bridge module failure is minimized, as derived in the analysis and listed in Table 6.1. Furthermore, this current phase-angle alteration method can be extended to cope with multiple faulty modules. The post-failure performance depends on the sequence of module breakdown. Nevertheless, a per-scenario torque optimization can be derived to offer a drive strategy with each combination of viable drive modules.

From the experimental verification it is concluded that the proposed method of current phase-angle adaption is suitable to regulate the system. Comparing the simulation and measurement results, it is concluded that both the control strategy as well as the implementation works as intended. However, by comparing the simulated with the measured common-mode current, it is concluded that the method of deriving $i^{\mathrm{cm}*}$ based on i_a is not ideal since i_a is both a time- and angular-velocity-variant signal. This limits the control bandwidth of the common-mode current required to re-balance the drive. By adapting the control system such that the $(d1, q1)$-axis components of both the balanced-mode and the common-mode currents are regulated independently, the

destined per-component values can be obtained independent of ω_m, as proposed in Section 2.6.3.

Looking at the objectives of this research, a method should be devised to prevent a total system halt after a failure. This chapter introduces a fault-tolerant operation strategy that covers the decreased reliability caused by the increased switch count of the dynamic drive concept. This is achieved with all the viable modules and without redundancy as strived for. Finally, the experiments verify the simulated concept and thereby the potential success of the method.

Part III

Closing

7

Conclusions and recommendations

"Closing the evolutionary research circle of conception, realisation, and verification"

Abstract: *In this chapter, the main conclusions of this thesis are presented. The significant contributions are listed and their importance is substantiated by the publications. Finally, recommendations for further investigation are given based on the possibilities offered by the proposed system.*

7.1 Conclusions

A generalized modular concept to drive an electrical machine is presented. The reconfigurable character of the proposed traction drive is used to alter the machine winding configuration as a function of the vehicle speed. **The developed fault-tolerant two windings per-phase drive system proves that the operating range and output power of the electrical machine are extended with the dynamic concept (objectives 1-3).** Thereupon, it is concluded that the research goal of improving the drive performance is achieved.

7.1.1 Part I: Dynamic drive operation

In Part I of this thesis, the limitations of a conventional drive system have been examined, existing solutions to cope with the limitations have been investigated, and the dynamic drive operation (DDO) concept has been proposed as alternative solution for electrical vehicle propulsion. **The dynamic drive concept is composed of equal modules with transitional series switches to connect the per-phase winding sections. The isolation between the different per-phase electrical machine winding sections is used beneficially to decouple the per-module AC output voltages. Consequently, the AC output voltage becomes scalable and is increased to multiples of the DC supply voltage using the parallel powered inverter modules (objective 1a,c).** The main limitation of a conventional VSI is the maximum AC voltage it can apply to an electrical machine, thereby limiting the maximum angular velocity. The scalable AC voltage of the dynamic drive eliminates this limitation, improving the obtained angular velocity range (objective 1b).

The dynamic drive system has been compared to a conventional drive configuration for the indicated electrical machine. An absolute angular velocity range improvement of a factor 3.49 is achieved, while the angular velocity ratio is boosted from a factor 1.73 to 3.34. Since the nominal torque is produced until the last base angular velocity, the nominal electromagnetic power is proportionally improved. Subsequently, the applied field weakening (FW) ratio may be reduced to protect the semiconductors (objective 2a). The different operating modes were successfully tested in simulations and experiments, confirming the predicted improvements (objective 3c,d).

Naturally, the dynamic system requires reconfiguration between drive modes. A transition between the two modes of the developed drive system was experimentally verified, thereby demonstrating the dynamic character of the concept (objective 1d). The presented experimental results demonstrate a fast reconfiguration with an 11% relative torque ripple, taking only 8 ms (objective 3c,d). The importance of making the drive system dynamic with the series switches has been confirmed, and a simulated drive loss reduction of 48% was achieved for the presented case.

The proposed alternative stationary two-axis model in combination with the per-mode

per-harmonic regulation and estimation method provides a unified modelling and control technique that allows for a steady state per-component regulation (objective 3a,b). The CS bandwidth is decoupled from the angular velocity of the electrical machine by the transformation in combination with the per-component regulation method. The different drive components are modelled adequately as proven by the uniformity between the simulations and experiments (objective 3d).

7.1.2 Part II: Open-winding concept extensions

The system composition of a modular drive structure consisting of an open-winding electrical machine and matching power electronics provides numerous possibilities for concept extension as explored in Part II. The aim of the extensions is to improve the performance, reliability, and/or versatility of the drive system. Other examples of versatility improvement are given in the recommendations.

To avoid the requirement of FW to improve the angular velocity above the base level, voltage range enhancement (VRE) is proposed (objective 2b). With this new concept, the open-winding machine structure is successfully used to enhance the voltage that is applied to the machine, and with that the drive performance in the form of the angular velocity range. The VRE method has been enunciated, a topology to unify VRE with DDO has been presented, and the VRE concept validity has been confirmed with experiments (objective 3). From the experimental verification it is concluded that an angular velocity ratio improvement of a factor 1.6 is obtained in the practical case, and that a normalized torque of 11.7% of the nominal toque is produced with 25% of the nominal RMS current. Unfortunately, the angular velocity range obtained with FW is higher than that with VRE for the electrical machine used in this research.

The modular system composition is used beneficially to improve the drive reliability, despite the increased component count (objective 2c). **A fault handling control method is proposed to cope with device and/or winding failures, thereby ensuring continued post-failure operation (objective 2d).** The open-winding machine configuration allows for the application of unbalanced per-phase currents in order to re-balance the produced torque at the cost of a small reactive current component. Since only the faulty drive module is halted, and continued operation with all the viable drive modules is realized, an optimized post-failure torque is achieved. The proposed fault-tolerant operation (FTO) concept realizes a measured post-failure torque of 80% of the nominal value when applied to the two windings per-phase drive system. This was achieved without overloading any of the windings, while the reactive current component required to re-balance the torque is 2.9% of the per-phase current. Redundancy is avoided since each viable module is used in both healthy and faulty operation (objective 2e). The experimental verification demonstrates that the proposed method of current phase-angle adaption is suitable to regulate the system (objective 3). Both the control strategy as well as the implementation works as intended.

7.2 Contributions

The main scientific contributions of the work presented in this thesis are:

1. **The development of a reconfigurable power electronic topology to drive an electrical machine composed of multiple three-phase winding sets.** A generalized modular machine drive topology is composed of a full-bridge converter per-winding per-phase complemented with windings series-connection switches to alter the circuit configuration based on the angular velocity. The transition between different operating modes has been tested and the proposed concept is compared to conventional machine drive configurations.

2. **The establishment of a modulation technique to boost the supply voltage of a floating voltage source inverter.** By employing the combined machine magnetizing inductances as boost inductors, a bidirectional DC-DC converter is composed together with the primary- and secondary-side inverters. The floating secondary-side inverter supply voltage is boosted to a higher level than the primary-side voltage using common-mode currents. A common-mode current minimization concept is presented to perform this voltage enhancement principle with minimized losses.

3. **The development of a multiple frequency domains drive concept improving the operating range of an electrical machine.** A machine type independent drive concept employing multiple harmonics of the fundamental machine frequency is introduced. By simultaneously powering the machine with the fundamental frequency and boosting the supply voltage of the floating secondary-side inverter using the third-harmonic, the machine is accelerated above the base angular velocity without employing reactive power on the fundamental frequency.

4. **The realization of a generalized strategy to handle hardware faults without adding redundancy to the system.** To assure reliability, a phase-current adjustment strategy is proposed which re-stabilizes the machine torque and allows for continued operation after system unbalance due to component failure(s).

5. **Unified drive method to regulate the steady state per-harmonic balanced- and common-mode currents for the introduced concepts.** Time- and position independent control is applied at each harmonic of the electrical machine frequency to regulate the alternating phase currents, by combining a rotating orthogonal reference frame transformation with a per-harmonic, per-mode estimation method.

6. **Experimental verification of (1)-(4) in a lab environment.** Two experimental setups have been designed and built to test the behaviour of two custom, two windings per-phase electrical machines. From the experimental results it is concluded that the presented idealized machine modelling technique is adequate to functionally test the proposed concepts.

7.3 Publications

The main results of the work presented in this thesis have been published in journals and are presented at conferences, as listed accordingly:

- T. Gerrits, C. G. E. Wijnands, J. J. H. Paulides, and J. L. Duarte, "Fault-tolerant operation of a fully electric gearbox equivalent," in *Industry Applications, IEEE Transactions on*, vol. 48, no. 6, November - December 2012, pp. 1855 – 1865

- T. Gerrits, C. G. E. Wijnands, J. J. H. Paulides, and J. L. Duarte, "Electrical gearbox equivalent by means of dynamic machine operation," in *Power Electronics and Applications (EPE 2011), Proceedings of the 2011-14th European Conference on*, August - September 2011, pp. 1 –10

- T. Gerrits, C. G. E. Wijnands, J. J. H. Paulides, and J. L. Duarte, "Fault-tolerant operation of a fully electric gearbox equivalent," in *IECON 2011 - 37th Annual Conference on IEEE Industrial Electronics Society*, November 2011, pp. 3686 –3691

- T. Gerrits, C. G. E. Wijnands, J. J. H. Paulides, and J. L. Duarte, "Dual voltage source inverter topology extending machine operating range," in *Energy Conversion Congress and Exposition (ECCE), 2012 IEEE*, September 2012, pp. 2840 –2846

- T. Gerrits, C. G. E. Wijnands, J. J. H. Paulides, and J. L. Duarte, "Loss minimization of boost mode dual inverter drive system," in *Power Electronics and Applications (EPE 2013), Proceedings of the 2013-15th European Conference on*, September 2013

- T. Gerrits, C. G. E. Wijnands, J. J. H. Paulides, and J. L. Duarte, "Dynamic machine operation transitions," in *9th Vehicle Power and Propulsion Conference (VPPC)*. IEEE, October 2013, pp. 132 – 137

- T. Gerrits, C. G. E. Wijnands, J. J. H. Paulides, J. L. Duarte, and E. A. Lomonova, "Machine integrated gearbox for electric vehicles," in *Fisita 2014 - World Automotive Congress*, June 2014, pp. 1–10

- T. Gerrits, J. L. Duarte, C. G. E. Wijnands, E. A. Lomonova, J. J. H. Paulides, and L. Encica, "Twelve-phase open-winding SPMSM development for speed dependent reconfigurable traction drive," in *Proceedings of the Tenth International Conference on Ecological Vehicles and Renewable Energies (EVER)*, 2015

7.4 Recommendations

This thesis proposes a new, unconventional dynamic drive concept with accompanying CS that significantly improves the angular velocity range of an electrical machine. This is especially useful when the drive-line is powered from a fixed DC voltage source, such as a battery. The system reliability is improved and the electrical machine weight for a required output power is reduced. Nevertheless, there is room for further improvements. Recommendations for further research could be as follows.

7.4.1 Part I: Dynamic drive operation

In order to obtain a reliable estimation of the regulated quantities, interaction between the estimation and the regulation controllers should be avoided to guarantee closed-loop system stability. The applied bandwidth is a trade-off between the required dynamics and accuracy of both systems. Experimental verification on system level should be executed to choose the optimal CS parameters.

By matching the applied IGBT type to the required winding current, a higher efficiency is achieved since the VSI switching losses are decreased. As demonstrated in Chapter 3, each efficiency contour plot of the drive has a different peak-efficiency in the torque versus angular velocity graph. Additional to the achievable operating range per-mode, the efficiency per-mode should be considered to determine the optimal mode for each operating point. The computed drive efficiency contours should be experimentally verified to provide reliable mode-decision data. Furthermore, measurements on the operating range in the wye-connected case should be performed for comparison with the presented concept.

The small variation in the measured torque during the transition from FB series to FB individual drive operation is due to a short current interruption. It is recommended to avoid this in a practical dynamic drive by executing the reconfiguration at the zero-crossing of the current. Therefore, sequential reconfiguration with a dual unidirectional, anti-parallel, series switch is required. In this way, natural commutation can be used to ensure an uninterrupted transition. To minimize the transitional voltage peak on the series switches in the simultaneous reconfiguration, the complete drive system should be designed and constructed as a whole. The parasitic inductances between the series switch and the HB switching legs can subsequently be minimized, reducing the voltage peak.

7.4.2 Part II: Open-winding concept extensions

In the VRE concept as proposed in Chapter 5, the secondary-side supply voltage is regulated to a constant value independent of the angular velocity above base level. The CM current losses are further reduced if the secondary-side voltage is boosted proportional to the electrical machine EMF. Additionally, the balance between the positive and negative voltage source at each supply-side can be regulated by adding an opposing homopolar offset current.

The third-harmonic injection method required for VRE affects the electrical machine efficiency and behaviour. Besides the unintended third-harmonic torque caused by the non-sinusoidal per-phase EMF, the increased iron- and winding-losses should be determined to find the actual system efficiency while performing VRE. Furthermore, the assumptions set to optimize the drive efficiency during VRE should be relaxed. With the applied restrictions, the nominal phase-current level is not achieved, indicating that the operating range can be extended further.

The combined harmonics solution on amplitude optimization should be linearized or derived analytically to make the use of lookup tables and optimization procedures superfluous and apply VRE efficiently. Closed-loop control in combination with the per-harmonic and per-mode regulation can subsequently be used to regulate the different currents with a higher accuracy.

The principle of FTO is tested by means of an a priori known fault, and only for a single failure case to demonstrate the method. To further improve the system reliability, it is recommended to investigate the fault instance detection, settlement, and the post-failure performance after multiple faults. Furthermore, the post-failure efficiency, torque disruption, and thermal behaviour of the short-circuit faults should be researched. Although the post-failure current is limited by the winding impedance, the effect cannot be diminished and should be analysed further. Electrical machine B is more suitable than electrical machine A for application in the dynamic drive concept because of the negligible mutual winding coupling and less harmonic EMF content. It is recommended to check whether the experimental FTO implementation is performed more accurately and with a smaller torque ripple by using electrical machine B.

The FTO CM current regulation based on a phase current is not accurate, the current drifts, and depends on the CS bandwidth. The per-mode, per-harmonic (dn, qn)-axis regulation method should be used to control the CM current based on the angular position, thereby improving the post-failure controllability, and make it independent of the angular velocity. The effect of the different possible failures on the consequently achievable angular velocity range should be further investigated. As demonstrated in Chapter 6, an adequate and stable post-failure torque is achieved. However, the effect on the post-failure obtainable angular velocity range and the applicability of VRE and FW should be investigated.

7.4.3 Exploratory research fields

The open-winding electrical machine in combination with modular power electronics provides research possibilities that are worthy to explore further. Two other examples of dynamic drive usage are proposed for further research.

Integrated charging with electrical machine

Charging an electrical vehicle is usually done with an auxiliary power electronics converter provided with the vehicle [8, 126, 158]. However, the dynamic drive concept can be used advantageously to integrate the charging functionality into the traction system. In [90, 95, 147] different methods are presented to integrate the charging system in the existing electrical machine drive electronics. The solution proposed in [147] can be directly integrated in the dynamic drive concept. However, these solutions lack an isolation transformer between the grid and the battery. The electrical machine can be used as isolation transformer by constructing it in a dual-layer concentrated winding configuration. The two stacked slot windings per-phase are subsequently used as primary- and secondary-side transformer winding, respectively. Since no net torque is allowed from the electrical machine during charging, the BM torque components should cancel out or, preferably, solely CM currents should be used to transfer the charging energy as applied in [147].

Wind turbine generator with winding reconfiguration

In a wind turbine generator, a large angular velocity range should be covered, comparable to a traction system. To match the generated voltage to that required by the grid connected inverter at different wind speeds, winding reconfiguration can be applied. In [69] a winding changeover system comparable to the traction solution in [108] is proposed for this purpose. However, by applying the modular reconfiguration concept as proposed in this thesis, the generated voltage is scaled better to the intended DC voltage level by increasing the per-phase winding count. As a result, the system is less vulnerable to failures since modular redundancy is added to ensure a minimum generated DC voltage for the grid-connected output inverter.

Appendices

A

Supplement to chapter 5

A.1 Combined harmonics amplitude optimization

For the optimization of the combined harmonics amplitudes, the fundamental frequency amplitude is maximized as a function of the third-harmonic amplitude and the mutual angle. The applied method and results are detailed here.

The intention is to allow for a free choice of the third-harmonic modulation amplitude, A_3, and the respective per harmonic angles, δ_1, δ_3, after which the fundamental frequency modulation amplitude, A_1, is derived independent of the electrical rotor position, θ_e, while maintaining a maximized combined peak value, $\hat{m}_x$. Correspondingly, by choosing

$$|\hat{m}_x| = 1, \tag{A.1}$$

$$\frac{\mathrm{d}m_x}{\mathrm{d}\theta_e} = 0, \tag{A.2}$$

where θ_e is removed from the modulation signals relation in (A.1) by solving the set (5.22b), (A.2).

The solving process is a nested combination of (A.1) computed in a θ_e-bounded maximization function over two mutually dependent domains to ensure it complies with (A.2). The maximization is solved numerically for a variation of the amplitude of the third-harmonic A_3, and the mutual displacement angle between the considered harmonics, δ_{13} in their respective domain like

$$A_3 \in [0,1] \qquad \text{in } N_A\text{-steps}, \tag{A.3}$$

$$\delta_{13} = \delta_1 - \delta_3 \in [0, \tfrac{2\pi}{3}] \qquad \text{in } N_\delta\text{-steps}, \tag{A.4}$$

forming a matrix of solutions for (A.1) on the (δ_{13}, A_3) plane. Combined, this is formulated as

$$\begin{array}{c}\text{solve} \\ A_3 \in [0,1], \\ \delta_{13} \in [0, \frac{2\pi}{3}]\end{array} \quad \text{for} \begin{cases} \delta_{13} < \frac{\pi}{3} : \max\limits_{\theta_e \in [\frac{\pi}{2}, \pi]} \left(A_1 \sin(\theta_e) + A_3 \sin(3(\theta_e - \delta_{13})) \right) = 1, \\ \delta_{13} \geq \frac{\pi}{3} : \max\limits_{\theta_e \in [0, \frac{\pi}{2}]} \left(A_1 \sin(\theta_e) + A_3 \sin(3(\theta_e - \delta_{13})) \right) = 1, \end{cases} \tag{A.5}$$

where $\delta_1 = 0$, and as a result $\delta_{13} = -\delta_3$ reducing the number of unknowns from three to two. Furthermore, the offset angle δ_{13} moves modulation m_3 backwards, demanding the bounds of the maximization to be reversed, i.e $\theta_e \in [\frac{\pi}{2}, \pi]$, for $\delta_{13} < \frac{\pi}{3}$, and vice versa. Additionally, a maximum and a minimum exist for $\theta_e \in [0, 2\pi]$, therefore (A.1) is solved for only half the domain, ensuring a unique solution. The resulting dependence of A_1 versus A_3 and δ_{13}, is illustrated in Figure A.1b for the extreme cases

$$\delta_{13} = 0 + k2\pi/3 \ \vee \ \delta_{13} = (\pi + k2\pi)/3 \qquad \text{where } k \in \mathbb{Z}, \tag{A.6}$$

and illustrated in Figure A.1c for $0 \leq \delta_{13} \leq 2\pi/3$. The combined amplitude optimization is executed for phase-a in (A.5). Due to the equal periodicity of the three-phase system and the third-harmonic, the solution is valid for each phase.

A voltage vector magnitude per harmonic maximization method to execute VRE within the linear PWM range is proposed. By applying modulation signals that satisfy this amplitude, angle relation (Figure A.1c) to drive both inverters in Figure 5.1a, assumption 5. is met. Figure A.1c shows that an exemplifying combination of $A_3 = 0.5$, $\delta_{13} = 7\pi/12$ rad., that leads to $A_1 = 0.675$. By subsequently plotting (5.22b) versus θ_e using these values and $\delta_1 = 0$, $\delta_3 = -\delta_{13}$, Figure A.1d shows that the combined harmonics peak modulation, $\hat{m} = 1$, confirming (A.1).

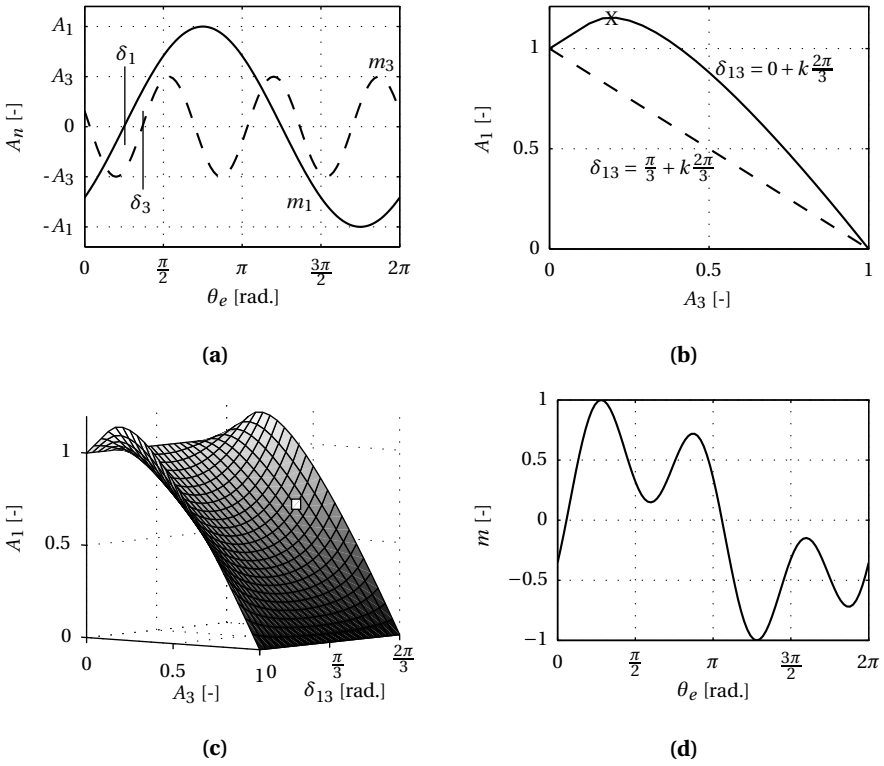

Figure A.1: Two frequencies linear PWM amplitude optimization; **(a)** two modulation signals definition, **(b)** numerical solution to (A.1) for the fundamental frequency amplitude, A_1, versus the third-harmonic amplitude, A_3, for the two indicated values of the mutual angle, δ_{13}, where ($k \in \mathbb{Z}$) and X indicates the maximized A_1 solution used in SVM **(c)** numerical solution $\left(N_A, N_\delta = 25, 25\right)$ to (A.1) for A_1 versus A_3 and δ_{13}, **(d)** an exemplifying resulting modulation signal, m, demonstrating that the modulation peak, $\hat{m} = 1$, corresponding to the values for A_3, δ_{13}, and A_1 at the white rectangle in **(c)**.

A.2 Idealized EMF common-mode current minimization

The minimization details of the required CM current to boost the secondary-side supply voltage in VRE operation are given here. In this situation, the EMF of the electrical machine is purely sinusoidal, corresponding to Section 5.2.

A.2.1 Constrained nonlinear optimization

The required usage of the amplitude lookup graph in Figure A.1c enforces a numerical minimization search, i.e. a constrained nonlinear optimization procedure, to find the minimum $\left|\vec{i}_3^{\,\mathrm{cm}}\right|$. The optimization is executed for each position by constructing a matrix for the produced electromagnetic power, P_{em}, as combination of current i_{q1}^{bm} and the relative angular velocity x_r, where

$$x_r = \frac{\omega_m}{\omega_b}. \tag{A.7}$$

A torque versus angular velocity profile in the VRE domain is acquired based on that. Presumed that the SPMSM parameters are identified, the EMF, e_{q1}^{bm}, is known from x_r. Additionally, the fundamental frequency voltage drop across the passive components, $\vec{v}_{R_1}^{\mathrm{bm}}$ and $\vec{v}_{L_1}^{\mathrm{bm}}$ is derived using assumption 1. (5.4) at each specific combination of $\left(i_{q1}, x_r\right)$. Resultantly, the required combination of fundamental frequency spacial voltages $\vec{v}_{p1}^{\mathrm{bm}}$, $\vec{v}_{s1}^{\mathrm{bm}}$ as input for the CM current minimization is known. The CM current magnitude, $\left|\vec{i}_3^{\,\mathrm{cm}}\right|$, is minimized by varying amplitude A_{p3} and angles δ_{p3}, δ_{s3} conforming the assumptions, and derived from the defined spacial voltage vectorial relations like

$$\min_{A_{p3},\delta_{p3},\delta_{s3}} \left|\vec{i}_3^{\,\mathrm{cm}}\right|\left(A_{p3},\delta_{p3},\delta_{s3}\right) \text{ such that } \begin{cases} \mathbf{c}_{eq}\left(A_{p3},\delta_{p3},\delta_{s3}\right) & = 0 \\ \mathbf{c}\left(A_{p3},\delta_{p3},\delta_{s3}\right) & \leq 0 \\ 0 & \leq A_{p3} \leq 1 \\ -\frac{\pi}{3} & \leq \delta_{p3},\delta_{s3} \leq \frac{\pi}{3} \end{cases}, \tag{A.8}$$

$$\text{with } \left|\vec{i}_3^{\,\mathrm{cm}}\right| = \frac{V_p}{6\omega_e L^{\mathrm{cm}}} A_{p3} \sin\left(\delta_{s3} - \delta_{p3}\right). \tag{A.9}$$

The constraints vectors, $\mathbf{c}_{eq}$, $\mathbf{c}$, list the limitations of the respective equality and inequality system parameters as will be defined in the following. The validity of the optimization results is ensured with the boundaries set for the optimization parameters $A_{p3},\delta_{p3},\delta_{s3}$ in (A.8). The amplitude boundary for A_{p3} is required to ensure linear PWM, while the angular boundaries on δ_{p3}, δ_{s3} guarantee a solution within one period.

A.2.2 Constraints definition

Besides the boundaries, certain constraints are applied to the minimization function (A.8) to comply with the requirements set for the each voltage, power, and amplitude.

Equality constraints

The nonlinear voltage constraints are based on the KVL. The sum of all spacial voltage vectors per harmonic is projected on each respective axis in Figure 5.2,a, b, and is computed with

$$v_{d1}^{\mathrm{bm}} = 0 = -v_{L_{q1}}^{\mathrm{bm}} + \left|\vec{v}_{s1}^{\mathrm{bm}}\right| \sin\left(\delta_{s1}^{\mathrm{bm}}\right) - \left|\vec{v}_{p1}^{\mathrm{bm}}\right| \sin\left(\delta_{p1}^{\mathrm{bm}}\right), \tag{A.10}$$

$$v_{q1}^{\mathrm{bm}} = 0 = e_{q1}^{\mathrm{bm}} + v_{R_{q1}}^{\mathrm{bm}} + \left|\vec{v}_{s1}^{\mathrm{bm}}\right| \cos\left(\delta_{s1}^{\mathrm{bm}}\right) - \left|\vec{v}_{p1}^{\mathrm{bm}}\right| \cos\left(\delta_{p1}^{\mathrm{bm}}\right), \tag{A.11}$$

$$v_{d3}^{\mathrm{cm}} = 0 = \left(\left|\vec{v}_{R_3}^{\mathrm{cm}}\right| + \left|\vec{v}_{s3}^{\mathrm{cm}}\right|\right) \sin\left(\delta_{s3}^{\mathrm{cm}}\right) - \left|\vec{v}_{L_3}^{\mathrm{cm}}\right| \cos\left(\delta_{s3}^{\mathrm{cm}}\right) - \left|\vec{v}_{p3}^{\mathrm{cm}}\right| \sin\left(\delta_{p3}^{\mathrm{cm}}\right), \tag{A.12}$$

$$v_{q3}^{\mathrm{cm}} = 0 = \left(\left|\vec{v}_{R_3}^{\mathrm{cm}}\right| + \left|\vec{v}_{s3}^{\mathrm{cm}}\right|\right) \cos\left(\delta_{s3}^{\mathrm{cm}}\right) + \left|\vec{v}_{L_3}^{\mathrm{cm}}\right| \sin\left(\delta_{s3}^{\mathrm{cm}}\right) - \left|\vec{v}_{p3}^{\mathrm{cm}}\right| \cos\left(\delta_{p3}^{\mathrm{cm}}\right), \tag{A.13}$$

where the voltages parallel to an axis are denoted as scalar due to (5.4). The inverter spacial voltage vector magnitudes in (A.10) - (A.13) are derived with (2.54)-(2.57), (5.3). The fundamental frequency vector angles $\delta_{p1}^{\mathrm{bm}}$, $\delta_{s1}^{\mathrm{bm}}$ are derived from (5.14), (5.15) respectively. The per-harmonic voltage vectors magnitude of the resistance and inductance are computed with (5.6) - (5.9).

The secondary-side power equilibrium constraint (5.19a) is used to ensure DC voltage stability on that side. Whether these equality constraints are met is checked in the minimization procedure as depicted in Figure A.2. The complete equality constraint vector, $\mathbf{c}_{eq}$, in (A.8) is constructed like

$$\mathbf{c}_{eq} = \begin{bmatrix} v_{d1}^{\mathrm{bm}} \\ v_{q1}^{\mathrm{bm}} \\ v_{d3}^{\mathrm{cm}} \\ v_{q3}^{\mathrm{cm}} \\ P_s \end{bmatrix}. \tag{A.14}$$

Inequality constraints

The inequality constrains are based on the notion that the PWM amplitude on the secondary-side must be limited in the linear region, thus

$$0 \leq A_{s3} \leq 1, \tag{A.15}$$

for this variable is not bounded in the optimization (A.8). From this, the inequality vector, **c**, in (A.8) is constructed as

$$\mathbf{c} = \begin{bmatrix} -A_{s3} \\ A_{s3} - 1 \end{bmatrix}. \tag{A.16}$$

A.2.3 Setup procedure

The values of electrical machine B (Appendix D) are used to demonstrate the current minimization method. In this analysis it is assumed that the machine constant $K_e = K_{e1}$, neglecting K_{e3} of electrical machine B. The balanced DC supply voltages are $V_p = 350$ V, $V_s = 700$ V, and both windings per-phase are connected in series. The upper limit of the fundamental frequency BM current, i_{q1}^{bm}, is determined by the maximum continuous machine phase current, i_x. Eventually, the combined harmonics phase current will be limited to i_x ensuring thermally stable operation. The relative angular velocity ratio in the series-connected configuration, x_r^{sr}, is varied from the unity ratio representing the base angular velocity, ω_b^{sr}, up to the series configuration angular velocity ratio, x_s^{sr} representing the top angular velocity as defined with FW, ω_t^{sr}. The minimization procedure is executed for different combinations of $\left\{ i_{q1}^{\mathrm{bm}}; x_r^{\mathrm{sr}} \right\}$, like

$$0 \le i_{q1}^{\mathrm{bm}} \le i_x \qquad \text{in } N_i\text{-steps}, \tag{A.17}$$

$$1 \le x_r^{\mathrm{sr}} \le x_s^{\mathrm{sr}} \qquad \text{in } N_x\text{-steps}, \tag{A.18}$$

resulting in a matrix of (N_i, N_x) solutions.

The numerical optimization procedure is implemented in MATLAB using the *fmincon*-function of the OPTIMIZATION TOOLBOX™. The function *fmincon* searches for the minimum of a constrained nonlinear multi-variable function such as (A.8). The nonlinear constraints, **c**, $\mathbf{c}_{eq}$ (A.14), (A.16) are supplied to *fmincon* to find the minimum current $\left|\bar{i}_3^{\mathrm{cm}}\right|$ by varying the optimization variables $\left(A_{p3}, \delta_{p3}, \delta_{s3}\right)$ for a given set of $\left\{ i_{q1}^{\mathrm{bm}}; x_r^{\mathrm{sr}} \right\}$. The complete minimization procedure is visualized in Figure A.2. The counters κ, ν, ς are used to step through the respective current, angular velocity ratio, and solver start domains. For each position, (κ, ν), in the (N_i, N_x)-matrix of input variables, $\left\{ i_{q1}^{\mathrm{bm}}; x_r^{\mathrm{sr}} \right\}$, the computation sequence is executed. The essential non-analytical computation step in this sequence is determining amplitude A_1 per-side by interpolating the applied amplitude, angle A_3, δ on Figure A.1c. The constraints are checked to verify that the solution found is viable. For each (κ, ν), *fmincon* is executed N_{start} times using different combinations of $\left(A_{p3}, \delta_{p3}, \delta_{s3}\right)$, which are varied within the bounds set in (A.8). After completing the first minimization iteration, $(\varsigma > N_{\mathrm{start}})$, the optimal combination of $\left(A_{p3}, \delta_{p3}, \delta_{s3}\right)$, the computation sequence variables, and the resulting $\left|\bar{i}_3^{\mathrm{cm}}\right|$ are saved. This procedure is continued until the (N_i, N_x)-matrix is filled with optimal solutions for $\left|\bar{i}_3^{\mathrm{cm}}\right|$ or marked as being unsolvable because the constraints cannot be satisfied.

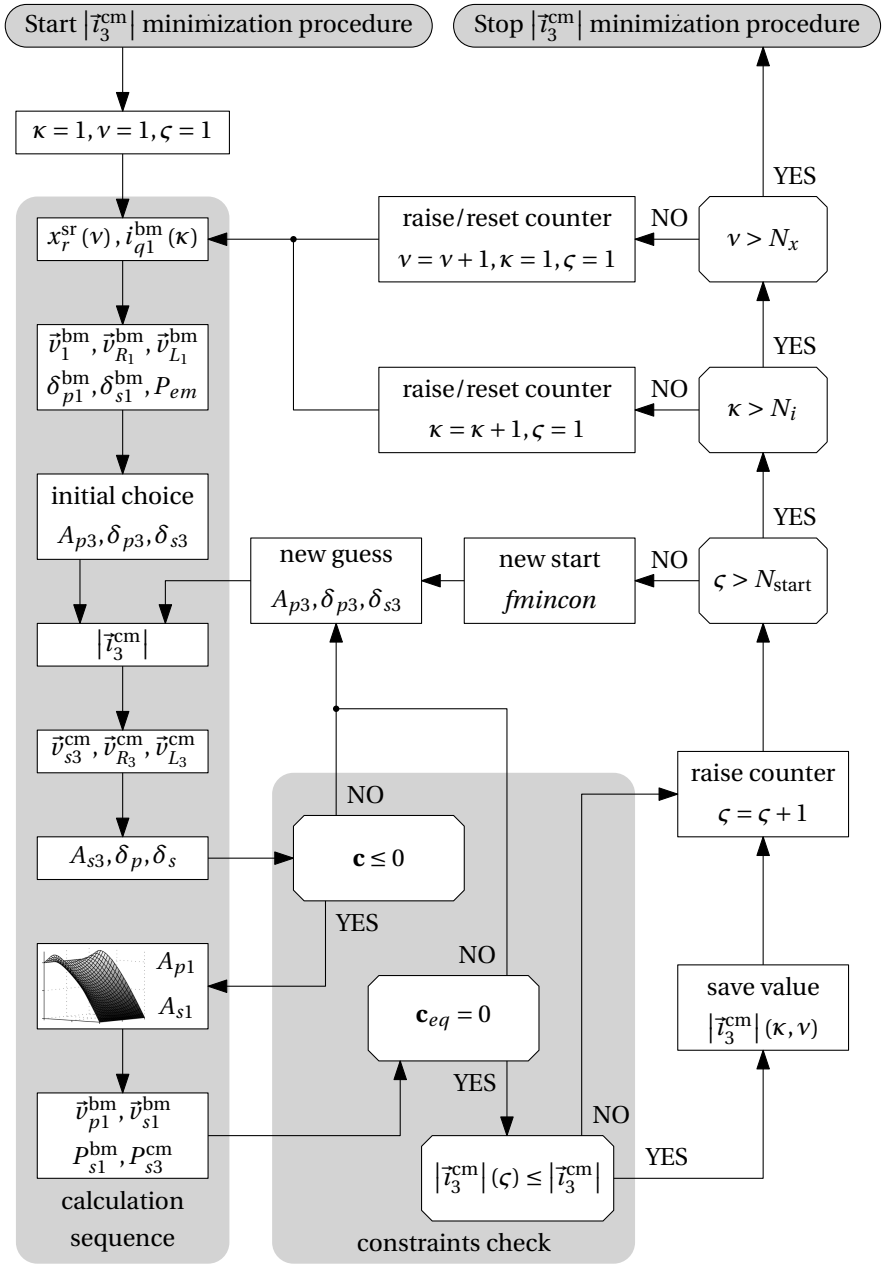

Figure A.2: Schematic overview of the constrained nonlinear optimization procedure.

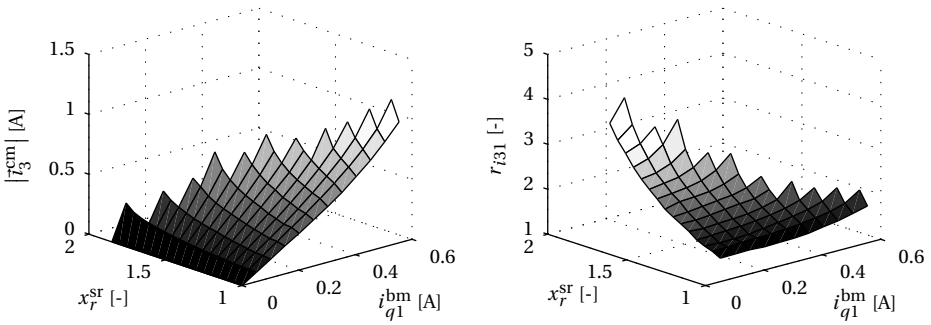

Figure A.3: Idealized VRE CM current minimization results; **(a)** minimized $\left|\vec{i}_3^{\,cm}\right|$ as a function of $\left\{i_{q1}^{bm}; x_r^{sr}\right\}$, **(b)** resulting current ratio, r_{i31} as a function of $\left\{i_{q1}^{bm}; x_r^{sr}\right\}$.

A.2.4 Results

The common-mode current minimization is executed for each combination of the torque producing current, i_{q1}^{bm}, and the relative angular velocity range, x_r^{sr}, using the constrained nonlinear optimization procedure described in Figure A.2. The minimum third-harmonic CM current, $\left|\vec{i}_3^{\,cm}\right|$, required for VRE is plotted in Figure A.3a if a solution is found for that combination in the domain $\left\{i_{q1}^{bm}; x_r^{sr}\right\}$. In Figure A.3b, the ratio, r_{i31}, between $\left|\vec{i}_3^{\,cm}\right|$ and i_{q1}^{bm} is plotted to show the relative current requirement per position, where

$$r_{i31} = \frac{\left|\vec{i}_3^{\,cm}\right|}{i_{q1}^{bm}}. \tag{A.19}$$

The maximum achievable electromagnetic torque T_{em} as function of the angular velocity ω_m, and the therefore required currents are shown in Section 5.6.

A.3 Non-ideal EMF common-mode current minimization

The details of the CM current minimization to boost the secondary-side supply voltage in VRE operation are given here. In this situation, the EMF of the electrical machine contains the third-harmonic, requiring adaptations to the constraints. The optimization procedure of Appendix A.2 is repeated using the electrical machine B parameters listed in Appendix D. The utilized voltage vector relations and power balance equations are explained in Section 5.3.

A.3.1 Constraints adaptation

The presence of a thirdharmonic component, e_{q3}^{cm}, in the EMF requires an adaptation of the constraints set for the CM current minimization procedure. Looking at Figure 5.4, solely the projection of the voltage vectors on the $q3$-axis changes compared to Figure 5.2b. To comply with the KVL, e_{q3}^{cm} is added to the equality constraint equation (A.13), resulting in

$$v_{q3}^{\mathrm{cm}} = 0 = e_{q3}^{\mathrm{cm}} + \left(\left|\vec{v}_{R_3}^{\mathrm{cm}}\right| + \left|\vec{v}_{s3}^{\mathrm{cm}}\right|\right)\cos\left(\delta_{s3}^{\mathrm{cm}}\right) + \left|\vec{v}_{L_3}^{\mathrm{cm}}\right|\sin\left(\delta_{s3}^{\mathrm{cm}}\right) - \left|\vec{v}_{p3}^{\mathrm{cm}}\right|\cos\left(\delta_{p3}^{\mathrm{cm}}\right). \quad \text{(A.20)}$$

The boundaries and other constraints as applied in the idealized EMF case, current minimization are still valid. Furthermore, also the minimization procedure setup, as explained in Appendix A.2, is kept constant to determine the minimum current magnitude, $\left|\vec{i}_3^{\mathrm{cm}}\right|$, for each combination of $\left\{i_{q1}^{\mathrm{bm}}; x_r^{\mathrm{sr}}\right\}$.

A.3.2 Results

The constrained optimization procedure is executed again to determine the minimum CM current, but now for the non-ideal EMF case. The minimum third-harmonic CM current, $\left|\vec{i}_3^{\mathrm{cm}}\right|$, required for VRE is plotted in Figure A.4a if a solution is found for that combination in the domain $\left\{i_{q1}^{\mathrm{bm}}; x_r^{\mathrm{sr}}\right\}$. In Figure A.4b, the current ratio, r_{i31} (A.19), is plotted. The maximum achievable electromagnetic torque, T_{em}, as function of the angular velocity, ω_m, and the currents required therefore, are shown in Section 5.6.

The optimization is also executed for the cases where the secondary-side third-harmonic voltage vector angle, $\delta_{s3}^{\mathrm{cm}}$, is limited. As described in Section 5.3, by limiting angle $\delta_{s3}^{\mathrm{cm}}$ during the optimization procedure, the average torque produced during VRE can be increased. However, in the domain $\left(-\pi/2 \leq \delta_{s3}^{\mathrm{cm}} \leq \pi/2\right)$ no valid solution is found by the optimization. This is the consequence of a sequence of steps enforced by the rules set in the assumptions from Chapter 5. The optimization minimizes the secondary-side phase difference, δ_s, to maximize the combination of the fundamental frequency amplitude, A_{s1}, and the third-harmonic amplitude, A_{s3} according to Figure A.1c. Which is required to comply with the KVL constraints. The secondary-side fundamental frequency angle, $\delta_{s1}^{\mathrm{bm}}$, is determined by the primary-side fundamental frequency angle, $\delta_{p1}^{\mathrm{bm}}$ according to (5.5). Current vector $\vec{i}_3^{\mathrm{cm}}$ is enforced to be parallel to voltage v_{s3}^{cm} to comply with assumption 3., resulting in a negative q-axis projection; $i_{q3}^{\mathrm{cm}} < 0$. The average third-harmonic torque, $\langle T_{em3} \rangle$, produced by the CM current will therefore be negative for the non-ideal EMF case.

To drive the VSIs, each PWM signal is constructed based on the per mode, per harmonic, per-axis voltages as derived from the optimization results. The resulting lookup graphs used for the experimental verification are depicted for the primary-side inverter and the secondary-side inverter in Figure A.5 and Figure A.6, respectively.

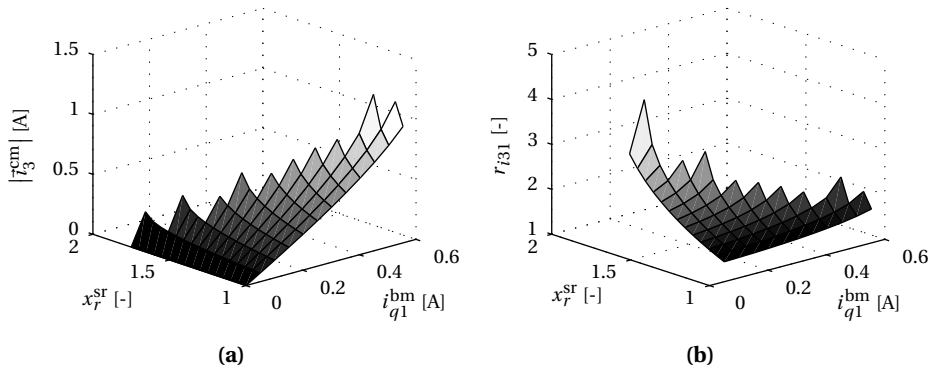

(a) **(b)**

Figure A.4: Non-ideal EMF CM current minimization results for VRE; **(a)** minimized $\left|\bar{i}_3^{cm}\right|$ as a function of $\left\{i_{q1}^{bm}; x_r^{sr}\right\}$, **(b)** resulting current ratio, r_{i31} as a function of $\left\{i_{q1}^{bm}; x_r^{sr}\right\}$.

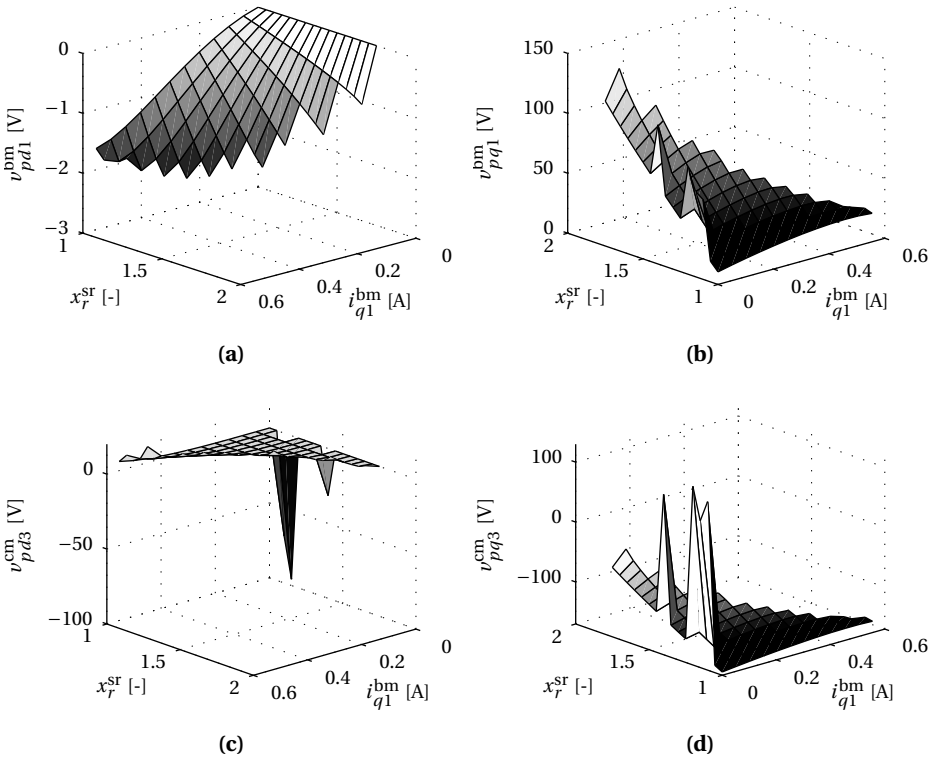

(a) **(b)**

(c) **(d)**

Figure A.5: Voltage lookup graphs for the primary-side inverter as a function of $\left\{i_{q1}^{bm}; x_r^{sr}\right\}$; **(a)** BM d-axis fundamental frequency voltage, v_{pd1}^{bm}, **(b)** BM q-axis fundamental frequency voltage, v_{pq1}^{bm}, **(c)** CM d-axis third-harmonic voltage, v_{pd3}^{cm}, **(d)** CM q-axis third-harmonic voltage, v_{pq3}^{cm}.

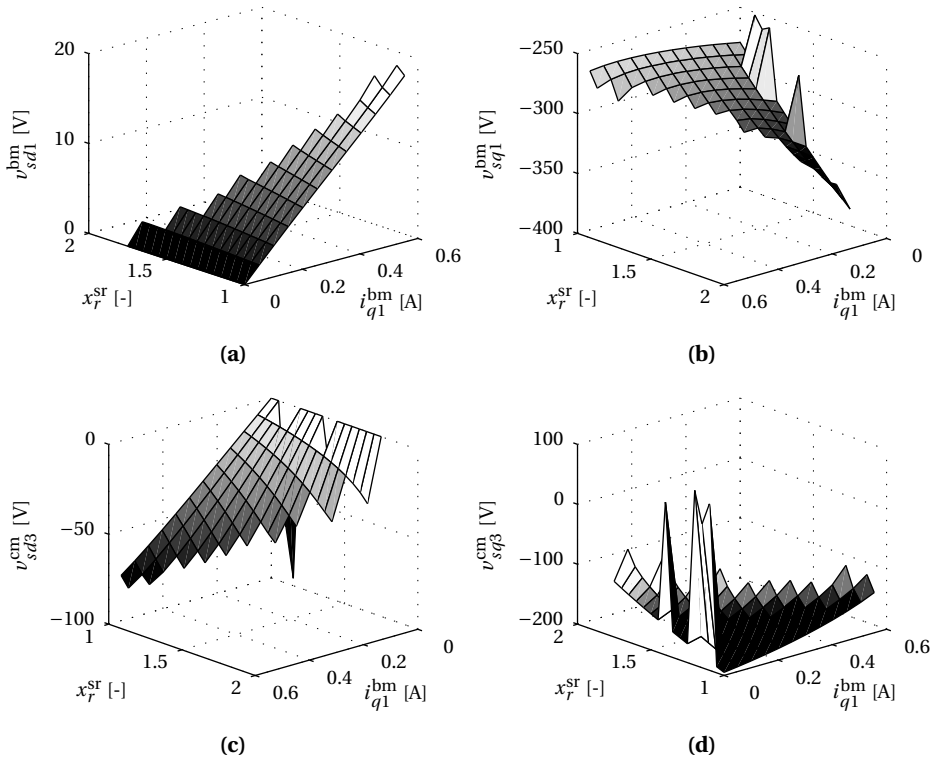

Figure A.6: Voltage lookup graphs for the secondary-side inverter as a function of $\left\{i_{q1}^{\mathrm{bm}}; x_r^{\mathrm{sr}}\right\}$; **(a)** BM d-axis fundamental frequency voltage, v_{sd1}^{bm}, **(b)** BM q-axis fundamental frequency voltage, v_{sq1}^{bm}, **(c)** CM d-axis third-harmonic voltage, v_{sd3}^{cm}, **(d)** CM q-axis third-harmonic voltage, v_{sq3}^{cm}.

A.4 Multilevel alternative topology

A possible solution to boost V_s without the requirement to use $v_{br} = 1200$ V devices, is the utilization of a multilevel inverter structure on the secondary-side [129]. Especially the three-level flying-capacitor multilevel topology [101] is suitable to combine the advantages of $v_{br} = 600$ V devices with the possibility to apply $V_s = 800$ V, as depicted in Figure A.7. The three levels are realized by constructing the secondary-side switching leg with four series-connected devices per-module ($S_{\blacktriangle}, S_{\blacktriangleright}, S_{\blacktriangleleft}, S_{\blacktriangledown}$ from top to bottom), realizing three mid-points (M_1, M_2, M_3 from top to bottom). Additionally, a flying capacitor, C_f, is connected from M_1 to M_3, where M_2 is the AC output of the secondary-side switching leg, s_x^u. The per-phase per-winding inverter module FB_x^u in Figure A.7 is a drop-in replacement for each module depicted in Figure 5.6.

During DDO, $S_{\blacktriangleright}, S_{\blacktriangleleft}$ are closed, ideally assuring that the voltage across C_f, $V_{C_f} = 0$. $S_{\blacktriangle}, S_{\blacktriangledown}$ act as the switching leg in conjunction with the primary-side. In order to execute VRE, V_{C_f} is boosted to $V_s/2$. By closing $S_{\blacktriangle}, S_{\blacktriangleright}$, the switching leg output voltage, $V_{M_2} = V_s$, which is allowed to be increased up to 800 V if $K_{br} = 2/3$. Subsequently, the combined voltage across $S_{\blacktriangleleft}, S_{\blacktriangledown}$ being $V_{\blacktriangleleft\blacktriangledown} = V_s$, which would be too high for either device. However, because $S_{\blacktriangleright}$ is closed, the voltage across $S_{\blacktriangleleft}$, being $V_{\blacktriangleleft} = 400$ V ($V_s - V_{C_f}$) and consequently, also the voltage across $S_{\blacktriangledown}$, being $V_{\blacktriangledown} = 400$ V. Safe operation during all operating modes of the flying capacitor switching leg within this drive is ensured as a result. Effectively, the high switching loss of a $v_{br} = 1200$ V device is exchanged for increased conduction loss, and reduced switching loss of two series-connected $v_{br} = 600$ V devices by applying this multilevel topology. An analysis of the complete drive system throughout the intended operating range must be conducted to derive whether this solution improves η_{sys} in that specific case.

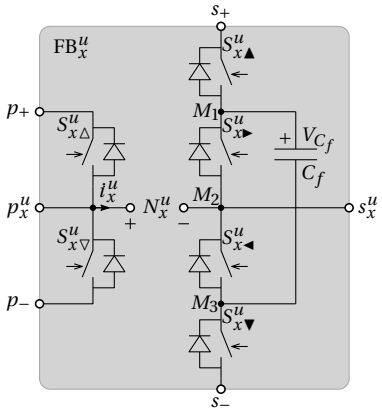

Figure A.7: Proposed alternative topology; three-level flying-capacitor, C_f, multilevel secondary-side solution allowing for the use of $v_{br} = 600$ V devices in a V_s=800 V inverter, where module FB_x^u is a drop-in replacement for each module depicted in Figure 5.6.

B

Transformation and notation

A straightforward transformation from the stationary three-phase stator reference frame to the rotating orthogonal reference frame was first described by Park in [115, 116]. It is therefore usually referred to as the Park transformation. The elegant steady state operation property for especially a non-salient PMSM is that by using this transformation, the per-phase time-variant quantities can be transformed to time-continuous quantities that directly represent the active and reactive power in the electrical machine. Various extensions of the Park, or fundamental angular velocity direct-, quadrature-axis transformation are presented in literature from which the spacial quantity relations as expounded in [21, 22, 108], are used here.

Numerous different versions of the transformations exist, causing confusion on the validity. In this appendix, the amplitude invariant transformations between the different reference frames are detailed. This notation is used throughout this research.

A stationary orthogonal transformation has been formulated by Clarke et al. [32] to represent a balanced three-phase system with two variables or an unbalanced three-phase system with three variables. The advantage of this method over the symmetrical components representation is the fact that the instantaneous positive- and negative-sequence of the transformed quantities of a rotating system may be unequal as exploited in [165]. The method is usually referred to as the Clarke transformation.

The reference frames considered are the stationary three-phase, $\equiv$, the stationary orthogonal, $\llcorner$, and the rotating orthogonal, $\vee$. In Figure B.1 the relation between the denoted frames is detailed. The variable x is used to denote the variables, which can either be a voltage, current, flux (linkage), inductance, and power.

The transformations between the indicated frames are executed with

$$\begin{bmatrix} x_\alpha \\ x_\beta \\ x_\gamma \end{bmatrix} = \mathbf{T}_{\vee\llcorner} \begin{bmatrix} x_d \\ x_q \\ x_0 \end{bmatrix} \qquad \begin{bmatrix} x_d \\ x_q \\ x_0 \end{bmatrix} = \mathbf{T}_{\llcorner\vee} \begin{bmatrix} x_\alpha \\ x_\beta \\ x_\gamma \end{bmatrix}$$

$$\begin{bmatrix} x_a \\ x_b \\ x_c \end{bmatrix} = \mathbf{T}_{\llcorner\equiv} \begin{bmatrix} x_\alpha \\ x_\beta \\ x_\gamma \end{bmatrix} \qquad \begin{bmatrix} x_\alpha \\ x_\beta \\ x_\gamma \end{bmatrix} = \mathbf{T}_{\equiv\llcorner} \begin{bmatrix} x_a \\ x_b \\ x_c \end{bmatrix}$$

$$\begin{bmatrix} x_d \\ x_q \\ x_0 \end{bmatrix} = \mathbf{T}_{\equiv\vee} \begin{bmatrix} x_a \\ x_b \\ x_c \end{bmatrix} \qquad \begin{bmatrix} x_a \\ x_b \\ x_c \end{bmatrix} = \mathbf{T}_{\vee\equiv} \begin{bmatrix} x_d \\ x_q \\ x_0 \end{bmatrix}$$

where the transformation matrices are given by

$$\mathbf{T}_{\vee\llcorner} = \begin{bmatrix} \cos(\theta_e) & -\sin(\theta_e) & 0 \\ \sin(\theta_e) & \cos(\theta_e) & 0 \\ 0 & 0 & 1 \end{bmatrix} \tag{B.1}$$

$$\mathbf{T}_{\llcorner\vee} = \begin{bmatrix} \cos(\theta_e) & \sin(\theta_e) & 0 \\ -\sin(\theta_e) & \cos(\theta_e) & 0 \\ 0 & 0 & 1 \end{bmatrix} \tag{B.2}$$

$$\mathbf{T}_{\llcorner\equiv} = \begin{bmatrix} 1 & 0 & 1 \\ -\frac{1}{2} & \frac{\sqrt{3}}{2} & 1 \\ -\frac{1}{2} & -\frac{\sqrt{3}}{2} & 1 \end{bmatrix} \tag{B.3}$$

$$\mathbf{T}_{\equiv\llcorner} = \frac{2}{3} \begin{bmatrix} 1 & -\frac{1}{2} & -\frac{1}{2} \\ 0 & \frac{\sqrt{3}}{2} & -\frac{\sqrt{3}}{2} \\ \frac{1}{2} & \frac{1}{2} & \frac{1}{2} \end{bmatrix} \tag{B.4}$$

$$\mathbf{T}_{\equiv\vee} = \frac{2}{3} \begin{bmatrix} \cos(\theta_e) & \cos(\theta_e - \frac{2\pi}{3}) & \cos(\theta_e + \frac{2\pi}{3}) \\ -\sin(\theta_e) & -\sin(\theta_e - \frac{2\pi}{3}) & -\sin(\theta_e + \frac{2\pi}{3}) \\ \frac{1}{2} & \frac{1}{2} & \frac{1}{2} \end{bmatrix} \tag{B.5}$$

$$\mathbf{T}_{\vee\equiv} = \begin{bmatrix} \cos(\theta_e) & -\sin(\theta_e) & 1 \\ \cos(\theta_e - \frac{2\pi}{3}) & -\sin(\theta_e - \frac{2\pi}{3}) & 1 \\ \cos(\theta_e + \frac{2\pi}{3}) & -\sin(\theta_e + \frac{2\pi}{3}) & 1 \end{bmatrix} \tag{B.6}$$

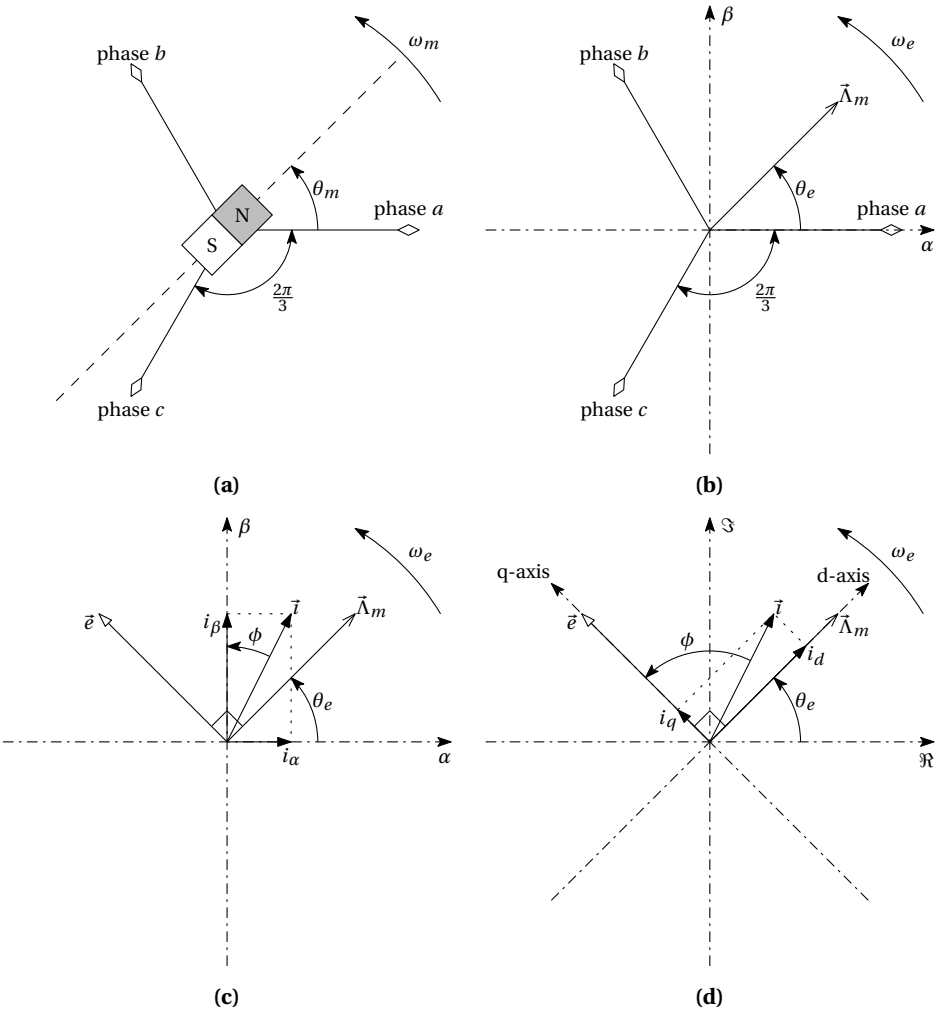

Figure B.1: Schematic representation of transformations; **(a)** relation between the stator phases and the mechanical rotor position, θ_m, and mechanical rotor angular velocity, ω_m, **(b)** stationary $(\Re, \Im)$ three-phase representation of the stator phases and the spacial rotor flux linkage vector, $\vec{\Lambda}_m$, which is a function of the electrical rotor position, θ_e, and electrical rotor angular velocity, ω_e, **(c)** stationary (α, β)-axis orthogonal reference frame relation between $\vec{\Lambda}_m$, the spacial EMF vector, $\vec{e}$, and an exemplifying spacial current vector, $\vec{i}$, decomposition onto each respective axis, **(d)** rotating $(d1, q1)$-axis orthogonal reference frame decomposition of the exemplary $\vec{i}$ into the resulting current components, i_d, i_q, furthermore $\vec{\Lambda}_m$ and $\vec{e}$ are by definition projected on the d-axis and q-axis, respectively.

C

Electrical machine A parameters

The methods and results regarding the identification of the electrical machine A parameters are described in this appendix. Machine A is a six-winding SPMSM without saliency and a negligible cogging torque. The physical structure, spacial EMF representation, and the winding scheme are detailed in the respective sub-figures of Figure C.2. The dual three-phase winding structure based on reversing the polarity of three of the six windings is clarified by combining Figure C.2b and Figure C.2c.

EMF measurement

The parameters are measured in two configurations. The EMF is measured while propelling the axle of the electrical machine, using the DCM, after which the per harmonic machine constant is derived from the magnitude plot of its FT. The EMF of this machine contains multiple harmonics, as indicated in Table C.1. The EMF of both winding sets is measured to verify that $e_x^{\mathrm{I}} = e_x^{\mathrm{II}}$ (Figure C.1). Based on the mutual coupling detailed in Figure C.1, the coupling matrix (C.1) is constructed. Couplings lower than 3% are neglected, as a result only adjacent windings are coupled.

R_{st}, L_{st}, M_{st} measurement

The passive components and their mutual couplings are measured with the rotor fixed to the same foundation plate as to which the stator is mounted. Different fixed rotor positions are applied to verify that the non-salient construction of electrical machine A prevents variation of L_{st} as a function of θ_m. By measuring L_{st} of each phase in different fixed positions, the variation as a function of θ_m is determined. This variation appeared to be negligible. The parameters shown in Table C.1 are the average measurement values of all phases in three different positions.

Table C.1: Measured electrical machine A parameters

Symbol	Value	Unit	Symbol	Value	Unit
N_{pp}	2	[-]	N^{set}	2	[-]
N_{sp}	36	[-]	N_{sl}	3	[-]
N_{ph}	6	[-]	N_{tu}	42	[-]
L_{st}	35.9	[mH]	R_{st}	1.10	[Ω]
L^{bm}	43.1	[mH]	k_{st}	-0.20	[-]
L^{cm}	21.5	[mH]	I_x	6.03	[A]
K_{e1}	2.47	[Vs/rad.]	K_{e3}	0.16	[Vs/rad.]
K_{e5}	43.6	[mVs/rad.]	K_{e7}	38.2	[mVs/rad.]
K_{e9}	34.5	[mVs/rad.]	K_{e15}	27.3	[mVs/rad.]
K_{e19}	36.4	[mVs/rad.]			
$\check{P}^{\text{sr}}$	3.41	[kW]	$\check{P}^{\text{in}}$	7.18	[kW]
$\check{T}$	62.9	[Nm]			

$$\mathbf{L}_A = \begin{bmatrix} 35.9 & -7.18 & 0 & 0 & 0 & -7.18 \\ -7.18 & 35.9 & -7.18 & 0 & 0 & 0 \\ 0 & -7.18 & 35.9 & -7.18 & 0 & 0 \\ 0 & 0 & -7.18 & 35.9 & -7.18 & 0 \\ 0 & 0 & 0 & -7.18 & 35.9 & -7.18 \\ -7.18 & 0 & 0 & 0 & -7.18 & 35.9 \end{bmatrix} \text{ mH} \tag{C.1}$$

Angular velocity estimations and measurements

The intended series and individual base and top angular velocity of electrical machine A are listed in the designated column of Table C.2. The actually obtained values are computed using (3.20) and (3.21), taking into account the values from Table C.1, as listed in the indicated column of Table C.2, thereby assuming that V_{inv} = 300 V. The other VSI parameters, required to derive $|\hat{v}_1|$ for the respective FBS and FBI cases are listed in Table F.1.

Table C.2: electrical machine A mechanical angular velocities applying V_{inv} = 300 V

Symbol	Intended value	Actual value	Unit
ω_b^{sr}	55.0	53.9	[rad./s]
ω_t^{sr}	110.0	89.2	[rad./s]
ω_b^{in}	110.0	112.3	[rad./s]
ω_t^{in}	220.0	179.9	[rad./s]
x_s^{sr}	2.0	1.65	[-]
x_s^{in}	2.0	1.60	[-]
x_o	4.0	3.34	[-]

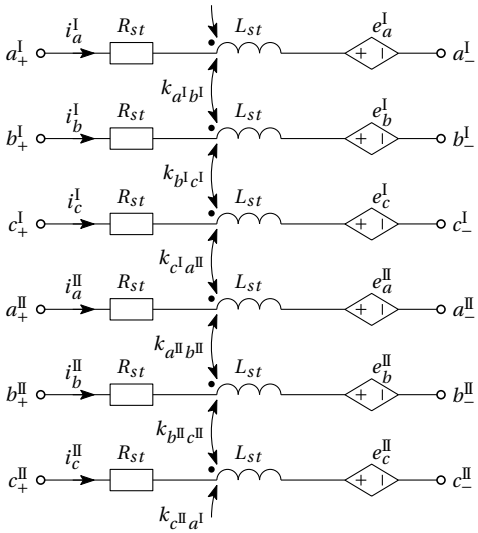

Figure C.1: Six winding equivalent circuit of electrical machine A showing the per winding resistance, R_{st}, magnetizing inductance, L_{st}, and EMF, e_x^u. Furthermore, the mutual coupling between the adjacent windings is indicated.

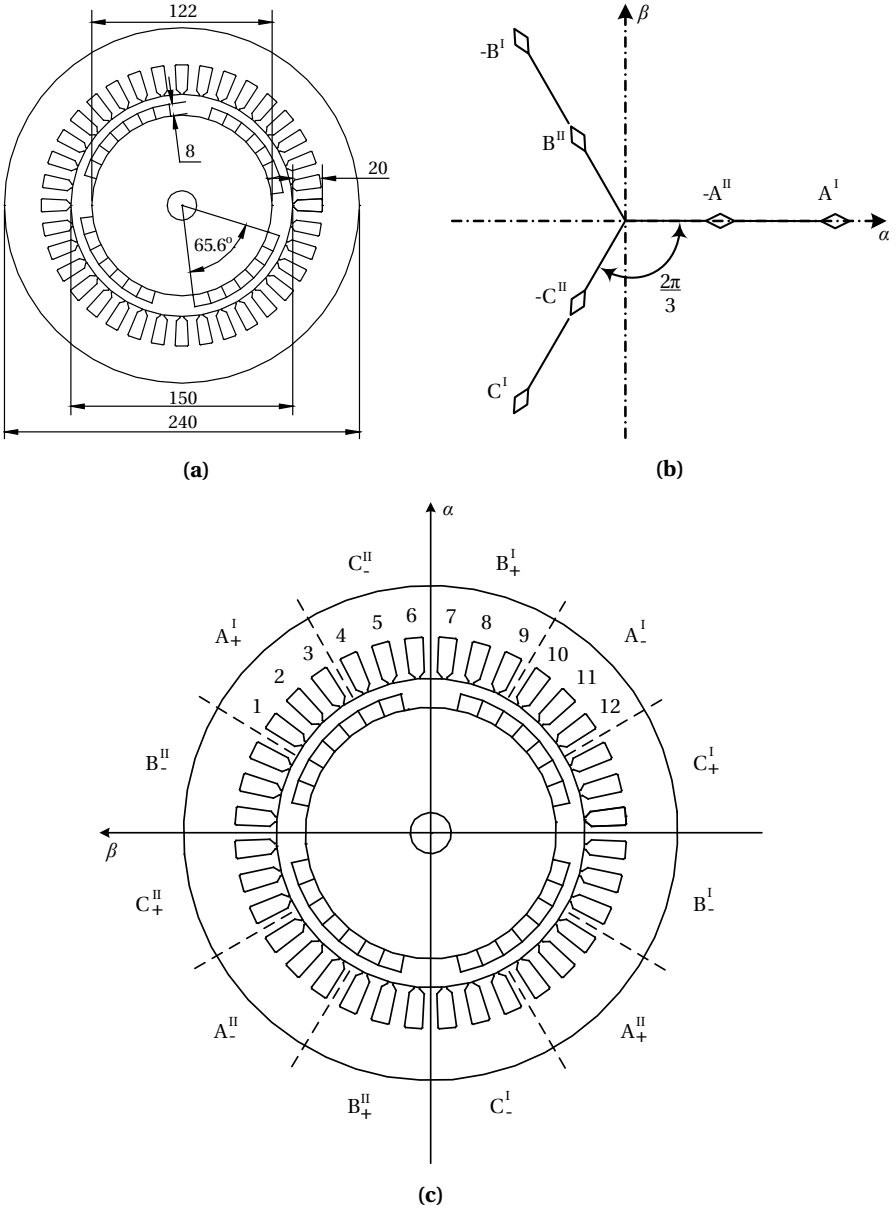

Figure C.2: (a) Cross-section of the physical structure of the 36 slots, 4 poles electrical machine A, detailing the most important dimensions in mm, the magnetized axial length of the rotor is 225 mm, **(b)** MMF spacial vector representation of the indicated six stator windings as a dual three-phase structure on the stationary orthogonal (α,β)-reference frame, **(c)** distributed windings scheme and detail of the single layer, series lap, per-coil distribution of winding A^{I} being a series connection of the three slot coils 1-10, 2-11, 3-12.

D

Electrical machine B parameters

The methods and results regarding the identification of the electrical machine B parameters are described in this appendix. An artist impression of the machine, which is custom-designed by ADVANCED ELECTROMAGNETICS [2], is depicted in Figure D.1, and the significant dimensions are indicated in Figures D.2, D.3, D.4. Electrical machine B is a six-winding SPMSM with a negligible cogging torque and without saliency as will be verified in the following.

EMF measurement

The parameters are measured in two configurations. The EMF is measured while propelling the axle of the electrical machine, using the DCM, after which the per harmonic machine constant is derived from the magnitude plot of its FT. Only the fundamental and its third-harmonic are present in the EMF as indicated in Table D.1. The maximum electrical machine power utilization case results are used for all the measurements. The EMF of both winding sets is measured to ensure that $e_x^{\mathrm{I}} = e_x^{\mathrm{II}}$ (Figure C.1). Based on the mutual coupling detailed in Figure C.1, the coupling matrix (D.1) is constructed. Couplings lower than 3% are neglected, and from (D.1) it is concluded that only adjacent windings are coupled.

R_{st}, L_{st}, M_{st} measurement

The passive components and their mutual couplings are measured with the rotor fixed to the same foundation plate as to which the stator is mounted. Different fixed rotor positions are applied to verify that the non-salient construction of electrical machine B prevents variation of L_{st} as a function of θ_m. By measuring each L_{st} in different fixed positions, the variation as a function of θ_m is determined and detailed in Table D.2. The parameters shown in Table D.1 are the average values over all phases in the two measurements.

The designated phase or combination of phases under test are driven with a sinusoidal current of frequency, $f_{\sin}$, and amplitude, $|i_x| = 4.5$ A, which is close to its nominal current. $f_{\sin}$ is chosen to be 1, 10, 50, and 350 Hz to represent different operating points

in the required fundamental frequency range of electrical machine B. The per-phase inductance and resistance (L_{st}, R_{st}) and the CM inductance, L^{cm}, are derived based on the phase voltage, current and their mutual angle. Subsequently, k_{st}, L^{bm} and the electrical machine B inductance matrix, $\mathbf{L}_B$ are computed using (2.31) and (2.27).

$$\mathbf{L}_B = \begin{bmatrix} 33.0 & -1.25 & 0 & 0 & 0 & -1.25 \\ -1.25 & 33.0 & -1.25 & 0 & 0 & 0 \\ 0 & -1.25 & 33.0 & -1.25 & 0 & 0 \\ 0 & 0 & -1.25 & 33.0 & -1.25 & 0 \\ 0 & 0 & 0 & -1.25 & 33.0 & -1.25 \\ -1.25 & 0 & 0 & 0 & -1.25 & 33.0 \end{bmatrix} \text{ mH} \tag{D.1}$$

Thermal stability measurement

An endurance test is executed to verify that electrical machine B can operate under nominal conditions for a long period of time. An individual powered nominal load test was conducted, thus $T_{em} = \check{T}, \omega_m = \omega_b^{\text{sr}}, P_{em} = \check{P}^{\text{sr}}$. The set is powered for an half-hour, during which the internal machine stator temperature, T_{st}, increases form $T_{st(begin)} = 25\ ^o$C to $T_{st(end)} = 37\ ^o$C. T_{st} was not completely stabilized after half an hour, but the temperature gradient was very small. Therefore, it is assumed that the steady state temperature will be well under the critical design level of $T_{st} = 100\ ^o$C.

Reluctance torque measurement

The surface mounting of the PMs theoretically results in a reluctance free PMSM, which ideally produces solely an electromagnetical torque, T_{em}. To verify this, and thus that $L_{st} = L_{d1} = L_{q1}$, the presence of a reluctance torque is measured. By controlling electrical machine B to a fixed angular velocity (i.e. 68 rad./s) and simultaneously vary the current angle, ϕ from zero $\left(|i_x| = i_{q1}\right)$ to $\pi/2$ $(|i_x| = -i_{d1})$ the produced torque, T_m, versus ϕ is measured, as illustrated in Figure D.5. By comparing T_m to the purely electromagnetic torque function $\check{T}\cos\left(\phi\right)$, a reluctance torque is neglected as shown in Figure D.5.

Table D.1: electrical machine B parameters

Symbol	Value	Unit	Symbol	Value	Unit
N_{pp}	7	[-]	N^{set}	2	[-]
N_{sp}	12	[-]	N_{sl}	1	[-]
N_{ph}	6	[-]	N_{tu}	136	[-]
L_{st}	33.0	[mH]	R_{st}	2.60	[Ω]
L^{bm}	34.2	[mH]	k_{st}	-37.8	[10^{-3}]
L^{cm}	30.5	[mH]	I_x	3.24	[A]
K_{e1}	1.91	[Vs/rad.]	K_{e3}	0.20	[Vs/rad.]
$\check{P}^{\text{sr}}$	2.02	[kW]	$\check{P}^{\text{in}}$	4.19	[kW]
$\check{T}$	26.3	[Nm]			

Table D.2: electrical machine B L_{st} for two positions of θ_m

Position 1, phase:	A^{I}	B^{I}	C^{I}	A^{II}	B^{II}	C^{II}	inductance
L_{st}	32.2	32.3	34.5	31.9	32.0	34.1	[mH]
Position 2, phase:	A^{I}	B^{I}	C^{I}	A^{II}	B^{II}	C^{II}	inductance
L_{st}	32.0	33.1	34.8	32.3	32.6	34.0	[mH]

Common-mode torque measurement

To avoid a time-variant torque during VRE tests, it is essential that the third-harmonic CM current, i_3^{cm}, required to boost V_s, does not produce a third-harmonic torque, T_3. Therefore, different levels of i_3^{cm} at a varying phase angle, ϕ, are supplied to electrical machine B to verify this. The machine-set is propelled by the DCM during this test, and the no-load torque, T_{nl}, at the test ω_m is indicated at $i_3^{\text{cm}} = 0$. In this case; $T_3 = T_{dyn}$ which measured with the dynamic TS in the setup (Figure F.2b). The resulting T_3 levels are listed for the indicated current levels in Table D.3. ϕ is thereby tuned such that i_3^{cm} is perpendicular to e_3.

Angular velocity estimations and measurements

The intended series and individual base and top angular velocity of electrical machine B are listed in the designated column of Table D.4. The top angular velocities are derived, assuming that FW is applied. The angular velocities that are obtained with VRE are denoted in the designated chapters in Part II. The actually obtained values, are computed using (3.20) and (3.21) with the values from Table D.1, as listed in the indicated column of Table D.4 assuming that $V_{inv}^{u} = 350$ V. The other VSI parameters, required to derive $|\hat{v}_1|$ for the respective FBS and FBI cases are listed in Table F.1.

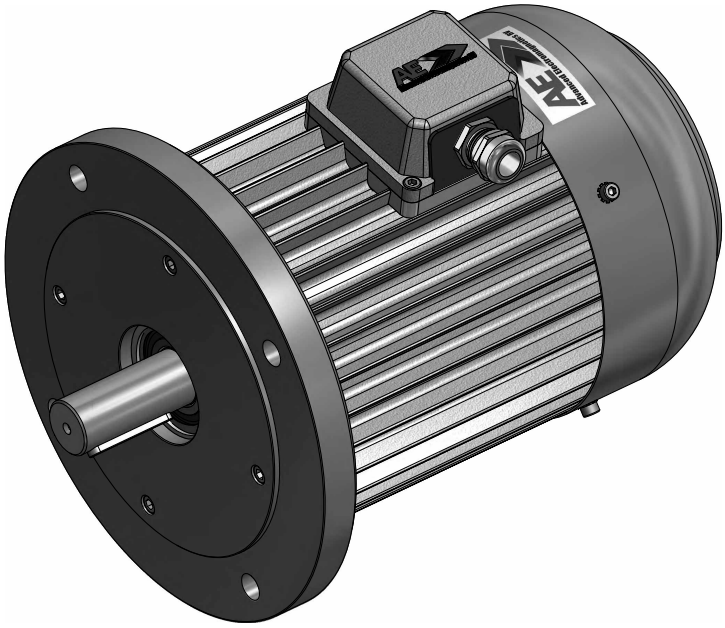

Figure D.1: Artist impression of the custom-made electrical machine B.

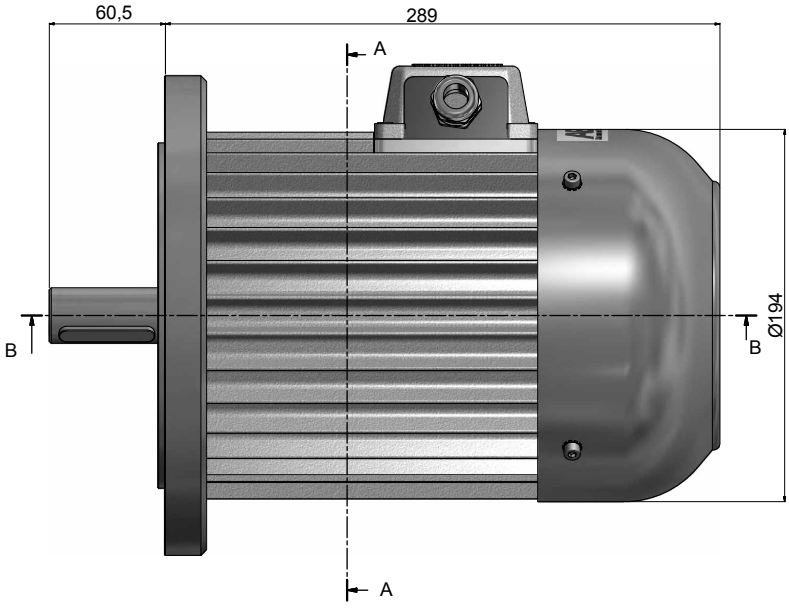

Figure D.2: Side-view of electrical machine B with dimensions and cross-section indications.

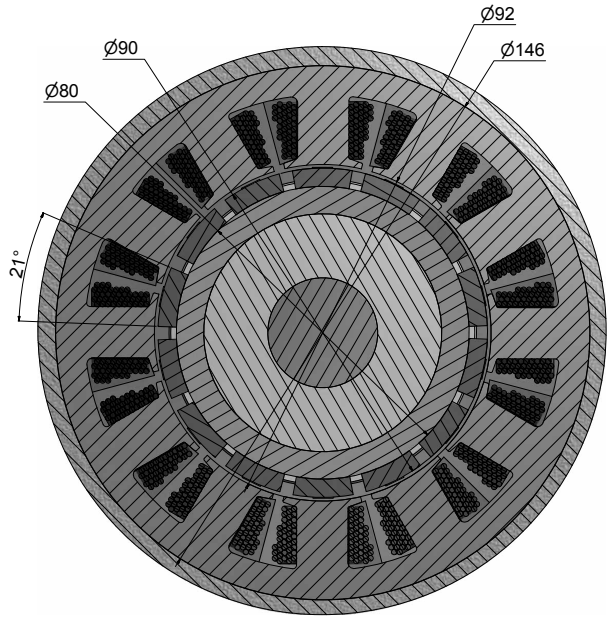

Figure D.3: Radial cross-section, A–A, of electrical machine B with dimensions.

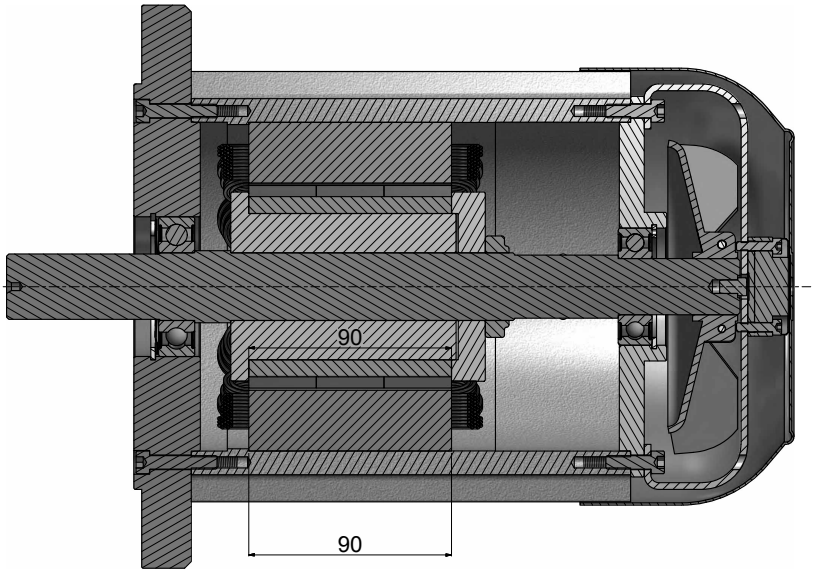

Figure D.4: Axial cross-section, B–B, of electrical machine B with dimensions.

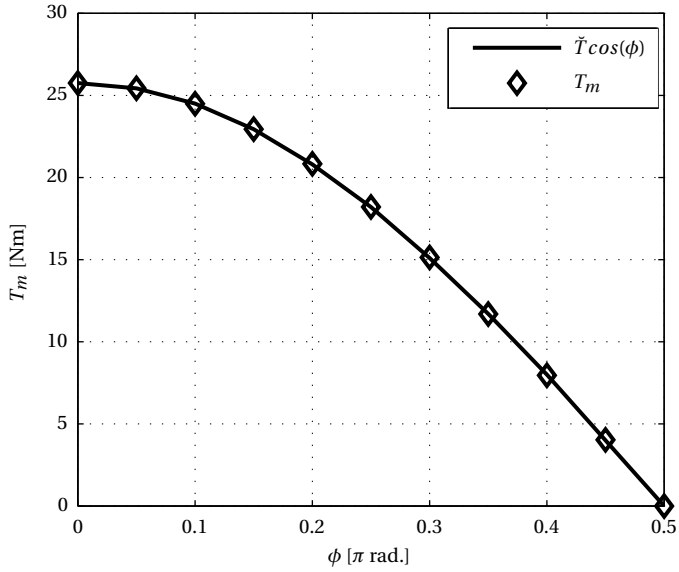

Figure D.5: Reluctance effect measurement of electrical machine B; T_m is measured for an increasing current angle ϕ to alter i_1 from i_{q1} to $-i_{d1}$, and compared to $\breve{T}\cos(\phi)$ to check whether a reluctance torque component is identified.

Table D.3: electrical machine B T_3 versus i_3^{cm}

i_3^{cm}	0	1	2	3	4	[A]
T_3	4.3	4.3	4.3	4.3	4.3	[Nm]

Table D.4: electrical machine B mechanical angular velocities applying V_{inv} = 350 V

Symbol	Intended value	Actual value	Unit
ω_b^{sr}	78.5	76.7	[rad./s]
ω_t^{sr}	314.2	277.0	[rad./s]
ω_b^{in}	157.1	159.3	[rad./s]
ω_t^{in}	628.3	558.3	[rad./s]
x_s^{sr}	4.0	3.61	[-]
x_s^{in}	4.0	3.50	[-]
x_o	8.0	7.28	[-]

E

Measurement setup A

Figure E.2 shows the measurement setup used for the experiments in Chapter 6. The drive inverters each consist of a four leg IGBT module and are controlled by a MATLAB SIMULINK model on the control system, and are interfaced via the DSPACE interface and an optical link. The measured sensor signals such as the winding currents and the rotor position are also fed back to the control system via the DSPACE interface. The DCM is angular velocity controlled and regulated from the SIMULINK model via the DC load machine regulator. The DCM field current is fixed, and supplied by the indicated variable DC supply. The DCM is coupled to the test PMSM (electrical machine A) using vibration isolators. The depicted machine-set is furthermore used for Part I, in combination with the power electronics cabinet from Appendix F in Figure F.1a.

The drive inverters are supplied by a DCM armature voltage, $V_{a(A)}$, which is propelled by a grid powered induction machine (IM) and V_{inv} is regulated by controlling the field voltage of the DCM. The regulator controlling the load DCM is a grid connected thyristor-based three-phase AC-chopper and is therefore also bidirectional. The complete string of AC, DC and mechanically connected components is bidirectional as a result, and power can circulate through the system.

The mechanical machine-set consists of a series connection of an incremental encoder (IE), load DCM, lamination couplings, and electrical machine A. The friction coefficient, B_m^A, is derived for various values of ω_m by measuring the no-load torque required to keep the set rotating at the intended ω_m. The set inertia, J_m^A is consequently determined by letting the set decelerate from $\omega_{m(\text{start})}$ to $\omega_{m(\text{stop})}$ for various angular velocity ranges and compute J_m^A based on (2.12).

The DCM is angular velocity controlled, CS_ω, by a PI controller, regulating ω_m to the intended ω_m^* by diminishing the error, Δ_ω. If $\Delta_\omega \neq 0$, CS_ω computes the intended DCM torque, T_{DCM}^*, to regulate ω_m. The intended armature current, I_a^*, is derived from T_{DCM}^* and the DCM machine constant, K_t^{DCM}, after which the difference with the measured current I_a, being Δ_I, is used to drive the MR. The armature voltage, V_a, produced by the MR drives the DCM, from which the angular velocity ω_m and current I_a are measured to regulate the respective quantities. The complete DCM controller diagram is shown in Figure E.1.

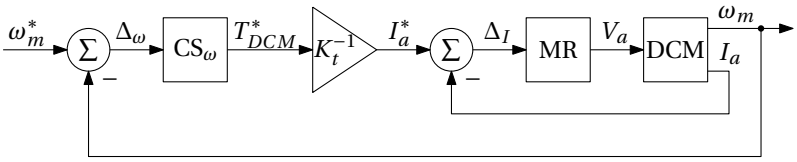

Figure E.1: Block diagram of the DCM CS used to regulate the angular velocity of the machine-set.

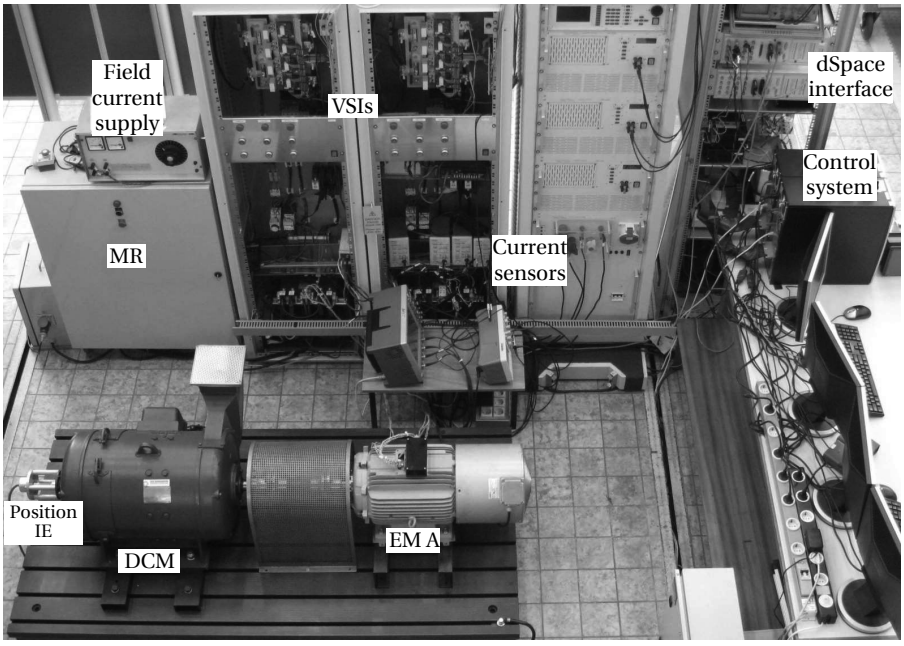

Figure E.2: Photograph of measurement setup A with the indicated components.

Concerning the main components of this measurement setup, specific technical data are given as follows:

Four-leg IGBT module

- Type: SEMIX202GB128D
- v_{br} IGBT & diode: 1200 V, 190 A (max) @ 25 ^{o}C and 135 A (max) @ 80 ^{o}C
- Applied switching frequency: 10 kHz (Gate resistor Rg = 6.8 Ω)
- IGBT conduction: forward voltage and resistance (1.7 V, 4.3 mΩ) @ 25 ^{o}C
- diode conduction: forward voltage and resistance (1.4 V, 2.8 mΩ) @ 25 ^{o}C

IGBT driver

- Type: SKYPER32
- Gate resistor (min): 2 Ω
- Switching frequency (max): 50 kHz
- Supply and input voltage: 15 V
- Output gate voltage: V_{on} = +15 V and V_{off} = -7 V

VSI DC supply, DCM A

- Type: Smit Slikkerveer G30/16
- Nominal power: 23.9 kW
- Maximum armature voltage, current ($V_{a(A)}, I_{a(A)}$): 440 V, 123 A
- Maximum field voltage, current ($V_{f(A)}, I_{f(A)}$): 220 V, 3.5 A
- Nominal ω_m: 157 rad./s
- Average machine constant over full range ($\langle K_{e(A)} \rangle = V_{a(A)}/V_{f(A)}$): 3.64

DC load machine

- Type: Siemens G 1292-4
- Nominal power: 22 kW
- Maximum armature voltage, current (V_a, I_a): 440 V, 57 A
- Maximum field voltage, current (V_f, I_f): 210..140 V, 2.3..1.5 A
- Nominal ω_m: 173 rad./s
- Machine constant ($K_e^{DCM} = K_t^{DCM}$) for I_f = 1.5 A: 2.2 Nm/A

Incremental encoder IE

- Type: Siemens V23465-H5000-M111
- Transceiver method: optical
- pulses per revolution (n_{ip}): 5000
- Interface: differential TTL

Coupled set of DCM and electrical machine A

- Inertia (J_m^A): 0.29 kgm^2
- Static friction coefficient (B_m^A): 50.9 mNms/rad.

Controller development environment

- DSPACE: DS1104 + Control-desk/real-time workshop
- MATLAB, SIMULINK
- Sample time (T_s): 100 μs
- Cycle time (T_c): $4T_s$

F

Measurement setup B

The measurement setup used for the verification of the concepts presented in Chapters 3 to 5 is specified here. The setup is built around a custom quad-VSI system from TRIPHASE [159], and controlled by a discrete MATLAB SIMULINK model running on a dedicated RTT. The model is constructed, controlled, and compiled on an EC connected to the RTT as detailed in Figure F.2a. The connections $s^{RTT}_{(I/O)}$, $s^{u}_{(I/O)}$, and s_B are all standard TCP/IP interfaced.

V_{inv}, i_{inv}, i^u_a, i^u_b, i^u_c, θ_m, and some additional current measurements are executed by an interface board on each VSI and read back via $s^{u}_{(I/O)}$. Obviously, the PWM signals are also send via $s^{u}_{(I/O)}$. The analog input (AI) signals; electrical machine B temperature, DCM A and DCM E armature voltages ($V_{a(A)}$, $V_{a(E)}$, Figure F.2b), LPF phase voltages, T_{dyn}, and some digital inputs (DIs) for safety checks and IGBT tri-state signal are read back with real-time ethernet (RTE) from the BECKHOFF™ [10] ethernet control automation technology (ECAT) interface module using s^{ECAT}_{RTE}. The BECKHOFF controlled analog output (AO) signals; DCM armature voltages, $V_{a([A,B,E,F])}$, are regulated by controlling their respective field voltages, $V_{f([A,B,E,F])}$. Additionally, the load DCM is angular velocity controlled by regulating its armature voltage, $V_{a(DCM)}$, and field current, $I_{f(DCM)}$, and thus K^{DCM}_e. The BECKHOFF controlled digital output (DO) signals are mainly used for relays to (dis)connect e.g each DCM to the VSIs, electrical machine B to the VSIs, S_s to VSI II and VSI III, and to drive S_s itself.

The mechanical machine-set consists of a series connection of the IE and load DCM detailed in Appendix E, a lamination coupling set, KTR TS, again a lamination coupling set, Apex planetary gearbox, and electrical machine B. The inertia and friction coefficient are measured in the same manner as described in Appendix E. Furthermore, the angular velocity of this mechanical set is regulated by applying the control structure shown in Figure E.1 and explained in Appendix E.

The DC voltages V^u_{inv} depicted in Figure F.2b are supplied in two different configurations; *DDO, operation*; equally powered, $V^u_{inv} = V_{a(E)} + V_{a(F)}$, *VRE operation*; different voltages powered, $V^{\mathrm{I}}_{inv} = V^{\mathrm{II}}_{inv} = V_{a(E)} + V_{a(F)}$ and $V^{\mathrm{III}}_{inv} = V^{\mathrm{IV}}_{inv} = V_{a(A)} + V_{a(B)}$. In both configurations, a balanced V_{inv} is achieved to avoid homopolar currents. During VRE operation, a CM current can return through the reference connection. The resulting DC supply voltage ranges are; $V^{\mathrm{I}}_{inv} = V^{\mathrm{II}}_{inv} = 0 - 440$ V and $V^{\mathrm{III}}_{inv} = V^{\mathrm{IV}}_{inv} = 0 - 880$ V.

Concerning the main components of this measurement setup, specific technical data are given as follows:

Planetary gearbox

- Type: APEX DYNAMICS^{TM}, AL150
- Gearbox input to output angular velocity ratio ($r_{gb} = \frac{\omega_m}{\omega_{DCM}}$): 2
- Nominal/maximum angular input velocity (ω_m): 272/545 rad./s
- Nominal/maximum output torque (T_{DCM}): 195/351 Nm
- Efficiency (η_{gb}): ≥ 97%

Dynamic torque sensor

- Type: KTR Dataflex 42/200
- Axle connections: RADEX steel servo lamination coupling
- Maximum angular input velocity (ω_m): 628 rad./s
- Rated torque (T_{dyn}): 200 Nm

Coupled set of DCM, gear, and electrical machine B

- Inertia (J_m^B): 0.17 kgm^2
- Static friction coefficient (B_m^B): 50.6 mNms/rad.

Assumed VSI IGBT parameters, S_x

- Type: SKiip25AC126V1
- IGBT & diode v_{br}: 1200 V, 73 A (max) @ 25 ^{o}C and 55 A (max) @ 70 ^{o}C
- IGBT conduction: forward voltage and resistance (1.0 V, 14 mΩ) @ 25 ^{o}C
- diode conduction: forward voltage and resistance (1.0 V, 12 mΩ) @ 25 ^{o}C
- Switching on/off/RR energy, typical: 5.8, 6.5, 5.1 mJ @ I_C = 50 A, V_{CE} = 600 V, T_J = 125 ^{o}C
- IGBT & diode conduction voltage operating range computation (V_{co}): 2 V

VSI DC supplies according to Figure F.2b

GMA

- Type: Smit Slikkerveer G30/16
- Nominal power: 23.9 kW
- Maximum armature voltage, current ($V_{a(A)}, I_{a(A)}$): 440 V, 123 A
- Maximum field voltage, current ($V_{f(A)}, I_{f(A)}$): 220 V, 3.5 A
- Nominal ω_m: 157 rad./s
- Average machine constant over full range ($\langle K_{e(A)} \rangle = V_{a(A)} / V_{f(A)}$): 3.64

GMB

- Type: Smit Slikkerveer G30/22
- Nominal power: 60 kW
- Maximum armature voltage, current ($V_{a(B)}, I_{a(B)}$): 440 V, 136 A
- Maximum field voltage, current ($V_{f(B)}, I_{f(B)}$): 220 V, 3.4 A
- Nominal ω_m: 157 rad./s
- Average machine constant over full range ($\langle K_{e(B)} \rangle = V_{a(B)} / V_{f(B)}$): 4.80

GME, GMF

- Type: HEEMAF GM 21 DCM
- Nominal power: 6 kW
- Maximum armature voltage, current ($V_{a(E/F)}, I_{a(E/F)}$): 220 V, 27.5 A
- Maximum field voltage, current ($V_{f(E/F)}, I_{f(E/F)}$): 220 V, 1.1 A
- Nominal ω_m: 151 rad./s
- Average machine constant over full range ($\langle K_{e(E)} \rangle = V_{a(E)} / V_{f(E)}$): 2.00
- Average machine constant over full range ($\langle K_{e(F)} \rangle = V_{a(F)} / V_{f(F)}$): 1.83

(a)

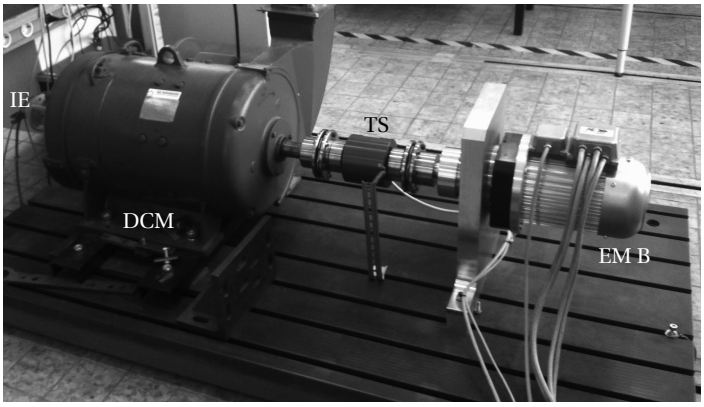

(b)

Figure F.1: Photographs of measurement setup B; **(a)** TRIPHASE power electronics cabinet with from top to bottom; quad VSI, BECKHOFF interface, control relays, thermal machine safety relays, fuses, output relays, DC input and AC output connections. **(b)** machine-set with from left to right; position IE, load DCM, dynamic TS, planetary gearbox (in the center of the aluminum mounting plate), adaptation plate, and electrical machine B.

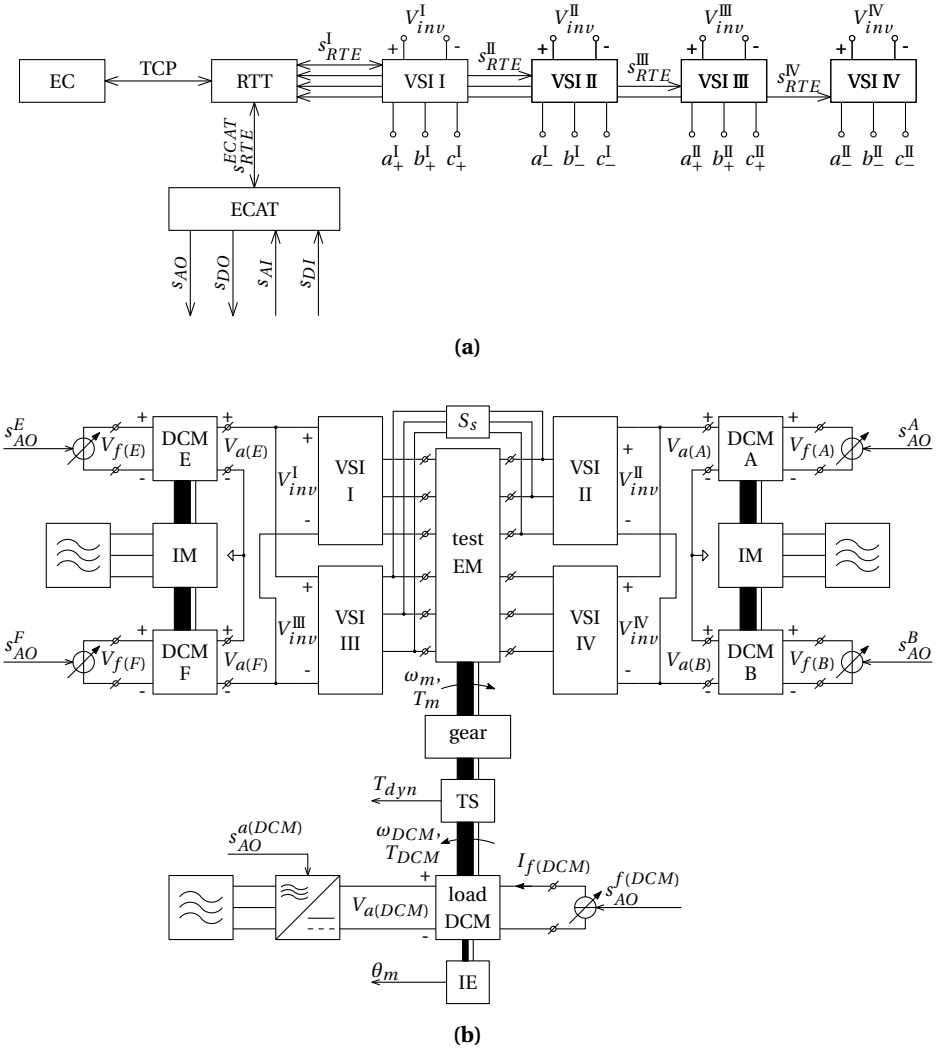

Figure F.2: Schematic representation of the interconnections within and around the TRIPHASE power electronics cabinet; **(a)** details of the RTE control I/O connections from the EC to the setup, **(b)** details of the electrical, mechanical and control connections for V^u_{inv} and the DCM. Furthermore the bidirectional power flow between the grid connected IMs, the DCM, and electrical machine B is shown.

Table F.1: TRIPHASE setup VSI parameters

Description	Symbol	Value	Unit
switching frequency	f_{sw}	4,8,16	[kHz]
modulation frequency	f_{mod}	0-800	[Hz]
BECKHOFF frequency	f_B	1	[kHz]
IGBT blanking time	t_b	2	[μs]
RTT sample time	T_s	125	[μs]
RTT delay	$\lceil k_{RTT} \rceil$	2	[periods]
PWM delay	$\lceil k_{PWM} \rceil$	1/2	[periods]
System cycle time	T_c	$(\lceil k_{RTT} \rceil + \lceil k_{PWM} \rceil)\, T_s$	[μs]
supply voltage range	V_{inv}^u	200-850	[V]
RMS phase current	I_x	33	[A]
apparent VSI power	S_{inv}^u	23	[kVA]

G

Series switch

The bidirectional series switch, S_s, used to (dis)connect the different winding sections of each phase is detailed in this appendix. The different specifications required for the experimental verification in Chapter 4 are listed, and the implemented S_s is depicted in Figure G.1. There it is shown that a quad STY139N65M5 MOSFETs series switch per-phase is constructed according to the schematic representation in Figure 4.1a. All the devices are mounted on an aluminum heat-sink, which is cooled by forcing air flow between the fins using a fan. The heat-sink surface temperature, T_S, is monitored to both trigger the fan and to turn off the series switches in case they are overheated despite the forced cooling. Throughout the simulations, the ambient temperature is considered equal to T_S. Further details on the motivations for this specific implementation are given in [6]. The applied conduction voltage of S_s, being $V_{coS_s} = 2$ V during the operating range computations in Chapter 3. The junction temperature is indicated with T_J.

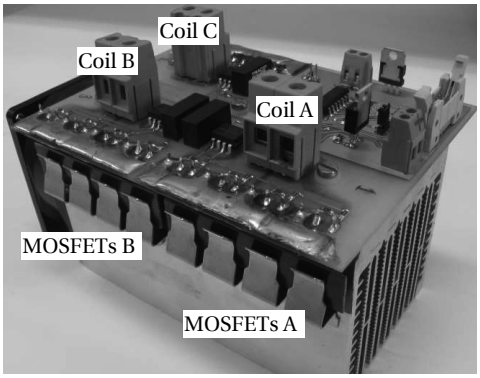

Figure G.1: Picture of the implemented series switch with two anti-series connected MOSFET pairs per-phase, the quad MOSFET set of for example phases a and b is indicated as well as the corresponding connector to connect each S_s to the HB mid-points.

Table G.1: Series Switch Loss Simulation Parameters

Description	Variable	Value	Unit
DC VSI supply voltage	V_{inv}	300	[V]
RMS source current	I_{S_s}	6.03	[A]
Ambient temperature	T_{amb}	80	[^{o}C]
Duty cycle HB devices	D	0.5	[-]

Series switch IGBT parameters, $S_{s(IGBT)}$

- Type: IXRH40N120
- IGBT breakdown voltage rating, v_{br}: 1200 V
- IGBT RMS collector current, I_C: 55 A (max) @ $T_S = 25\ ^oC$, 35 A (max) @ $T_S = 90\ ^oC$
- IGBT conduction: forward voltage: 2.3 V @ $I_C = 30$ A, $T_J = 25\ ^oC$

Series switch MOSFET parameters, $S_{s(MOSFET)}$

- Type: STY139N65M5
- MOSFET breakdown voltage rating, v_{br}: 650 V
- MOSFET RMS drain current, I_D: 130 A (max) @ $T_J = 25\ ^oC$, 78 A (max) @ $T_J = 100\ ^oC$
- MOSFET conduction resistance, $R_{DS(on)}$: 14 mΩ @ $I_D = 65$ A, $V_{GS} = 10$ V, $T_J = 25\ ^oC$
- MOSFET diode conduction forward voltage, V_{SD}: 1.5 V @ $I_D = -130$ A

Switching loss versus conduction loss comparison VSI IGBT parameters, S_x

- Type: SK50GB067
- IGBT & diode breakdown voltage rating, v_{br}: 600 V @ $T_J = 25\ ^oC$
- IGBT collector current rating, I_C: 83 A @ $T_J = 125\ ^oC$
- IGBT conduction forward voltage, V_{CE}: 2.0 V @ 40 A, 3.0 V @ 120 A ($T_J = 125\ ^oC$)
- IGBT conduction resistance, R_{CE}: 12.5 mΩ @ $T_J = 150\ ^oC$
- diode conduction forward voltage, resistance: 1.25 V, 4 mΩ @ $T_J = 150\ ^oC$
- Switching on/off/RR energy, typical: 7.5,2.5,1.6 mJ @ $I_C = 120$ A, $V_{CE} = 400$ V, $T_J = 125\ ^oC$

Nomenclature

Symbols

Symbol	Unit	Description
A	[-]	modulation amplitude
A_F	[m^2]	aerodynamic frontal area
a	[m/s^2]	acceleration
B	[Nms/rad.]	bearing friction
C	[F]	capacitance
C_d	[-]	aerodynamic drag coefficient
D	[-]	duty-cycle
D	[-]	diode
E_{spe}	[Wh/kg]	specific energy
e	[V]	EMF; AC, instantaneous, or magnitude
F_A	[N]	aerodynamic drag force
F_a	[N]	acceleration force
F_d	[N]	drag force
F_g	[N]	gravitational force
F_r	[N]	rolling resistance force
F_s	[N]	slip force
F_t	[N]	traction force
F_z	[N]	normal force on tyres
f	[Hz]	frequency
f_B	[Hz]	BECKHOFF frequency
f_{mod}	[Hz]	modulation frequency
f_r	[-]	rolling resistance coefficient
f_{sw}	[Hz]	switching frequency
I	[A]	current; DC, RMS, or amplitude
i	[A]	current; AC, instantaneous, or magnitude
J	[kgm^2]	inertia
j	[-]	imaginary unit, $\sqrt{-1}$
K_{br}	[-]	relative breakdown voltage rate
K_e	[Vs/rad.]	electrical machine constant
K_t	[Nm/A]	torque machine constant
k	[periods]	number of discrete periods relative to T_s
k_{ab}	[-]	magnetic coupling factor between in this case a and b

Symbol	Unit	Description
L	[H]	inductance
M	[H]	mutual inductance
m	[kg]	mass
m	[-]	modulation signal for PWM
N_x	[-]	number of x (indicated by subscript)
n	[-]	harmonic number
P	[W]	active power
p	[W]	instantaneous power
Q	[VAr]	reactive power
R	[Ω]	resistance
r	[m]	radius
r_{gb}	[-]	gearbox ratio
r_i	[-]	current ratio
S	[VA]	apparent power
S_s	[-]	series connection switch
S_x	[-]	switching leg switch
s	[-]	steering signal
s_N	[-]	normalized wheel slip
T	[^{o}C]	temperature
T	[Nm]	torque
$\mathbf{T}$	[-]	transformation matrix
T_{amb}	[^{o}C]	ambient temperature
T_c	[s]	cycle time
T_{dyn}	[Nm]	dynamic torque measured by sensor
T_s	[s]	sample time
t	[s]	time
t_a	[s]	acceleration time
t_b	[s]	blanking time
u	[m/s]	speed
V	[V]	voltage; DC, RMS, or amplitude
V_{inv}	[V]	inverter DC supply voltage
v	[V]	voltage; AC, instantaneous, or magnitude
v_{br}	[V]	breakdown voltage of semiconductor device
v_{dev}	[V]	instantaneous semiconductor device voltage
$\mathbf{W}$	[-]	transformation function matrix
x	[$\star$]	general variable in transformations
x_o	[-]	overall system angular velocity ratio
x_r	[-]	angular velocity ratio relative to ω_b
x_s	[-]	angular velocity ratio
α	[rad.]	angle between the $\Re$-axis and the stationary reference frame horizontal axis

Symbol	Unit	Description
α_r	[rad.]	angle between earth surface and road
β	[rad.]	angle between the $\Im$-axis and the stationary reference frame vertical axis
Δ	[$\star$]	error, difference between reference and actual value
δ	[rad.]	angle between voltages
ζ	[Nm/s]	angular jerk
η_{gb}	[%]	gearbox efficiency
η_{sys}	[%]	system efficiency
θ	[rad.]	angular position
Λ	[Wb]	magnetic flux linkage
λ	[Wb]	magnetic flux
Π, Γ	[$\star$]	magnitude, amplitude of CM quantity
ϕ	[rad.]	angle between currents
φ	[rad.]	angle between voltage and current
ω	[rad./s]	angular velocity

Superscripts

Symbol	Description
$*$	reference value
bm, cm	balanced-mode, common-mode
f,h	indication for faulty, healthy situation
set, sr, in, u	winding number; set, series, individual, winding u
T, $\dagger$	transpose, inverse transformation
x, y	projection coordinates of phasor on real-, imaginary-axis
FW	field weakening
VRE	voltage range enhancement

Subscripts

Symbol	Description
$\vee, \llcorner, \equiv$	rotating orthogonal, stationary orthogonal, three-phase
$(\triangle, \triangledown), (\blacktriangle, \blacktriangledown)$	S_x device indication; left-leg (up,down), right-leg (up,down)
$\blacktriangleleft, \blacktriangleright$	S_s device indication; left, right
$1, 3, n$	harmonic number
A, i, x, δ	index for size of different matrices

* Unit depends on context

Symbol	Description
a, b, c	machine phases
a, f	armature, field
b, t	base, top
C, G, E	collector, gate, emitter connection of an IGBT
cc, sc	cross-conduction, short-circuit
co, sw	conduction, switching
D, G, S	drain, gate, source connection of a MOSFET
d, q	rotating orthogonal reference frame direct-, quadrature-axis
g	ground
h	rotating orthogonal reference frame homopolar-line
inv, bat, ll	inverter, battery, line-to-line
J, S	junction, surface (semiconductor temperature)
l, nl, dyn	load, no-load, dynamic
m, em, e	mechanical, electromagnetic, electric
m	magnet, in relation to flux (linkage)
on, off	indicating the state; on or off
p, s	primary, secondary
pe, re, hy, fr	power electronics, resistive, hysteresis, friction
ph, wi, tu, sl	phase, winding, turn, slot
pp, sp	rotor pole pairs, stator poles
r, v, w, gb	road, vehicle, wheels, gearbox
ss, spe	steady state, specific
st, r	stator, rotor
start,stop	start, stop condition
x, y	general phase indication, general inverter indication
α, β, γ	stationary orthogonal reference frame axis
κ, ν, ς	counter variables
CS	control system
DCM	DC machine
SVM	wye connected, SVM operated
WYE	wye connected, linear PWM operated

Acronyms

CPSR	constant-power speed region 27
CS	control system 5
CTSR	constant-torque speed region 27
CVT	continuously variable transmission 80
DC	direct current 3
DCM	DC machine 3
DDO	dynamic drive operation 16
DI	digital input 201
DO	digital output 201
$d1, q1$	fundamental angular velocity direct-, quadrature-axis 22
dn, qn	n^{th}-harmonic of $d1, q1$ 42
EC	engineering computer 73
ECAT	ethernet control automation technology 201
EMF	back electromotive force 36
EV	electrical vehicle 2
EVP	electrical vehicle propulsion 3
FB	full-bridge 31
FBI	FB individual 61
FBS	FB series 61
FEA	finite-element analysis 45
FF	feed-forward 46
FT	Fourier transform 45
FTO	fault-tolerant operation 17
FW	field weakening 8
HB	half-bridge 32
ICE	internal combustion engine 1
IE	incremental encoder 197
IGBT	insulated-gate bipolar transistor 75
IM	induction machine 197
KVL	Kirchhoff voltage law 24
LPF	low-pass filter 48
MMF	magnetomotive force 144
MOSFET	metal-oxide-semiconductor field-effect transistor 81
MR	machine regulator 113
MTPA	maximum torque per-Ampère 55
PF	power factor 34
PI	proportional and integral 71
PM	permanent magnet 4
PMSM	permanent magnet synchronous machine 11
PWM	pulse width modulation 27
RB	reverse blocking 82
RMS	root mean square 15

RPM	revolutions per-minute	11
RR	reverse-recovery	68
RTE	real-time ethernet	201
RTT	real-time target	72
SMPS	switched-mode power supply	15
SPMSM	surface permanent magnet synchronous machine	23
SVM	space vector modulation	27
TS	torque sensor	131
VRE	voltage range enhancement	17
VSI	voltage source inverter	5
ZOH	zero-order-hold	114
ZS	zero-sequence	99

Physical constants

Constant	Value	Unit	Quantity
ρ_a	1.225	[kg/m^3]	mass density of air @ 15 ^{o}C and sea level
g	9.81	[m/s^2]	gravitational acceleration

General conventions

Symbol	Description
$\Re(\cdot), \Im(\cdot)$	real, imaginary part
j	imaginary unit, $j = \sqrt{-1}$
x	scalar or instantaneous value
$\langle x \rangle, \check{x}, \tilde{x}$	average, nominal, estimated value
$(x), [x]$	continuous-time, discrete-time
X	time-invariant or steady state value (DC, RMS, phasor amplitude)
$\vec{x}$	two or three dimensional vector
$\underline{X}$	phasor ($\underline{X} \triangleq Xe^{j\phi}$), steady state representation of periodic signal
$\lvert\vec{x}\rvert, \lvert\underline{x}\rvert$	magnitude of $\vec{x}$, amplitude of $\underline{x}$
$\angle\underline{x}$	argument of $\underline{x}$
$\mathbf{x}$	row or column vector
$\mathbf{x}^{\mathrm{T}}, \mathbf{x}^{\dagger}$	transpose of $\mathbf{x}$, inverse transformation of $\mathbf{x}$
$\mathbf{X}$	matrix

Bibliography

[1] 24/7 Wallst. http://www.247wallst.com/special-report/2012/01/26/the-best-selling-cars-of-all-time/. Cited on pages 3 and 9.

[2] Advanced Electromagnetics. http://www.ae-grp.nl/. Cited on page 191.

[3] H. Akagi, E. Watanabe, and M. Aredes, *Instantaneous Power Theory and Applications to Power Conditioning*, I. press editorial board, Ed. Wiley-IEEE Press, 2007. Cited on page 36.

[4] P. Alger, *Induction Machines: Their Behavior and Uses*, 2nd ed. Gordon and Breach, 1970. Cited on page 40.

[5] Autoweek, subsidiary company of Sanoma Media Netherlands B.V. http://www.autoweek.nl/auto/12171/toyota-corolla-16-gxi. Cited on page 9.

[6] N. H. Baars, "Bidirectional switch," 2013, unpublished paper. Cited on pages 83, 84, and 207.

[7] T. L. Balyovski, E. Ilhan, Y. Tang, C. G. E. Wijnands, J. J. H. Paulides, and E. A. Lomonova, "Control of DC-excited flux switching machines for traction applications," in *Ecological Vehicles and Renewable Energies (EVER), 9th International Conference and Exhibition on*, 2014. Cited on page 35.

[8] Bayerische motoren werke, (BMW) AG. http://www.bmw.com. Cited on page 168.

[9] A. M. Bazzi, "Electric machines and energy storage technologies in EVs and HEVs for over a century," in *Electric Machines & Drives Conference (IEMDC), 2013 IEEE International*. IEEE, 2013, pp. 212–219. Cited on page 23.

[10] Beckhoff Automation GmbH. http://www.beckhoff.com/. Cited on page 201.

[11] K. Benz and Co., "Fahrzeug mit gasmotorenbetrieb," German Patent 37 435, 1886. Cited on page 1.

[12] F. Blaschke, "Das verfahren der feldorientierung zur regelung der drehfeldmaschine," Ph.D. dissertation, University of Braunschweig, 1973, in German. Cited on page 22.

[13] S. Bolognani, M. Zordan, and M. Zigliotto, "Experimental fault-tolerant control of a PMSM drive," *IEEE Transactions on Industrial Electronics*, vol. 47, no. 5, pp. 1134–1141, 2000. Cited on page 138.

[14] S. G. Bosga, "Asymmetrical supply of induction machines: remedial operating strategies in case of converter faults," Ph.D. dissertation, Eindhoven University of Technology, 1997. Cited on pages 39 and 138.

[15] M. G. J. v. d. Brand and J. F. Groote, "Software engineering: Redundancy is key," *Science of Computer Programming*, vol. 97, Part 1, no. 0, pp. 75 – 81, 2013, special Issue on New Ideas and Emerging Results in Understanding Software. Cited on page 138.

[16] H. W. v. d. Broeck, H. C. Skudelny, and G. V. Stanke, "Analysis and realization of a pulsewidth modulator based on voltage space vectors," *Industry Applications, IEEE Transactions on*, vol. 24, no. 1, pp. 142–150, 1988. Cited on pages 31 and 65.

[17] R. W. Campbell, "Vehicle propulsion and control system," Jan. 10 1967, uS Patent 3,297,926. Cited on pages 33 and 89.

[18] J. Cao, N. Schofield, and A. Emadi, "Battery balancing methods: A comprehensive review," in *Vehicle Power and Propulsion Conference, 2008. VPPC'08. IEEE*. IEEE, 2008, pp. 1–6. Cited on pages 4 and 5.

[19] F. Caricchi, F. Crescimbini, F. Mezzetti, and E. Santini, "Multistage axial-flux PM machine for wheel direct drive," *IEEE Transactions on Industry Applications*, vol. 32, no. 4, pp. 882–888, 1996. Cited on pages 11, 13, and 33.

[20] M. Caris, H. Huisman, J. Schellekens, and J. Duarte, "Generalized harmonic elimination method for interleaved power amplifiers," in *IECON 2012 - 38th Annual Conference on IEEE Industrial Electronics Society*, October 2012, pp. 4979–4984. Cited on page 5.

[21] B. J. Chalmers, L. Musaba, and D. F. Gosden, "Performance characteristics of synchronous motor drives with surface magnets and field weakening," in *Proc. Conf Industry Applications Conf. Thirty-First IAS Annual Meeting, IAS '96. Record of the 1996 IEEE*, vol. 1, 1996, pp. 511–517. Cited on pages 23 and 183.

[22] B. J. Chalmers, L. Musaba, and D. F. Gosden, "Variable-frequency synchronous motor drives for electric vehicles," *Industry Applications, IEEE Transactions on*, vol. 32, no. 4, pp. 896–903, 1996. Cited on page 183.

[23] P. L. Chapman and S. D. Sudhoff, "A multiple reference frame synchronous estimator/regulator," *Energy Conversion, IEEE Transactions on*, vol. 15, no. 2, pp. 197–202, 2000. Cited on pages 41 and 48.

[24] P. L. Chapman, S. D. Sudhoff, and C. A. Whitcomb, "Multiple reference frame analysis of non-sinusoidal brushless DC drives," *Energy Conversion, IEEE Transactions on*, vol. 14, no. 3, pp. 440–446, 1999. Cited on page 41.

[25] C. Chen and J. Angeles, "Virtual-power flow and mechanical gear-mesh power losses of epicyclic gear trains," *Journal of Mechanical Design*, vol. 129, no. 1, pp. 107–113, 2007. Cited on page 11.

[26] Y. Dajsuren, M. G. J. van den Brand, A. Serebrenik, and S. Roubtsov, "Simulink models are also software: Modularity assessment," in *Proceedings of the 9th international ACM Sigsoft conference on Quality of software architectures*. ACM, 2013, pp. 99–106. Cited on page 138.

[27] R. W. De Doncker and J. P. Lyons, "The auxiliary resonant commutated pole converter," in *Industry Applications Society Annual Meeting, 1990., Conference Record of the 1990 IEEE*, October 1990, pp. 1228 –1235 vol.2. Cited on page 81.

[28] R. De Doncker, D. W. Pulle, and A. Veltman, *Advanced Electrical Drives: Analysis, Modeling, Control*. Springer, 2010. Cited on pages 8 and 22.

[29] Delta Elektronika BV. http://www.delta-elektronika.nl. Cited on pages 15 and 60.

[30] L. A. M. v. Dongen, *Efficiency Characteristics of Manual and Automatic Passenger Car Transaxles*. Society of Automotive Engineers, 1982, in Dutch. Cited on pages 3 and 4.

[31] H. J. v. Doorne and H. H. J. Ludoph, "Flexible continuous power transmission means," March 1973, uS Patent 3,720,113. Cited on page 80.

[32] W. C. Duesterhoeft, M. W. Schulz, and E. Clarke, "Determination of instantaneous currents and voltages by means of alpha, beta, and zero components," *American Institute of Electrical Engineers, Transactions of the*, vol. 70, no. 2, pp. 1248–1255, 1951. Cited on pages 47 and 183.

[33] B. Eberleh and T. Hartkopf, "A high speed induction machine with two-speed transmission as drive for electric vehicles," in *Power Electronics, Electrical Drives, Automation and Motion, 2006. SPEEDAM 2006. International Symposium on*, May 2006, pp. 249 –254. Cited on pages 11 and 13.

[34] E. Echenique, O. Keysan, and M. Mueller, "Rotor loss prediction in air-cored permanent magnet machines," in *Electric Machines Drives Conference (IEMDC), 2013 IEEE International*, May 2013, pp. 303–310. Cited on page 46.

[35] M. Ehsani, Y. Gao, and S. Gay, "Characterization of electric motor drives for traction applications," in *Proc. 29th Annual Conf. of the IEEE Industrial Electronics Society IECON '03*, vol. 1, 2003, pp. 891–896. Cited on page 9.

[36] (2011, January) Communication from the commission to the european parliament, the council, the european economic and social committee and the committee of the regions; a resource-efficient Europe - flagship initiative under the Europe 2020 strategy. European commission. http://ec.europa.eu. Cited on page 14.

[37] (2011, June) Market observatory for energy; key figures. European commission. http://ec.europa.eu. Cited on page 14.

[38] European road transport research advisory council, "multi-annual implementation plan for horizon 2020," March 2013. Cited on page 14.

[39] J. Everts, "Modeling and optimization of bidirectional dual active bridge AC-DC converter topologies," Ph.D. dissertation, Arenberg doctoral school, 2014. Cited on page 5.

[40] J. Ewanchuk, J. Salmon, and C. Chapelsky, "A method for supply voltage boosting in an open-ended induction machine using a dual inverter system with a floating capacitor bridge," *Power Electronics, IEEE Transactions on*, vol. 28, no. 3, pp. 1348–1357, March 2013. Cited on pages 34 and 98.

[41] M. Faraday, "On some new electro-magnetical motions, and on the theory of magnetism," vol. 12, pp. 74–96, 1822. Cited on page 2.

[42] T. Finken, M. Felden, and K. Hameyer, "Comparison and design of different electrical machine types regarding their applicability in hybrid electrical vehicles," in *Proc. 18th Int. Conf. Electrical Machines ICEM 2008*, 2008, pp. 1–5. Cited on page 4.

[43] F. Forest, E. Laboure, T. A. Meynard, and J. J. Huselstein, "Multicell interleaved flyback using intercell transformers," *IEEE Transactions on Power Electronics*, vol. 22, no. 5, pp. 1662–1671, 2007. Cited on pages 5, 15, 58, and 60.

[44] C. Fortescue, "Method of symmetrical co-ordinates applied to the solution of polyphase networks," *American Institute of Electrical Engineers, Transactions of the*, vol. XXXVII, no. 2, pp. 1027–1140, July 1918. Cited on page 36.

[45] A. Fratta, P. Guglielmi, F. Villata, and A. Vagati, "Efficiency and cost-effectiveness of AC drives for electric vehicles improved by a novel, boost DC-DC conversion structure," in *Proc. Power Electronics in Transportation*, 1998, pp. 11–19. Cited on page 32.

[46] V. Fynn, "A new single-phase commutator motor," *Electrical Engineers, Journal of the Institution of*, vol. 36, no. 177, pp. 324–367, April 1906. Cited on page 4.

[47] F. Gao, L. Zhang, Q. Zhou, M. Chen, T. Xu, and S. Hu, "State-of-charge balancing control strategy of battery energy storage system based on modular multilevel

converter," in *Energy Conversion Congress and Exposition (ECCE), 2014 IEEE*, September 2014, pp. 2567–2574. Cited on page 5.

[48] T. Gerrits, "Comparison of semiconductor losses in a PWM-voltage source inverter," 2009. Cited on page 82.

[49] T. Gerrits, J. L. Duarte, C. G. E. Wijnands, E. A. Lomonova, J. J. H. Paulides, and L. Encica, "Twelve-phase open-winding SPMSM development for speed dependent reconfigurable traction drive," in *Proceedings of the Tenth International Conference on Ecological Vehicles and Renewable Energies (EVER)*, 2015. Cited on pages 55 and 117.

[50] T. Gerrits, C. G. E. Wijnands, J. J. H. Paulides, and J. L. Duarte, "Electrical gearbox equivalent by means of dynamic machine operation," in *Power Electronics and Applications (EPE 2011), Proceedings of the 2011-14th European Conference on*, August - September 2011, pp. 1 –10. Cited on page 55.

[51] T. Gerrits, C. G. E. Wijnands, J. J. H. Paulides, and J. L. Duarte, "Fault-tolerant operation of a fully electric gearbox equivalent," in *IECON 2011 - 37th Annual Conference on IEEE Industrial Electronics Society*, November 2011, pp. 3686 –3691. Cited on page 138.

[52] T. Gerrits, C. G. E. Wijnands, J. J. H. Paulides, and J. L. Duarte, "Dual voltage source inverter topology extending machine operating range," in *Energy Conversion Congress and Exposition (ECCE), 2012 IEEE*, September 2012, pp. 2840 –2846. Cited on page 98.

[53] T. Gerrits, C. G. E. Wijnands, J. J. H. Paulides, and J. L. Duarte, "Fault-tolerant operation of a fully electric gearbox equivalent," in *Industry Applications, IEEE Transactions on*, vol. 48, no. 6, November - December 2012, pp. 1855 – 1865. Cited on pages 31 and 138.

[54] T. Gerrits, C. G. E. Wijnands, J. J. H. Paulides, and J. L. Duarte, "Dynamic machine operation transitions," in *9th Vehicle Power and Propulsion Conference (VPPC)*. IEEE, October 2013, pp. 132 – 137. Cited on page 89.

[55] T. Gerrits, C. G. E. Wijnands, J. J. H. Paulides, and J. L. Duarte, "Loss minimization of boost mode dual inverter drive system," in *Power Electronics and Applications (EPE 2013), Proceedings of the 2013-15th European Conference on*, September 2013. Cited on page 106.

[56] T. Gerrits, C. G. E. Wijnands, J. J. H. Paulides, J. L. Duarte, and E. A. Lomonova, "Machine integrated gearbox for electric vehicles," in *Fisita 2014 - World Automotive Congress*, June 2014, pp. 1–10. Cited on page 55.

[57] J. J. Goedbloed, *Elektromagnetische compatibiliteit: analyse en onderdrukking van stoorproblemen*. Ten Hagen en Stam, 2000, in Dutch. Cited on page 36.

[58] M. Goetz, M. C. Levesley, and D. A. Crolla, "Dynamics and control of gearshifts on twin-clutch transmissions," *Proceedings of the institution of mechanical engineers, Part D: Journal of Automobile Engineering*, vol. 219, no. 8, pp. 951–963, 2005. Cited on pages 89 and 91.

[59] T. Gopalarathnam, H. Toliyat, and J. Moreira, "Multi-phase fault-tolerant brushless dc motor drives," in *Industry Applications Conference, 2000. Conference Record of the 2000 IEEE*, vol. 3, 2000, pp. 1683–1688 vol.3. Cited on page 138.

[60] S. Gunturi and D. Schneider, "On the operation of a press pack igbt module under short circuit conditions," *Advanced Packaging, IEEE Transactions on*, vol. 29, no. 3, pp. 433–440, August 2006. Cited on page 140.

[61] B. L. J. Gysen, E. Ilhan, K. J. Meessen, J. J. H. Paulides, and E. A. Lomonova, "Modeling of flux switching permanent magnet machines with fourier analysis," *Magnetics, IEEE Transactions on*, vol. 46, no. 6, pp. 1499–1502, June 2010. Cited on page 36.

[62] P. W. Hammond, "Enhancing the reliability of modular medium-voltage drives," *IEEE Transactions on Industrial Electronics*, vol. 49, no. 5, pp. 948–954, 2002. Cited on pages 138, 139, and 147.

[63] D. C. Hanselman, "Minimum torque ripple, maximum efficiency excitation of brushless permanent magnet motors," *Industrial Electronics, IEEE Transactions on*, vol. 41, no. 3, pp. 292–300, 1994. Cited on pages 38 and 45.

[64] J. Haylock, B. Mecrow, A. Jack, and D. Atkinson, "Operation of a fault tolerant pm drive for an aerospace fuel pump application," in *Electrical Machines and Drives, 1997 Eighth International Conference on (Conf. Publ. No. 444)*, September 1997, pp. 133–137. Cited on pages 139 and 144.

[65] J. R. Hendershot and T. J. E. Miller, *Design of brushless permanent-magnet machines*. Motor Design Books, 2010. Cited on pages 22, 28, 39, 45, 99, and 139.

[66] M. J. Hoeijmakers and J. A. Ferreira, "The electric variable transmission," *Industry Applications, IEEE Transactions on*, vol. 42, no. 4, pp. 1092–1100, 2006. Cited on page 80.

[67] I. Hofman, P. Sergeant, and A. Vandenbossche, "Optimization of motor and gearbox for an ultra light electric vehicle," in *Fisita 2014 - World Automotive Congress*, 2014. Cited on page 11.

[68] J. Hong, H. Lee, and K. Nam, "Charging method for the second battery in dual inverter drive systems for electric vehicles," in *Applied Power Electronics Conference and Exposition (APEC), 2014 Twenty-Ninth Annual IEEE*, 2014, pp. 2407–2414. Cited on pages 34, 55, and 60.

[69] M. F. Hsieh, F. S. Hsu, and D. G. Dorrell, "Winding changeover permanent-magnet generators for renewable energy applications," *Magnetics, IEEE Transactions on*, vol. 48, no. 11, pp. 4168–4171, 2012. Cited on page 168.

[70] W. Hua, M. Cheng, Z. Q. Zhu, and D. Howe, "Design of flux-switching permanent magnet machine considering the limitation of inverter and flux-weakening capability," in *Industry Applications Conference, 2006. 41st IAS Annual Meeting. Conference Record of the 2006 IEEE*, vol. 5, October 2006, pp. 2403–2410. Cited on page 36.

[71] H. Huisman, "Zero-ripple torque control in brushless DC motors: a straightforward approach," in *Power Electronics and Applications (EPE 1995), Proceedings of the 1995-6th European Conference on*, 1995, pp. 3851–3856. Cited on page 45.

[72] I. Husain, *Electric and hybrid vehicles: design fundamentals*. CRC press, 2011. Cited on pages 3, 6, 22, and 27.

[73] E. Ilhan, T. L. Balyovski, J. J. H. Paulides, and E. A. Lomonova, "Servo flux switching PM machines," in *Electrical Machines (ICEM), XXIth International Conference on*, 2014. Cited on page 36.

[74] E. Ilhan, M. F. J. Kremers, T. E. Motoasca, J. J. H. Paulides, and E. A. Lomonova, "Nonlinear performance characteristics of flux-switching PM motors," *Journal of Engineering*, vol. 2013, 2012. Cited on page 36.

[75] Infineon Technologies AG. http://www.infineon.com/. Cited on pages 31 and 75.

[76] Y. Inoue, S. Morimoto, and M. Sanada, "Examination and linearization of torque control system for direct torque controlled ipmsm," *Industry Applications, IEEE Transactions on*, vol. 46, no. 1, pp. 159–166, January 2010. Cited on page 90.

[77] Integrated control systems (IXYS). http://www.ixys.com. Cited on pages 31 and 83.

[78] J. Jacob, B. Rosca, and S. Wilkins, "Battery pack modelling from the perspective of battery management systems," in *Proceedings of the third European Electric Vehicle Congress (EEVC), Brussels*, 2014. Cited on page 4.

[79] T. Jahns, "Improved reliability in solid-state ac drives by means of multiple independent phase drive units," *Industry Applications, IEEE Transactions on*, vol. IA-16, no. 3, pp. 321–331, May 1980. Cited on page 139.

[80] T. Jahns, "Flux-weakening regime operation of an interior permanent-magnet synchronous motor drive," *Industry Applications, IEEE Transactions on*, vol. IA-23, no. 4, pp. 681–689, July 1987. Cited on pages 29 and 117.

[81] T. Kato, N. Limsuwan, C. Yu, K. Akatsu, and R. D. Lorenz, "Rare earth reduction using a novel variable magnetomotive force, flux intensified IPM machine," in

Energy Conversion Congress and Exposition (ECCE), 2012 IEEE, September 2012, pp. 4346 –4353. Cited on page 35.

[82] J. Kim, J. Jung, and K. Nam, "Dual-inverter control strategy for high-speed operation of EV induction motors," *Industrial Electronics, IEEE Transactions on*, vol. 51, no. 2, pp. 312 – 320, April 2004. Cited on pages 34, 98, and 110.

[83] J. W. Kolar. (2013, July) Envision on future power electronics. ETH. Zurich. Cited on page 60.

[84] J. W. Kolar, R. S. Wieser, and H. Ertl, "Analysis of a wide speed range starter/alternator system based on a novel converter topology for series/parallel stator winding configuration," in *Industry Applications Conference, 1999. Thirty-Fourth IAS Annual Meeting. Conference Record of the 1999 IEEE*, vol. 4. IEEE, 1999, pp. 2631–2641. Cited on page 33.

[85] J. W. Kolar and F. C. Zach, "A novel three-phase utility interface minimizing line current harmonics of high-power telecommunications rectifier modules," in *Telecommunications Energy Conference, 1994. INTELEC '94., 16th International*, October - November 1994, pp. 367 –374. Cited on page 81.

[86] A. Kolli, O. Bethoux, A. De Bernardinis, E. Laboure, and G. Coquery, "Space-vector PWM control synthesis for an H-bridge drive in electric vehicles," *Vehicular Technology, IEEE Transactions on*, vol. 62, no. 6, pp. 2441–2452, 2013. Cited on pages 31, 65, and 117.

[87] R. Krishnan, *Electric motor drives: modeling, analysis, and control*. Prentice Hall Englewood Cliffs, 2001, vol. 626. Cited on pages 4, 8, 22, 28, 55, and 102.

[88] T. Kume, T. Iwakane, T. Sawa, T. Yoshida, and I. Nagai, "A wide constant power range vector-controlled AC motor drive using winding changeover technique," *IEEE Transactions on Industry Applications*, vol. 27, no. 5, pp. 934–939, 1991. Cited on page 33.

[89] M. S. Kwak and S. K. Sul, "Flux weakening control of an open winding machine with isolated dual inverters," in *Proc. 42nd IAS Annual Meeting Industry Applications Conf. Conf. Record of the 2007 IEEE*, 2007, pp. 251–255. Cited on page 41.

[90] S. Lacroix, E. Laboure, and M. Hilairet, "An integrated fast battery charger for electric vehicle," in *Proc. IEEE Vehicle Power and Propulsion Conf. (VPPC)*, 2010, pp. 1–6. Cited on page 168.

[91] W. Leonhard, *Control of electrical drives*, 2nd ed. Springer, 1996. Cited on page 40.

[92] A. Lesnicar and R. Marquardt, "An innovative modular multilevel converter topology suitable for a wide power range," in *Proc. IEEE Bologna Power Tech*, vol. 3, 2003. Cited on pages 5 and 138.

[93] E. Levi, "Multiphase electric machines for variable-speed applications," *Industrial Electronics, IEEE Transactions on*, vol. 55, no. 5, pp. 1893–1909, 2008. Cited on pages 5, 33, and 139.

[94] T. Li and G. Slemon, "Reduction of cogging torque in permanent magnet motors," *Magnetics, IEEE Transactions on*, vol. 24, no. 6, pp. 2901–2903, November 1988. Cited on page 45.

[95] C. Liaw and H. Chang, "An integrated driving/charging switched reluctance motor drive using three-phase power module," *IEEE Transactions on Industrial Electronics*, no. 99, 2010, early Access. Cited on page 168.

[96] L. d. Lillo, L. Empringham, P. W. Wheeler, S. Khwan-On, C. Gerada, M. N. Othman, and X. Huang, "Multiphase power converter drive for fault-tolerant machine development in aerospace applications," *Industrial Electronics, IEEE Transactions on*, vol. 57, no. 2, pp. 575–583, 2010. Cited on page 138.

[97] E. A. Lomonova, E. V. Kazmin, Y. Tang, and J. J. H. Paulides, "In-wheel PM motor: compromise between high power density and extended speed capability," *COMPEL: The International Journal for Computation and Mathematics in Electrical and Electronic Engineering*, vol. 30, no. 1, pp. 98–116, 2011. Cited on pages 29 and 35.

[98] R. Marquardt, "Modular multilevel converter: An universal concept for HVDC-networks and extended DC-bus-applications," in *Proc. Int. Power Electronics Conf. (IPEC)*, 2010, pp. 502–507. Cited on pages 5, 58, 60, and 138.

[99] Mathworks. http://www.mathworks.com. Cited on page 48.

[100] B. C. Mecrow, A. G. Jack, J. A. Haylock, and J. Coles, "Fault-tolerant permanent magnet machine drives," *Electric Power Applications, IEE Proceedings* -, vol. 143, no. 6, pp. 437–442, November 1996. Cited on pages 139, 141, and 144.

[101] T. A. Meynard and H. Foch, "Multi-level conversion: high voltage choppers and voltage-source inverters," in *Power Electronics Specialists Conference, 1992. PESC '92 Record., 23rd Annual IEEE*, June 1992, pp. 397–403 vol.1. Cited on page 182.

[102] H. Michelet, *L'inventeur Isaac De Rivaz (1752-1828), Ses recherches techniques et ses tentatives industrielles.* Pillet Martigny, 1965, in French. Cited on page 1.

[103] S. Miorimoto, M. Sanada, and Y. Takeda, "Wide-speed operation of interior permanent magnet synchronous motors with high-performance current regulator," vol. 30, no. 4, pp. 920–926, 1994. Cited on pages 35, 46, 117, and 118.

[104] Y. Mizuno, R. Ibaraki, K. Kondo, K. Odaka, H. Watanabe, T. Mizutani, K. Kaneshige, and D. Kitada, "Development of new hybrid transmission for compact-class vehicles," SAE Technical Paper, Tech. Rep., 2009. Cited on page 9.

[105] N. Mohan, T. M. Undeland, and W. P. Robbins, *Power electronics: Converters, applications, and design*. Wiley, 2003. Cited on pages 4, 5, 22, 27, 68, 81, 82, and 92.

[106] K. H. Nam, *AC Motor Control and Electric Vehicle Applications*. CRC Press, 2010. Cited on pages 6, 7, 11, 22, 27, 29, 67, and 99.

[107] E. Nipp, "Alternative to field-weakening of surface-mounted permanent-magnet motors for variable-speed drives," in *Proc. Conf Industry Applications Conf. Thirtieth IAS Annual Meeting, IAS '95. Record of the 1995 IEEE*, vol. 1, 1995, pp. 191–198. Cited on page 33.

[108] E. Nipp, "Permanent magnet motor drives with switched stator windings," Ph.D. dissertation, Royal Institute of Technology, Stockholm, Sweden, 1999. Cited on pages 4, 5, 12, 13, 33, 54, 80, 81, 89, 168, and 183.

[109] P. F. v. Oorschot, I. J. M. Besselink, E. Meinders, and H. Nijmeijer, "Realization and control of the lupo EL electric vehicle," in *Proceedings of the Electric Vehicle Symposium (EVS26)*, 2012. Cited on pages 8, 11, 13, and 34.

[110] V. Ostovic, "Memory motors-a new class of controllable flux PM machines for a true wide speed operation," in *Industry Applications Conference, 2001. Thirty-Sixth IAS Annual Meeting. Conference Record of the 2001 IEEE*, vol. 4, September 2001, pp. 2577–2584 vol.4. Cited on page 35.

[111] Oxford dictionaries. Oxford University Press. http://www.oxforddictionaries.com. Cited on page 138.

[112] C. T. Pan and J. H. Liaw, "A robust field-weakening control strategy for surface-mounted permanent-magnet motor drives," *IEEE Transactions on Energy Conversion*, vol. 20, no. 4, pp. 701–709, 2005. Cited on pages 29, 63, 65, 117, and 118.

[113] D. Pan, F. Liang, Y. Wang, and T. A. Lipo, "Extension of the operating region of an IPM motor utilizing series compensation," in *Energy Conversion Congress and Exposition (ECCE), 2012 IEEE*, September 2012, pp. 823 –830. Cited on pages 29, 34, 74, 98, and 110.

[114] J. S. Park and K. H. Nam, "Dual inverter strategy for high speed operation of HEV permanent magnet synchronous motor," in *Proc. 41st IAS Annual Meeting Industry Applications Conf. Conf. Record of the 2006 IEEE*, vol. 1, 2006, pp. 488–494. Cited on pages 34 and 98.

[115] R. H. Park, "Two-reaction theory of synchronous machines generalized method of analysis-part I," *American Institute of Electrical Engineers, Transactions of the*, vol. 48, no. 3, pp. 716 –727, July 1929. Cited on pages 22 and 183.

[116] R. H. Park, "Two-reaction theory of synchronous machines-II," *American Institute of Electrical Engineers, Transactions of the*, vol. 52, no. 2, pp. 352 –354, June 1933. Cited on pages 22 and 183.

[117] L. Parsa and H. Toliyat, "Fault-tolerant interior-permanent-magnet machines for hybrid electric vehicle applications," *Vehicular Technology, IEEE Transactions on*, vol. 56, no. 4, pp. 1546–1552, July 2007. Cited on page 139.

[118] B. Pennings, "Recent material developments for further optimization of the push-belt CVT," in *FISITA World Automotive Congress*, June 2014. Cited on page 80.

[119] Plexim GmbH. http://www.plexim.com. Cited on page 72.

[120] K. Popp and W. O. Schiehlen, *Ground Vehicle Dynamics*. Springer, 2010. Cited on page 6.

[121] J. Pyrhonen, T. Jokinen, and V. Hrabovcova, *Design of rotating electrical machines*. Wiley, 2009. Cited on pages 22, 28, and 69.

[122] W. Qian, H. Cha, F. Z. Peng, and L. M. Tolbert, "55-kW variable 3x DC-DC converter for plug-in hybrid electric vehicles," *IEEE Transactions on Power Electronics*, vol. 27, no. 4, pp. 1668–1678, 2012. Cited on page 32.

[123] K. Rahman, S. Jurkovic, C. Stancu, J. Morgante, and P. Savagian, "Design and performance of electrical propulsion system of extended range electric vehicle (EREV) chevrolet voltec," in *Proc. IEEE Energy Conversion Congress and Exposition (ECCE)*, 2012, pp. 4152–4159. Cited on pages 11 and 13.

[124] S. E. Rauch and L. J. Johnson, "Design principles of flux-switch alternators," *Power Apparatus and Systems, Part III. Transactions of the American Institute of Electrical Engineers*, vol. 74, no. 3, pp. –, January 1955. Cited on page 36.

[125] B. V. Reddy and V. T. Somasekhar, "A decoupled SVPWM technique for a dual inverter four-level open-end winding induction motor drive with voltage balancing of DC-link capacitors," in *Power Electronics, Drives and Energy Systems (PEDES) 2010 Power India, 2010 Joint International Conference on*, December 2010, pp. 1 –6. Cited on page 34.

[126] Renault SA. http://www.renault.com. Cited on pages 11, 13, 35, and 168.

[127] J. Richter, T. Gemasmer, and M. Doppelbauer, "Predictive current control of saturated cross-coupled permanent magnet synchronous machines," in *Power Electronics, Electrical Drives, Automation and Motion (SPEEDAM), 2014 International Symposium on*, June 2014, pp. 830–835. Cited on page 117.

[128] J. Riedemann, R. Pena, R. Cardenas, J. Clare, P. Wheeler, and R. Blasco-Gimenez, "Control strategy of a dual-inverter system for an open-end winding induction machine based on indirect matrix converter," in *Power Electronics and Applications (EPE'14-ECCE Europe), 2014 16th European Conference on*, August 2014, pp. 1–8. Cited on page 55.

[129] J. Rodriguez, J.-S. Lai, and F. Z. Peng, "Multilevel inverters: a survey of topologies, controls, and applications," *Industrial Electronics, IEEE Transactions on*, vol. 49, no. 4, pp. 724–738, August 2002. Cited on page 182.

[130] T. M. Rowan and R. J. Kerkman, "A new synchronous current regulator and an analysis of current-regulated PWM inverters," *Industry Applications, IEEE Transactions on*, vol. IA-22, no. 4, pp. 678–690, July 1986. Cited on page 22.

[131] P. W. Rowland, "Low impact motor control with star-delta starting," in *Textile, Fiber and Film Industry Technical Conference, 1998 IEEE Annual*, May 1998, pp. 10/1 –10/9. Cited on pages 32 and 89.

[132] RUG. (1835) Prominente Groningse hoogleraren; Sibrandus Stratingh (1785-1841) professor of chemistry and technology. Website. Rijksuniversiteit Groningen. http://www.rug.nl/science-and-society/university-museum/prominent-professors/stratingh. Cited on page 2.

[133] S. Sadeghi, L. Guo, H. A. Toliyat, and L. Parsa, "Wide operational speed range of five-phase permanent magnet machines by using different stator winding configurations," *Industrial Electronics, IEEE Transactions on*, vol. 59, no. 6, pp. 2621–2631, 2012. Cited on pages 33 and 54.

[134] J. Salmon and B. Williams, "A split-wound induction motor design to improve the reliability of pwm inverter drives," in *Industry Applications Society Annual Meeting, 1988., Conference Record of the 1988 IEEE*, October 1988, pp. 97–103 vol.1. Cited on page 140.

[135] R. M. Schupbach and J. C. Balda, "Comparing DC-DC converters for power management in hybrid electric vehicles," in *Electric Machines and Drives Conference, 2003. IEMDC'03. IEEE International*, vol. 3, 2003, pp. 1369–1374 vol.3. Cited on page 32.

[136] T. Sebastian and G. Slemon, "Operating limits of inverter-driven permanent magnet motor drives," *Industry Applications, IEEE Transactions on*, vol. IA-23, no. 2, pp. 327–333, 1987. Cited on page 29.

[137] T. Sebastian, G. R. Slemon, and M. A. Rahman, "Modelling of permanent magnet synchronous motors," *Magnetics, IEEE Transactions on*, vol. 22, no. 5, pp. 1069–1071, 1986. Cited on page 29.

[138] F. Senicar, C. Junge, S. Gruber, and S. Soter, "Zero sequence current elimination for dual-inverter fed machines with open-end windings," in *IECON 2010 - 36th Annual Conference on IEEE Industrial Electronics Society*, November 2010, pp. 853 –856. Cited on page 34.

[139] A. Serrarens, T. Purnot, and G. J. Vogelaar, "Twinspeed powershift gearbox for full and range extended EVs," in *FISITA 2014 World Automotive Congress, Maastricht, the Netherlands*, June 2014, pp. 1–7. Cited on pages 11, 13, and 30.

[140] A. Serrarens, W. van Liempt, N. Weel, and L. Merkx, "Powershift module combination of friction brake and planetary gearset," *ATZ worldwide*, vol. 112, no. 6, pp. 30–34, 2010. Cited on page 11.

[141] E. G. Shivakumar, V. Somasekhar, K. Mohapatra, K. Gopakumar, L. Umanand, and S. K. Sinha, "A multi level space phasor based PWM strategy for an open-end winding induction motor drive using two inverters with different DC link voltages," in *Power Electronics and Drive Systems, 2001. Proceedings., 2001 4th IEEE International Conference on*, vol. 1, October 2001, pp. 169–175 vol.1. Cited on page 34.

[142] B. Sneyers, D. Novotny, and T. Lipo, "Field weakening in buried permanent magnet ac motor drives," *Industry Applications, IEEE Transactions on*, vol. IA-21, no. 2, pp. 398–407, March 1985. Cited on pages 29 and 117.

[143] Solar team Eindhoven (STE). http://www.solarteameindhoven.nl. Cited on pages 7 and 8.

[144] V. T. Somasekhar, K. Gopakumar, and M. R. Baiju, "Dual two-level inverter scheme for an open-end winding induction motor drive with a single DC power supply and improved DC bus utilisation," *Electric Power Applications, IEE Proceedings* -, vol. 151, no. 2, pp. 230 – 238, March 2004. Cited on page 55.

[145] V. T. Somasekhar, S. Srinivas, and K. K. Kumar, "Effect of zero-vector placement in a dual-inverter fed open-end winding induction-motor drive with a decoupled space-vector PWM strategy," *Industrial Electronics, IEEE Transactions on*, vol. 55, no. 6, pp. 2497 –2505, June 2008. Cited on pages 34 and 41.

[146] W. L. Soong and T. J. E. Miller, "Field-weakening performance of brushless synchronous AC motor drives," *IEE Proceedings-Electric Power Applications*, vol. 141, no. 6, pp. 331–340, 1994. Cited on pages 29 and 74.

[147] L. d. Sousa and H. Dogan, "Method of evaluating the zero-sequence inductance ratio for electrical machines," in *Power Electronics and Applications (EPE 2011), Proceedings of the 2011-14th European Conference on*, 2011, pp. 1–10. Cited on pages 55 and 168.

[148] R. Spee and A. Wallace, "Remedial strategies for brushless dc drive failures," *Industry Applications, IEEE Transactions on*, vol. 26, no. 2, pp. 259–266, March 1990. Cited on page 138.

[149] W. Stevenson, *Elements of power system analysis*, ser. McGraw-Hill series in electrical engineering: Power and energy. McGraw-Hill, 1982. Cited on page 22.

[150] STMicroelectronics (ST). http://www.st.com. Cited on pages 31 and 83.

[151] B. Stumberger, G. Stumberger, D. Dolinar, A. Hamler, and M. Trlep, "Evaluation of saturation and cross-magnetization effects in interior permanent-magnet synchronous motor," *Industry Applications, IEEE Transactions on*, vol. 39, no. 5, pp. 1264–1271, September 2003. Cited on page 38.

[152] M. Takei, Y. Harada, and K. Ueno, "600 V-IGBT with reverse blocking capability," in *Power Semiconductor Devices and ICs, 2001. ISPSD '01. Proceedings of the 13th International Symposium on*, 2001, pp. 413–416. Cited on page 82.

[153] M. Takei, M. A. Takei, and H. Fujimoto, "Application technologies of reverse-blocking IGBT," *Fuji Electric*, vol. 75, no. 8, p. 4, 2002. Cited on page 81.

[154] Y. Tang, J. J. H. Paulides, I. J. M. Besselink, F. Gardner, and L. E. A., "Indirect drive in-wheel system for HEV/EV traction," in *Proceedings of the EVS27 International Battery, Hybrid and Fuel Cell Electric Vehicle Symposium, Barcelona, Spain*, vol. 27. EVS, November 2013, pp. 1–9. Cited on pages 11 and 13.

[155] Y. Tang, J. J. H. Paulides, T. E. Motoasca, and E. A. Lomonova, "Flux-switching machine with DC excitation," *Magnetics, IEEE Transactions on*, vol. 48, no. 11, pp. 3583 –3586, November 2012. Cited on page 35.

[156] J. A. Tapia, M. Aydin, S. H., and T. A. Lipo, "Sizing equation analysis for field controlled PM machines: a unified approach," in *Electric Machines and Drives Conference, 2003. IEMDC'03. IEEE International*, vol. 2, June 2003, pp. 1111–1116 vol.2. Cited on page 35.

[157] World's first electric car built by victorian inventor in 1884. The Telegraph. http://www.telegraph.co.uk. Cited on page 2.

[158] Tesla Motors, Inc. http://www.teslamotors.com. Cited on pages 4 and 168.

[159] Triphase NV. http://www.triphase.be/. Cited on pages 73, 91, and 201.

[160] C. Turpin, P. Baudesson, F. Richardeau, F. Forest, and T. Meynard, "Fault management of multicell converters," *Industrial Electronics, IEEE Transactions on*, vol. 49, no. 5, pp. 988–997, October 2002. Cited on page 140.

[161] University racing Eindhoven (URE). http://universityracing.tue.nl/. Cited on pages 8 and 32.

[162] P. A. Veenhuizen, B. Bonsen, T. W. G. L. Klaassen, P. H. W. M. Albers, C. Changenet, and S. Poncy, "Pushbelt CVT efficiency improvement potential of servo-electromechanical actuation and slip control," in *2004 CVT Congress*, 2004. Cited on page 80.

[163] B. Vermulst, J. Duarte, C. Wijnands, and E. Lomonova, "Single-stage three-phase AC to DC conversion with isolation and bi-directional power flow," in *Proceedings of the 40th Annual Conference on IEEE Industrial Electronics Society (IECON 2014)*. IEEE, October - November 2014. Cited on page 5.

[164] G. Waltrich, *Energy management of fast-charger systems for electric vehicles; experimental investigation of power flow steering using bidirectional three-phase three-port converters*. G. Waltrich, 2013. Cited on pages 4 and 5.

[165] F. Wang, "Flexible operation of grid-interfacing converters in distribution networks: Bottom-up solutions to voltage quality enhancement," Ph.D. dissertation, Eindhoven University of Technology, Eindhoven, The Netherlands, 2010. Cited on pages 25, 40, and 183.

[166] L. Weeks, *The History of the Automobile and Its Inventors; from the beginning until 1900*, ser. 9783861952428. TEC books, 2010. Cited on page 1.

[167] B. A. Welchko, T. A. Lipo, T. M. Jahns, and S. E. Schulz, "Fault tolerant three-phase AC motor drive topologies: a comparison of features, cost, and limitations," *Power Electronics, IEEE Transactions on*, vol. 19, no. 4, pp. 1108 – 1116, July 2004. Cited on pages 138 and 139.

[168] T. J. Woolmer and M. D. McCulloch, "Analysis of the yokeless and segmented armature machine," in *Electric Machines Drives Conference, 2007. IEMDC '07. IEEE International*, vol. 1, May 2007, pp. 704–708. Cited on pages 11 and 13.

[169] J. Wouters, *De elektrische auto; is het marktaandeel van 1914 in 2020 haalbaar?* Uitgeverij Pepijn BV, 2013, in Dutch. Cited on pages 2, 3, and 4.

[170] Y.-P. Yang, J.-J. Liu, T.-J. Wang, K.-C. Kuo, and P.-E. Hsu, "An electric gearshift with ultracapacitors for the power train of an electric vehicle with a directly drive wheel motor," *IEEE Transactions on Vehicular Technology*, vol. 56, no. 5, pp. 2421–2431, September 2007. Cited on page 32.

[171] Yasa Motors. http://www.yasamotors.com/products/yasa-750/. Cited on pages 11 and 13.

[172] Zahnradfabrik (ZF) Friedrichshafen AG. http://www.ZF.com. Cited on page 9.

[173] B. Zhang, Y. Wang, M. Doppelbauer, and M. Gregor, "Mechanical construction and analysis of an axial flux segmented armature torus machine," in *Electrical Machines (ICEM), 2014 International Conference on*. IEEE, 2014, pp. 1293–1299. Cited on page 11.

[174] M. T. Zhang, M. M. Jovanovic, and F. C. Lee, "Analysis and evaluation of interleaving techniques in forward converters," *Power Electronics, IEEE Transactions on*, vol. 13, no. 4, pp. 690–698, 1998. Cited on pages 5 and 15.

[175] K. Zhou and D. Wang, "Relationship between space-vector modulation and three-phase carrier-based PWM: a comprehensive analysis [three-phase inverters]," *IEEE Transactions on Industrial Electronics*, vol. 49, no. 1, pp. 186–196, 2002. Cited on pages 31 and 65.

[176] Z. Q. Zhu and D. Howe, "Electrical machines and drives for electric, hybrid, and fuel cell vehicles," *Proceedings of the IEEE*, vol. 95, no. 4, pp. 746–765, 2007. Cited on page 22.

[177] Z. Q. Zhu, Y. Pang, D. Howe, S. Iwasaki, R. Deodhar, and A. Pride, "Analysis of electromagnetic performance of flux-switching permanent-magnet machines by nonlinear adaptive lumped parameter magnetic circuit model," *Magnetics, IEEE Transactions on*, vol. 41, no. 11, pp. 4277–4287, November 2005. Cited on page 36.

About the author

Thomas Gerrits was born on July 23th, 1983 in Wanssum, the Netherlands. He attended secondary school at Raayland College in Venray, the Netherlands. He received the B.Eng. degree in electrical engineering from Fontys University of Applied Sciences, Eindhoven, the Netherlands, in 2004, and the M.Sc. degree in electrical engineering from Eindhoven University of Technology, Eindhoven, the Netherlands, in 2009, specializing in power electronics.

After working as a research assistant from 2009 to 2010 within the Electromechanics and Power Electronics group of the Eindhoven University of Technology, Eindhoven, the Netherlands, he started a Ph.D. project within the same group, of which the results are presented in this dissertation. Since 2015 he is employed at Heliox B.V. in Best, the Netherlands.

Starting with a paper based on his M.Sc. graduation assignment, he authored or co-authored 1 journal publication, 1 international patent, and 10 conference publications. In 2011, he received the IEEE industry application society (IAS) award for second best paper of the year, and in 2015 he received the award for best paper on ecological vehicles from the ecological vehicles and renewable energies (EVER) conference, 2015, both as first author.